Monitoring the Gelation Mechanism of Resorcinol-Formaldehyde Xerogels

Stewart John Taylor

Thesis submitted to the University of Strathclyde for the degree of Doctor of Philosophy

Department of Chemical and Process Engineering

University of Strathclyde

2014

Abstract

Resorcinol-Formaldehyde (RF) xerogels are a type of porous material used in many applications, such as gas storage. These applications often require fine control of the material's porosity, and while it is known that the porosity of a xerogel can be changed through altering synthesis variables, it is not clear why these changes have such an impact.

To understand this effect, the gelation process was studied using dynamic light scattering (DLS), with the xerogel products undergoing low temperature nitrogen adsorption measurements to determine textural properties. RF gels are composed of cross-linked clusters and DLS was used to study changes in how these clusters grow. It was found that cluster growth was a thermodynamically controlled process, and for a given catalyst, how the cluster size grows with time was independent of the catalyst concentration. However, the catalyst did kinetically control the number concentration of clusters initially formed, and in turn, the size to which they, therefore, had to grow to reach a critical volume fraction to form the gel, such that higher catalyst concentrations led to smaller clusters making up the gel. This resulted in smaller intercluster voids, hence, smaller pores.

The catalysts used also demonstrated a range of different abilities to stabilise the colloidal suspension of clusters. This also affected cluster size, with less stabilising catalysts resulting in larger clusters.

This knowledge led to the ability to further tailor the porosity by introducing a secondary catalyst, in various forms, into a separate gelling mixture. The different catalysts, with their varied abilities to stabilise the growing clusters, and the range of concentrations used, resulted in a variety of cluster sizes within the final gel, which changed the porosity of the xerogel products formed.

Table of Contents

List of Figures

List of Tables

List of Reactions

List of Schemes

1 Introduction

Aerogels are a class of materials with low densities, high porosities and large surface areas, made from a wide range of precursors. This combination of properties makes them ideally suited to a wide range of applications. The aerogel structure is composed of small particles tightly bound together. The size of these particles determines how closely they can pack, and in turn, the size of the voids between particles which become the pores. This also then relates to the volume of these pores and the surface area of the material. Porosity will be covered in much greater detail in subsequent chapters.

Different types of aerogel, their synthesis and some applications will now be discussed.

1.1 Origin of Aerogels

S. S. Kistler developed the first aerogels in 1932, made from inorganic silica precursors.[1] The chosen starting material was sodium silicate, which, when reacted with hydrochloric acid produced a silica network according to Reaction 1. The water and sodium chloride generated by the reaction remained trapped within the silica network, producing a hydrogel.

$$Na_2SiO_3 + 2.HCl + (x-1)H_2O \rightarrow SiO_2.xH_2O + 2.NaCl$$
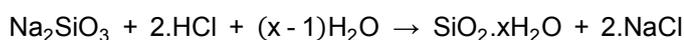
Reaction 1: Kistler's silica hydrogel formation reaction.

In 1846, Graham had noted that the water within a silica gel could be successfully exchanged with an organic liquid.[2] Kistler used this observation to postulate that, as the water and solid silica network were separate phases within the material, they could be treated independently. As such, the water could be replaced with a gas without destroying the network structure.

To facilitate this removal process, Kistler first tried a simple evaporative method. Unfortunately, he found that the surface tension and capillary forces within the pores of the network caused the structure to collapse. To prevent this collapse from occurring, the vapour-liquid equilibrium causing these forces had to be eliminated. To do this, the gels were heated under pressure until the critical temperature of water was reached. With the pressure subsequently reduced, while maintaining the temperature, gaseous water would expand out of the pores leaving the structure intact. However, this supercritical drying process required extreme conditions, but

worse still, the supercritical water reacted with the silica network and caused it to break down.

To overcome this problem, Kistler exchanged the aqueous pore liquid for ethanol. This did not react with the silica structure, and had the added benefit of becoming supercritical under much less harsh conditions. However, the solvent exchange was a time consuming process and limited the usefulness of these new materials.

It wasn't until the 1970s that the Teichner group at the University of Lyon in France discovered a way to eliminate the issue of the time consuming solvent exchange.[3] By replacing the sodium silicate with an organosilane, namely tetramethoxysilane (TMOS), a silica alcogel was formed directly, with methanol as the pore fluid, as shown in Reaction 2.

$$Si(OCH_3)_4 + 2.H_2O \rightarrow SiO_2 + 4.CH_3OH$$
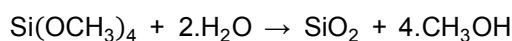
Reaction 2: Teichner group direct silica alcogel formation.

Supercritical extraction of the entrained methanol, once more yielded a silica aerogel.

1.2 Development of Aerogels

The silica aerogels produced had a number of remarkable properties, including high porosity (~99%) and large surface area (1000 m^2/g), leading to apparent densities between 0.03 and 0.35 g cm^{-3}. They were also found to have low thermal conductivity (~0.01 W/m.K), high transmission of visible light (99%), low dielectric constant (~1.0 – 2.0), low refractive index (~1.05) and low sound velocity (100 m/s).[4] This makes them ideally suited to a number of applications.

1.2.1 Applications of Silica Aerogels

Aerogels have seen much interest in the field of thermal insulation.[5] Exhibiting such low thermal conductivity make them ideal for this purpose. As they also transmit visible light, it is possible to use these materials to construct windows.[6]

Silica aerogels have also been used by NASA in their space program.[7] Thanks to the extremely low density, the material is light enough to be carried aboard space craft and has been used to collect samples of cosmic dust. NASA has also used the aerogel as insulation on the Mars rovers. Figure 1 shows silica aerogel being used.
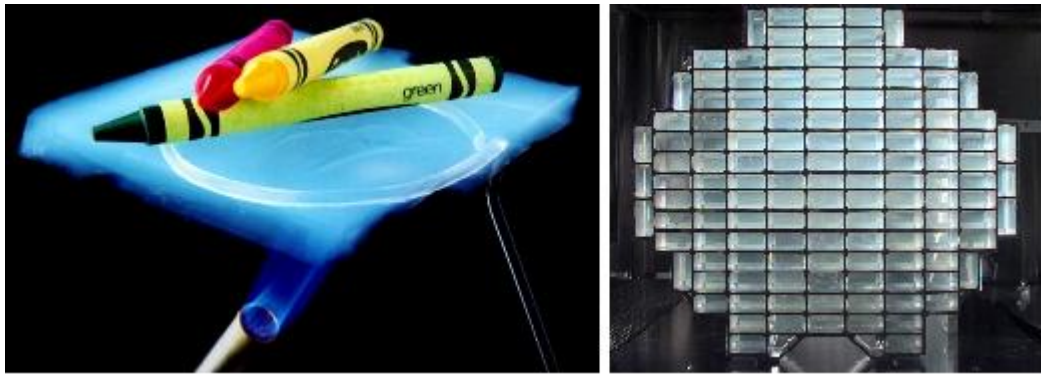
Other applications include clothing[4] and particle detectors, such as Geiger counters and Cherenkov detectors.[10] The applications of other aerogel materials will be covered in detail in Section 1.8.

1.2.2 Metal Based Aerogels

Silica is not the only inorganic material with which aerogel structures can be produced. Many of both the main group and transition metals can be formed into aerogels of many types. The metal tends to be in compound form in order to produce the gel.

1.2.2.1 Metal Oxide Aerogels

Like in silica gels, the metal is most commonly in the oxide form in the final aerogel structure. As mentioned above, both main group and transition metals are often used.

Alumina has been the focus of many studies to improve its usefulness as an aerogel.[11, 12] At first difficult to produce in monolithic form due to the precursor reactivity, low mechanical strength and propensity to crack during drying, their envisaged usefulness could not be realised. However, through the development of new synthesis routes, stable monoliths could be produced that showed superior properties such as thermal conductivity, when compared with a silica aerogel of equivalent density.

Likewise, titania aerogels have become popular due to their many uses, in particular as a photocatalytic or catalyst support material.[13, 14] By altering the synthesis parameters such as precursor to solvent ratio and the type of catalyst used, it was possible to tailor the textural properties and surface acidity of the materials for a particular catalytic purpose.[15]

Other metal oxides that have been studied include chromia,[16, 17] zirconia[18, 19] and ruthenium oxide.[20] In 2001 Gash *et al.* developed a new aerogel synthesis route for both the main group and transition metals. Using inorganic salts as precursors, it was possible to develop aerogels from iron, indium, gallium, hafnium, tantalum, niobium and tungsten.[21] Despite the number of metals mentioned, this list is by no means exhaustive.

Figure 2 shows a selection of metal oxide aerogels, demonstrating the wide range of colours that are produced.
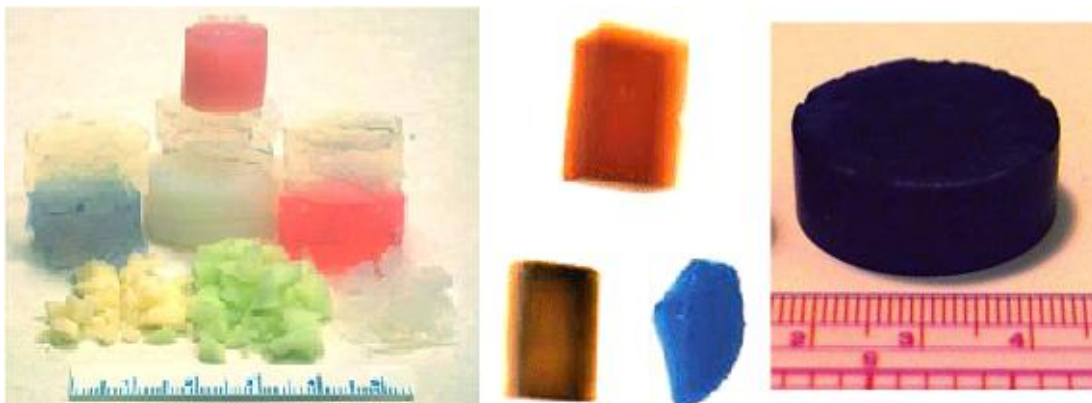
Figure 2: A selection of metal oxide aerogels, showing the wide variety of colours produced.[22]

1.2.2.2 Metal Chalcogenide Aerogels

Metal chalcogenides have properties which make them particularly useful in the fields of luminescence, electronics and optics. By converting these materials to aerogel form, it would therefore be possible to take advantage of the additional porous properties imparted to the gel.

Cadmium sulphide was the first metal chalcogenide turned into an aerogel. It was found that optical properties, such as the band-gap and band-edge emission of the aerogel could be easily controlled through heating the material. This heating process increased the primary particle size and changed the quantum confinement effects of the particle.[23]

Semiconducting metal chalcogenides such as germanium sulfide have also been studied due to their optoelectronic properties, due to exhibiting substantially lower optical transmission losses in the IR region when compared with silica.[24]

It is also possible to produce hybrid aerogels, wherein both silica and a metal oxide are mixed in the final gel product. Traditional methods have seen silica co-gelated with various lanthanide oxides,[25] vanadium oxide[26] and iron oxide[27] to name but a few. The mixed oxide gels could then be sintered into full density glasses,[25] exhibit catalytic and ionic properties of great interest[26] and allow greater control over the molecular scale mixing and flexibility of the chemical composition when compared to other materials and methods of production.[27]

However, in most cases, silica was the dominant component within the gel, with the metal oxide dispersed throughout the silica structure. The method of synthesis also had to be altered, depending on the metal oxide required to be introduced to the silica matrix. To remedy this, Clapsaddle *et al.* developed a new method for creating hybrid aerogels with the metal oxide as the dominant component.[28] This was achieved by the addition of an epoxide during gelation. Altering the epoxide used led to controllability of the metal oxide-silica composition. Due to the large number of organosilanes available, this method also made it possible to incorporate a number of organic functionalities into a bulk metal oxide matrix.

Having the metal oxide as the dominant phase was desirable when using the gels as energetic materials in thermite reactions, where the metal oxide is reacted with a fuel metal. The silica within the system was used to tailor the energy released by the reaction, by not taking part in the redox reaction.[29, 30]

1.3 Resorcinol-Formaldehyde Aerogels

In 1989, Pekala and Kong, working at the Lawrence Livermore National Laboratory, reacted resorcinol with formaldehyde in aqueous solution in the presence of basic sodium carbonate.[31, 32] This resulted in the formation of a resorcinol-formaldehyde (RF) hydrogel. Tewari *et al.*, working at the same institute, had previously developed a method of drying silica alcogels using supercritical carbon dioxide.[33] The critical point of the carbon dioxide was reached at much lower temperature and pressure, further reducing the severity of the conditions required to dry the gels. Pekala subsequently made use of this development in order to dry the newly formed RF hydrogels. In order to facilitate this drying process, the water within the hydrogel structure had first to be exchanged with acetone. This step was required to guarantee complete miscibility of the pore fluid with the liquid CO_2 used during

drying, and ensuring that complete removal would occur. Once drying was complete, the first organic aerogel had been produced.

1.4 Reactants in the Synthesis of RF Gels

1.4.1 Resorcinol

Resorcinol is the common name for the compound designated 1,3-dihydroxybenzene.[34] As the name suggests, it is an aromatic molecule, with hydroxyl groups at the 1 and 3 positions of a benzene ring. Its structure is shown in Figure 3.
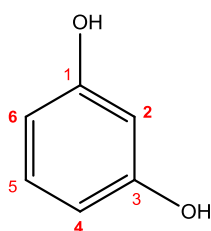
Figure 3: Structure of a resorcinol molecule.

The electron donating ability of the two hydroxyl groups in the structure greatly increases the reactivity at the adjacent 2, 4 and 6 positions.[34] This makes resorcinol an excellent nucleophile. By considering the resonance forms of the structure in Figure 4, the nature of this activation at carbons 2, 4 and 6 can be seen.
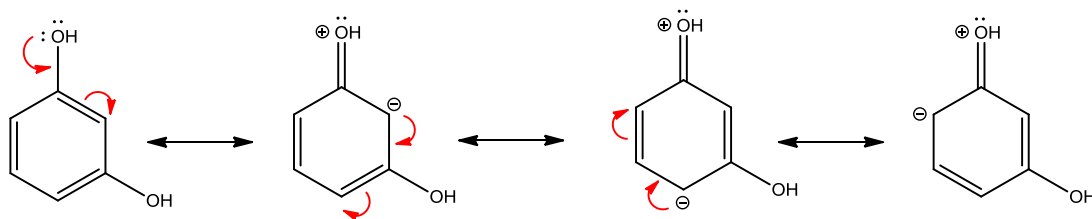
Figure 4: Resonance forms of the resorcinol molecule.

The carbon at position 5 remains unactivated, rendering it virtually unreactive under normal reaction conditions.[34]

1.4.2 Formaldehyde

Formaldehyde is the simplest of the carbonyl group containing aldehyde family. By once more considering all of the resonance forms of the molecule, it can be seen that the carbon plays host to a partial positive charge (Figure 5).
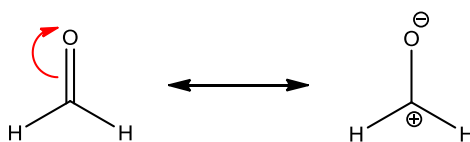
The subsequent polarisation makes the carbon centre susceptible to nucleophilic attack. As previously stated, resorcinol is a nucleophile, and these complimentary charges lead to reaction between the two molecules.

1.4.3 Alternative Precursors

Organic gels have not been limited to being made from resorcinol and formaldehyde. There are many other precursors that have been used.

1.4.3.1 Alternatives to Resorcinol

As resorcinol is a derivative of phenol, phenol itself has commonly been used in the creation of phenol-formaldehyde gels. The structure of phenol is shown in Figure 6. Phenol tends to be cheaper than resorcinol, reducing the costs associated with gel production. However, the loss of the second hydroxyl group from the structure makes phenol both less soluble and less reactive than resorcinol. Higher catalyst concentrations are therefore required to promote the reaction between phenol and formaldehyde (see Section 1.5 for further details on the role of the catalyst). Both Wu *et al.*[35] and Scherdel and Reichenauer [36] conducted detailed studies on phenol-formaldehyde gels, changing a number of synthesis variables and studying the effect this had on the gel properties. The flexibility of the gel making process will be discussed in greater depth in Section 1.7. Both bodies of work found that gels could be made that had comparable properties to those of the resorcinol-formaldehyde counterparts. However, the ranges in which the process variables could be changed were significant reduced.

Hair *et al.* attempted to use the isomeric forms of resorcinol to make gels, those being catechol (the 1,2-isomer) and hydroquinone (the 1,4-isomer) as shown in Figure 6.[37] In theory, the placing of the hydroxyl groups should lead to all of the unsubstituted carbons in the ring being activated. However, this is not the case and only two of the sites are active at any given time, in contrast with resorcinol having three active sites at all times. Furthermore, the use of hydroquinone resulted in precipitation of reactants, while catechol produced a very dense product, making both of the isomers unsuitable for gel making.

More promising was the use of trisubstituted phloroglucinol (Figure 6), which like resorcinol has three permanently active sites.[37] Kim *et al.* investigated several phloroglucinol-formaldehyde gels synthesised under various conditions.[38] It was found that the phloroglucinol based gels had improved properties when compared to the analogous resorcinol gels but the preparation had to be carried out in ethanol to ensure dissolution of the phloroglucinol precursor.
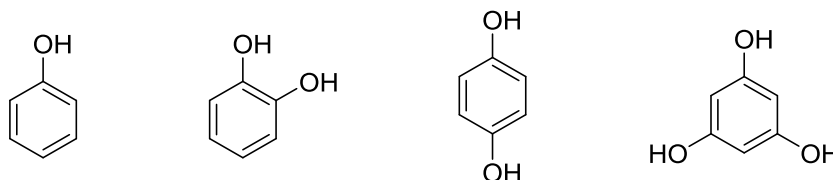
Figure 6: Alternatives to resorcinol, showing from left to right, phenol, catechol, hydroquinone and phloroglucinol respectively.

Further investigation into the replacing of resorcinol with cheaper alternative precursors has looked at the cresol family of isomers shown in Figure 7.
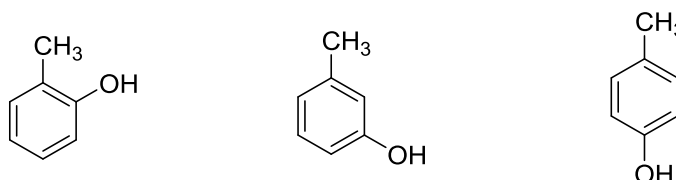
Figure 7: Isomeric forms of cresol, showing from left to right the ortho-, meta- and para- forms respectively.

The isomers are difficult to separate and so preparation of gels tends to be carried out by utilising a mixture of the three. Li and his associates have conducted a number of studies on cresol-formaldehyde gels.[39-42] The results of these studies showed that like RF gels, cresol-formaldehyde gels are predominantly mesoporous (pores with sizes between 2 and 50 nm) with comparable surface areas. They also found that they were similar to RF gels in that the catalyst concentration was vital in controlling the porosity of the synthesised gel (see Section 1.7 for more detail).

1.4.3.2   Alternatives to Formaldehyde

Formaldehyde can also be substituted in the creation of organic gels. The most common alternative is furfural, as shown in Figure 8.
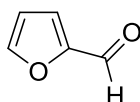
Furfural is not soluble in water, resulting in the need to carry out the synthesis in an organic solvent such as ethanol. It can also self-condense under acidic conditions in a process known as furfural resinification.[36]

However, this has not stopped several studies into the formation of resorcinol-furfural gels. Tian and his associates used acetic acid to catalyse the reaction between resorcinol and furfural.[43, 44] They found that, once more, the gel properties were dependent on the initial catalyst concentration and could be modified accordingly. In contrast, Wu *et al.* used an organic base as catalyst.[45] The concentration of catalyst that would produce a viable gel was found to be limited to below a resorcinol to catalyst ratio of 350.

1.4.3.3 Nitrogen Containing Precursors

Figure 9 shows the structure of melamine and urea, nitrogen containing precursors used in the formation of organic gels.
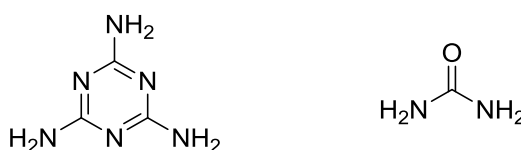
Figure 9: Nitrogen containing precursors, showing melamine on the left and urea on the right.

Replacing resorcinol with melamine can result in optically transparent gels, as reported by both Ruben and Pekala,[46] and Nguyen and Dao.[47] These studies found that producing a transparent gel was highly dependent on the synthesis conditions, being reliant on the pH of the system and the reactant concentration. Out with the viable range, the gels produced were opaque or translucent. The limited solubility of melamine in water makes the preparation of these gels more complicated, involving several heating and cooling steps.

Alternatively, it is possible to replace only part of the resorcinol and formaldehyde with melamine or urea to create nitrogen doped RF gels. This was the case in the work of Gorgulho *et al.*[48] and Rocha *et al.*[49] This process resulted in varying nitrogen functionality on the surface of the gel matrix,[48] making the materials excellent

catalysts for advanced oxidation processes (see Section 1.8 for more on the uses of RF gels).[49]

1.5   The Reaction between Resorcinol and Formaldehyde

As noted, the complimentary partial charges on resorcinol and formaldehyde make them likely to react. Indeed, this is the case at room temperature; however, the reaction is very slow. One of the methods routinely used in order to increase the rate of reaction is through the addition of an acid or a base. This added acid or base is routinely known as the catalyst in the formation of RF gels, due to its ability to speed up the initial reaction. However, as it decomposes/is consumed during the gelation process, and is subsequently not recoverable, this name is not strictly accurate.

1.5.1   Acid Promoted Reactions

The acid promoted reaction between resorcinol and formaldehyde is thought to occur in multiple stages.[50] First, formaldehyde is protonated by the acid (Scheme 1).
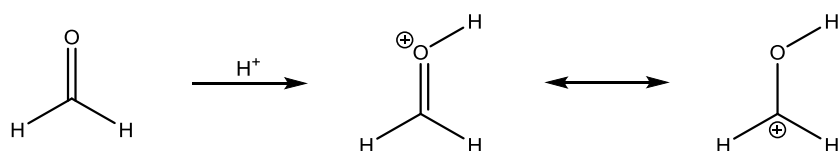
Scheme 1: Protonation of formaldehyde.

This protonated formaldehyde then reacts with the 2, 4 or 6 position on resorcinol to form the hydroxymethyl derivative, which is also subsequently protonated (Scheme 2).
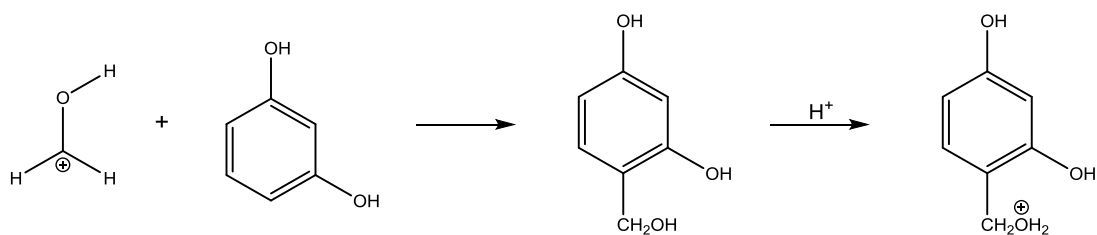
Scheme 2: Formation and protonation of hydroxymethyl derivatives.

Further reaction with resorcinol, hydroxymethyl derivatives and formaldehyde, with the loss of water, leads to the formation of methylene and methyl ether bridged oligomers (Scheme 3).
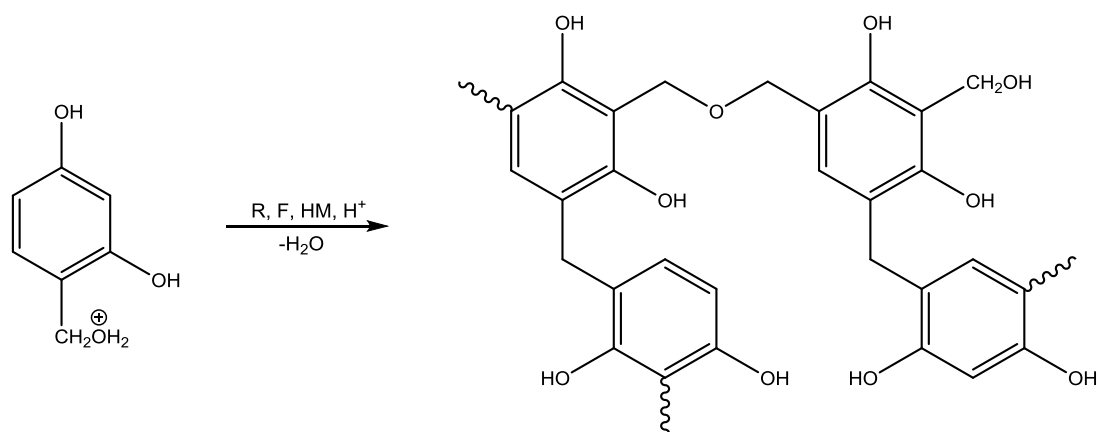
Scheme 3: Formation of growing oligomers.

These oligomers continue to grow, forming clusters, which then through cross-linking make up the gel network.

1.5.2 Base Promoted Reactions

The more popular base promoted route[51, 52] also involves a multi-stage process, having been described as such since the original work by Pekala.[31] The process begins with base abstraction of a proton from resorcinol to form an anion (Scheme 4).
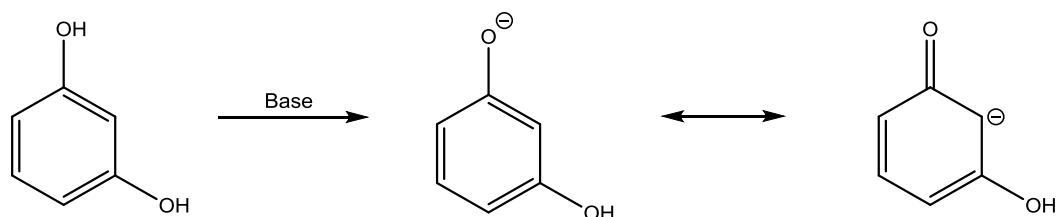
Scheme 4: Proton abstraction from resorcinol to form the corresponding anion.

This anion then reacts with formaldehyde to, once more, form the hydroxymethyl derivative (Scheme 5).
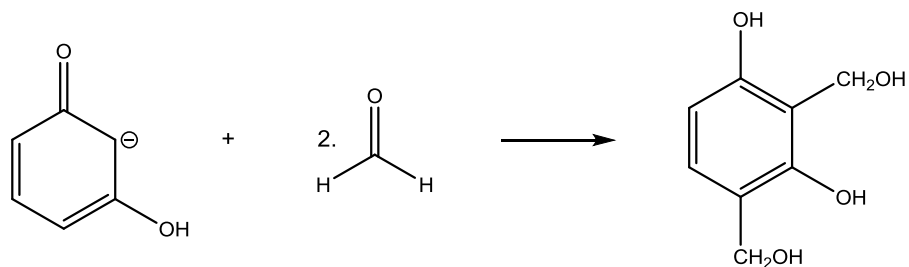
Scheme 5: Formation of hydroxymethyl derivatives, with common resorcinol:formaldehyde stoichiometry of 1:2.

The hydroxymethyl derivative is again protonated and reacts further with resorcinol, formaldehyde and hydroxymethyl derivatives to form the growing oligomers, which aggregate and cross-link into the network structure (Scheme 6).
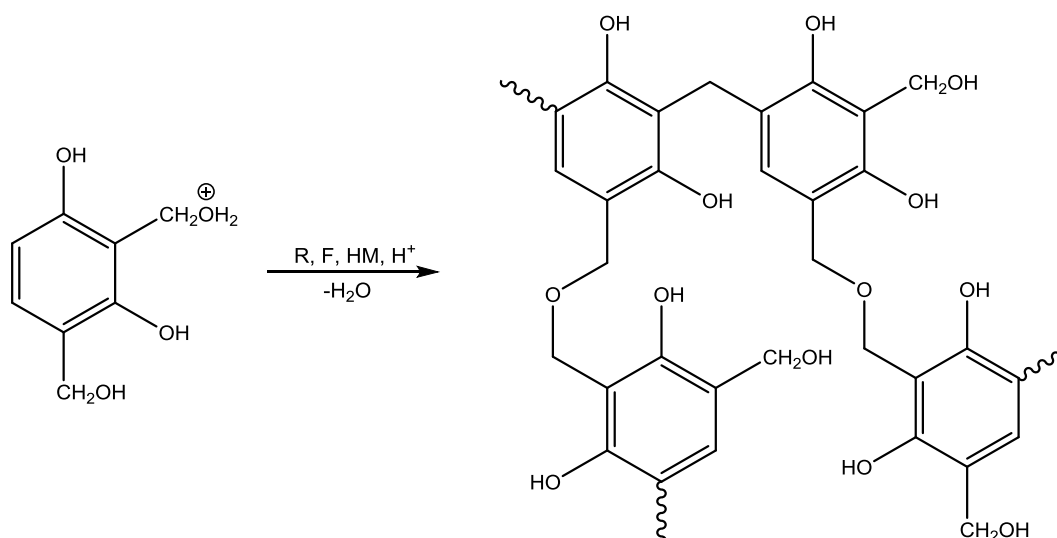
Scheme 6: Formation of growing oligomers.

The addition of either an acid or a base, to determine the level of protonation or proton abstraction respectively, will obviously have a major influence on the initial pH of the reaction. This factor will be covered in more detail in Section 1.7.

1.6   Resorcinol-Formaldehyde Gel Formation

As outlined above (Section 1.3), the formation of resorcinol-formaldehyde gels is, like for the analogous silica gels, a multi-step process. However, when broken down into the individual steps it can be seen that the process is not complicated. Figure 10 shows each of these steps in order.
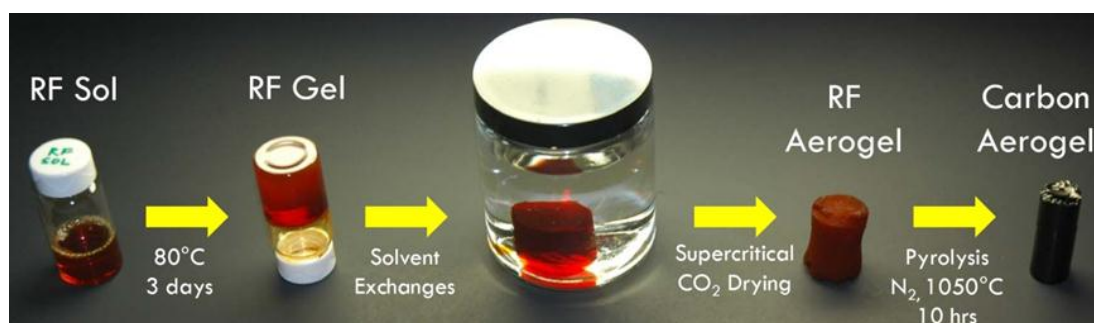
Figure 10: Multi-step RF gel formation process.[53]

1.6.1 Sol-Gel Transition

As for the formation of silica gels, the first step in the synthesis of RF gels is a sol-gel transition. As the name implies, this involves the making of a sol, which gradually transforms into a gel over time. A schematic diagram of the process is shown in Figure 11.
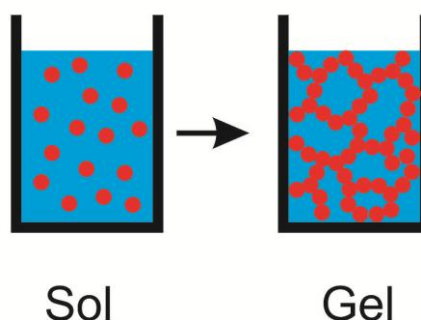
Figure 11: Schematic diagram of the general sol-gel transition.[54]

1.6.1.1 Sols and Gels

A sol is simply described as a liquid phase containing colloidal particles suspended throughout. The colloidal particles have sizes in the range of 1 – 1000 nm, meaning they are so small that gravity has little influence. Instead, the particles move through Brownian motion, where collisions between the particles and solvent molecules cause random movements.[55] More detail on the Brownian motion of particles will be provided in Section 3.5.

On the other hand, a gel is a continuous, three dimensional solid network that spans the entire volume of the original dispersion medium. As the network encompasses the entire volume, the sol will no longer flow, due to the trapping of the solvent. The solute (gel network) transmits any forces applied to the system and so resists flow. The time period that this takes is known as the gelation time, with gelation immediately preceded by a rapid increase in viscosity, as well as the development of an elastic response to stress.[55, 56]

1.6.1.2 Transition Mechanisms

The transition from sol to gel has typically been described in the literature as occurring in one of two ways; microphase separation or colloidal aggregation.[57]

Many inorganic gels, such as those detailed above in Sections 1.1 and 1.2, are described as forming through colloidal aggregation. At first, polymerisation of the

precursor occurs, which forms dense particles with colloidal dimensions. These dense particles subsequently aggregate together and fill the gel volume.[57]

Yamamoto *et al.* described the RF sol-gel transition as being a result of colloidal aggregation.[58] Through the use of both static and dynamic light scattering, they were able to monitor the growth of colloidal particles during the gelation process. At a certain time in the sol-gel transition, a rapid increase in the particle size was observed. This increase was subsequently attributed to the aggregation process.

Formation of the gel in this way would result in the 'string of pearls' appearance often used to describe the look of RF gels. A scanning electron microscopy (SEM) image showing this appearance is shown in Figure 12.
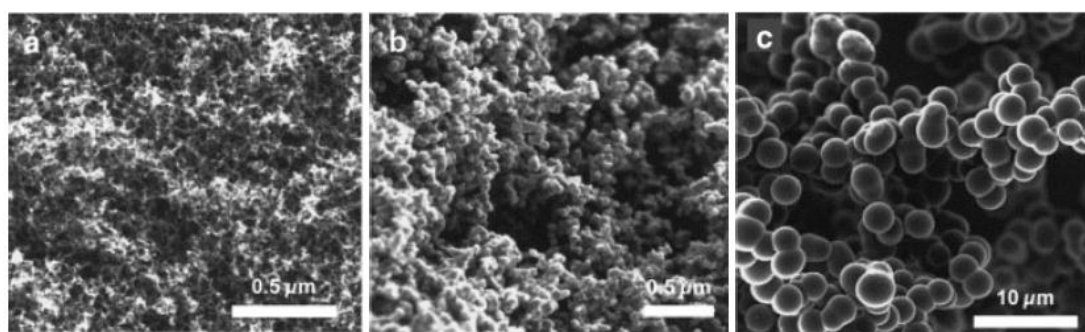
Figure 12: SEM images of various RF gels showing the 'string of pearls' appearance.[59]

In contrast, for RF gels and other organic systems, the most commonly described method of formation is a microphase separation.[60-62] As the oligomeric chains grow, their solubility in the aqueous solvent decreases. This leads to the eventual demixing of the oligomers from the bulk solution. As the oligomers demix, they fold in on themselves, trapping pockets of the solvent in what will become the pores of the gel. This process can also explain the 'string of pearls' appearance.

It was this microphase separation model that Schaefer *et al.*[60] and Pekala and Schaefer[61] postulated as being responsible for RF gel formation. Depending on the catalyst concentration, cross-linking within the system occurred to varying degrees. This lead to differing size domains, although, in all cases, it was their interpretation that microphase separation was the result.

Gommes and Roberts used small-angle x-ray scattering (SAXS) to try and distinguish between the two theories.[57] The study found that each method could generate morphologies that were very similar. They therefore reasoned that

microphase separation and colloidal aggregation were the two extreme views of the same gelation process.

1.6.2 Curing

Immediately after gelation, the formed structure tends to be soft and easily deformable. A curing step is therefore required to strengthen the gel. By leaving the newly formed gel at elevated temperatures for a period of time, significant cross-linking occurs within the structure. The new links give the gel mechanical strength, allowing it to be dried without destroying the porous network.

1.6.3 Solvent Exchange

As for the original silica aerogels, a solvent exchange step is often required to replace the water entrained within the gel network with a more suitable alternative solvent. The new solvent chosen tends to have a lower boiling point and lower surface tension than water, while also being compatible with the chosen drying method.

1.6.4 Drying

Drying the gels to remove solvent from within the porous network plays an important role in determining the properties of the dried product. There are several methods of drying gels, with each resulting in a slight variation of the final product. The three most commonly used are supercritical drying, subcritical drying and freeze drying.

1.6.4.1 Supercritical Drying

As described above (Section 1.3) RF gels can be supercritically dried, typically using carbon dioxide. In this case, removal of the water from the system in exchange for an organic solvent such as acetone is essential to ensure complete miscibility between the pore liquid and liquid CO_2. After being placed in a temperature controlled pressure vessel, the pressure is increased to above the critical pressure of the drying solvent. The temperature is then also increased to exceed the solvent's critical temperature. Subsequently, the pressure in the vessel is reduced, removing the solvent from the pores in a gaseous state. Drying in this way creates an aerogel.

1.6.4.2 Subcritical Drying

Subcritical drying typically involves heating the wet gels at ambient pressure or under vacuum. This results in the formation of a vapour-liquid equilibrium which can destroy the porous network through capillary forces.

The liquid molecules within the pore network experience cohesive forces in all directions. At the liquid surface, these forces are stronger, due to a greater attraction to the adjacent water molecules rather than the air above. This results in a surface tension, the force required to break the surface of the liquid. As water molecules have a strong cohesive force, it has a correspondingly large surface tension.

In the confines of a pore, liquid is drawn up the pore walls by capillary action, with attractive forces between the wall and the liquid molecules balancing the liquid-liquid cohesive forces. As the liquid is removed from the pores, these attractive forces cause the pore walls to be drawn in, resulting in a collapse of the structure.

By replacing the water with a lower surface tension solvent, the forces exerted on the pore structure are reduced, leading to reduced collapse and a preservation of the porous network. A gel prepared via subcritical drying is known as a xerogel. All samples in this study will be prepared in this way.

1.6.4.3 Freeze Drying

As the name suggests, this method involves freezing the solvent within the pores, before removing through sublimation. This process also eliminates the vapour-liquid equilibrium, giving greater preservation of the pores within the gel. A suitable solvent must be chosen to ensure complete freezing at the operating temperature. Gels prepared in this way are called cryogels.

1.6.5 Pyrolysis and Activation

Pyrolysis involves the heating of an RF gel sample to high temperatures in an inert atmosphere. The process removes hydrogen and oxygen atoms from the structure, resulting in a purely carbon network. The continuous nature of the structure also means that the carbon framework becomes electrically conductive.[63] Levels of conductivity have been recorded as between 25 and 100 S cm^{-1}.[64] This compares with 6.2×10^5 and 5.9×10^5 S cm^{-1} for the best metallic conductors, silver and copper respectively.[65] However, it is very comparable with the conductivity of graphite, 100 S cm^{-1}.[65] The removal of material during the pyrolysis process leads to the formation of micropores (sizes < 2 nm), whereas pre-pyrolysis, RF gels tend to be predominantly meso- (2 – 50 nm) and macroporous (> 50 nm).

Activation can be used to selectively introduce new surface functionalities to the gels. This can be done physically or chemically. Physical activation, like pyrolysis, takes place in the gas phase, with the activating agent being passed over the solid

carbon gel network. On the other hand, chemical activation takes place in the liquid phase, by submerging the gel in the appropriate activation agent.

1.7 RF Sol-Gel Reaction Process Variables

Since their discovery in 1989, a large number of studies have been carried out in order to investigate the impact of changing specific synthesis variables on the final properties of RF gels.[51, 52] These variables include; the resorcinol:formaldehyde molar ratio (R/F), the type of catalyst, the resorcinol:catalyst molar ratio (R/C), the initial solution pH, the total solids content or resorcinol:water ratio (R/W) sometimes known as the dilution, the solvent used, the gelation temperature, curing conditions, and drying method.

1.7.1 Resorcinol:Formaldehyde Molar Ratio (R/F)

The most commonly used ratio of R:F is 1:2, giving an R/F stoichiometric proportion of 0.5. Petricevic *et al.* increased this to a 1:3 ratio and found that this gave a significant increase in the size of observed clusters as the result of a dilution effect.[66] However, Mulik *et al.* used ratios of 1:2, 1:3, 1:5 and 1:10, in conjunction with hydrochloric acid, instead of a base, and found that altering the R/F ratio had little effect on the bulk density or porosity of the gels.[50] Particle diameter increased only slightly, from 8.03 nm at a 1:2 ratio, to a peak of 12.0 nm at a ratio of 1:5.[50]

1.7.2 Type of Catalyst

As explained in Section 1.5, the reaction between resorcinol and formaldehyde can be promoted by either an acid or a base. Basic sodium carbonate is the most commonly used catalyst in the preparation of RF gels.[51, 52] It was used by Pekala in his original synthesis, and in many subsequent studies on RF gels.[31]

However, it is easy to change both the cation and anion within the base while still forming comparable RF gels. Job *et al.* investigated the impact of changing the cation, by synthesising gels in the presence of the hydroxides of lithium, sodium, potassium, calcium, strontium and barium, finding clear patterns for the Group I and Group II metals, respectively.[67] Meanwhile, Fairen-Jimenez *et al.* also performed a comparison between cations, utilising both sodium and potassium carbonate.[68] Likewise, Horikawa *et al.* compared both cation and anion, making use of the carbonates, and hydrogencarbonates, of both sodium and potassium, with properties showing groupings dependent on the anion when a constant R/C of 50 was used.[69]

While the basic catalysts tend to fall into groups containing either an alkali, or alkaline earth metal cation, there is less order in the choice of acid catalysts, with both mineral and organic acids having been used to synthesise RF gels, giving rise to a wide range of possible catalysts.

Mulik *et al.* used hydrochloric acid as their catalyst of choice, reporting that gel times could be reduced to as little as 10 minutes at 80 °C, while the gels were chemically similar to the analogous base catalysed gels.[50] Merzbacher *et al.* investigated nitric acid as a catalyst. In comparisons with conventional base catalysed gels, they found that the acid catalysed gels were slightly more reflective, due to the reduced porosity observed by these materials (96.7 % vs. 91.3 %).[59] The base catalysed gel was made up of nanometer sized particles, as opposed to the micrometer sizes of the acid catalysed gels. In conjunction with the increased porosity, and therefore lower density, caused by these smaller particles, the incident light achieved greater penetration into the material. This, in turn, lead to more internal scattering and subsequently, higher absorption levels. As a result, lower levels of reflected light were observed.

Brandt *et al.* used acetic acid to prepare RF gels.[70, 71] These studies found that the acid catalysed gels could give comparable properties to base catalysed gels, with the advantage of having no metallic impurities, from the basic metal salt, present. However, SEM imaging in conjunction with energy dispersive x-ray spectroscopy (EDX) of our own samples failed to detect residual metallic impurities. This suggests that any metal species have been removed from the gel, most likely during the solvent exchange. Fairen-Jimenez *et al.* used both oxalic and *p*-toluenesulfonic acid as catalysts, with direct comparison to the aforementioned sodium and potassium carbonate; it was observed that the acid catalysed gels were much denser than the analogous base catalysed gels.[68] This was explained as being caused by an increase in the level of aggregation of clusters, resulting in a reduction in interparticle voids, which agrees with the results of Merzbacher *et al.* that the acid catalysed gels had less porosity, as described above.[59]

1.7.3 Resorcinol:Catalyst Molar Ratio (R/C)

The resorcinol:catalyst molar ratio plays an important role in the formation of RF gels. Changes in the amount of catalyst present have a profound impact on gel properties. For the commonly used sodium carbonate, R/C values tend to fall into the range of 50 – 3000.[51, 52]

Low R/C values correspond to a high catalyst concentration and have been found to result in smaller clusters, with reduced pore sizes and larger surface areas. Conversely, high R/C values give larger cluster sizes and pore sizes, with correspondingly lower surface areas. The reasoning for this is that in terms of the base catalysed reaction between R and F, a higher concentration (low R/C) of base will deprotonate a larger number of resorcinol molecules to the anion. The anions will react with F to form the hydroxymethyl derivative monomer unit, a species which is more reactive than R and will quickly react to form a bridged dimer unit. Once more, this is more reactive than the monomer, leading Pekala and Kong to describe the process as an "autocatalytic growth mechanism", followed by "preferential growth of polymer clusters".[32] The larger number of initial anions formed by the higher catalyst concentration leads to more clusters of a smaller size.[32]

1.7.4 Initial pH of the Reactant Solution

Initial pH of the reactant solution and R/C ratio are closely related in the gel formation process as it is through the addition of either an acid or base that the initial pH is altered. This link means it therefore plays an important role in determining the properties of the gel.

It has been shown that in the presence of a basic catalyst, only a sol with a pH in the range of 5.5 – 7.5 will form a viable gel structure.[52, 72] If the pH becomes more basic, the resulting solid is non-porous,[73] while more acidic pHs give excessively long gelation times.[74] However, if an acid is added to further lower the pH to within the range of 1 – 4, gel times are reduced and the gel formation becomes viable once more.[50, 74] Beyond this range, using a pH of less than 0.8 causes precipitation of the reactants.[52]

This dependence on pH can be explained in terms of both the acid and base promotion of the initial reaction between R and F. Under basic conditions, a proton is abstracted from resorcinol and the reaction begins. At this time, the pH of the gelling sample decreases, allowing for cluster growth, through condensation reactions, and eventual cross-linking within the structure. If the initial pH is too high, R will be deprotonated but the pH will not drop sufficiently, and the cluster growth and cross-linking steps will be inhibited. This will result in a very weak structure, likely to collapse, under drying, to become non-porous. On the other hand, insufficient base will slow the initial reaction and lead to greatly extended gelation times.

Similar reasoning can also be applied to the acid catalysed route. Low acid concentrations, with a pH higher than 4, will once more inhibit the gel formation and extend the gelation process. Increasing the acid concentration to within the given range will subsequently promote the protonation of formaldehyde and the subsequent polycondensation and aggregation cross-linking steps (Scheme 1 through 3).

Lin and Ritter used nitric acid to adjust the pH of a sodium carbonate gel with fixed R/C of 50 in an attempt to decouple the relationship between R/C and pH.[73] However, the acid and base are likely to react with each other, reducing the concentration of either that is available to take part in the sol-gel process. The resulting gel properties will therefore not give a true representation of the initial pH or R/C used.

1.7.5 Total Solids Content

The solids content of a gel is typically expressed in one of three ways, as a mass percentage or ratio, a resorcinol:water ratio (R/W), or a dilution ratio, D. Altering the total solids content can have a major influence on the properties of RF gels.

Similar to the addition of extra formaldehyde, diluting the reactant concentration through the addition of further solvent leads to a decrease in the density of the final gel structure, as observed by Fairen-Jimenez *et al.*[68] Bock *et al.* also found that increasing the reactant density lead to a significant decrease in pore size, with small angle x-ray analysis (SAXS) also showing a decrease in particle size.[75]

It was discovered by Tamon *et al.* that altering the solids content influenced the dispersity of the pore sizes in RF gels.[76] They reported that high solids content produced mondisperse pores, i.e. all pores were of the same size. Decreasing the solids content produced polydisperse porosity, with pores being of multiple different sizes.

1.7.6 Solvent Used in the RF Sol-Gel Transition

The RF sol-gel transition is typically carried out under aqueous conditions, with the resulting hydrogel containing water as the pore fluid. However, it is possible to make gels in a number of alternative organic solvents, which can prove advantageous.

Both Barbieri *et al.* and Berthon *et al.* used acetone as their solvent.[77, 78] The synthesised gels, therefore, had acetone within the pores and negated the need for a solvent exchange step, saving time in the production process.

Mulik *et al.* used acetonitrile as a solvent, and found that in this case, the gelation process was much quicker than when running the sol-gel reaction in acetone. This was explained as being the result of cross-aldol condensation between the acetone and formaldehyde.[50]

Other organic solvents used include methanol and ethanol. All of these organic solvent based gels are known as lyogels.

While removing the need for the solvent exchange step is a positive, the possible unwanted reactions and potential cost of the solvents may prove disadvantageous.

1.7.7 Gelation Temperature

The temperature at which gelation is carried out can have a profound influence on the formation of RF gels. The most commonly used reaction temperature is 85 ± 5 °C, as used by Pekala in his original synthesis, and in many studies since.[31]

Tamon and Ishizaka found that gels of the same composition synthesised at temperatures of 25 and 50 °C gave very comparative properties of surface area, mesopore volume and peak pore radius.[79] In contrast, Job *et al.* obtained results at 50, 70 and 90 °C, and observed that these same gel properties varied significantly.[74]

A common feature of the gel synthesis influenced by the reaction temperature is the gelation time. In all cases, increasing the reaction temperature decreased the reaction time.

Gaca and Sefcik found that increasing the reaction temperature from 55 to 80 °C, increased the size of primary RF clusters after an identical amount of time had passed.[80] They subsequently argued that temperature influenced only the reaction rate, and not the reaction mechanism itself.

1.7.8 Curing Conditions

After gelation has occurred, samples tend to be cured for a period of time. Depending on the gel composition and reaction temperature, this curing time can range from hours to days. Curing allows further cross-linking to occur within the structure, which gives the gel its mechanical strength.

Job *et al.* investigated the impact of differing curing times at temperatures of 50, 70 and 90 °C.[74] From this they found that a minimum of 24 hours of aging was required at 90 °C, while at 70 °C at least 48 hours were required. Exceeding these times had

little influence on the gel properties. However, at 50 °C, a stable gel structure had still not been formed after 72 hours, with the pore characteristics still changing.[74]

In addition to curing at the reaction temperature, both Despetis *et al.*[81] and Liang *et al.*[82] submerged the cured gels in a dilute acetic acid solution in order to further increase the mechanical strength of the gel. The additional acid promotes further cross-linking within the gel, making the structure stronger. The addition of this step is commonly referred to as aging. Liang *et al.* found that aging in acid increased the elastic modulus of the gels quickly, through the speeding up of the formation of cross-linking. However, after one week of curing at elevated temperature, an equivalent elastic modulus could be obtained, with the final mechanical properties appearing to be uninfluenced by the cross-linking method.[82]

1.7.9 Drying Method

As described above (Section 1.6.4), there are many ways in which the pore fluid can be removed in order to give a dry gel. Depending on the method chosen, the properties of the dried gel will change.

In his original synthesis, Pekala made use of supercritical CO_2 drying. This method was used to eliminate the vapour-liquid equilibrium, reduce the capillary forces acting on the pore walls and maintain the porous structure. To this day, it remains a very popular method.

However, other methods of drying have become popular. Subcritical drying, be it at ambient pressure or under vacuum, has risen in popularity due to supercritical drying being a time consuming, expensive and more dangerous procedure, as well as being difficult to achieve on an industrial scale. Fischer *et al.* found that RF gels could be dried subcritically, without major shrinkage, if the R/C ratio was ≥ 1000.[83] This produced large clusters that formed a network strong enough to withstand the forces exerted during drying.

In looking at the industrial relevance of RF gels, Job *et al.* used a convective air drying method to produce RF xerogels.[74] They found that significant porosity was maintained, while the drying process took only 8 hours at 70 °C. The hydrogels required no pre-treatment prior to drying, further reducing the overall production time.

In a further study, Job *et al.* produced gels via vacuum drying, again with no pre-treatment after gelation and curing.[72] A porous structure was maintained, with the pore size dependent on the initial sol pH (between 5.45 and 7.35 in this work) rather than the drying method. After some initial shrinkage, the mechanical strength of the gel becomes such that it can counteract the capillary forces experienced from the vapour-liquid equilibrium produced during drying.

Freeze drying produces cryogels; Job *et al.* found it difficult to freeze dry gels containing water, which resulted in the breakdown of the monolithic structure.[84] This problem was especially so when high dilution ratios were used. The breakdown was caused by thermal shock in the gel structure, in conjunction with the expansion of the water as it froze. The samples were frozen by immersion in liquid nitrogen, and the rapid cooling caused the structure to fracture. Furthermore, very large channels (> 10 μm wide) were found to form in the cryogel as the result of the formation of ice crystals which distorted the structure.[84]

It is now common to exchange the water in hydrogels for *t*-butanol prior to freeze drying, as demonstrated by Yamamoto *et al.* who were successfully able to produce monolithic structures.[85] This was due to the lack of expansion in *t*-butanol upon freezing. However, Job *et al.* still found the issue of ice crystal formation to be a problem, at high dilution ratios, when *t*-butanol was used.[84]

Czakkel *et al.* performed a comparison between three different drying methods, ambient pressure drying under an inert atmosphere, freeze drying and supercritical drying.[86] The results showed that the highest surface area was obtained after freeze drying, whilst they also exhibited the greatest pore volume. However, the freeze dried structure was not stable, and over time the surface area decreased.

Job *et al.* ran a similar comparative study and showed that the supercritically dried aerogel showed superior properties of surface area and pore volumes.[84] However, they also showed that each method was not without its own drawbacks, with all of the methods being best suited to gaining a dried gel depending on the particular porous texture required.

Since 2006, microwave drying has become more prevalent. This method has advantages over the others such as requiring no external heating, a fast drying rate and reduced operating costs, all important factors for an industrially viable process.

Tonanon *et al.* compared microwave drying to freeze drying.[87] They found that, in general, the microwave dried gels had a lower porous volume than the equivalent freeze dried gels. However, by dosing the samples, using ultrasonic irradiation, during the gelation phase, the porous properties of the microwave dried gels could be improved, becoming more comparable with the traditionally dried cryogels to which they were comparing.[87]

Zubizarreta *et al.* compared gels synthesised using methanol as a solvent and various microwave drying methods, using both a unimodal and multimodal microwave dryer.[88] It was discovered that the different drying methods had little effect on the initial porous structure post drying, but after activation with CO_2, the multimode microwave drying produced the best surface area.

As methanol and ultrasonic irradiation are not commonly used during RF gel production, Zubizarreta *et al.* moved on and investigated microwave drying of standard aqueous gels.[89] With no solvent exchange performed, the results showed that the surface area and porosity of the samples was dictated by the gel composition rather than the microwave drying, similar to what has been observed for other, more conventional, drying methods.

1.8 Applications of RF gels

The porous nature of RF gels makes them ideally suited to a number of applications. The ability to produce the gels in a number of different forms, e.g. monoliths or powders, also increases the scope of their use.

1.8.1 Catalysis Applications

Carbon gels have found many applications as catalyst support materials.[90] Some examples of this include the oxidation of glycerol,[91] hydrodechlorination of 1,2-dichloroethane,[92] and the heterogeneous oxidation of phenol.[93]

Many methods have been developed to introduce the active catalytic material, commonly a metal, onto the carbon gel substrate. As the sol-gel process is so flexible, an easy method of metal introduction is through the addition of a metal salt to the precursor solution.[94] After gelation and pyrolysis, metal nanoparticles are left dispersed throughout the gel framework. Iron is one of many metals to have been introduced in this way, for the combustion synthesis of carbon fibrous nanostructures.[95]

Wet impregnation has also been used to deposit the desired metal on the dried gel substrate. Nickel, platinum, iridium and ruthenium have all been introduced in this manner.[96, 97]

Platinum has also been successfully added to the structure post pyrolysis through the use of a strong electrostatic adsorption process.[98] Here, aqueous H_2PtCl_6 solution is impregnated into the carbon xerogel, before drying and reducing under a flow of hydrogen gas. Repetition of the cycle will increase the metal loading within the structure.

1.8.1.1 Fuel Cell Electrodes

The catalytic support ability of carbon xerogels has seen them become an attractive alternative for electrode materials in both proton exchange, and direct methanol fuel cells.[66, 99, 100] In replacing carbon blacks, carbon xerogel materials have demonstrated encouraging results in terms of both degradation of the active surface over time, and the voltage loss at a constant current density of 1000 mA cm^{-2}.[101]

1.8.2 Electrochemical Applications

In a similar manner, carbon xerogels are ideally suited to a number of electrochemical applications.[102]

1.8.2.1 Supercapacitors

Supercapacitors are charge storage devices that make use of the electric double layer.[64] Two layers of carbon xerogel are separated by a membrane which is conductive to ionic species, but insulating to electrons. The remaining space is filled by an electrolyte solution such as potassium hydroxide.[103] A schematic diagram is shown in Figure 13.
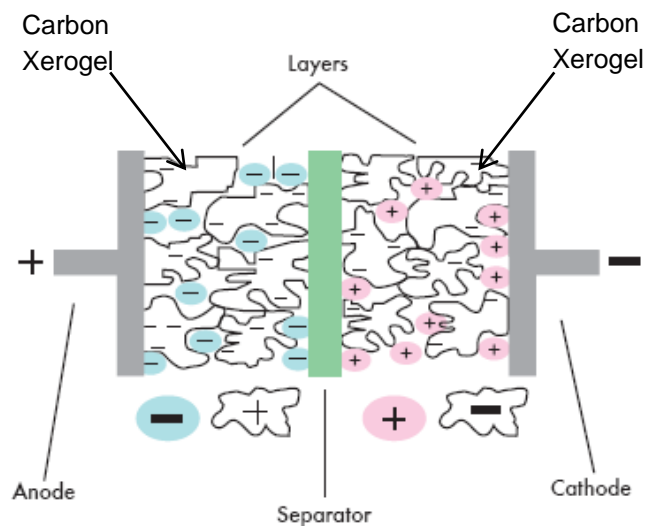
A voltage is supplied across the system causing migration of the charged species to the respective electrode. The energy is then stored in the electric double layer on the surface of the carbon xerogel. The high surface areas obtained with xerogels gives greater charge storage ability. Many of the metal doped gels studied for catalytic applications have been studied in supercapacitor projects.[90]

1.8.2.2   Capacitive Deionisation

The migration of various ions towards the gel surface can be used to remove contaminants from a flowing aqueous solution in a technique known as capacitive deionisation.[103] By passing a voltage across the two plates of xerogel, ions move towards the electrode of opposite charge where they are stored on the xerogel surface. This method has been successfully applied in the removal of copper,[105] bromide and iodide,[106] and in the desalination of brackish water.[107]

1.8.3   Gas Storage and Separation Applications

The large surface areas and porosities of carbon xerogels also make them useful in the area of gas storage and separation.

1.8.3.1   Hydrogen Storage and Generation

Doping carbon xerogels with both nickel[108] and nitrogen[109] have shown promise in the storage of hydrogen gas, with uptake values of 6 wt.% and 3.2 wt.% reported for the respective methods. More recently, studies have looked at using liquid organic hydrides (LOH's) to generate hydrogen gas from the easier to use liquid form.[110] This process involves taking the LOH, commonly a cycloalkane such as cyclohexane or decalin, and fully dehydrogenating it to the aromatic derivative. This

process takes place over a metal catalyst supported on a carbon substrate. Carbon xerogels have shown great promise in providing this support material.[111] Furthermore, the hydrogen gas generated is free from both carbon monoxide and dioxide, allowing it to be directly fed into fuel cells, without the risk of poisoning the electrodes.

1.8.3.2 Air Separation

It has also been reported that air can be successfully separated by carbon xerogels using pressure swing adsorption (PSA).[112] Nitrogen adsorbs onto the xerogel surface with a much greater affinity than that of oxygen, causing the gases to be separated. The same materials have also shown comparable capabilities with regards to temperature swing adsorption (TSA).

1.8.3.3 Membrane Additives

Carbon xerogel materials have been packed inside polysulfone mixed matrix hollow fibre membranes.[113] The addition of the xerogel increased the selectivity of the membranes when separating two similar gases such as CO_2 and O_2. There was also the added benefit of strengthening the hollow fibres after packing with xerogel material.

2 Aims and Objectives

The many applications of RF xerogels, as outlined in Section 1.8, require such materials to have a particular set of textural and physical properties, specific to the chosen application. Being able to carefully control these properties is, therefore, vital to achieving useful materials. While it is clear that altering the synthesis variables and processing conditions plays a fundamental role in determining the final porosity (Section 1.7), there is still a lack of understanding as to why these differences in xerogel production lead to such varied products. This is especially true of the gelation process, during which time the 3D network, which makes up the porous structure of the gel, is formed. If this process were better understood, the tailoring of xerogel properties to a particular application would become more commonplace, potentially making the materials more efficient, and opening them up for use in many further applications.

The aim of this body of work is, therefore, to study the gelation mechanisms that occur during the sol-gel transition of RF xerogels. Using dynamic light scattering (DLS), it is possible to measure nanoscale size changes in the RF oligomers and clusters that make up the 3D gel network. The changes in size and growth rate can then be compared when various synthesis variables are altered, showing the effect that these alterations have had on the gelation mechanism.

Carrying out low temperature nitrogen adsorption measurements allows determination of the textural properties of the xerogel materials. Changes in these properties can be linked to the observed changes in the gelation process, caused by altering the synthesis variables.

Studying a wide range of systems will allow for the maximum possible insight into how the gelation mechanism is altered, and the resulting impact on the textural properties of the gel. In turn, this may open up new avenues to explore in the tailoring of RF xerogel products for particular applications.

To achieve this range of systems, it was decided to study seven different basic catalysts over a wide range of R/C ratios. The catalysts all contain the commonly used carbonate anion, and vary only in the choice of cation. As such, the catalysts can be grouped into three types. The first set of cations is the Group I metals, and consists of lithium, sodium, potassium and caesium. The second set is the Group II

metals, making use of calcium and barium. Lastly, a non-metallic base will be trialled, with ammonium chosen as the cation to study.

All of these catalysts are studied over the R/C range of 100 – 600 to be consistent (and allow for direct comparison) with previous work in the literature. Through the combination of these variables, 33 separate systems will be studied, in depth, to provide information on the gelation mechanism.

The results of these initial investigations will inform the direction of further study. Systems containing various concentrations of a mixture of the catalysts will be studied, to gain further insight into the gelation mechanism and development of porosity in RF gels.

3   Techniques and Theory

There are many techniques and theories used in this body of work to study both the formation, and resulting textural properties, of resorcinol-formaldehyde gels. This section explains the principles behind each of them.

3.1   Porosity in Solid Materials

As defined by The International Union of Pure and Applied Chemistry (IUPAC), a porous solid is 'a solid with pores, i.e. cavities, channels or interstices, which are deeper than they are wide'.[114]

Pores can be classified into several types, as seen in Figure 14. This definition is based on the ability of pores to interact with an external fluid.
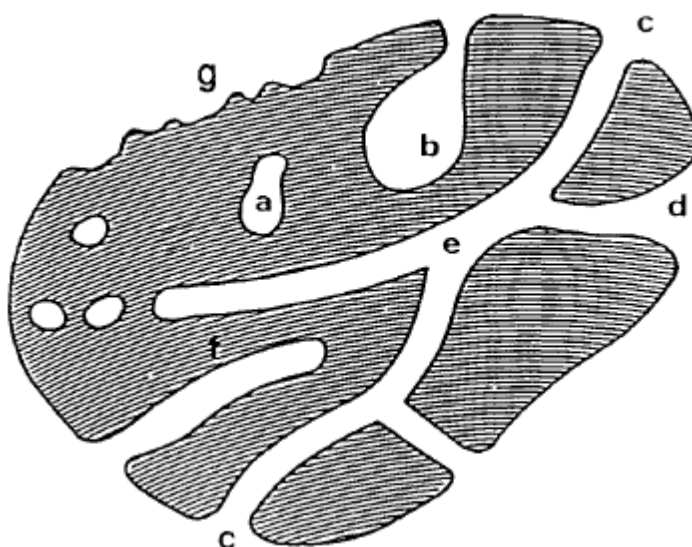
Figure 14: Representation of a porous solid, showing the different types of pores that can be observed.[114]

Region (a) is known as a closed pore. Closed pores are isolated from the external surface and do not interact with the external fluid. However, they do play a role in determining the bulk density, mechanical strength and thermal conductivity of the material. Regions (b), (c), (d), (e) and (f) are known as open pores, with a connection to the external surface. Open pores can be further defined as being blind (regions (b) and (f)), where only one end of the pore is connected to the external surface, or through pores (like at (c), (d) and (e)) where both ends are open to the external surface. Further sub-division of the pores can be achieved based on the shape of the pore, with bottle-neck (b), funnel (d) and cylindrical (f) pores shown.[114] Region (g) shows surface artefacts that are wider than they are deep, and so are not classified as pores. Instead, this is an area of surface roughness.[114]

Porous materials often have a high surface area; and it is useful to split this quantity into the external and internal surface areas. The external area includes any surface roughness, such as that exhibited in region (g) above. The internal area, therefore, corresponds to the walls of all the porous features accessible to the external fluid.[115]

It has been found useful to differentiate pores by their size. IUPAC have defined three sizes of pore as outlined in Table 1.[115]

Table 1: IUPAC pore size classification.[115]

Pore Classification	Size Range (nm)
Micropore	< 2
Mesopore	2 - 50
Macropore	> 50

3.2   Adsorption onto a Porous Solid

IUPAC have defined adsorption as 'the enrichment of one or more components at an interfacial layer'.[115] Once more, subdivision of adsorption is possible, these categories being chemisorption and physisorption.[115]

Chemisorption involves the formation of new chemical bonds between the adsorbate and the adsorbent surface. These bonds must be broken in order to desorb the adsorbate, resulting in chemisorption being a high energy process.

In contrast, physisorption involves the formation of weak van der Waal's forces, allowing the adsorbate to be easily desorbed.

3.2.1   Physisorption onto Porous Solids

The atoms in the bulk of a porous material are fully bonded in all directions. In a similar manner to surface tension, the surface atoms in the solid are lacking complete bonding, making the surface reactive. It will, therefore, rapidly physisorb gases, vapours or liquids, with the weak interactions completing this bonding, making it an energetically favourable process.[116]

Figure 15 outlines the stages in the physisorption process.[116] Stage 1: at low pressures, adsorbate molecules start to adsorb onto the surface of the adsorbent. Stage 2: as the pressure increases, more adsorbate molecules adsorb until complete monolayer coverage of the surface is achieved. Stage 3: further increasing the pressure results in the formation of multilayers, where none of the newly adsorbed molecules are in contact with the surface and adsorbate-adsorbate

interactions take place. Stage 4: at saturation pressure, complete coverage of the sample is achieved, with all pores of the material filled completely.
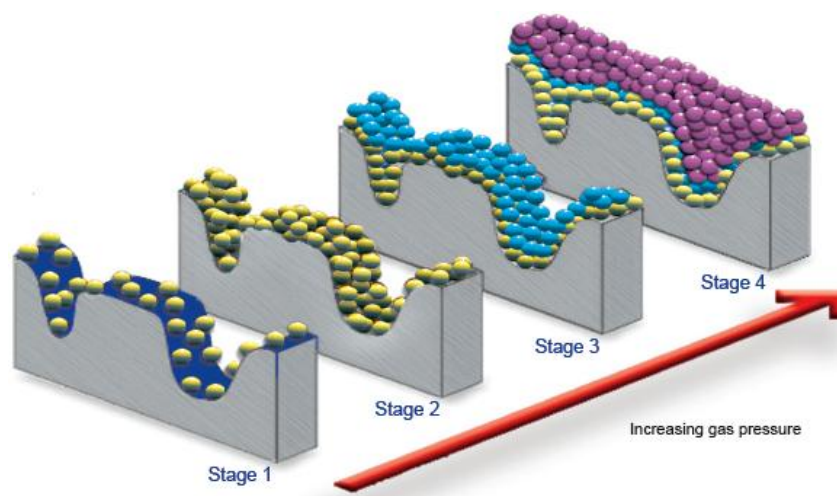
Figure 15: The stages in the physisorption of gas onto a surface, showing mono- and multilayer formation.[116]

The size of the pore plays a role in how the gas adsorbs onto the surface of the material. In very narrow pores, few gas molecules are needed to fill the pores. Due to the bonding deficiency at the surface of the material, all of the molecules are attracted to the wall of the pore. The interactions between gas molecules are therefore almost negligible in comparison. However, as the pore size increases to the mesopore region, further layers of gas molecules must be adsorbed in order to fill the pore. As the thickness of the gas molecule layer covering the surface increases, it reaches a critical point, where the molecules furthest from the solid surface experience an increase in molecular forces, causing a surface tension to develop. This results in the outer layer becoming liquid-like, in a process known as capillary condensation.[117]

3.2.2 Adsorption Isotherms

During adsorption, gases are dosed onto the adsorbent surface in increasing pressure steps. At each step, the pressure is allowed to come to equilibrium, where the maximum amount of gas has been adsorbed at that pressure. Dividing each pressure step by the saturation pressure, results in the relative pressure of the system, with values ranging between 0.0 and 1.0.

At a constant temperature, the relationship between the amount of gas adsorbed by a surface and the relative pressure of the gas is defined, by IUPAC, as an adsorption isotherm.[115] As different gases and surfaces interact in a number of

ways, the shape of the adsorption isotherm will change correspondingly. For this reason, IUPAC has classified six types of isotherms, depending on the interactions occurring.[115] These are shown in Figure 16.
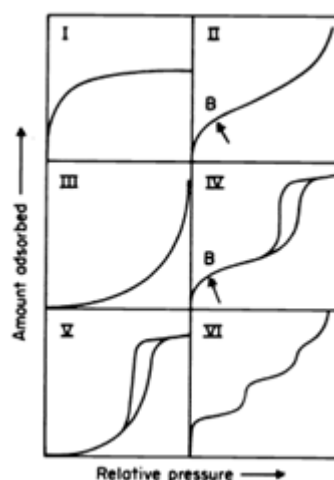
Figure 16: Adsorption isotherms as classified by IUPAC.[115]

Type I isotherms are characteristic of microporous materials with small external surface area, where micropore filling occurs at low relative pressure, and uptake is limited by the accessible pore volume. Type II isotherms indicate non-porous or macroporous adsorbents, with unlimited monolayer-multilayer adsorption. Similarly, Type III isotherms also occur with non- or macroporous surfaces. However, in the case of Type III isotherms, interactions between the adsorbent and adsorbate are very weak, and adsorbate-adsorbate interactions play a key role. Type IV isotherms are also related to Type II, in that they show monolayer-multilayer adsorption. However, Type IV isotherms are associated with mesoporous materials. The characteristic difference between the adsorption and desorption branches, known as a hysteresis loop, is indicative of the capillary condensation described above in Section 3.2.1. Type V isotherms, like Type III, show weak adsorbent-adsorbate interactions, in this case occurring on certain porous materials. Both Type III and Type V isotherms are uncommon. Finally, Type VI isotherms are associated with stepwise multilayer formation on a non-porous material.[115]

Both Type II and Type IV isotherms exhibit almost linear adsorption in the mid pressure range of the isotherm, beginning at the points marked B on the isotherms in Figure 16. These points indicate that monolayer coverage is complete, and multilayer coverage has begun.[115]

3.2.3 Hysteresis in Adsorption Isotherms

The hysteresis loops exhibited by Type IV and V isotherms can take various shapes depending on the geometry of the pores being studied. IUPAC have, therefore, classified hysteresis into four types.[115] These are shown in Figure 17.
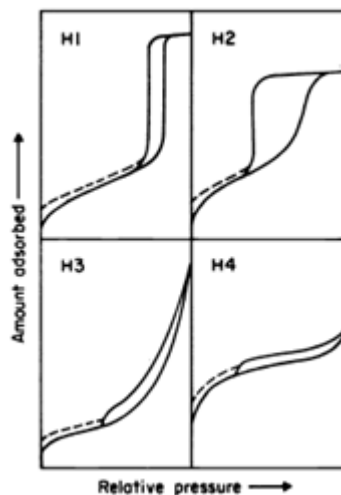
Figure 17: Hysteresis loops as classified by IUPAC.[115]

Type H1 loops are associated with materials made of packed, uniform spheres, leading to a narrow distribution of pore sizes. Type H2 loops are the result of a wider distribution of pore sizes. Both Type H3 and H4 are associated with slit-shaped pores. In Type H4, these slits are narrower, as indicated by the Type I like nature of the adsorption isotherm.[115]

3.3 Determination of the Surface Area of Porous Solids

Several models have been developed that attempt to explain the adsorption of molecules onto surfaces. Two of the most commonly used are the Langmuir model and Brunauer-Emmett-Teller (BET) theory.

3.3.1 Langmuir Theory

Langmuir published his theory on the adsorption of gases onto solids in 1916.[118] This model was based on three assumptions:

- The surface of a material is composed of a number of identical adsorption sites
- Each site can adsorb only one molecule at a given time
- Coverage is limited to a monolayer, no multilayer adsorption occurs, due to no interaction between gas molecules

If S denotes a surface site, and M denotes a gas molecule, then, at equilibrium:

$$S + M \rightleftharpoons SM$$
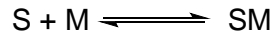
$$\text{Rate of forward reaction} = k_a[S][M]$$

$$\text{Rate of backward reaction} = k_d[SM]$$

At equilibrium, the rates of the forward and backward reactions are equal, so:

$$k_a[S][M] = k_d[SM]$$

This can be rearranged to give an equilibrium constant of:

$$K = \frac{k_a}{k_d} = \frac{[SM]}{[S][M]}$$

If the fraction of surface sites occupied is denoted θ, and the pressure of the gas denoted p, then the fraction of unoccupied sites is $1 - \theta$, and, at equilibrium:

$$\text{Rate of adsorption} = k_a p(1 - \theta)$$

$$\text{Rate of desorption} = k_d \theta$$

Again, at equilibrium, the rate of adsorption equals the rate of desorption, so:

$$k_a p(1 - \theta) = k_d \theta$$

This can be rearranged to give:

$$\theta = \frac{k_a p}{k_d + k_a p} = \frac{Kp}{1 + Kp}$$

which is commonly known as the Langmuir equation.

The fraction of surface sites occupied, i.e. the surface coverage, θ, can be thought of in terms of the actual volume of gas adsorbed, V, and the volume of gas required to complete monolayer coverage, V_m, such that:

$$\theta = \frac{V}{V_m}$$

Substitution into the Langmuir equation gives:

$$\frac{V}{V_m} = \frac{Kp}{1 + Kp}$$

Rearrangement of this equation results in a linearized form:

$$\frac{p}{V} = \frac{1}{KV_m} + \frac{p}{V_m}$$

A plot of p/V vs. p will therefore have a gradient of $1/V_m$, from which the monolayer volume can be calculated.

The specific surface area of the material can then also be calculated:

$$S_a = \frac{V_m A_m L}{m}$$

where S_a = specific surface area ($m^2 g^{-1}$)

A_m = the cross-sectional area of a gas molecule, i.e. the area on the surface it occupies (1.62×10^{-19} m^2 molecule^{-1} for the most commonly used gas, nitrogen)

L = Avogadro's constant (6.022×10^{23} molecule mol^{-1})

m = the mass of the sample (g)

3.3.2   Brunauer-Emmett-Teller (BET) Theory

In 1938, Brunauer, Emmett and Teller expanded on the Langmuir equation, with a theory that could also take into account multilayer adsorption.[119] In addition to those

of the Langmuir model, a number of extra assumptions were first required when developing the theory:

- The uppermost layer of adsorbed molecules is in equilibrium with the bulk gas
- The first adsorbed layer has a heat of adsorption, while subsequent layers have a heat of condensation
- At saturation pressure, an infinite number of layers become adsorbed onto the surface

The surface of a material is again composed of a number of identical adsorption sites, S. The number of sites covered by i molecules is n_i. As such, the total number of sites is given by:

$$S = \sum_{i=0}^{\infty} n_i$$

It follows that the total number of nitrogen molecules adsorbed, N, is given by:

$$N = \sum_{i=0}^{\infty} i.n_i$$

Like for the Langmuir model, at equilibrium, the rate of formation of layer i is equal to the rate of destruction of layer i. However, both the formation and destruction of a layer can happen in two ways.

Layer i will be formed if:
- Adsorption occurs on layer i – 1; rate = $(k_a)_i n_{i-1} p$
- Desorption occurs on layer i + 1; rate = $(k_d)_{i+1} n_{i+1}$

Layer i will be destroyed if:
- Adsorption occurs on layer i; rate = $(k_a)_{i+1} n_i p$
- Desorption occurs on layer i; rate = $(k_d)_i n_i$

For layer i, these terms can be equated such that:

$$(k_a)_i n_{i-1} p + (k_d)_{i+1} n_{i+1} = (k_a)_{i+1} n_i p + (k_d)_i n_i$$

Expanding this summation over all of the adsorbed layers gives:

$$(k_d)_{i+1} n_{i+1} = (k_a)_{i+1} n_i p$$

$$n_{i+1} = \frac{(k_a)_{i+1}}{(k_d)_{i+1}} p$$

From the assumptions made to produce this model, the first layer has a heat of adsorption, with all subsequent layers having a smaller heat of condensation. As such, and additional constant must be added for the adsorption of layer 1 to give:

$$n_1 = C \frac{(k_a)_{i+1}}{(k_d)_{i+1}} p.n_0$$

As the heat of condensation is assumed to be constant for all layers, the rate constants for adsorption and desorption should also be equal, such that $k_a = (k_a)_{i+1}$ and $k_d = (k_d)_{i+1}$.

For the condensed phase, where bulk saturation is taking place:

$$k_a p_0 = k_d$$

Combination with Equation 18 gives:

$$\frac{k_a}{k_d} p = \frac{p}{p_0} = x$$

With this simplification in place, Equation 19 becomes:

$$n_i = x.n_{i-1} = x_2.n_{i-2} = x_3.n_{i-3} = \ldots = x_{i-1}.n_1 = C.x_1.n_0$$

This means that:

$$n_i = C.x_i.n_0$$

From Equation 15, it was shown that the total number of molecules adsorbed was given by:

$$N = \sum_{i=0}^{\infty} i.n_i$$

This can be combined with Equation 23 to give:

$$N = C.n_0 \sum_{i=0}^{\infty} i.x_i = C.n_0.x \left(\frac{d}{dx} \sum_{i=1}^{\infty} x_i \right)$$

<div align="right">Equation 24</div>

From Equation 14, it was shown that the total number of sites was given by:

$$S = \sum_{i=0}^{\infty} n_i$$

By again making use of Equation 23, this becomes:

$$S = n_0 + \sum_{i=1}^{\infty} n_i = n_0 + C.n_0 \sum_{i=1}^{\infty} x_i = n_0 \left(1 + C \sum_{i=1}^{\infty} x_i \right)$$

<div align="right">Equation 25</div>

When $p < p_0$, it follows that $x < 1$, therefore:

$$\sum_{i=1}^{\infty} x_i = \frac{x}{1-x} \quad \text{and} \quad \frac{d}{dx}\left(\frac{x}{1-x}\right) = \frac{1}{(1-x)^2}$$

<div align="right">Equation 26</div>

Substitution into the expressions for N (Equation 24) and S (Equation 25), results in:

$$N = \frac{C.n_0.x}{(1-x)^2}$$

<div align="right">Equation 27</div>

$$S = n_0 \left(1 + \frac{C.x}{1-x} \right)$$

<div align="right">Equation 28</div>

The number of molecules adsorbed, N, is proportional to the volume of gas that has been adsorbed, V, while the number of adsorption sites, S, is proportional to the volume of a monolayer, V_m. As such, the surface coverage (Equation 10) can be determined:

$$\frac{V}{V_m} = \frac{N}{S} = \frac{\frac{C.n_0.x}{(1-x)^2}}{n_0\left(1+\frac{C.x}{1-x}\right)}$$

Equation 29 simplifies to:

$$\frac{V}{V_m} = \frac{C.x}{(1-x)(1-x+C.x)}$$

Equation 30 is known as the BET equation. It is most commonly used in the linearized form (with the reversal of the simplification from Equation 21):

$$\frac{p}{V(p_0-p)} = \frac{1}{V_mC} + \frac{(C-1)p}{V_mCp_0}$$

where p = equilibrium pressure

p_0 = saturation pressure

V = volume adsorbed at equilibrium

V_m = volume adsorbed to form complete monolayer

C = constant related to the adsorbate-adsorbent interaction energy

A plot of $p/V(p_0 - p)$ vs. p/p_0 yields a plot with slope, $(C - 1)/V_mC$, and intercept, $1/V_mC$, from which values of V_m and C may be calculated. To calculate these values requires a linear relationship between the variables. To ensure this, the relative pressure (p/p_0) range over which the data can be plotted is limited to between 0.05 and 0.3. This linear portion (as seen in Figure 18) is known as a BET plot.[115]
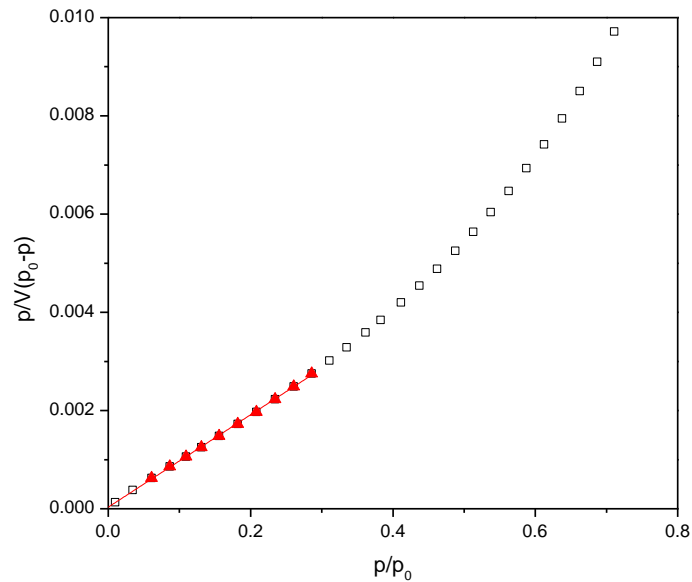
Figure 18: The BET plot of a porous material (□), with highlighted linear region (▲) and accompanying linear fit.

After determining the value of V_m, Equation 13 can again be used to calculate the specific surface area of the sample.

3.4 Determination of the Porosity of Porous Solids

Depending on the dimensions of the pores to be analysed, different models can be used to calculate the pore size.

3.4.1 Barrett-Joyner-Halenda (BJH) Theory

In 1951, Barrett, Joyner and Halenda developed a method to calculate pore volumes and size distributions within the mesoporous range.[120] Based on a decreasing pressure model, it relates the quantity of nitrogen lost at each pressure step, to the average radius of the pores emptied in that step.

The nitrogen within the pores is made up of two regions, the condensed liquid, known as the core, and the adsorbed layer covering the walls of the pore, as seen in Figure 19. The nitrogen at the end area of the pore is considered to be negligible in comparison to the height of the pore.
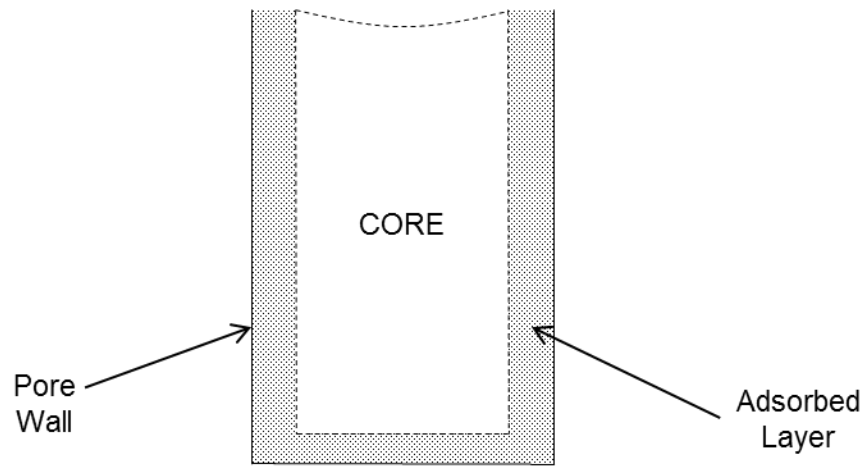
Figure 19: Capillary condensation within a pore, showing the layer adsorbed onto the pore wall, and the core of condensed fluid.

Different sized pores will have different sized cores, with the size of the core related to the pressure at which it empties. When this critical pressure is reached, the entirety of the core desorbs from the pore, leaving behind the adsorbed layer of nitrogen on the pore walls. The relationship between core radius and this critical pressure can be taken from the Kelvin equation,[121] shown in Equation 32.

$$\ln\frac{p}{p_0} = \frac{-2\gamma V}{r_c RT}\cos\theta$$

where p/p_0 = relative pressure

γ = surface tension (N m^{-1})

V = the volume of gas adsorbed (m^3)

r_c = core radius (m)

R = the universal gas constant (8.3144 J mol^{-1} K^{-1})

T = absolute temperature (K)

θ = contact angle of the core meniscus with the pore wall (rad)

As the pressure continues to decrease, the thickness of the nitrogen layer on the pore walls also decreases, such that, at each pressure step the volume of nitrogen that desorbs is the sum of the evaporating cores, plus the volume which desorbs from the walls of the pores whose cores have evaporated in previous steps.

Calculations are started at the point where all pores are filled; therefore the first relative pressure is taken to be close to 1.[122]

The thickness of the adsorbed layer is calculated by way of the Halsey equation:[123]

$$t_w = 3.54 \left(\frac{5}{\log \frac{p_0}{p}} \right)^{1/3}$$

where t_w = wall layer thickness (Å)

Assuming cylindrical pores, the average pore radius, r_p, can now be calculated from the previously determined core radius and wall thickness, such that:

$$r_p = r_c + t_w$$

As the adsorption isotherm gives the volume of nitrogen adsorbed, V, as a function of relative pressure, it is now possible to give V as a function of the pore radius, r_p. The differential of this function, dV/dr_p, and the subsequent logarithmic form, $dV/d\log r_p$, allows for the determination of the change in volume with changing diameter, providing a visual representation of the average pore size.[124]

The cumulative BJH surface area can also be calculated:

$$S_{BJH} = 2 \frac{\sum V_{p_i}}{\sum r_{p_i}}$$

where S_{BJH} = BJH cumulative surface area (m^2)

V_{pi} = pore volume for each pressure step, for the total of *i* steps (m^3)

r_{pi} = pore radius for each pressure step, for the total of *i* steps (m)

Once more assuming pores are of cylindrical form, the average pore diameter can be calculated:

$$d_p av = \frac{4V_p}{S_{BJH}}$$

where d_p av = average pore diameter (m)

V_p = total pore volume (m^3)

3.4.2 t-Plot Method

The t-plot method of determining surface area was conceived by Lippens and de Boer.[125, 126] They proposed plotting the volume of nitrogen adsorbed, not as a function of the relative pressure, but rather as a function of thickness of the layer of nitrogen adsorbed. Assuming that:

- At the given temperature, the adsorbed layer behaves like normal liquid nitrogen with the density of the bulk liquid state
- The nitrogen molecules pack together densely, in a hexagonal pattern

The number of layers of nitrogen molecules on the surface can be calculated from:

$$n = \frac{V}{V_m}$$

<div align="right">Equation 37</div>

where n = the number of layers

V = the volume of nitrogen adsorbed (m^3/g)

V_m = the volume of nitrogen in a monolayer (m^3/g)

As a single layer of nitrogen has an average statistical thickness of 0.35 nm, then the total layer thickness, t, can be calculated from:

$$t = 0.35n$$

<div align="right">Equation 38</div>

It was found that this thickness gave excellent agreement with results obtained by the equation of Harkins and Jura:[127]

$$t = \left(\frac{13.99}{0.34 - \log \frac{p}{p_0}} \right)^{1/2}$$

<div align="right">Equation 39</div>

With the layer thickness at each relative pressure now known, a comparative t-plot can be produced (see Figure 20). This involves the plotting of the volume of nitrogen adsorbed at each relative pressure, $V(p/p_0)$, against the corresponding layer thickness, $t(p/p_0)$, as calculated by both of the methods described above.
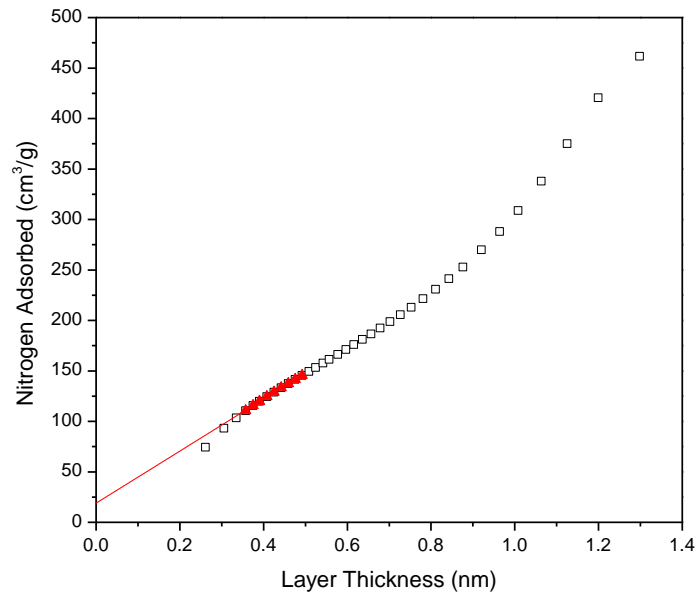
Figure 20: Comparative t-plot, showing the adsorption isotherm layer thickness (□), and the corresponding Harkins and Jura calculated values (▲) with accompanying linear fit.

The t-plot has a linear region between the layer thicknesses of 0.35 and 0.5 nm, corresponding to the beginning of multilayer formation, and capillary condensation, respectively. As micropores are filled during monolayer formation, they are not included in the calculated values.

The linear region of the t-plot can be fitted to:

$$V\left(\frac{p}{p_0}\right) = V_{micro} + kS_{ex}t\left(\frac{p}{p_0}\right)$$

Equation 40

The slope of the t-plot, kS_{ex}, can be used to calculate the external surface area, S_{ex}, that is the surface area contributed by mesopores, macropores and the outside surface of the material, such that:

$$S_{ex} = 1.547\frac{V}{t}$$

Equation 41

The coefficient 1.547 comes from k and is known as the density correction factor (value given for nitrogen, in this case). It is required to convert the volume adsorbed into an occupied surface area.

The corresponding micropore surface area, S_{micro}, can then also be calculated:

$$S_{micro} = S_{BET} - S_{ex}$$

<div align="right">Equation 42</div>

Returning to the t-plot, the micropore volume, V_{micro}, can be taken from the y-intercept.

3.5 Dynamic Light Scattering

Dynamic Light Scattering (DLS), also known as photon correlation spectroscopy, or quasi-elastic light scattering, is a technique used to determine the size of particles in a dispersion medium.[128]

When the light from a monochromatic light source, such as a laser, interacts with matter, it can be absorbed or scattered.[129] If the wavelength of the incident light is much larger than the size of the dispersed particles, this scattering will occur evenly in all directions. This phenomenon is known as Rayleigh scattering.[128]

The light scattered in all directions by the matter in a homogeneous solution will interfere destructively with itself. No scattered light can therefore be observed from these systems. However, in a system of particles dispersed within a medium of different refractive index, this destructive interference does not occur, and scattered light is observed.[129]

After interacting with the matter, the frequency of the scattered light is shifted slightly, with respect to the frequency of the incident beam. A photomultiplier tube is commonly used to detect the scattered light.[129] A schematic diagram of a typical DLS equipment set-up is shown in Figure 21, with the scattering angle set to 90°.
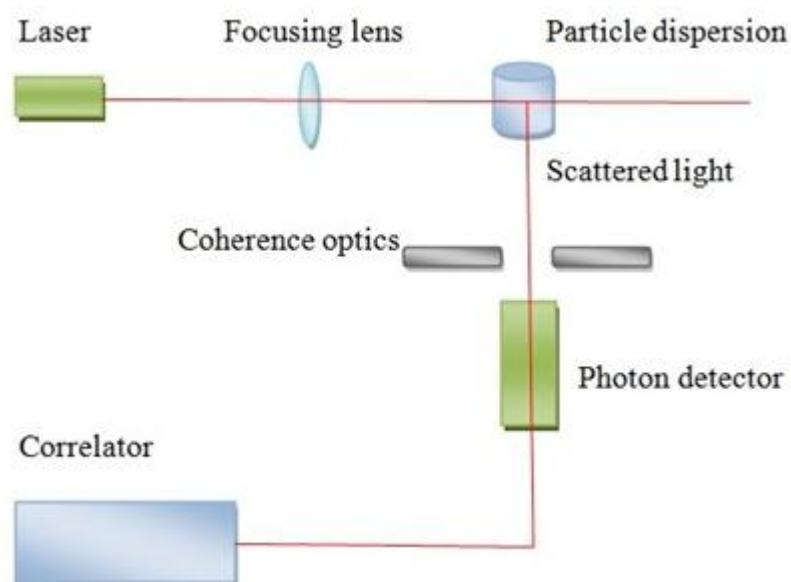
The particles in suspension will undergo random movement due to Brownian motion, caused by collisions between the particles and molecules of the dispersion medium.[131] As such, these collisions cause small particles to move quickly, while large particles move slowly. The particle transport imparted by Brownian motion is described by the translational diffusion coefficient, D, an important parameter in determining the size of the particles.[128]

As the particles move through the area of the dispersion illuminated by the incident beam of the laser, the intensity of light scattered by particles at the angle of detection will randomly fluctuate with time.[131] Small, fast moving particles, therefore, cause a more rapid fluctuation than large, slow moving particles.[128] This is demonstrated by Figure 22.
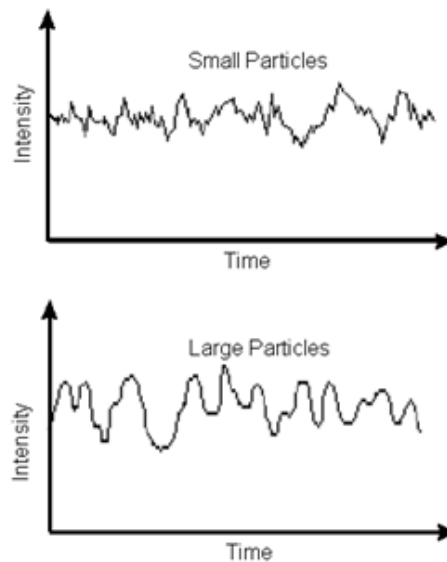
Figure 22: Fluctuations in scattered light intensity observed for small and large particles respectively.[128]

At a given time, t, the scattered intensity will have a certain value, attributable to the configuration of particles in the volume of the system under study. This intensity randomly fluctuates with time, due to the Brownian movement of the particles. At very short intervals, τ, after t, i.e. t + τ, comparison between the intensities at t and t + τ, will show a correlation depending on how much the particle configuration has changed. Further comparison at sequential intervals of τ, i.e. t + 2τ, t + 3τ, t + 4τ…, will show a decreasing correlation with the original value at t, until no correlation is observed after a sufficiently long time.[128]

Slow moving large particles, with their less rapid fluctuations, will result in these intensity values staying correlated for longer than fast moving small particles. The changes in correlation can be plotted against time, to give a correlation function as shown in Figure 23.
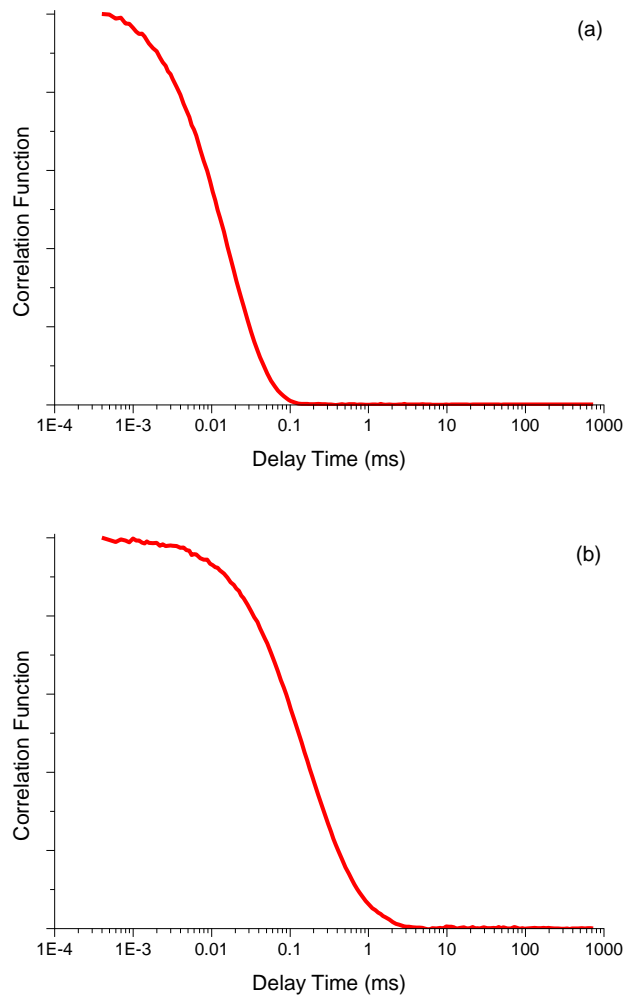
Figure 23: Correlation functions for (a) small particles and (b) large particles respectively.

Small particles show fast decay of the correlation function, while large particles show a delay before the onset of decay. This change in delay, therefore, gives information about the size of the particles being studied.

The second-order correlation function, $g_2(\tau)$, is calculated from the average of the product of the intensity at t, I(t), multiplied by the intensity at time t + τ, I(t + τ),[129] such that:

$$g_2(\tau) = \langle I(t).I(t + \tau) \rangle$$

Equation 43

This is related to the electric field correlation function, $g_1(\tau)$, such that:

$$g_1(\tau) = \sqrt{g_2(\tau) - 1} = e^{-\Gamma\tau}$$

Equation 44

where Γ = decay rate of the electric field correlation function (s^{-1})

The decay rate is obtained by performing a cumulant analysis on the correlation function.[129] This involves the fitting of a Taylor polynomial curve (typically 3rd order) to the decaying correlation function. From this polynomial, the value of the coefficient for the x-term can be extracted. It is this coefficient that corresponds to the decay rate. Subsequently, the decay rate is related to the translational diffusion coefficient through:

$$\Gamma = D.q^2$$

where q = the scattering vector (m^{-1})

The scattering vector is defined as the difference between the vectors of the incident and scattered light respectively,[129] such that:

$$q = \frac{4\pi n_0}{\lambda}.\sin\frac{\theta}{2}$$

where n_0 = refractive index of the dispersion medium

λ = wavelength of the monochromatic light source (m)

θ = scattering angle (rad)

With Γ and q now known, a value for D can be calculated from Equation 45. This can subsequently be substituted into the Stokes-Einstein equation shown in Equation 47, allowing calculation of the hydrodynamic radius.[132, 133]

$$R_H = \frac{k_B T}{6\pi\mu D}$$

Where R_H = the hydrodynamic radius (m)

k_B = Boltzmann constant ($J\ K^{-1}$)

T = absolute temperature (K)

μ = dynamic viscosity (Pa s)

In all cases, the value of μ was assumed to be that of pure water at the experimental temperature, i.e. 8.9×10^{-4} Pa s.

The Stokes-Einstein equation is based on the diffusion of a single isolated spherical particle. The calculated value (R_H) is referred to as the hydrodynamic radius. It is the size of a spherical particle that diffuses at the same rate as the particles under investigation.[128] The actual particles may not be spherical and are likely to have a range of sizes (polydispersity) around this calculated average.

4 Experimental Methods

The following describes in detail the methods used to create RF xerogels. This starts with the preparation of the sol, through gelation, curing and solvent exchange, to the drying of the xerogel products. Also covered is how the analysis techniques used to study the various samples were performed.

4.1 Hydrogel Formation

To investigate the effect that altering various synthesis variables has on the final properties of RF xerogels, several different compositions of hydrogel were prepared. These compositions can be grouped by type to allow various comparisons to be made. All preparations were based on the same basic procedure, with slight modifications, as required, to study the influence of changing the chosen variables.

4.2 Standard Hydrogel Formation

Standard hydrogels are those produced using a single metal carbonate. These samples were made by directly following a previously established method,[134] ensuring consistency between samples prepared in this study, and allowing comparison with samples prepared by different gel makers working within the research group.

4.2.1 Naming of Standard Hydrogel Samples

To allow for easy identification of samples, and to once more ensure consistency, a standard sample naming practice was adopted. This practice took the form X_R/C_Y, where X is the metal carbonate chosen, R/C is the resorcinol to carbonate molar ratio and Y is the date of hydrogel production. For example, a gel produced on the 1st of June 2014, using sodium carbonate, at an R/C of 200, would be labelled as Na_2CO_3_200_1/6/14.

4.2.2 Reactant Quantities for Standard Hydrogels

In the preparation of all standard gels, three experimental parameters were kept constant; these being the R/F molar ratio, fixed at 0.5, total liquid volume, fixed at 60 ml, and total solids content, i.e. mass of R, F and C, fixed at 20% w/v. For the 60 ml volume used, the total solids content, therefore, corresponded to a mass of 12 g. Parameters that were varied in order to study the associated effects were R/C molar ratio and the metal carbonate catalyst chosen. As the 12 g total mass of solids was composed of all R, F and C, it was necessary to calculate the individual mass of each component required. The solids composition was initially determined on a mole basis from the molar ratios of R/F and R/C. These molar quantities were converted

to an equivalent mass, and subsequently, a percentage of the total equivalent mass. From the starting mass of 12 g, this allowed for calculation of the individual component masses.

Hence, depending on the R/C and metal carbonate chosen, the individual masses of R, F and C were altered accordingly. Table 2 shows the reactant composition of a hydrogel synthesis made using Na_2CO_3 at an R/C of 100. Appendix A contains a complete set of gel compositions for all metal carbonates and at each R/C ratio used for standard hydrogel formation.

Table 2: Hydrogel reactant composition for $Na_2CO_3\_100$.

	Equivalent Moles	Equivalent Mass (g)	Percentage Mass (%)	Required Mass (g)
Resorcinol	1.0000	110.1100	64.3082	7.7170
Formaldehyde	2.0000	60.0524	35.0728	4.2087
Carbonate	0.0100	1.0599	0.6190	0.07428
Total		171.2223	100.0000	12.0000

As formaldehyde was supplied as an aqueous solution, known as formalin, containing 37 wt.% formaldehyde and 10-15% methanol as a stabiliser, it was required to calculate the volume of formalin needed in each case. Formalin has a density of 1.09 g/ml and contains 37 wt.% formaldehyde, therefore:

*1 ml formalin = 1.09 g = 0.37 * 1.09 = 0.4033 g formaldehyde/ml formalin*

Volume of formalin required (ml) = mass of formaldehyde/0.4033

Formaldehyde has a density of 0.815 g/ml, therefore:

Volume of F in formalin (ml) = mass of formaldehyde /0.815

The remaining volume of formalin comes from water and methanol, therefore:

Volume of H_2O/MeOH (ml) = Volume of formalin required – Volume of F in formalin

This volume of water and methanol contributes to the total gel volume, so the required volume of deionised water to give a total volume of 60 ml is, therefore:

Volume of deionised water (ml) = 60 – Volume of H_2O/MeOH

Table 3 shows the values calculated for the $Na_2CO_3\_100$ gel reactant composition outlined in Table 2.

Table 3: Calculated reactant/solvent volumes required for $Na_2CO_3\_100$ hydrogel formation.

Volume of Formalin (ml)	10.44
Volume due to Formaldehyde (ml)	5.16
Volume due to Water/Methanol (ml)	5.28
Volume of Additional Deionised Water (ml)	4.72

Appendix B details the volumes of additional deionised water and formalin added for each gel composition.

4.2.3 Standard Hydrogel Preparation

To begin making a standard hydrogel, 50 ml of deionised water was pipetted into a clean, 500 ml glass jar with sealable lid. The required mass of resorcinol (SigmaAldrich, ReagentPlus, 99 %), obtained as a solid in the form of plate-like chunks, was weighed out accurately and added to the jar along with a magnetic stirrer bar. After placing on a magnetic stirrer plate, the contents of the jar were stirred to encourage complete dissolution of resorcinol. As this occurred, the required mass of metal carbonate was accurately weighed into a crucible. The various metal carbonates used are shown in Table 4.

Table 4: Metal carbonates used to synthesise hydrogels produced in this study.

Name	Formula	Description
Lithium carbonate	Li_2CO_3	SigmaAldrich, purum, ≥ 99 %
Sodium carbonate	Na_2CO_3	SigmaAldrich, anhydrous, ≥ 99.5 %
Potassium carbonate	K_2CO_3	SigmaAldrich, anhydrous powder, 99.99 %
Caesium carbonate	Cs_2CO_3	SigmaAldrich, ReagentPlus, 99 %
Calcium carbonate	$CaCO_3$	SigmaAldrich, ≥ 99 %
Barium carbonate	$BaCO_3$	SigmaAldrich, ACS reagent, ≥ 99 %
Ammonium carbonate	$(NH_4)_2CO_3$	SigmaAldrich, ACS reagent, ≥ 30.0 % NH_3 basis

Once the resorcinol was dissolved, the metal carbonate was added to the reaction mixture in the jar with continued stirring, again until complete dissolution was

achieved. It should be noted that both calcium and barium carbonate have very limited solubility in water (< 0.01 g/100 ml at 20 °C). As such, complete dissolution of the catalysts is not possible, and undissolved material will remain. Next, the remaining deionised water and required volume of formalin (SigmaAldrich) were added to the jar, which was tightly sealed and allowed to stir, uninterrupted, for a period of 30 min to ensure thorough mixing.

During this period, a Hanna Instruments pH20 bench top pH meter fitted with an HI 1110-B pH probe (Figure 24) was calibrated using neutral and acidic buffer solutions of pH 7.01 and pH 4.01 (Fluka Analytical). After the 30 min stir was complete, the jar was unsealed and the magnetic stirrer bar removed. The pH of the newly prepared solution was measured and recorded, before the jar was resealed tightly. Unfortunately, due to recurrent problems with the pH probe, only the Group I metal carbonate catalysed gels had their initial pH accurately recorded.

Figure 24: Hanna Instruments pH 20 pH meter.[135]

On resealing the jar, it was subsequently placed in an electric oven (Memmert ULE-500), preheated to 85 ± 5 °C, where it was left for three days to allow for gelation and curing of the hydrogel. The RF reaction will occur at room temperature; however, the elevated temperatures used greatly decrease the time scales involved.

4.2.4 Gelation Time Monitoring

As changes in R/C are known to influence gelation time (Section 1.7.3), each sample was monitored after it was placed in the oven to determine the gelation time for the combination of metal carbonate and R/C used. This was achieved via periodic tilting of the jars to an angle of 45° as they were being heated in the oven. This tilting was carried out at initial intervals dependent on the R/C, with lower R/C values requiring shorter intervals. However, as the sample neared gelation and the viscosity began to noticeably increase, these intervals were reduced to approximately 30 s in all cases. Gelation was said to have occurred when no flow was observed on tilting the jar.

4.3 Preheated Hydrogel Formation

With bench top preparation typically carried out at room temperature, the reaction mixtures will require time to heat up to the reaction temperature of 85 °C; this temperature profile is likely to influence the hydrogel formation. To investigate the possible effects, a selection of hydrogels was also prepared at an initial temperature of 55 °C, using an incubator. The standard hydrogel procedure from Section 4.2.3 was followed, but all liquid components were allowed to equilibrate at 55 °C before use. The 30 min stirring period was also performed at 55 °C. To compare with the room temperature samples, gelation times were again monitored.

4.4 Delayed Metal Carbonate Hydrogel Formation

In a slight modification of the standard hydrogel formation process, delayed metal carbonate hydrogels involve heating a solution containing only resorcinol and formaldehyde, with a solution containing the required mass of metal carbonate added only after a pre-determined period of time.

4.4.1 Naming of Delayed Addition Hydrogel Samples

The naming convention for delayed metal carbonate hydrogels is also only slightly changed from that of the standard hydrogels, i.e. X_R/C_Y. In order to specify the length of time (in minutes) that the resorcinol-formaldehyde solution was heated before addition of the metal carbonate, this time was added to the name after the date of production, i.e. X_R/C_Y_Z, e.g. Na_2CO_3_200_1/6/14_30 for a delay time (Z) of 30 min.

4.4.2 Reactant Quantities for Delayed Addition Hydrogels

As the final composition of the delayed metal carbonate hydrogels was identical to those of the standard hydrogels, the masses and volumes of reactants and deionised water could be used as previously calculated.

4.4.3 Delayed Addition Hydrogel Preparation

A great deal of similarity exists between the preparation of standard hydrogels and those with delayed addition of metal carbonate.

To begin, 40 ml of deionised water was pipetted into a clean 500 ml jar, while 10 ml of deionised water was added to a smaller 20 ml vial in the same way. The required mass of resorcinol was added to the jar and allowed to dissolve under stirring, as before. After weighing out the metal carbonate, this was added to the 10 ml of water in the small vial and shaken to dissolve fully. The remaining deionised water and the

required volume of formalin were then added to the resorcinol solution in the jar and the contents stirred, again for 30 min. Both the jar and small vial were subsequently sealed and placed in the preheated oven (85 ± 5 °C). After a pre-determined time had elapsed, both containers were removed from the oven and the metal carbonate solution quickly added to the resorcinol-formaldehyde solution. To ensure complete mixing, the contents of the jar were stirred for 30 s, before the stirrer bar was removed, the jar resealed and returned to the oven to allow gelation and curing over three days.

4.5 Ammonium Carbonate Containing Hydrogel Formation

Several hydrogels were formed which contained ammonium carbonate in place of the metal carbonate. When only ammonium carbonate was used, the procedure exactly followed that of the standard hydrogels, given in Section 4.2. However, gels were also made which contained equal molar ratios of ammonium carbonate and a metal carbonate.

4.5.1 Naming of Metal Carbonate/Ammonium Carbonate Hydrogel Samples

The naming convention for these ammonium carbonate containing gels again only slightly varied from that of the standard hydrogels. To reflect the presence of the ammonium carbonate, names were updated to $X/(NH_4)_2CO_3\_R/C\_Y$ (50:50), where X is the metal carbonate used, R/C is total when both carbonates have been added and Y is the production date. The (50:50) has been added to indicate equal molar concentration of the two carbonates.

4.5.2 Reactant Quantities for Metal Carbonate/Ammonium Carbonate Hydrogel Samples

Calculation of the required reactant quantities was based on the method used for the standard hydrogels, with the addition of ammonium carbonate accounted for. Depending on the total R/C chosen, each of the carbonates present had an individual R/C double that of the total, e.g. a total R/C of 100 would correspond to R/C ratios of 200 for each of the carbonates. Appendices C and D outline the required quantities of all the hydrogel constituents used in the metal carbonate/ammonium carbonate gels.

4.5.3 Metal Carbonate/Ammonium Carbonate Hydrogel Preparation

The preparation method varied little from that of the standard hydrogels (Section 4.2.3). After dissolution of the resorcinol, both carbonates were weighed out and

added to the resorcinol solution at the same time. All subsequent steps followed the standard hydrogel procedure exactly.

4.6   Secondary Metal Carbonate Hydrogel Formation

Secondary metal carbonate addition hydrogels are produced using two different metal carbonates. A parent metal carbonate is added to the stirring resorcinol solution, as in the standard hydrogel formation, and a secondary metal carbonate is then added to the existing solution at a pre-determined time. This addition time varied from simultaneous adding of the two metal carbonates, to a value close to the gelation point of the original solution.

4.6.1   Naming of Secondary Metal Carbonate Hydrogel Samples

The addition of a second metal carbonate necessitated some changes to the naming convention. Based on the system used for standard hydrogels, names took the form X_1/X_2_Total R/C_Y_Ratio_Z, where X_1 is the parent metal carbonate, X_2 is the secondary metal carbonate, total R/C is the final R/C ratio once both metal carbonates had been added, Y is the production date, Ratio is the ratio of parent metal carbonate: secondary metal carbonate, and Z is the time of secondary metal carbonate addition, expressed as a percentage of the gel time of the parent metal carbonate gel. For example, $CaCO_3/Na_2CO_3$_100_1/6/14_50:50_70%, would involve adding Na_2CO_3 to a $CaCO_3$ gel solution, at 70% of the gel time of the $CaCO_3$ gel. The 50:50 ratio and total R/C of 100 give information on the individual R/C values of the two metal carbonates. In this instance, both metal carbonates are added in equal molar quantities, with each having an R/C of 200. When combined this gives a total R/C of 100.

4.6.2   Reactant Quantities for Secondary Metal Carbonate Hydrogel Samples

In addition to the previously established constant variables of R/F, solids content and total volume, all secondary addition hydrogels had a fixed total R/C of 100, with only the ratio of each individual metal carbonate being altered. Individual component masses were calculated in the same way as for standard hydrogels, taking into account the additional number of moles contributed by the secondary metal carbonate, while maintaining a total mass of 12 g. Table 5 shows the composition of a hydrogel made with $CaCO_3$ as the parent metal carbonate, Na_2CO_3 as the secondary metal carbonate, and carbonate ratio of 50:50. Appendix E details the composition of all metal carbonate combinations and ratios used.

	Equivalent Moles	Equivalent Mass (g)	Percentage Mass (%)	Required Mass (g)
Resorcinol	1.0000	110.1100	64.3193	7.7183
Formaldehyde	2.0000	60.0524	35.0788	4.2095
Carbonate 1 (Ca)	0.0050	0.5005	0.2923	0.03508
Carbonate 2 (Na)	0.0050	0.5299	0.3096	0.03715
Total		171.1928	100.0000	12.0000

The required volume of both formalin and deionised water were calculated as before, from the required mass of formaldehyde, with these volumes given in Appendix F.

4.6.3 Secondary Metal Carbonate Hydrogel Preparation

Depending on the addition time of the secondary metal carbonate, the hydrogel preparation procedure varied slightly. For simultaneous addition of the two metal carbonates, the procedure closely followed that of standard hydrogel formation. 50 ml of deionised water was pipetted into a clean, 500 ml jar. The required resorcinol was weighed out, added to the jar and dissolved with magnetic stirring. Both the parent metal carbonate and secondary metal carbonate were weighed out, added to the contents of the jar, and dissolved. The required volumes of deionised water and formalin were added to the jar, which was sealed and allowed to stir for 30 min. The jar was then transferred to an oven, preheated to 85 ± 5 °C.

Meanwhile, secondary addition of metal carbonate after a pre-determined time followed a procedure similar to that of delayed metal carbonate addition. 40 ml of deionised water was added to a clean 500 ml jar and 10 ml to a small 20 ml vial. Resorcinol and the parent carbonate were dissolved in the jar, with the secondary carbonate dissolved in the small vial. After adding the formalin and additional deionised water to the jar and leaving to stir for 30 min, both the jar and small vial were placed in the 85 °C preheated oven.

Samples made with simultaneous metal carbonate addition were allowed to gel and cure uninterrupted for three days, as for standard hydrogel formation. Delayed secondary metal carbonate addition samples followed the procedure as outlined for the delayed metal carbonate hydrogel formation. The jar and corresponding vial

were removed from the oven at the predetermined time and the contents mixed. After stirring for 30 s, the stirrer bar was removed, the lid resealed and the jar returned to the oven to allow gelation and curing to occur.

4.7 Alternative Secondary Metal Carbonate Hydrogel Formation

These hydrogels expand on the process of adding a secondary metal carbonate to a standard hydrogel (see Section 4.6). Instead of adding just the secondary metal carbonate, two partially formed hydrogels at various stages of the gelation process are mixed. This, therefore, also adds additional R and F to the original hydrogel composition, with various extents of gelation depending on the addition time.

4.7.1 Naming of Alternative Secondary Addition Hydrogel Samples

To account for the mixing of two partially formed hydrogels, they are named as a combination of those of the hydrogels being mixed, including the degree of gelation each hydrogel has attained before mixing. They, therefore, take the form $X_1\_R/C_1\_Z_1/X_2\_R/C_2\_Z_2\_Y$, where X is the metal carbonate, followed by its associated R/C, and Z is the degree of completion of gelation. Y once more corresponds to the date of production. $CaCO_3\_100\_70\%/Na_2CO_3\_100\_70\%\_1/6/14$ would, therefore, involve the mixing of a $CaCO_3$ R/C 100 and a Na_2CO_3 R/C 100 sample, with both at 70% of their gelation time.

4.7.2 Reactant Quantities for Alternative Secondary Addition Hydrogel Samples

To ensure a consistent final gel volume of 60 ml, pre-mixing samples had a total volume of 30 ml, with an associated halving of the solids mass to 6 g. Individual component masses were calculated as before, taking into account the reduced total mass. Table 6 shows the half volume hydrogel composition for $Na_2CO_3\_100$. Further half volume compositions are provided in Appendix G.

Table 6: Half volume hydrogel reactant composition for $Na_2CO_3\_100$.

	Equivalent Moles	Equivalent Mass (g)	Percentage Mass (%)	Required Mass (g)
Resorcinol	1.0000	110.1100	64.3082	3.8585
Formaldehyde	2.0000	60.0524	35.0728	2.1044
Carbonate	0.0100	1.0599	0.6190	0.03714
Total		171.2223	100.0000	6.0000

Volumes of formalin and additional deionised water were calculated, as before, using the new mass of formaldehyde as a basis. Table 7 shows the new volumes required.

Table 7: Calculated reactant/solvent volumes required for half volume Na$_2$CO$_3$_100 hydrogel formation.

Volume of Formalin (ml)	5.22
Volume due to Formaldehyde (ml)	2.58
Volume due to Water/Methanol (ml)	2.64
Volume of Additional Deionised Water (ml)	2.36

Appendix H contains the required volumes for the other gel compositions used.

4.7.3 Alternative Secondary Addition Hydrogel Formation

This process follows the procedure as detailed for standard hydrogel formation. The starting volume of deionised water was reduced to 25 ml in order to account for the reduced total volume being used.

Jars were sealed and placed into the electric oven at 85 ± 5 °C, as before. They were removed from the oven at the appropriate time, the contents mixed together and stirred for 30 s, before removal of the stirrer bar, resealing and returning to the oven where they were left to gel and cure for three days.

4.8 Solvent Exchange in the Synthesised Hydrogels

As previously established (Section 1.6.3), exchange of the water entrained within the cured gel network will reduce shrinkage during the drying phase. The solvent chosen for this process was acetone, due to its relative cheapness, low surface tension, and the high frequency of use in the literature. This allowed for a better comparison with RF gels prepared in other studies.

After removing the cured hydrogel from the oven, it was allowed to cool to room temperature. Once cooled, any excess water was drained from the solid, and the monolithic gel disc cut into several pieces to increase the effectiveness of the solvent exchange process. To induce solvent exchange, 100 ml of acetone (SigmaAldrich, ACS Reagent, ≥99.5 %) was poured into the jar containing the gel pieces and the lid resealed. The jar was then shaken vigorously for several minutes. The acetone was subsequently drained, replaced by a further 180 ml of fresh acetone and the jar resealed, with the addition of Parafilm® wrapped around the lid

to prevent leakage. The sealed jar was then placed on a shaker unit (VWR 3500 Analog Orbital Shaker) for three days.

4.9 Drying of the Solvent Exchanged Gels

Sub-critical drying was chosen due its ease and the lack of specialist high pressure equipment needed to carry out a supercritical drying process.

The solvent exchanged gel was removed from the shaker and the acetone drained. The open jar was covered with a piece of aluminium foil, into which five small holes were pierced. The covered jar was placed in the chamber of a Townson and Mercer 1425 Digital Vacuum Oven, with attached Vacuubrand MZ 2C NT vacuum pump. Samples were dried under vacuum at 85 °C, while iced water in two solvent traps condensed the acetone vapour removed from the chamber. For safety reasons, the vacuum oven was cooled overnight and the vacuum pump switched off. However, the chamber was isolated to maintain full vacuum. The drying cycle was repeated for a second day to ensure complete removal of acetone from the porous structure.

The solvent traps were emptied on a regular basis, by isolating them from the vacuum chamber. This also allowed for the monitoring of the drying process. When no further acetone was collected in the traps, the samples were taken as dry.

Once drying was complete, samples were removed from the vacuum oven and transferred to labelled containers ready for further analysis. To indicate that the sample had been dried, _D was added to the sample name.

The same solvent exchange and drying process was used for all hydrogels, no matter the composition or synthesis method. This was to minimise the influence of these factors on the structure of the dried xerogel. However, it is likely that complete solvent is never achieved, with some water remaining trapped in the pores. This will be especially so if the pores are small. As a result, any remaining water will have an impact on the textural properties of the dried gel, with the increased surface tension causing greater collapse of the porous structure.

4.10 Surface Area and Porosity Measurements

All dried gel samples underwent surface area and porosity measurements in order to determine their characteristics and to allow comparison between the properties imparted by varying synthesis conditions.

Measurements were performed on a Micromeritics ASAP 2420 surface area and porosity analyser (see Figure 25) through analysis of nitrogen adsorption/desorption isotherms.
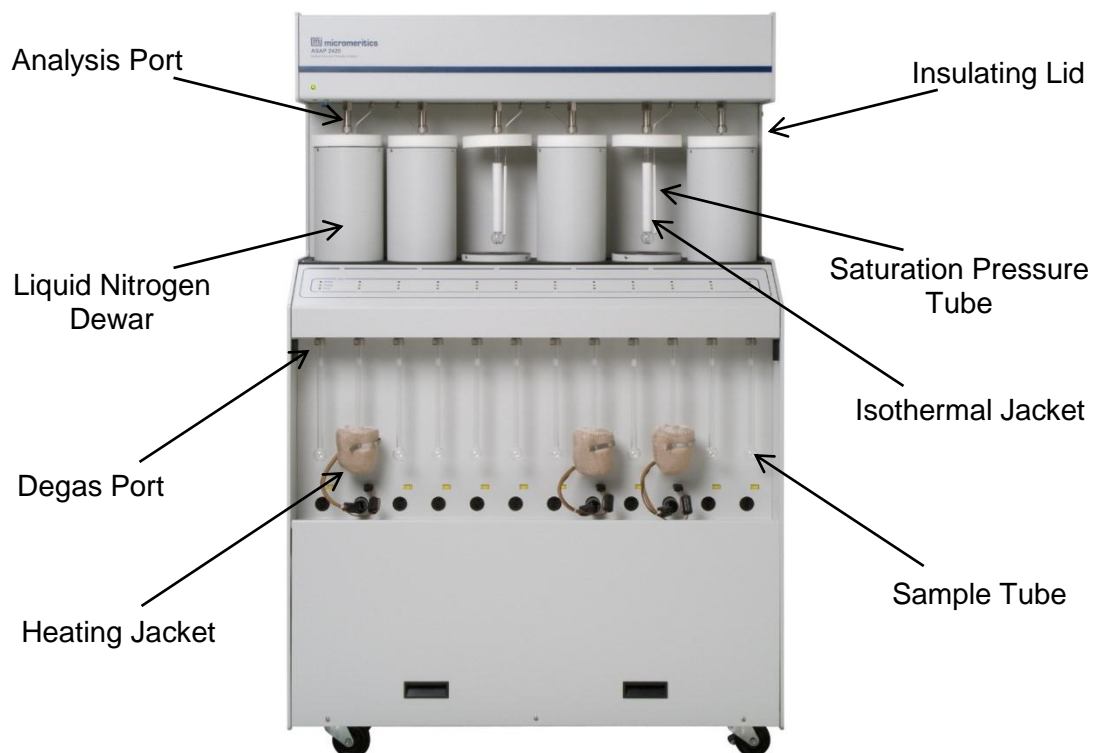
Figure 25: Micromeritics ASAP 2420 Surface Area and Porosity Analyser.[136]

The analysis methods described above (Sections 3.3 and 3.4) were applied to determine both the surface area and pore size distribution of the sample. Pore volumes were determined from the volume of nitrogen adsorbed at the highest pressure step, i.e. relative pressure close to 1.0.

4.10.1 Sample Degassing in Preparation for Surface Area and Porosity Analysis

In order to remove any adsorbed impurities (e.g. residual acetone or moisture) from the material surface, which would interfere with the accuracy of measurements, the samples were first degassed. This involved reheating the sample under vacuum, before backfilling with pure nitrogen.

Approximately 0.5 g of the sample to be analysed was accurately weighed into a sample tube (see Figure 26). The tube was then attached to a degas port on the ASAP instrument and secured in place. A heating jacket was then slipped over the bulb of the tube, ensuring that the internal thermocouple was in contact with the glass. To stop the heating jacket from moving during the degas process; it was

secured in place with a clip. Samples were degassed by initially heating to 50 °C while reducing the pressure first to 5 mmHg, followed by a further reduction to 10 μmHg. Upon reaching this second pressure, the sample was held at 50 °C for 30 min, before the temperature was ramped to 110 °C, at which it was held for 120 min. On the completion of the degas cycle, samples were cooled to room temperature and backfilled with pure nitrogen.

Figure 26: Micromeritics ASAP 2420 Sample Tube.[137]

Incomplete degassing (e.g. degassing at lower temperatures or for shorter times) would lead to incomplete removal of impurities from the surface of the material. This would lead to blocking of adsorption sites on the surface, resulting in an apparent reduction in measured surface area, and potential filling/blocking of pores within the network.

4.10.2 Xerogel Sample Analysis through Nitrogen Adsorption/Desorption

Once backfilled, the sample tube was removed from the degas port and reweighed accurately. This new sample mass was used to determine specific values for the surface area and porosity measurements. After reweighing, a volume displacement insert was placed in the tube, and an isothermal jacket applied to the outside. These features reduced the empty space within the neck of the tube, and maintained a constant temperature at the tube surface, respectively. The tube was then attached to an analysis port on the instrument. Analysis was performed at -196 °C, which was maintained through the use of liquid nitrogen surrounding the sample tube. Capillary

action saw a thin layer of liquid nitrogen drawn up between the isothermal jacket and the tube surface. The level of liquid nitrogen in contact with the tube was therefore kept constant, even if the bulk volume dropped significantly. The analysis cycle consisted of 40 nitrogen adsorption steps in the relative pressure range of 0.01 - 1, followed by a 30 point desorption branch, conducted between the relative pressures of 1 - 0.1.

4.11 Dynamic Light Scattering

DLS measurements were conducted on an ALV/GCS-3 Compact Goniometer System (Figure 27) allied to an ALV/LSE-5004 Multiple Tau Digital Correlator. Experiments were conducted in a room which was climate controlled to 22 °C. The laser used was He:Ne, producing monochromatic light with a wavelength of 632.8 nm.

He:Ne Laser

Scattered Light Detector

Sample Holder

Laser Attenuator
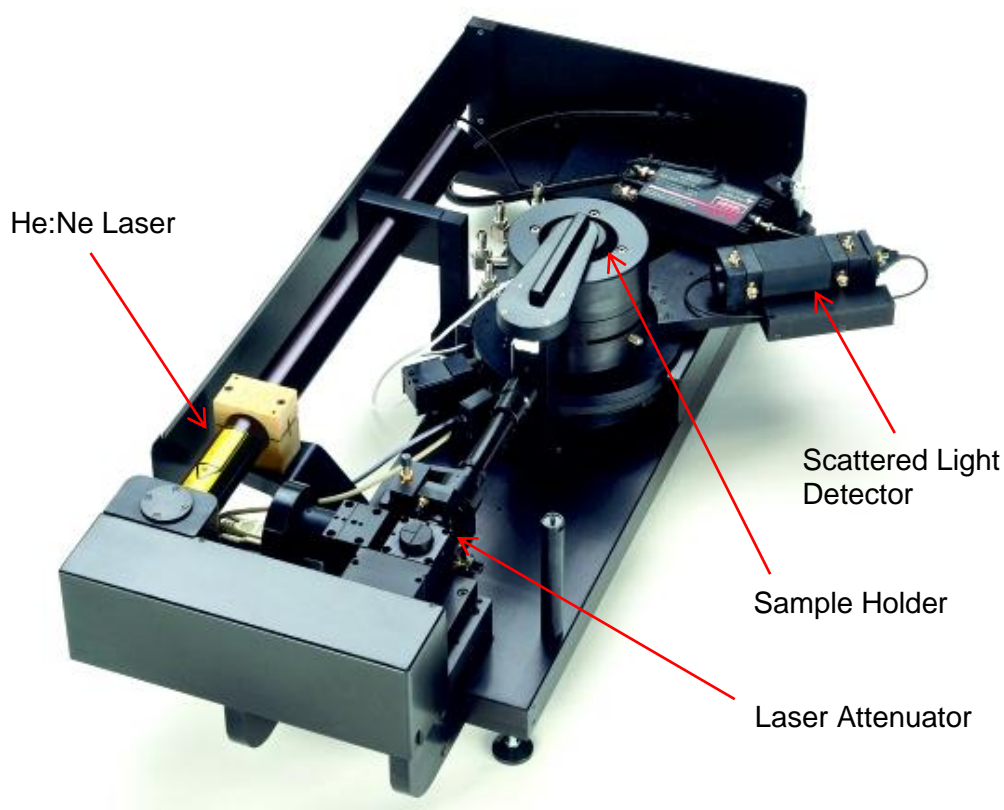
Figure 27: ALV/CGS-3 Compact Goniometer System with detector guard removed.[138]

Samples to be analysed using DLS were prepared as for the appropriate hydrogel formation described above. At the conclusion of the 30 min stirring period, equal volumes of approximately 3 ml of the bulk solution were transferred into the required number of small borosilicate glass cells, diameter 10 mm and height 75 mm (Fisher

Scientific). The solution was filtered through a 0.2 μm pore size PTFE syringe filter (Whatman Puradisc) in order to remove any undesired residual particulates that would interfere with scattering experiments. After filling, each of the cells was sealed with a polypropylene cap, and all but one of the cells were placed in the electric oven at 85 ± 5 °C. The remaining cell was taken directly to the scattering instrument and placed in the sample holder. Scattering experiment run times were set at 10 s, with the detector angle fixed at 90° to the beam path.

Subsequent cells were removed from the oven at intervals of 10% of the total sample gel time, allowing for comparison between samples at equivalent percentage points in the gelation process. Upon removal from the oven, samples were rapidly quenched to room temperature. This effectively stopped the gelation process, while also eliminating thermal currents which could disrupt the scattering exhibited by the sample. Once quenched, the samples were analysed, as before. The final cell corresponded to a sample that had gelled immediately prior to removal from the oven.

Secondary addition hydrogels were analysed in two stages; 'before' and 'after' secondary addition. 'Before' addition samples were analysed as described previously, with filtering of the samples before transferring to the sample cells. At the time of addition, the mixing process took place as described above. Once the 30 s stir was complete, equal volumes of approximately 3 ml were again transferred to a sufficient number of cells to cover the remainder of the gelation period, these being the 'after' addition samples. Samples were not filtered, to ensure that none of the developing clusters were removed. The small samples were returned to the oven to continue the gelation process, and removed and quenched as previously described at the requisite intervals. Intervals were maintained at 10% of the gel time of the parent hydrogel.

Autocorrelation functions generated for each experimental time point were analysed using the cumulant method, as described in Section 3.5. This resulted in the calculation of the average hydrodynamic radius at each point in the gelation process.

5 Results Part 1 - Gels Synthesised with Group I Metal Carbonate Catalysts

Sodium carbonate is the most commonly used catalyst in the synthesis of RF gels; however, lithium, potassium and caesium carbonate can also be used. The effect of changing the metal carbonate, and altering the R/C ratio, were studied using DLS to monitor the growth of primary clusters, in conjunction with surface area and porosity measurements to probe the textural properties of the resultant gels. Following on from these results, the influence of the preparation temperature, and the timing of catalyst addition were further investigated.

5.1 Gelation Time Monitoring

In order to ascertain the window during which the analysis and experimentation of gelling samples could be performed, it was necessary to determine the time taken for gelation to occur. The gelation time monitoring process was carried out for all of the gels synthesised using a Group I metal carbonate catalyst. A total of 24 samples were, therefore, monitored, covering each of the 4 metal carbonates used (lithium, sodium, potassium and caesium), at the 6 chosen R/C ratios (100, 200, 300, 400, 500 and 600). It was found that for an equivalent R/C, gels synthesised using each of the metal carbonates required the same gelation time. These times are shown in Table 8.

Table 8: Gelation times for Group I metal carbonate catalysed RF gels.

R/C	Gelation Time (min)
100	35
200	43
300	55
400	65
500	80
600	120*

*It should be noted that the sample synthesised using caesium carbonate, at an R/C of 600, failed to gel within an experimentally viable time frame, and so will not be included in any further analysis.

All gelation times were measured to within ± 30 s of the times given in Table 8. As the viscosity of the samples noticeable increased as gelation neared, it was possible to pre-empt the approaching gelation point and accurately determine the time at which it occurred.

The gelation times obtained agree with those of Job *et al.*, who also found that increasing R/C corresponded to an increase in gelation time.[139] However, they contrast with the results of Morales-Torres *et al.*, who found that at a fixed R/C of 300, gelation time increased when descending the Group I series of metals, i.e. lithium gave the shortest time and caesium the longest.[140] This increase may be explained by the thermal regimes used in the study of Morales-Torres *et al.*, where gels were left at room temperature for 1 day, followed by heating of the samples to 50 °C.[140]

Based on these determined gel times, the decision was taken to carry out further analyses at 10% intervals of the total gelation time. This, therefore, allowed direct comparison between all gel samples at an 'equivalent' point in the gelation process. However, as the changing synthesis variables are known to influence the gelation process, it is unlikely that the gels themselves will be equivalent. Instead, only the percentage of the gel time which has passed at the point of analysis is the same. It should also be noted that choosing a percentage time based analysis system gave an equal number of data points for each sample. Choosing an arbitrary time interval would have prevented these comparisons from being made and resulted in inconsistent levels of data. The interval times are shown in Table 9.

Table 9: Interval times used in the analysis of Group I metal carbonate catalysed RF gels.

R/C	Interval Time (min)
100	3.5
200	4.3
300	5.5
400	6.5
500	8.0
600	12.0

5.2 Dynamic Light Scattering Studies

DLS measurements were performed on all samples at the relevant interval times. For each analysis point, the digital correlator provided two sets of raw data; an autocorrelation function and scattered light intensity. Analysis of this data allowed for the determination of valuable information on the gelation process.

The first set of data from the correlator generated the autocorrelation function for each sample. The normalised autocorrelation functions obtained over the entire gelation period for both a sodium carbonate and caesium carbonate gel, with R/C 100, are shown in Figure 28.
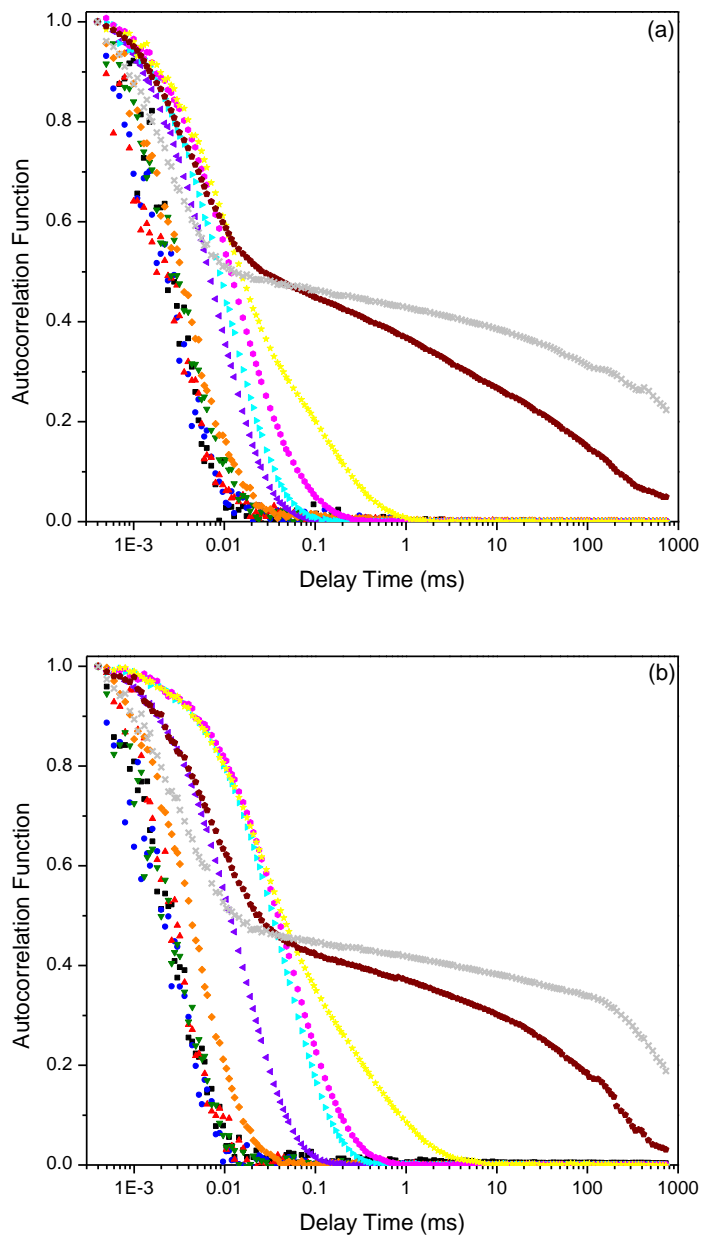
Figure 28: DLS autocorrelation functions obtained for a (a) sodium carbonate and (b) caesium carbonate gel with R/C 100 at 0% (■), 10% (●), 20% (▲), 30% (▼), 40% (◆), 50% (◀), 60% (▶), 70% (⬤), 80% (★), 90% (⬣) and 100% (✕) of the total gel time.

It can be seen that, as gelation proceeds, the autocorrelation function changes according to the particle size detected. Initially, the decay of the function is exponential. As the number of intervals increase, the delay time, before decay

begins, also increases. These features correspond to free Brownian motion, implying that, at these times, the primary clusters are growing and are moving without obstruction or intercluster interaction. Plotting the autocorrelation functions on a linear time-scale clearly demonstrates how the profiles exhibit an exponential decay, as shown in Figure 29.
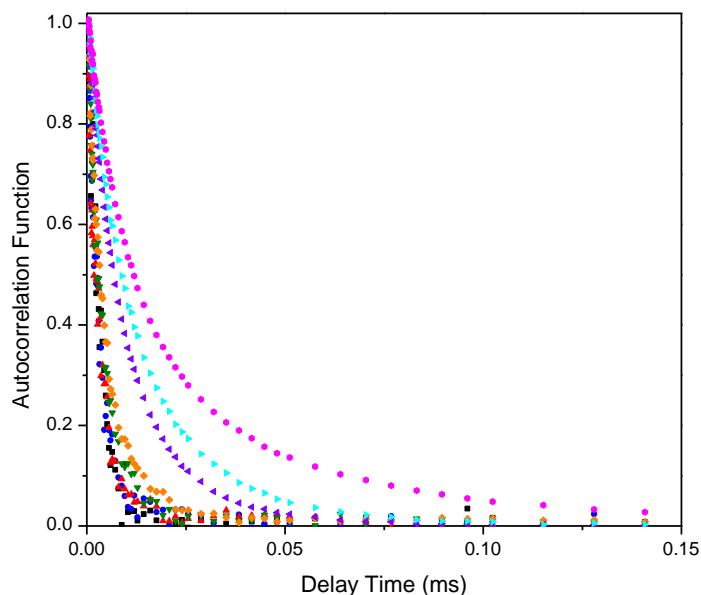
Figure 29: DLS autocorrelation functions for a sodium carbonate gel with R/C 100 at 0% (■), 10% (●), 20% (▲), 30% (▼), 40% (◆), 50% (◄), 60% (►) and 70% (⬤). Delay time is plotted on a linear scale to demonstrate the exponential decay of these profiles in the early stages of gelation.

At later experimental times (e.g. t = 80%, i.e. 28 min for R/C 100), the shape of the autocorrelation function changes, moving away from a purely exponential decay, with the introduction of a small secondary decay. This suggests that additional species with slower dynamics are now present, indicating that the processes of networking and aggregation have begun, and the movement of clusters is now hindered. Detailed models of how the cluster populations present evolve over time, which could subsequently be fitted to the measured autocorrelation functions, would be needed to clearly discriminate between aggregation and networking.[141] However, these models are outwith the scope of this work, and have not been developed here.

Finally, at times approaching, and at, gelation, the autocorrelation functions become non-ergodic, i.e. they do not fully decay to zero. This feature is indicative of a gel network which has some degree of permanent structure. The residual initial decay also suggests that a degree of motion is still possible, with complete rigidity of the

network not yet achieved. It is possible that these residual movements are caused by partially bound polymeric branches that have yet to completely connect with the rest of the 3D network; however, it is likely that these branches would provide slower contributions than the corresponding diffusivity of primary clusters.[141] This reinforces the need for curing of the newly formed gel in order to form a stable structure and resulting pore texture.

To clearly demonstrate how the decay of the autocorrelation functions deviate away from a purely exponential profile at later times in the gelation process, they can be plotted using a second logarithmic scale on the y-axis. This is demonstrated in Figure 30, for each of the profile types: single exponential decay at 50%, secondary decay at 80%, and non-ergodic at 100%.
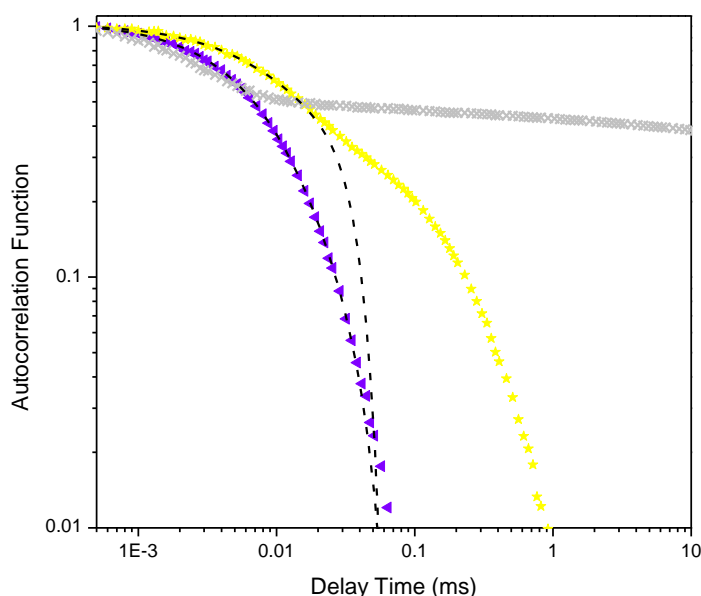
Figure 30: Autocorrelation functions obtained from DLS for a sodium carbonate gel with R/C 100 at 50% (◀), 80% (★) and 100% (✕) of the total gel time. Dashed lines represent the theoretical exponential decay of a monodisperse cluster population with hydrodynamic radius determined from the initial decay.

Dashed lines are included in Figure 30, which represent the theoretical exponential decays that would be exhibited by a monodisperse sample with hydrodynamic radius determined from the initial decay. These hydrodynamic radii values will be covered in more detail shortly. It can be seen that in the case of 50% of the total gel time, the theoretical decay follows the experimental data exactly. In the case of 80%, the experimental data follows the theoretical decay in the initial stages, before deviating away at later delay times.

Appendix I shows the corresponding autocorrelation functions for higher R/C ratios, i.e. 400 and 600; which show that the gelation process changes with R/C. As R/C is increased, the percentage time at which the secondary decay is observed decreases; indicating that the networking and aggregation portion of gelation occurs over longer time scales. However, the increasing interval times mean that as R/C increases, the absolute time at which the secondary decay first develops also increases. Along with the longer networking and aggregation processes, this suggests that the catalyst promotes these processes. These features are summarised in Table 10.

Table 10: Comparison of the networking and aggregation times for gels with increasing R/C ratio.

R/C	Time at which secondary decay occurs (min)	Time between onset of secondary decay and gelation (min)
100	28	7
400	45.5	19.5
600	48	72

As described in detail in Section 3.5, the cumulant method can be applied to each of the autocorrelation functions obtained in order to determine the hydrodynamic radius of the growing clusters. In this study, cumulant method analysis was limited to only those autocorrelation functions exhibiting a single exponential decay profile, corresponding to freely moving clusters. Near gelation, at which point the clusters start to experience networking and aggregation, the clusters are no longer diffusing freely and the exponential decay is lost. As a result, the true hydrodynamic radius at these times can no longer be determined. Hydrodynamic radii values were, therefore, determined for each suitable data set obtained for all of the gels studied with the results shown in Figure 35.
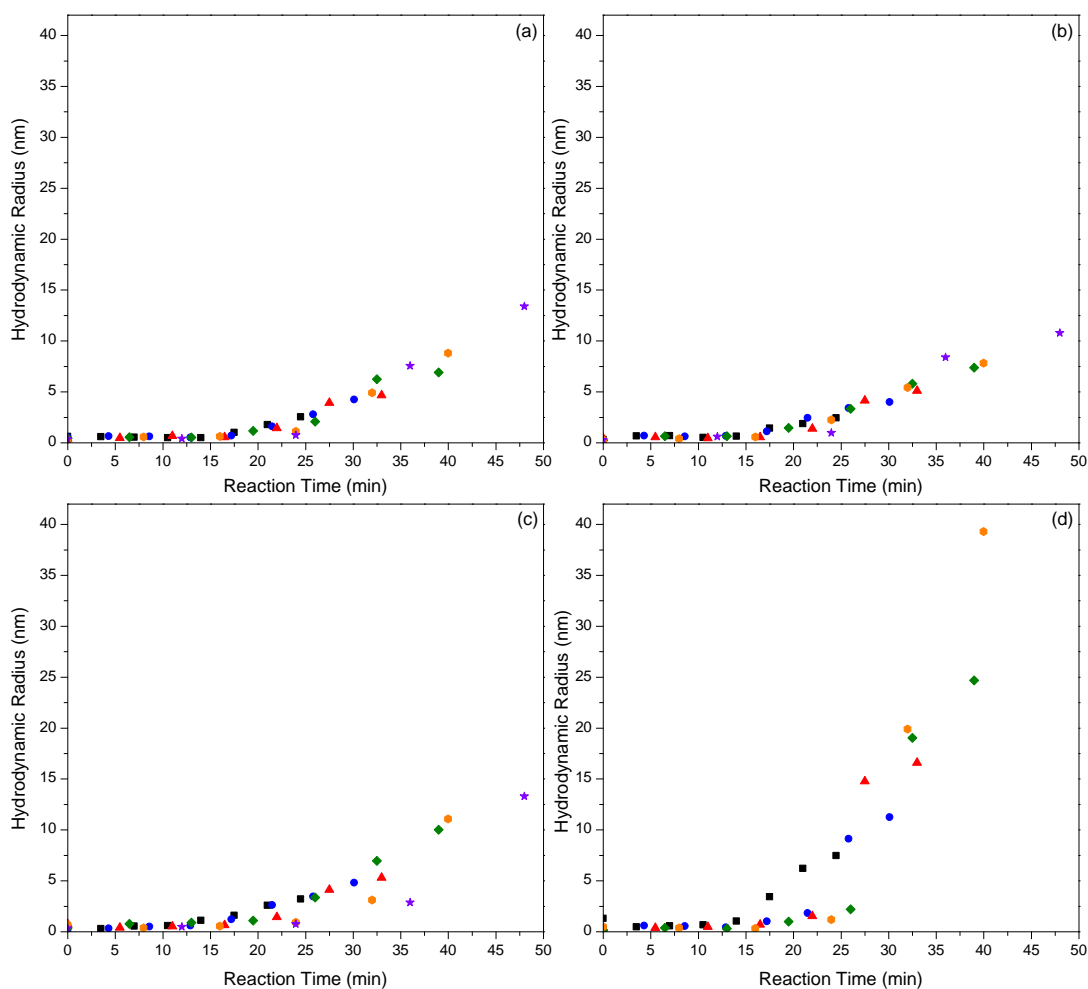
Figure 31: DLS hydrodynamic radii values for (a) lithium carbonate, (b) sodium carbonate, (c) potassium carbonate and (d) caesium carbonate, at R/C ratios of 100 (■), 200 (●), 300 (▲), 400 (◆), 500 (●) and 600 (★).

It can be seen that, in all cases, there is a period of time wherein the hydrodynamic radius remains constant at less than 1 nm. This size corresponds to a hydrodynamic radius of 0.4 nm for a hydrated resorcinol molecule,[80] suggesting that only hydroxymethyl derivatives are present during this time. This delay in growth is investigated further in Section 5.5.

By examining and comparing the results for lithium, sodium and potassium carbonate more closely, it was found that the hydrodynamic radii fall into a narrow, overlapping band, as seen in Figure 32.
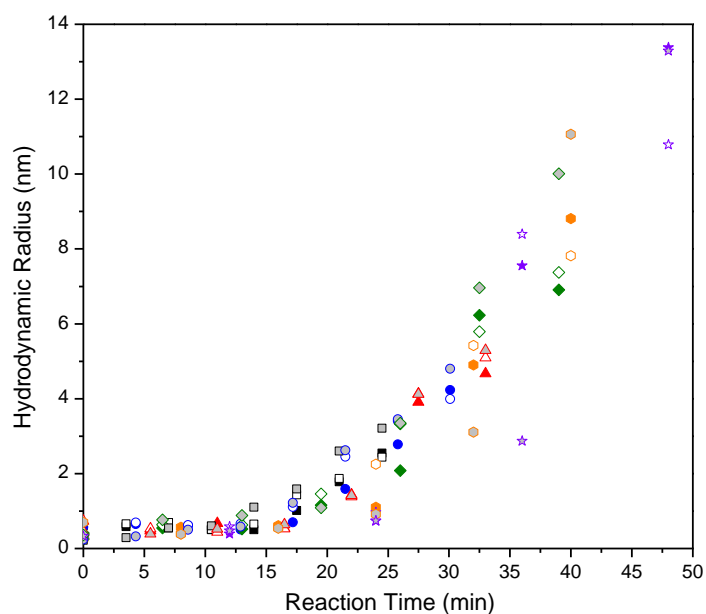
Figure 32: DLS hydrodynamic radii comparison between Li_2CO_3 (closed symbols), Na_2CO_3 (open symbols) and K_2CO_3 (grey filled symbols) at R/C ratios of 100 (■), 200 (●), 300 (▲), 400 (◆), 500 (⬤) and 600 (★).

The results in Figure 32 suggest that cluster growth occurs in a near linear fashion. For this radial increase to happen, it implies that growth sites are available across the entire cluster surface. The cation interaction with these clusters also implies a net negative charge on the clusters. However, as cluster growth is thought to occur through protonation of the growing species at low pH values, it is unlikely that the clusters exhibit specific negative charges. Instead, the system contains a large number of aromatic rings, with delocalised π-electron clouds. Cation-π interactions could therefore explain the affinity between the clusters and the cations.

This comparison also indicates that the growth of clusters is virtually independent of the R/C ratio or metal carbonate used for lithium, sodium and potassium. However, when comparing the maximum, pre-aggregation hydrodynamic radii, a dependence on R/C can be seen. It is clear that as R/C increases, so does the maximum observed radius. For clarity, the maximum pre-gelation values are plotted against R/C in Figure 33.
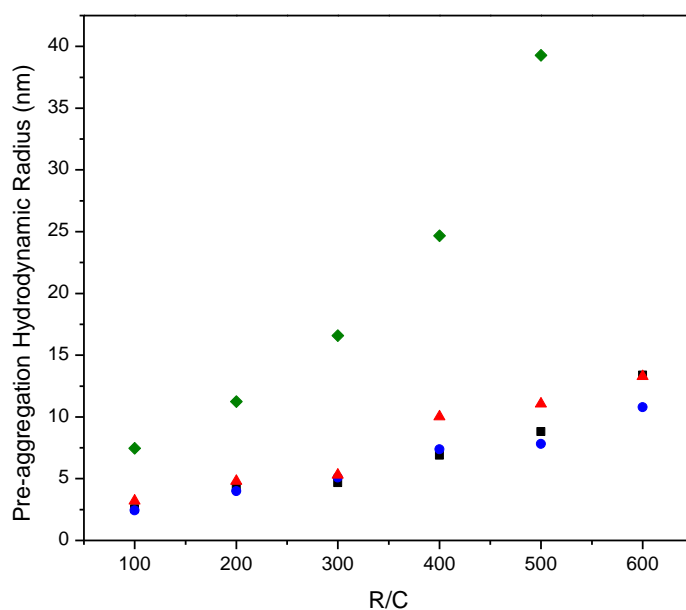
In contrast, caesium carbonate catalysed systems exhibit significantly different cluster growth patterns to the other Group I metals. The growth is no longer consistent across the R/C spectrum, with clusters in systems with low R/C ratios appearing to grow faster than those for systems with higher R/C. There also appears to be little order in the delay between the placing of samples in the oven and the onset of cluster growth, with times ranging from around 14 min, to more than 25 min. It can also be seen from Figure 33 that the maximum pre-aggregation sizes are much larger than the lithium, sodium and potassium counterparts.

The differences exhibited by the caesium systems may be as a result of the coalescence of small clusters. As the exponential decay of the autocorrelation functions is maintained, despite the increased size, the clusters are free to diffuse and are, therefore, not at the point of networking and aggregation. Further work would be required on these caesium systems to confirm this hypothesis.

The increasing observed cluster size, with increasing R/C, from Figure 33 may explain the results presented in Table 10. Hsu et al. reported that as particle size increased, so did the repulsion between particles.[142] As a result, smaller clusters were more likely to come together and aggregate than their larger counterparts. This agrees with the observations presented here, where higher R/C ratios result in larger clusters, which in turn take longer to aggregate.

The second set of data provided by the correlator is the time dependent scattered light intensity. By taking the average intensity over the 10 s run time for each measurement point, further information on the gelation process can be discerned. These average intensities are shown in Figure 34, with the results for lithium and potassium carbonate given in Appendix I.
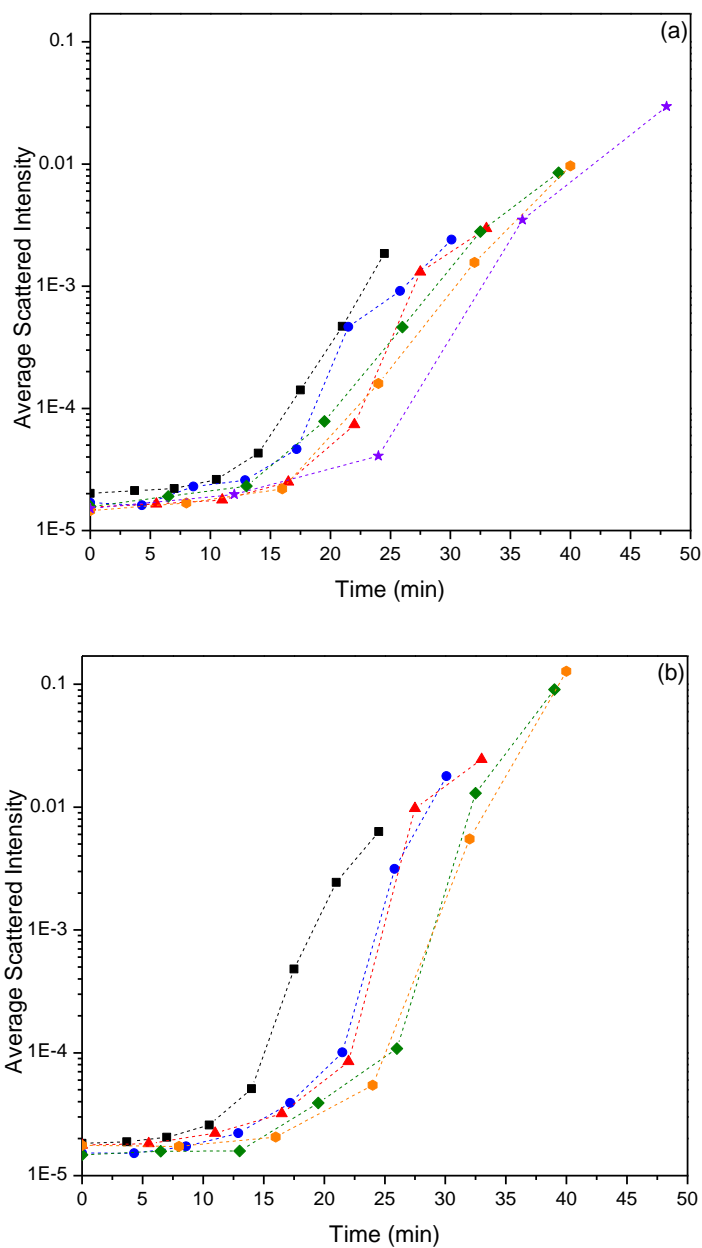
Figure 34: Average DLS scattered intensities for both (a) sodium carbonate and (b) caesium carbonate gels series at R/C ratios of (■) 100, (●) 200, (▲) 300, (◆) 400, (⬤) 500 and (★) 600.

Once more, the values for lithium, sodium and potassium carbonate are very similar. Close examination of the results shows that, in general, the scattered intensity

decreases with increasing R/C at a given time. The hydrodynamic radii data discussed previously showed that at this given time, the size of the clusters is very similar, independent of R/C. The decrease in scattered intensity, therefore, suggests a corresponding decrease in the number concentration of scatterers, i.e. clusters. An increase in R/C ratio, therefore, leads to a decrease in the number concentration of clusters at a given time. Hence, a sample prepared at R/C 100 produces many more clusters than the corresponding R/C 600 sample. Despite this, the clusters continue to grow at the same rate.

The average intensities displayed by the caesium carbonate gels synthesised in this work follow the same general patterns as the other metals studied, with increasing R/C resulting in a decreased intensity at a given time. However, changes in scattered intensity can be due not only to changes in the cluster number concentration, but also the cluster size. In the case of caesium carbonate gels, despite still being monodisperse, the hydrodynamic radii are not consistent with time over the R/C range investigated. As a result, it is not possible to decouple the relationship between cluster size and number concentration for these systems.

5.3 Xerogel Characterisation

Surface area and porosity measurements were carried out on each of the dried xerogels. Figure 35 shows the nitrogen adsorption/desorption isotherms obtained for both the sodium carbonate and caesium carbonate gel series, with the corresponding plots for lithium and potassium carbonate given in Appendix I. All of the isotherms exhibit Type IV behaviour, with various types of hysteresis. This is indicative of mesoporous materials with capillary condensation present. As will be seen throughout the remainder of this body of work, all isotherms shown for the RF gels studied have similar character, being of Type IV.
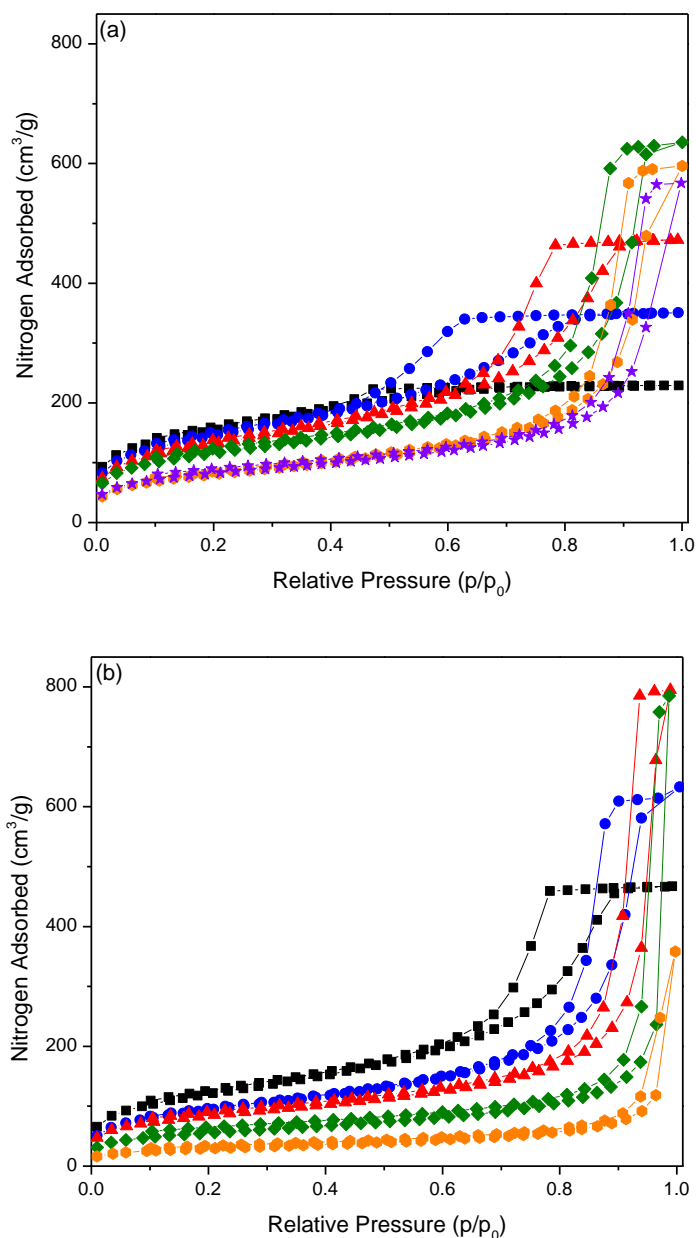
As can be seen from the nitrogen adsorption isotherms, and consistent with the results obtained through DLS, the lithium, sodium and potassium gels are very similar, while those produced with caesium carbonate differ greatly. For a given R/C, the caesium gels show a greatly increased nitrogen uptake, with a shifting of the hysteresis loop to higher relative pressures when compared to the lithium, sodium and potassium gels, observations which indicate an increase in both pore volume and pore size (see Table 11). An exception lies with the R/C 500 caesium gel. This shows a significant reduction in the nitrogen uptake, suggesting a decrease in the

total pore volume. However, the pre-solvent exchanged, cured gel is much softer than the corresponding lithium, sodium and potassium gels at higher R/C values. This leads to greater collapse during the drying phase and a resultant reduction in the pore volume. As has been previously noted, the R/C 600 caesium sample failed to gel, suggesting that the upper R/C limit (500) to produce feasible gels has been reached.

Despite these differences, there are some general trends that can be applied to all of the metal carbonates studied. Increasing the R/C ratio again causes an initial increase in nitrogen uptake, peaking at R/C 400, with shifting of the hysteresis loop to higher relative pressures. Once more, this suggests an increase in pore size as R/C is increased. The observed trend in the uptake suggests that the pore volume reaches a maximum with an R/C of 400. Figure 36 shows the pore size distributions associated with the isotherms given in Figure 35. Results for lithium and potassium carbonate are again displayed in Appendix I.
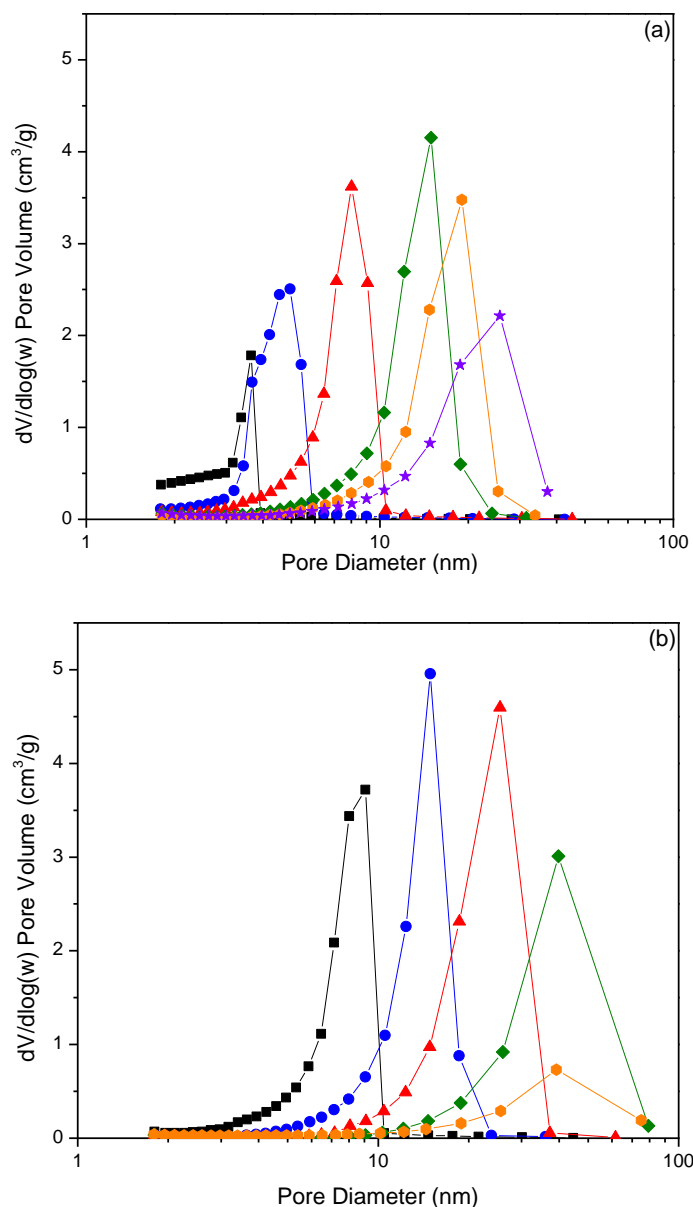
Figure 36: Pore size distributions for (a) sodium carbonate and (b) caesium carbonate gels, at R/C ratios of 100 (■), 200 (●), 300 (▲), 400 (◆), 500 (⬢) and 600 (★).

Examination of the pore size distributions supports the conclusions drawn from the adsorption isotherms; increasing R/C causes a shift in pore size to larger diameters while the areas under the curves, i.e. pore volumes, also initially increase. For R/C ratios of 500 and 600 this area decreases, implying that the pore volume is indeed decreasing. It is notable that caesium again differs from the other catalysts with larger pore sizes and pore volumes than the other metals at equivalent R/C.

Table 11 provides textural properties for each of the dried gels, i.e. BET surface area (S_{BET}), total pore volume (V_{Tot}), micropore volume (V_μ) and average pore

diameter (d_p avg). Included for reference is the initial pH, as measured at the end of the 30 min stirring period (see Section 4.2).

Table 11: Textural properties of all dried xerogel samples prepared in this study.

R/C	S_{BET} (m^2/g)	V_{Tot} (cm^3/g)	V_μ (cm^3/g)	d_P avg (nm)	pH
Li_2CO_3					
100	527 ± 5	0.35	0.05	2.9	7.31
200	542 ± 4	0.59	0.04	4.4	7.07
300	498 ± 5	0.82	0.04	7.3	6.91
400	438 ± 5	1.05	0.04	11.4	6.85
500	376 ± 4	1.03	0.04	13.7	6.74
600	320 ± 4	1.00	0.03	16.0	6.65
Na_2CO_3					
100	533 ± 5	0.35	0.05	2.9	7.39
200	508 ± 4	0.54	0.03	4.2	7.09
300	461 ± 4	0.73	0.03	6.7	6.91
400	403 ± 4	0.98	0.04	11.5	6.84
500	284 ± 2	0.92	0.02	14.3	6.77
600	282 ± 4	0.88	0.03	16.5	6.66
K_2CO_3					
100	472 ± 4	0.33	0.03	3.0	7.36
200	554 ± 5	0.64	0.04	4.7	7.07
300	476 ± 5	0.85	0.04	7.9	6.92
400	465 ± 5	1.08	0.04	10.9	6.84
500	272 ± 2	0.94	0.02	15.2	6.75
600	299 ± 3	0.93	0.03	16.4	6.66
Cs_2CO_3					
100	425 ± 3	0.72	0.02	6.9	7.37
200	329 ± 3	0.98	0.02	12.6	7.09
300	293 ± 3	1.23	0.02	20.3	6.92
400	206 ± 2	1.15	0.02	28.0	6.85
500	103 ± 1	0.55	0.01	27.5	6.74

It can be seen that the initial pH values are consistent between all of the metal carbonates, with the same R/C giving approximately identical pH values. There are also several trends that can be established, which agree with observations made in

the literature. The initial pH decreases with increasing R/C, as would be expected with the addition of lesser amounts of the base. Average pore sizes and pore volumes all initially increase with increasing R/C, before decreasing when R/C ratios of 500 or 600 are used, and this is consistent with the observations made regarding the isotherms and pore size distributions. The increase in pore size leads to a corresponding decrease in the BET surface area. It can also be seen that there is again a great deal of similarity between the lithium, sodium and potassium gels, while caesium shows notable differences.

The decrease in uptake, and subsequently, the pore volume would not be expected to decrease as is observed. This is especially true as the average pore size continues to increase. It is, therefore, possible that not all of the porosity is being probed by the nitrogen adsorption measurements, with pore sizes exceeding those detectable through this analysis. Incomplete measurement of the porosity would explain the apparent decrease in nitrogen uptake. To probe these larger pores, mercury porosimetry could be used; this technique can detect pores which are larger than those measured by nitrogen adsorption (see Future Work).

5.4 Further Interpretation of the Acquired Data

The data gathered on both pre-aggregation cluster radius and average pore diameter can be combined, illustrating a clear correlation between the two values. They can, therefore, be plotted in a Master Curve, as shown in Figure 37.
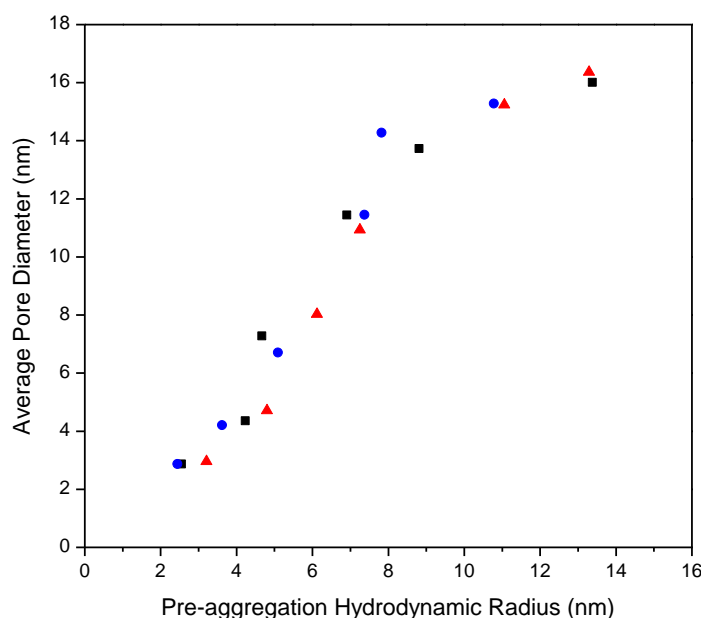
Figure 37: Master curve showing average pore diameter vs. maximum hydrodynamic radii for lithium carbonate (■), sodium carbonate (●) and potassium carbonate (▲).

As would be expected, the data for lithium, sodium and potassium fall onto a single curve, illustrating the range of pore sizes accessible in these systems. In contrast, the caesium gels do not conform to the Master Curve exhibited by the other metals. However, the obtained data does follow a similar trend, showing the same dependence between pore diameter and pre-aggregation cluster radius. This second curve is shown in Figure 38.

Figure 38: Expanded master curve, to include the data associated with caesium carbonate (◆), with data on lithium carbonate (■), sodium carbonate (●) and potassium carbonate (▲) reproduced for comparison.

The Master Curve (Figure 38) demonstrates the wide range of pore sizes which these xerogels can provide; showing how the pore size can be systematically tailored for a particular application. Use of caesium carbonate gives access to a region of pore sizes not accessible by the other metal carbonates. As such, lithium, sodium and potassium give pores ideally suited to gas phase applications, while those sizes obtained with caesium carbonate are in the range for aqueous phase applications.

5.4.1 Colloidal Stability During RF Gel Formation

In 1888, Hofmeister studied the effect of several metal salts on the stability of egg protein in solution.[143] He found that salts used had different abilities to stabilise the egg protein molecules, where the cations make the protein less soluble, resulting in the protein salting out of solution in the order lithium > sodium > potassium. A typical Hofmeister series is shown in Figure 39. The series also shows how caesium displays favourable effects. High charge density species (such as Li^+) stabilise the

structure of water molecules. This depletes the solvation layer around the protein, exposing the hydrophobic patches. These patches on the different proteins will interact, leading to aggregation and precipitation of the proteins, known as salting out. Conversely, low charge density species (like Cs^+) destabilises the water structure and in turn enhances the solvation layer on the protein. Any hydrophobic interactions are reduced and the proteins stay dispersed in solution. This is known as salting in. As a result, it is expected that lithium should cause salting out and caesium salting in. Lithium would, therefore, give larger cluster sizes than caesium.
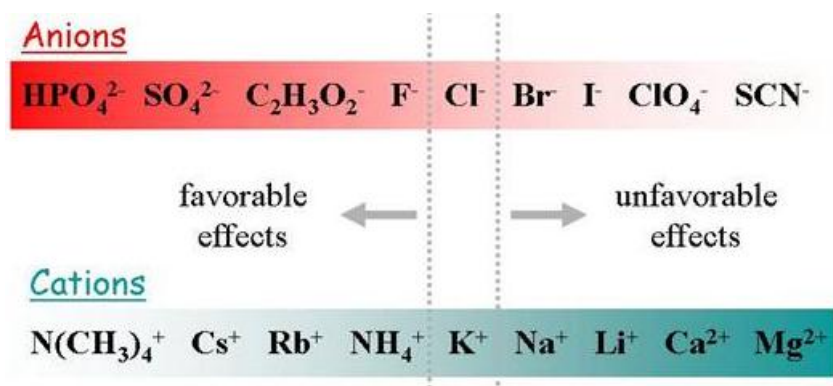
Figure 39: A typical Hofmeister series showing the ordering of both anions and cations.[144]

In contrast to Hofmeister's work, the metals in this study show the trend lithium = sodium = potassium < caesium with regard to cluster size. Lithium, sodium and potassium exhibit an approximately equal ability to destabilise the interactions between oligomeric RF chains, resulting in salting in of the chains and smaller clusters. On the other hand, the larger, more hydrated caesium cation[145] appears less able to destabilise these RF oligomers interactions, resulting in salting out of the chains and larger clusters. The metals, therefore, appear to follow a reverse Hofmeister series. The differences in the observed trends may be the result of the nature of the species being studied. While the RF oligomers are relatively small molecules and show a high level of –OH groups on the surface, egg proteins are large macromolecules with hydrophobic areas, and the interactions with the cations may differ.

However, it may also be that the true size of the caesium clusters is being masked. The rapid cluster size increase seen in Figure 31 was thought to be due to the coalescence of small clusters. The actual cluster size may be smaller than those observed for the other metals, but the rapid coalescence obscures this fact. This

may also be the reason for the inconsistences in the cluster growth for the different concentrations of caesium carbonate. At high catalyst concentrations, i.e. large cluster number concentration, this rapid increase in cluster size starts at earlier times than when lower concentrations are used. However, as previously stated, further work investigating these caesium carbonate systems would be required.

5.4.2 RF Sol-Gel Transition

As discussed above (Section 1.6), a microphase separation model has commonly been used to describe RF sol-gel transitions. However, the classic microphase separation scenario does not support the observations made here. Microphase separation results in the formation of two interpenetrating microphases. This is inconsistent with the freely diffusing clusters shown by DLS. Therefore, an alternative nanoscale phase transition must be considered.

The DLS results obtained support the formation of a mesostructured liquid phase, where a single liquid phase consists of localised pockets of the liquid-like organic phase, surrounded by the bulk solution.[80, 146] Lithium, sodium and potassium show that primary cluster growth in the pre-aggregation stages is independent of the metal or R/C used. This suggests that, in all cases, similar oligomeric species are being formed, which form monodisperse clusters with the observed hydrodynamic radius, surrounded by the bulk water/resorcinol/formaldehyde solution. This process can be depicted schematically, as in Figure 40.
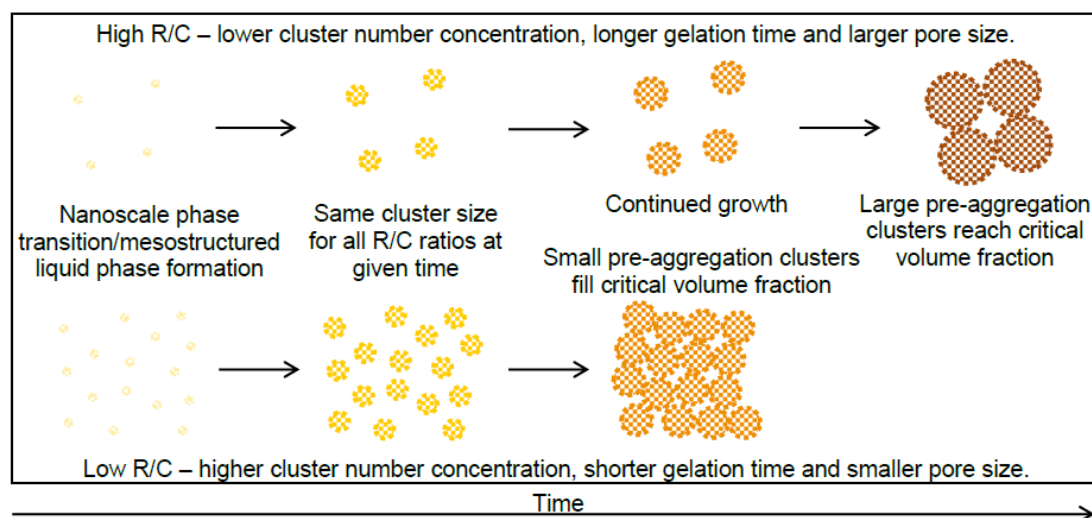
Figure 40: Schematic diagram outlining the cluster formation and growth process during RF gel synthesis. Clusters are depicted as spheres for clarity.

The primary clusters are depicted as spherical species in the schematic for reasons of clarity; the exact shape and internal structure is not yet known. It is likely that the clusters will contain oligomers with a range of branching that are aggregating and undergoing further polymerisation. It is unlikely that the clusters are composed of individual polymeric species, as it has been found that their size is independent of R and F concentration at a given catalyst concentration.[80] Cluster growth, therefore, appears to be controlled by thermodynamics, rather than by kinetics of the polymerisation process.

In reality, these clusters can have any arbitrary shape, be it irregular and/or fractal. However, the DLS results indicate that they have a well-defined hydrodynamic radius and, therefore, a corresponding occupied volume.[147] As the clusters grow and reach a critical total volume fraction, they are subject to further physical aggregation to form a 3D network, which leads to gelation. This aggregation may be accompanied and/or followed by chemical bonding due to underlying polymerisation processes. As such, the formation of 3D networks has been shown to be the result of physical aggregation of primary particles in many different molecular and colloidal systems.[148-150] The size to which clusters have to grow in order to reach this critical volume fraction will be dependent on the number concentration of clusters present. High R/C values produce fewer clusters, which will have to grow to large sizes before reaching the critical volume fraction. Conversely, as all the clusters are growing at the same rate, the greater number of clusters produced by low R/C values will surpass this critical volume fraction at much smaller sizes. This also explains the observations made for the gelation times of all gel samples. The larger the clusters have to grow to reach this critical cluster volume fraction, the longer it will take, therefore, higher R/C values of base lead to increased gelation times.

Yamamoto *et al.* proposed a model for cluster growth that differs from the scenario presented here in several key aspects.[58, 85] The Yamamoto model proposes that both the size and growth rate of clusters are driven by reaction kinetics, and as a result, are highly dependent on R/C. As such, higher catalyst concentrations lead to an apparent increase in the cluster growth rate. However, in their work non-exponential autocorrelation functions were analysed to determine the apparent cluster size under conditions that were likely to be in the regime of networking and aggregation. At these times, cluster mobility is likely to be severely hindered and cluster sizes cannot be reliably determined. In contrast, this work proposes that only

the cluster number concentration is kinetically controlled. Higher catalyst concentrations lead to faster production of the hydroxymethyl derivatives and resulting oligomers, leading to a larger number of primary clusters.

The results presented here are also inconsistent with the mechanism first proposed by Pekala and Kong, the 'autocatalytic growth' mechanism.[32] This mechanism intimates that increasing carbonate concentration results in an increased number of hydroxymethyl derivatives. As these are more reactive than the initial resorcinol molecules, they quickly form bridged dimer molecules. Once again, these dimers are more reactive than the initial addition product, leading to a greater possibility that they will react further into growing oligomers. As such, an increased catalyst concentration, therefore, leads to a faster reaction and quicker cluster growth, while decreasing the carbonate concentration slows the reaction. The results obtained in this work, by contrast, show that cluster growth is independent of the chosen R/C.

5.5   Thermal Influence on the Growth of Clusters

As the DLS results show, there is a time delay between placing RF gel samples in the oven and the onset of cluster growth. Cluster hydrodynamic radii remain constant at ~0.5 nm for approximately 15 min before the size begins to increase rapidly. To investigate why a delay exists, it was decided to examine the temperature changes of the gelling solution and the possible influences that this could have on the reaction profile.

5.5.1   Determination of the Temperature Profile

For convenience, sample temperatures were measured at the DLS time intervals used previously. This allowed direct comparison between sample temperature and cluster size. Figure 41 shows the temperature profiles for Na_2CO_3 gels at R/C 100, 200 and 400. As would be expected, for samples of equal volume prepared in an identical manner and placed in approximately the same position in the same oven, the temperature profiles for all samples are the same.
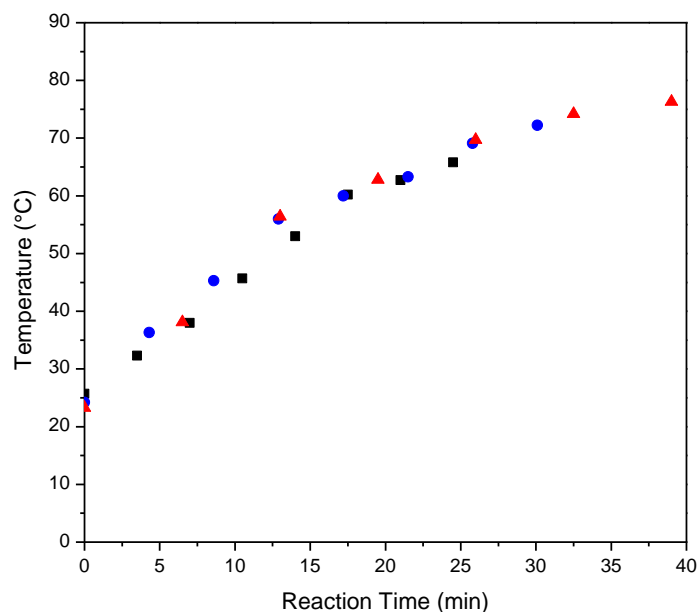
As such, a comparison can be made between the temperature profile and the previously calculated hydrodynamic radii. The comparison for sodium carbonate at R/C 100 is shown in Figure 42.
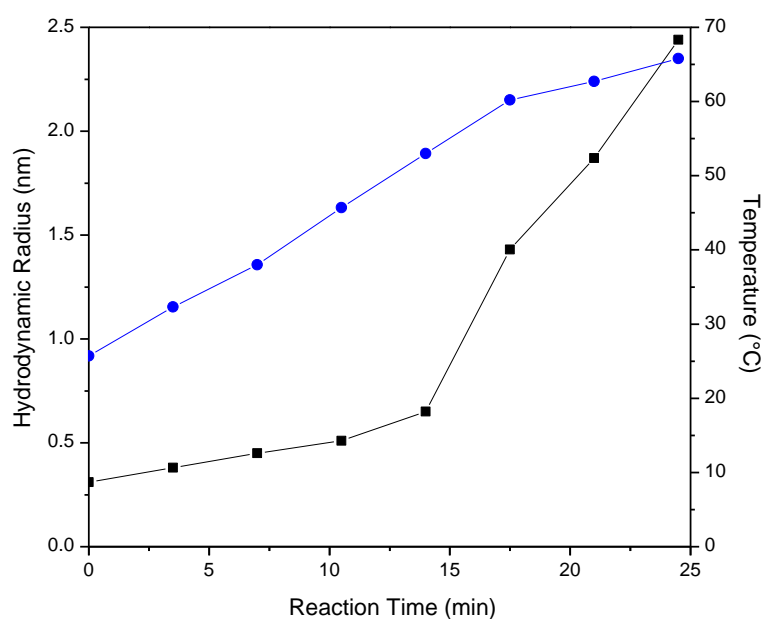
From the data presented here, and considering that both the temperature profile and cluster growth curves overlap for all samples, it can be seen that after the

temperature reaches 55 °C, cluster growth begins. This temperature would, therefore, seem to be applicable to all of the Group I catalysed gels, bar caesium, with their differing growth profiles.

5.5.2 Preheating the Initial Sol to 55 °C

To further investigate the importance of the gel sample reaching 55 °C, each of the three gels, for which temperature profiles were previously measured, were remade under a new set of conditions. All the starting materials were preheated to 55 °C prior to mixing, while the samples were maintained at this temperature throughout the 30 min stirring period; after which the samples were transferred to the Memmert ULE-500 oven at 85 °C, where gelation proceeded as normal. Solvent exchange and vacuum drying were carried out as before to produce the respective xerogels.

5.5.3 Dynamic Light Scattering Studies

DLS was performed on the preheated gels to study any changes in the cluster growth profile imparted by the increased starting temperature. This increased starting temperature caused a corresponding decrease in the gelation time and, therefore, DLS measurement intervals had to be adjusted accordingly. The new gelation and interval times are displayed in Table 12.

Table 12: Total gelation and DLS interval times for Na_2CO_3 gels preheated to 55 °C, with room temperature interval times included for comparison.

Sample	Gelation Time (min)	Interval Time (min)	RT Interval Time (min)
Na_2CO_3_100	30	3.0	3.5
Na_2CO_3_200	40	4.0	4.3
Na_2CO_3_400	60	6.0	6.5

With new interval times calculated, DLS was performed as for the room temperature gels. Figure 43 shows the comparison between results obtained for the room temperature and three preheated sodium carbonate gels, with R/C 100, 200 and 400.
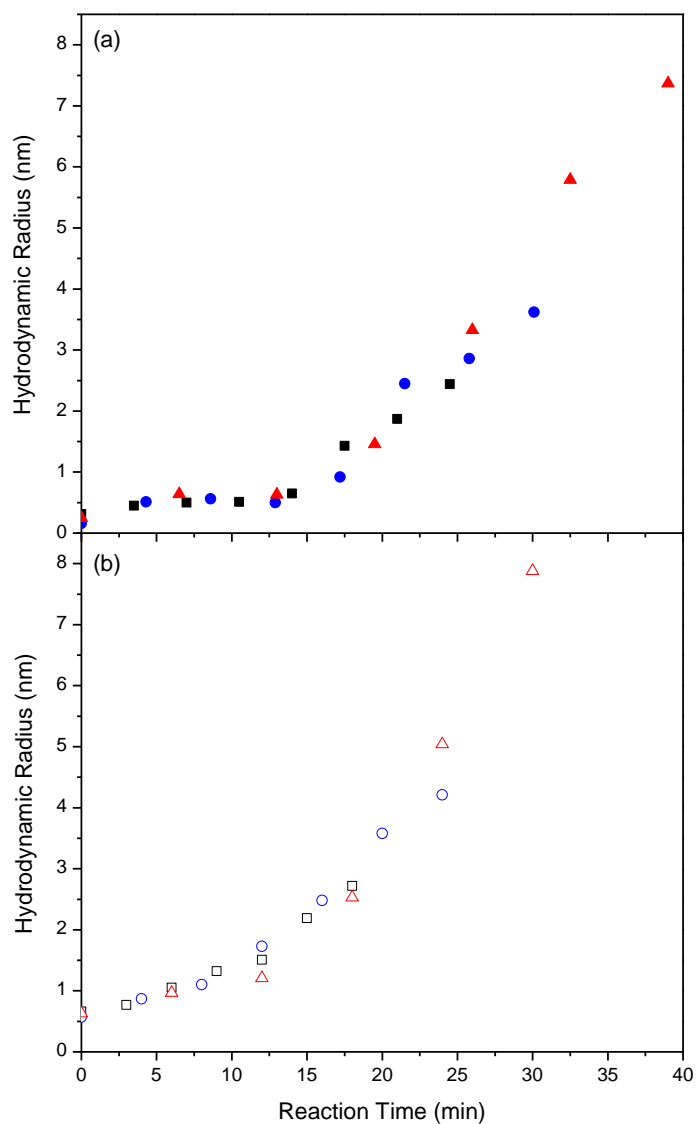
Figure 43: DLS hydrodynamic radii comparison for Na$_2$CO$_3$ samples with R/C of 100 (■), 200 (●) and 400 (▲) placed in the oven at (a) room temperature and (b) preheated to 55 °C before placing in the oven.

The room temperature results in Figure 43a visibly show a delay before cluster growth begins; however, when the same gel composition is preheated to 55 °C (Figure 43b) before the first measurement, this delay is clearly eliminated, and cluster growth occurs in a much smoother, progressive manner from the start. It can also be seen that the initial cluster diameter, i.e. t = 0, is slightly larger. This implies that cluster growth has already started during the 30 minute stirring period. As a result, the clusters have very slightly larger final hydrodynamic radii values, with clusters growing to larger observable sizes before the networking process begins. However, the results for all three R/C ratios still fall into a consistent, overlapping

narrow band, meaning that the increased initial temperature has influenced all prepared gels to the same degree.

In addition to this increase in hydrodynamic radius, the observed maximum radius, before the appearance of secondary decays, itself occurs one measurement point earlier in the gelation process, i.e. for R/C 100 the maximum value occurs at 70 % of the gel time starting at room temperature, while it occurs at 60 % of the gel time for the preheated sample. As a result, the networking process takes proportionally longer, in the case of R/C 100 this corresponds to 10.5 and 12 minutes for room temperature and preheated gels, respectively. This is a phenomenon already witnessed with the room temperature series previously discussed, with increasing R/C leading to increased cluster size and longer networking times. The slightly larger, slower moving clusters observed when preheating the gels have greater repulsion, and, therefore, take longer to associate, aggregate, and cross-link sufficiently to hold together, in turn taking longer to form the gel network structure.

It is also possible that the true maximum size is not observed for the room temperature samples. In particular when considering the R/C 400 gel, interval times of 6.5 minutes are comparatively long. It could, therefore, be that the true maximum observable radius occurs somewhere inbetween the last single decay function and the first secondary decay function. However, interval times of 10% of the total gel time were chosen so that cluster growth could be compared at equivalent points in the gelation process, as opposed to an arbitrary time period that was the same in each case. This could be addressed by decreasing the intervals to only 5 % of the initial gel time; giving less time between measurements and doubling the number of data points for each experimental run (see Future Work).

5.5.4 Characterisation of the Preheated Xerogels

To quantify changes in the dried xerogels, nitrogen characterisation was performed as for the room temperature samples. Figure 44 shows the nitrogen adsorption/desorption isotherms for all of the sodium carbonate samples studied in the comparison.
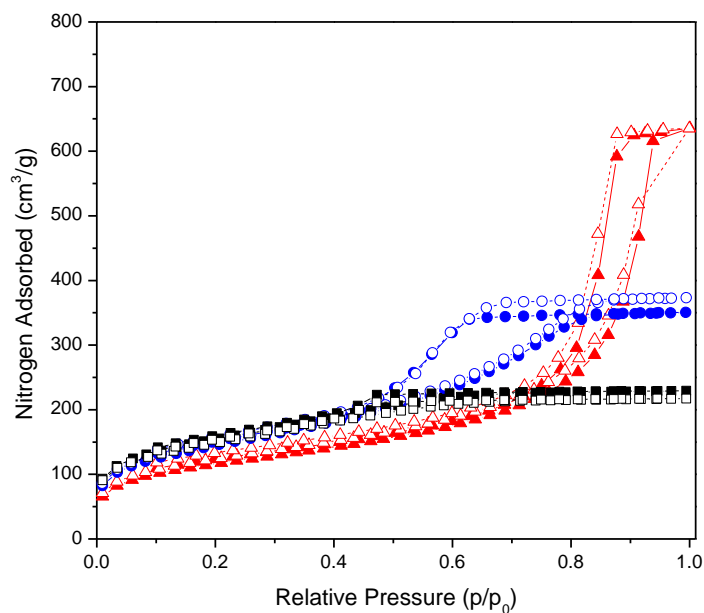
Figure 44: Nitrogen adsorption/desorption isotherm comparisons for Na$_2$CO$_3$ at R/C 100 (■), 200 (●) and 400 (▲) prepared at room temperature (closed symbols) and 55 °C (open symbols).

Each sodium carbonate R/C value shows overlapping isotherms when comparing the room temperature and preheated samples, with very similar uptakes and hysteresis loops. These results suggest that, despite the slight increase in observed cluster size and reduced gelation time, the preheated gels have very similar textural properties to their room temperature counterparts.

These conclusions are mirrored in the pore size distribution data seen in Figure 45, which show that the three preheated sodium carbonate gels have very similar porosity when compared to those prepared at room temperature.
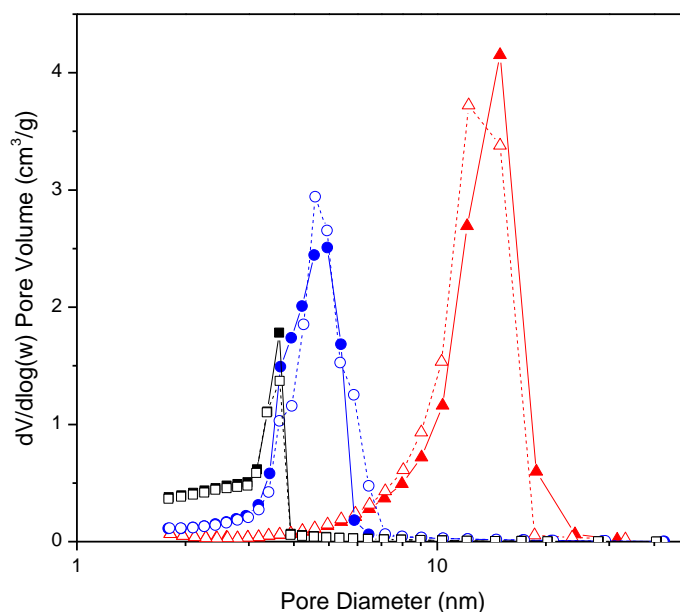
Figure 45: Pore size distribution comparisons for Na_2CO_3 at R/C 100 (■), 200 (●) and 400 (▲) prepared at room temperature (closed symbols) and 55 °C (open symbols).

Examining the properties of the dried gels also provides some interesting data. The preheated xerogel properties are shown in Table 13, which can be compared with the results of the analogous room temperature gels shown above in Table 11.

Table 13: Properties of Na_2CO_3 gels preheated to 55 °C.

Sample	S_{BET} (m^2/g)	V_{Tot} (cm^3/g)	V_μ (cm^3/g)	d_p avg. (nm)
Na_2CO_3_100 @ 55 °C	513 ± 5	0.34	0.05	2.8
Na_2CO_3_200 @ 55 °C	525 ± 4	0.58	0.03	4.4
Na_2CO_3_400 @ 55 °C	429 ± 4	0.98	0.04	10.9

As expected from the adsorption isotherm and pore size distribution data, the sodium carbonate gels show very little difference in terms of BET surface area, pore volume and average pore size when comparing room temperature and preheated gels at the equivalent R/C.

Preheating the initial sol, therefore, has very little effect on RF gels prepared using sodium carbonate as a catalyst. Only the time taken for gelation to occur differs, decreasing by approximately 5 min in each case. Properties of the dried gels do not change upon preheating. The extra energy and time required to preheat the

individual components cannot, therefore, be justified, by any advantages to the final xerogel product.

5.6 Delayed Addition of the Metal Carbonate

To elaborate on the role played by the metal carbonate, further studies were conducted, where resorcinol and formaldehyde were initially allowed to react without a metal carbonate present, before addition of the catalyst after a predetermined time.

5.6.1 No Carbonate Gels

To gain a baseline result for comparison, a sample was prepared in which no metal carbonate was present; allowing the extent to which the uncatalysed reaction between R and F would proceed, and the nature of the product, to be determined. Curing, solvent exchange and drying processes were identical to those used for metal carbonate gels in order to ensure consistency and to eliminate further variables. On removal from the oven, an orange coloured, dense solid layer had formed at the bottom of the liquid volume. On drying, the resultant product was unrecognisable when compared to the standard metal carbonate gels where the standard gels ranged from orange to very dark red, almost black, monolithic structures, the no carbonate sample was a red-orange powder (see Figure 46) with little mechanical strength, indicating a severe lack of network formation and cross-linking within the structure.

Figure 46: A dried RF gel sample made with no metal carbonate present.

These differences are further evidenced by nitrogen sorption characterisation of the sample and comparison with a gel made in the presence of a metal carbonate (Figure 47 and 48). These results show that while the catalysed gel (sodium carbonate R/C 100 has been chosen as an example) has a significant N_2 uptake and porous volume, the gel with no carbonate present has very little uptake or discernible porosity.
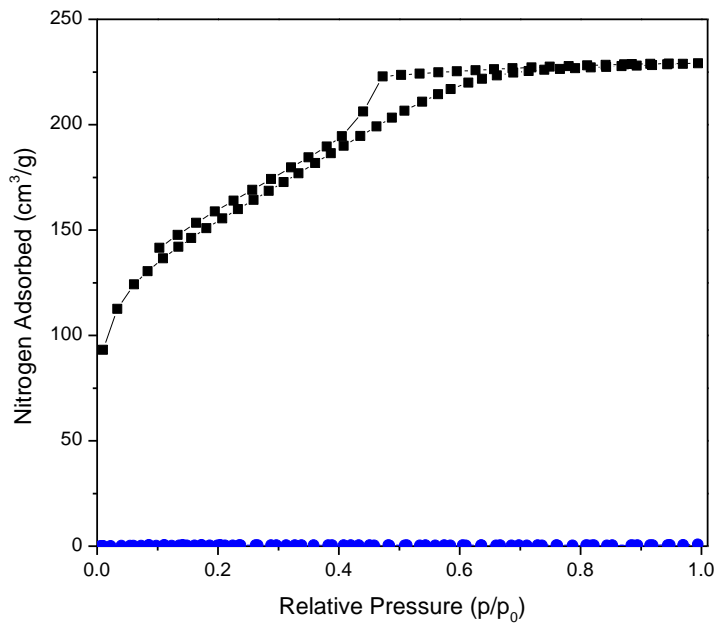
Figure 47: Nitrogen adsorption/desorption isotherm comparison between $Na_2CO_3\_100$ (■) and a carbonate free gel (●).
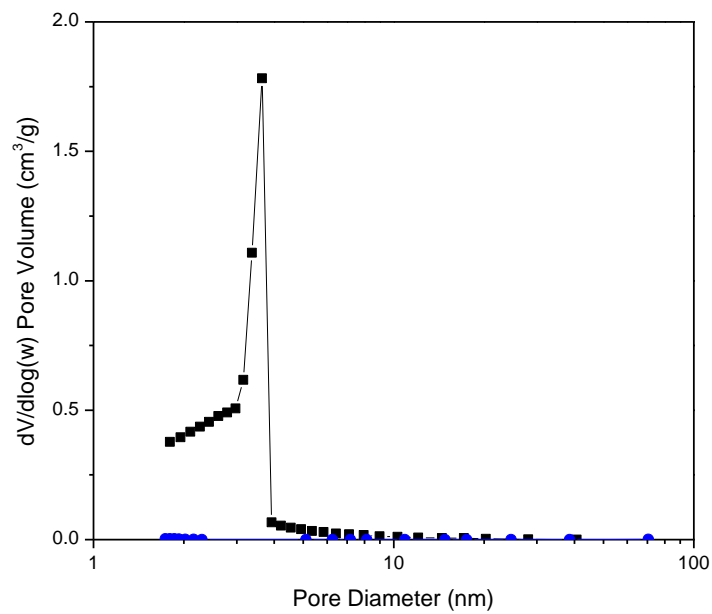
Figure 48: Pore size distribution comparison between (■) $Na_2CO_3\_100$ and (●) a carbonate free gel.

The surface area and pore volume are, consequently, significantly reduced, as seen in Table 14. All of these results suggest that a lack of metal carbonate produces a non-porous product.

Sample	S_{BET} (m^2/g)	V_{Tot} (cm^3/g)	V_m (cm^3/g)	d_p avg. (nm)
No C	2 ± 0	-	-	6.7

However, visual inspection of the carbonate free sample during heating showed that after 90 minutes, turbidity developed within the sample. This was followed by visible sedimentation within the sample after 120 minutes. DLS was therefore used to study the samples with no carbonate present, over this time frame. Figure 49 and 50 show the autocorrelation functions, and corresponding hydrodynamic radii obtained, respectively.
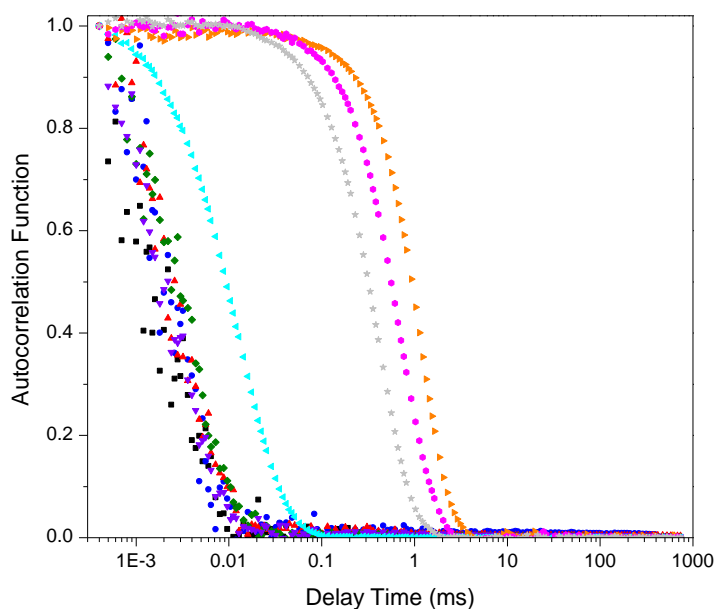
Figure 49: DLS autocorrelation functions for carbonate free samples at 15 minute intervals: 0 min (■), 15 min (●), 30 min (▲), 45 min (◆), 60 min (▼), 75 min (◄), 90 min (▶), 105 min (●) and 120 min (★).
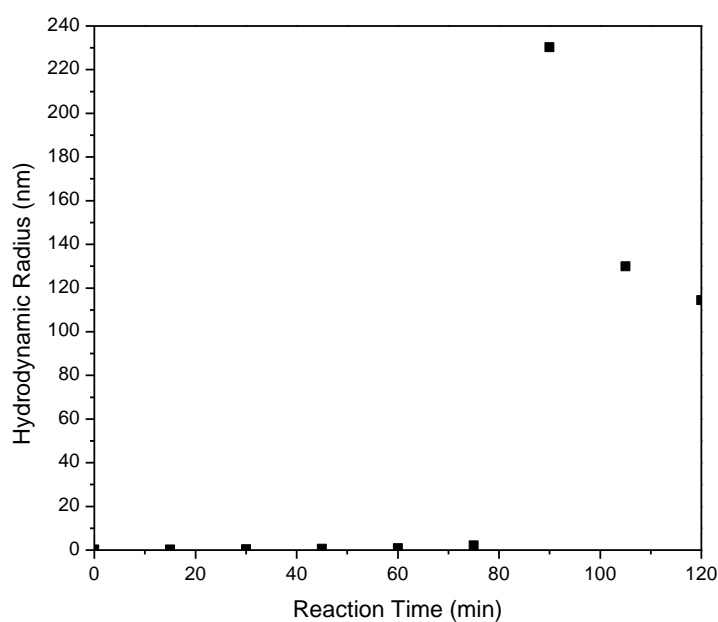
Figure 50: DLS hydrodynamic radii of carbonate free samples at 15 minute intervals.

Although the turbidity and sedimentation in the system prevent accurate sizes from being determined, it is clear that there is a large increase in particle size once turbidity develops, with the sizes also being much larger than anything seen when the metal carbonate is present, hence the turbidity and sedimentation observed. This also agrees with the results of Scherdel *et al.*, who observed visible sedimentation when particles reached sizes in excess of 200 nm, after 24 hours, for RF gels prepared with R/C between 700 and 3000, and solids weight percentages between 10 and 25 %.[151]

Such large particles are also consistent with the surface area and porosity data obtained. Pores within the RF gel structure result from the interparticle voids between clusters. Small clusters pack more tightly leading to smaller pores, while large particles cannot pack as tightly and the resultant pores are larger. As seen from the results obtained using Group I metal carbonates, there is a clear correlation between pre-gelation cluster size and corresponding average pore diameter. With the carbonate free sample appearing to produce particles with sizes of several hundred nanometers, the voids within the sample could be assumed to be correspondingly larger, with sizes well into the macroporous range (> 50 nm). As such, pores of this size are not detectable using nitrogen adsorption/desorption measurements, being outwith the range detectable by the available equipment, which has an upper limit of approximately 100 nm. Samples made in this way,

therefore, appear to be 'non-porous'. Such large pores would also limit the usefulness of the materials, with the common applications described in Section 1.8 requiring pores in the micro- and mesoporous range.

The results obtained also show that when no carbonate is present, the reaction between R and F is much slower, so forming very few primary clusters, than when a metal carbonate is present. From previous results within this chapter, it is known that the growth rate of clusters is independent of the R/C present, whereas the cluster number is highly dependent. As the catalyst concentration tends to zero, the very few clusters produced would need to grow to such large sizes, in order to reach the critical volume fraction that they become too big and sediment out before gelation can occur. Furthermore, in addition to the slower reaction, without the presence of a metal carbonate there is a lack of networking and cross-linking in the sample, leading to the powdery product observed. These results agree with the process of the metal cation influencing the water structure around the RF oligomeric chains, as described in Section 5.4. The absence of a suitable cation leads to eventual destabilisation of the colloidal suspension and the resultant salting out of the RF polymer causes flocculation into large particles, observed as turbidity and sedimentation within the sample.

5.6.2 Delayed Addition of Carbonate

With this knowledge that R and F will react slowly in the absence of a metal carbonate, before the colloidal suspension destabilises, it was decided to investigate how a delay in the addition of the metal carbonate would influence the gel formation process, through potential restabilisation of the colloidal suspension. As the most widely utilised catalyst, sodium carbonate was used for this investigation. The limited solubility of the Group II metal carbonates prevented them from being used in a similar manner.

Carbonate addition time intervals of 15 minutes were retained from the DLS study of the carbonate free system. Addition at t = 0, therefore, corresponded to the standard gel previously analysed.

Addition of sodium carbonate at an R/C of 100 was performed at all eight delayed addition times. Figure 51 shows the adsorption/desorption isotherms obtained for all of the samples, and their comparison with the standard gel.
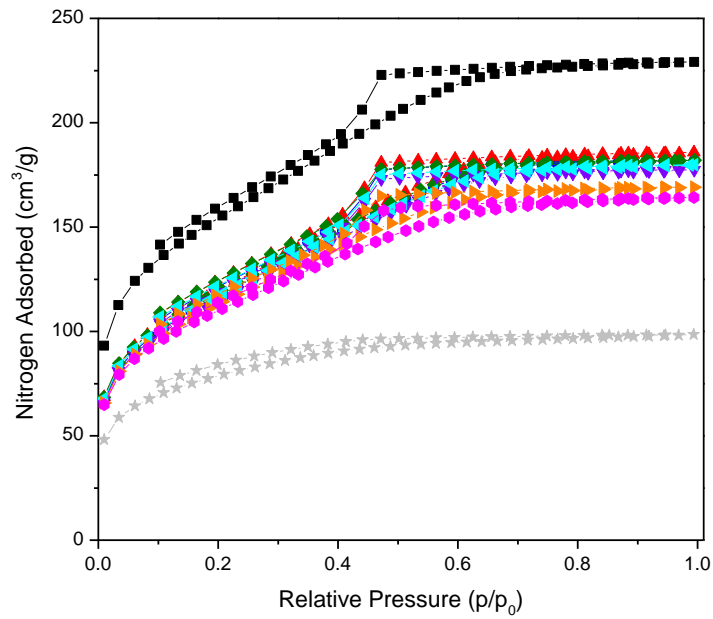
The isotherms show a clear grouping, with a single outlier both above and below the main group, corresponding to the standard gel and addition at t = 120 min respectively. However, it can be seen that all of the isotherms have a very similar shape, in terms of the hysteresis loop exhibited. These observations imply that while the pore size will be very similar in all cases, the varying nitrogen uptake will cause the pore volume to fall into three groups. This conclusion is reinforced by examining the pore size distributions seen in Figure 52.
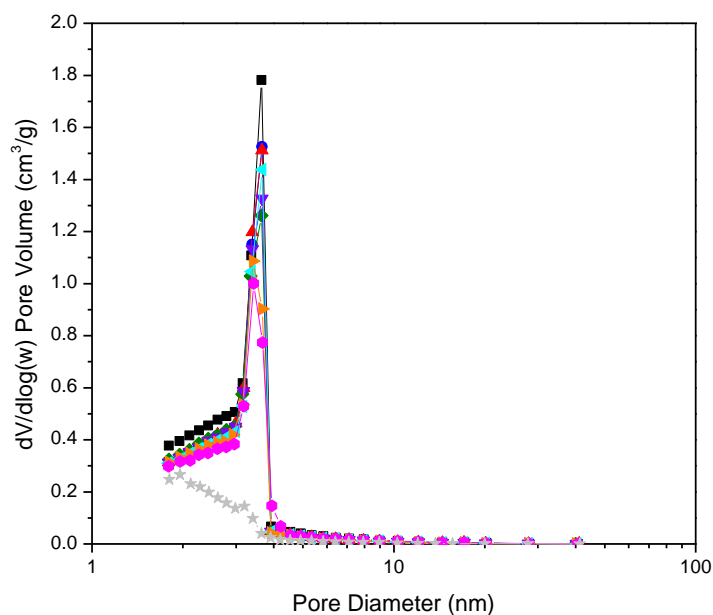
These show that all of the distributions overlap in terms of pore size on the x-axis, but show differing peak area, suggesting variation in the pore volume. The distribution corresponding to addition at t = 120 min shows very little area, indicating that addition at this time severely reduces the pore volume imparted to the gel structure. Table 15 shows additional textural properties of the delayed addition gels.

Table 15: Properties comparison of Na$_2$CO$_3$_100 gels, with addition of Na$_2$CO$_3$ at each time interval.

Sample	S_{BET} (m^2/g)	V_{Tot} (cm^3/g)	V_μ (cm^3/g)	d_p avg. (nm)
15 min	413 ± 3	0.28	0.02	2.9
30 min	423 ± 3	0.29	0.02	2.9
45 min	419 ± 3	0.28	0.02	2.8
60 min	406 ± 3	0.27	0.02	2.9
75 min	412 ± 3	0.28	0.02	2.9
90 min	398 ± 3	0.26	0.02	2.8
105 min	384 ± 3	0.25	0.03	2.8
120 min	282 ± 2	0.15	0.04	2.5

As expected these results show that the average pore size in all cases, bar a very slight reduction for the t = 120 min sample, are identical. As was also expected, the

total pore volumes are grouped as for the adsorption isotherms, with the standard gel and the t = 120 min sample being outliers, with corresponding groupings in the BET surface area.

These observations suggest that standard addition of the metal carbonate speeds up the reaction and stabilises the resultant colloidal suspension as explained above. In delaying addition of the metal carbonate, only a small portion of the R and F reacts together, slowly. The leftover R and F remain unreacted until the addition of the sodium carbonate at the appropriate time. The relatively large amount of catalyst added allows the reaction to proceed as normal, increasing the reaction rate and influencing the hydration layer around the RF oligomers, as it would if added at t = 0. As the same amount of catalyst is present here, as for the standard gel, the number concentration of clusters is likely to be very similar. These clusters will, therefore, grow to similar sizes as in the standard gel, resulting in pores of the same size. However, the initial uncatalysed reaction between R and F results in the formation of a partially 'non-porous' product, as exhibited by the carbonate free sample, and explains the reduction in pore volume and surface area observed with the delayed addition gels.

However, by t = 120 min, the extent to which R and F have reacted becomes such that they rapidly sediment out of solution. As such, on addition of the sodium carbonate, there is little unreacted R and F left to be catalysed and stabilised, or suspended RF oligomers to interact with. The resultant product is, therefore, mainly composed of the 'non-porous' sediment, and the resultant pore volume and surface area are significantly reduced. However, the 120 min addition sample still has significantly greater detectable porous character than the carbonate free sample. A visual comparison shows that while these two samples are very similar in colour, the 120 min sample has a much more gel like appearance, retaining a small degree of mechanical strength and, therefore, monolithic character.

5.7 Summary of Findings

Gels catalysed with lithium, sodium, potassium and caesium carbonate at R/C ratios of 100, 200, 300, 400, 500 and 600 were analysed in detail using DLS in conjunction with surface area and porosity measurements.

In order to gauge the influence of heating conditions on the porous properties of RF gels, a selection of samples were prepared at 55 °C, instead of the standard room

temperature. This temperature was chosen as it corresponded to the onset of rapid cluster growth during the heating of a standard room temperature gel.

To further investigate the role of the metal carbonate, several gels were made with sodium carbonate at an R/C of 100. However, the time at which the catalyst was added was varied, allowing for uncatalysed reaction between R and F for a set interval.

In summary, it was found that:

- For typical xerogel formation:
    - Average pore size and pore volume generally increase with increasing R/C for all catalysts, with a corresponding decrease in surface area.
    - Lithium, sodium and potassium show very similar results for a given R/C, while caesium shows a significantly increased pore size/volume.
    - Primary cluster growth is independent of R/C and metal chosen in the case of lithium, sodium and potassium, suggesting thermodynamic control.
    - Cluster number concentration is dependent on R/C for these metals, with higher catalyst concentrations giving a greater cluster number concentration, suggesting kinetic control.
    - Caesium results are inconclusive in this regard, possibly as a result of small cluster coalescence, and require further work.
    - Aggregation of gel network occurs when a critical cluster volume fraction is reached, therefore, the lower the cluster number concentration; the larger the clusters must grow to fill this volume.
    - Cluster size and pore size are strongly correlated for each metal carbonate at each R/C, falling into two Master Curves (lithium, sodium and potassium, and caesium) showing the tuneable range of properties achievable.
- On preheating to 55 °C:
    - Gelation times were reduced by approximately 5 minutes in each case when preheated to 55 °C.
    - A starting temperature of 55 °C eliminated the delay in growth for sodium carbonate gels.

- o Maximum observable hydrodynamic radii for sodium carbonate gels are slightly larger when preheating was used.
  - o Porous properties of preheated sodium carbonate gels are virtually identical to those of their room temperature counterparts. Increased temperature increases the speed of gel formation but does not influence the final structure of the dried xerogel.
- On delaying the addition of catalyst:
  - o Allowing complete gelation with a lack of metal carbonate present results in an apparently non-porous product.
  - o Addition of sodium carbonate between 15 and 105 min of placing in the oven results in a gel with slightly reduced pore volume and surface area, but identical pore size, to a standard gel.
  - o Addition of sodium carbonate 120 min after placing in the oven results in a gel with significantly reduced pore volume and surface area, and slightly reduced pore size, to a standard gel.

RF xerogels can be made with tailored pore size by careful choice of catalyst and R/C ratio. Preheating of the starting materials slightly decreases the gelation time but has no benefits to the textural properties of the gel. The metal cation plays an important role in the stabilisation of the RF suspension. Introduction of this stabilising element up to 105 min after starting the reaction between R and F will result in a viable gel structure.

6 Results Part 2 - Gels Synthesised with Group II Metal Carbonate Catalysts

As has been demonstrated in the preceding results chapter (Chapter 5), various Group I metal carbonates can be used to synthesise RF gels, which exhibit differing textural properties. It is also possible to use the carbonates of the Group II metals, namely calcium and barium, as catalysts. The effects of changing the metal carbonate and the R/C used were studied using DLS and surface area and porosity measurements. A comparative study on the preparation temperature was also performed.

6.1 Gelation Time Monitoring

In order to once more determine the experimental window available for analysis of gelation, the time taken for gelation to occur was determined for the two Group II metal carbonate catalysts used (calcium and barium); R/C ratios of 100, 200 and 400 were studied, resulting in the determination of six gelation times.

As was the case for the Group I metal carbonates, it was found that an equivalent R/C resulted in the same gelation time for both of the Group II catalysts studied. The newly determined gel times are shown in Table 16.

Table 16: Gelation times for Group II metal carbonate catalysed RF gels.

R/C	Gelation Time (min)
100	40
200	45
400	50

As for the Group I catalysts, it was found that increasing the R/C led to an increase in the gelation time, consistent, once more, with the results of Job *et al.*[139] While the gelation times of the R/C 100 samples are 5 min longer than those of the corresponding Group I gels, the differences between the gel times as R/C increases are much less, such that the R/C 400 samples have a significantly shorter gel time than the analogous Group I samples.

Nevertheless, intervals of 10% of total gelation time were retained in order to analyse these new gels at the same points in the gelation process as previously used for the Group I gels. Table 17 gives these new interval times.

Table 17: Interval times used in the analysis of Group II metal carbonate catalysed RF gels.

R/C	Interval Time (min)
100	4.0
200	4.5
400	5.0

6.2 Dynamic Light Scattering Studies

The determined interval times were used to perform DLS studies on each of the Group II metal carbonate catalysed gels produced. These analyses provided a great deal of data at each measurement point, in the form of autocorrelation functions and scattered light intensities. Figure 53 provides the autocorrelation functions obtained for both calcium and barium carbonate at R/C 100.
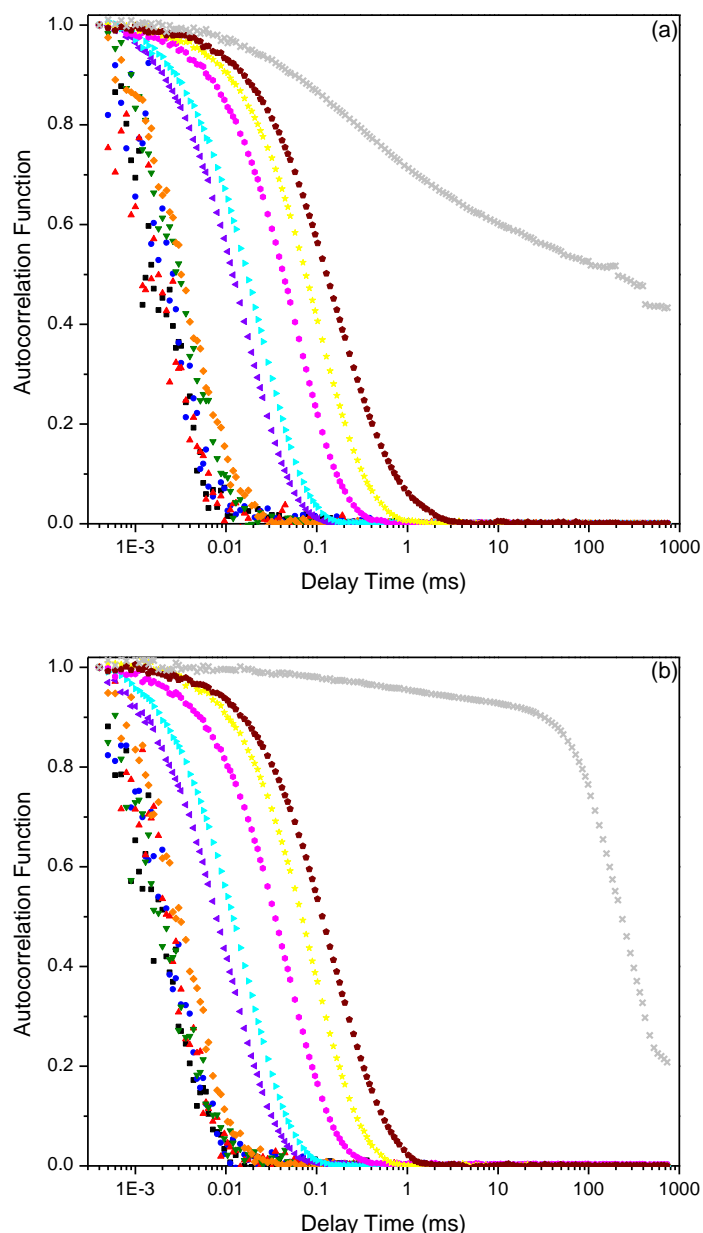
Figure 53: DLS autocorrelation functions obtained for a (a) calcium carbonate and (b) barium carbonate gel with R/C 100 at 0% (■), 10% (●), 20% (▲), 30% (▼), 40% (◆), 50% (◀), 60% (▶), 70% (●), 80% (★), 90% (⬟) and 100% (✕) of the total gel time.

The similarities and differences between the autocorrelation functions given above, in Figure 53, and those of the Group I metal carbonates, given in Figure 29, are clear to see. At early times in the gelation process, the decay profiles follow an exponential path. As the time increases, so does the timescale of the exponential decay of the function, suggesting that at these times, the growing clusters are once more forming without obstruction or intercluster interaction. However, as the time increases further, the expected secondary decay, as was observed with the Group I

metal carbonates, and interpreted as the onset of aggregation and networking processes, does not develop, with the profiles retaining an exponential decay.

Only once the gelation time has been reached does the shape of the profile change, becoming non-ergodic, as previously observed at this point. However, there is no initial decay corresponding to the residual diffusivity of primary clusters in the gel sample, as observed for the Group I samples. Instead, there is an apparent decay associated with a species larger than the cluster size indicated by the exponential decay of the last purely exponential profile.

Plotting the autocorrelation functions on a log-log scale provides further proof of the profiles retaining exponential decay until gelation is reached; this is shown in Figure 54.
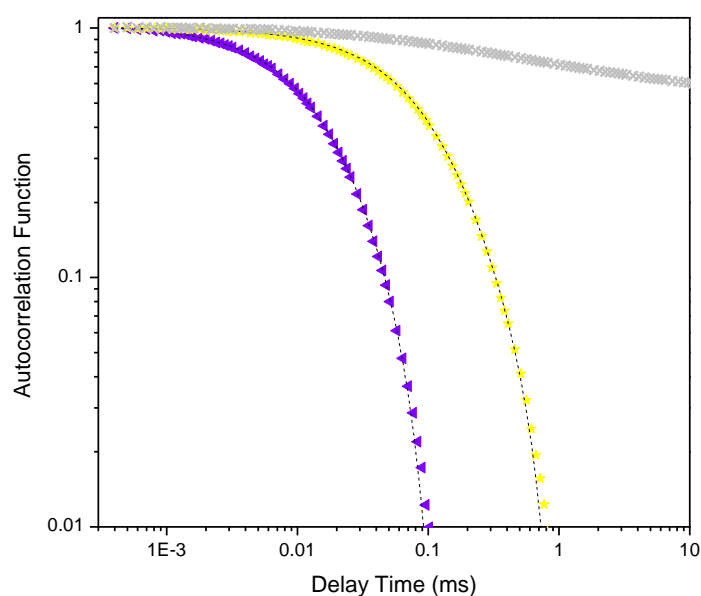
Figure 54: DLS autocorrelation functions obtained for a calcium carbonate gel with R/C 100 at 50% (◀), 80% (★) and 100% (✕) of the total gel time. Dashed lines represent the theoretical exponential decay of a monodisperse cluster population with hydrodynamic radius determined from the initial decay.

Dashed lines are included in Figure 54 to again represent the theoretical exponential decay of a monodisperse sample with hydrodynamic radius, as determined from the initial decay. It can be seen that the decays at 50 and 80% of the total gel time follow these theoretical decays exactly, while the 100% measurement point is non-ergodic.

Appendix J shows further autocorrelation functions obtained with calcium carbonate at R/C ratios of 200 and 400, which show little change to the R/C 100 profiles in

Figure 54. This is opposed to the marked differences when comparing the autocorrelation functions of the Group I metal carbonates over the R/C range studied.

These decay profiles suggest that growth of the primary clusters could be monitored up to 90% of the total gelation period of the R/C 100 gels shown. Unfortunately, these samples become turbid between the measurements taken at 80 and 90% of the gelation time, and even earlier for the higher R/C values studied, which is maintained for all subsequent samples, including the non-ergodic decay which occurs at the gelation point. This turbidity causes a high optical contrast within the system under study, resulting in strong, multiple scattering of the light, especially at visible wavelengths, and is indicative of larger cluster sizes. However, the turbidity means that accurate hydrodynamic radii values can no longer be calculated. As a result, cumulant analysis was limited to only those samples that were non-turbid, where accurate values could be determined. Figure 55 shows the hydrodynamic radii values determined for all of the Group II metal carbonate catalysed samples analysed.
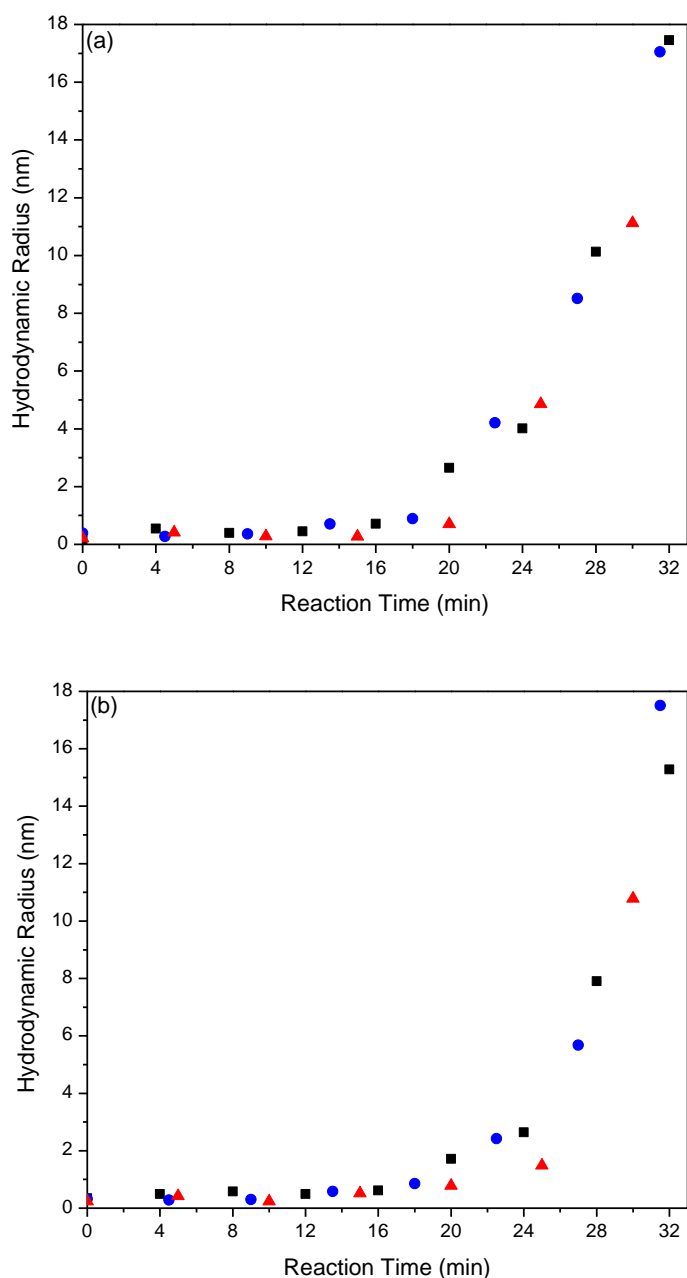
For each of the metal carbonates used, the cluster growth curves show an overlapping nature, similar to the trends observed for the Group I catalysts, with very limited cluster growth in the first 15 min of the reaction. The size of these initial clusters corresponds to the hydrated resorcinol molecule radius of 0.4 nm, suggesting only hydroxymethyl derivatives are present. This delay is further investigated in Section 6.5. By closely inspecting the results, it can be seen that both sets of data overlap into the same narrow band, as demonstrated in Figure 56.
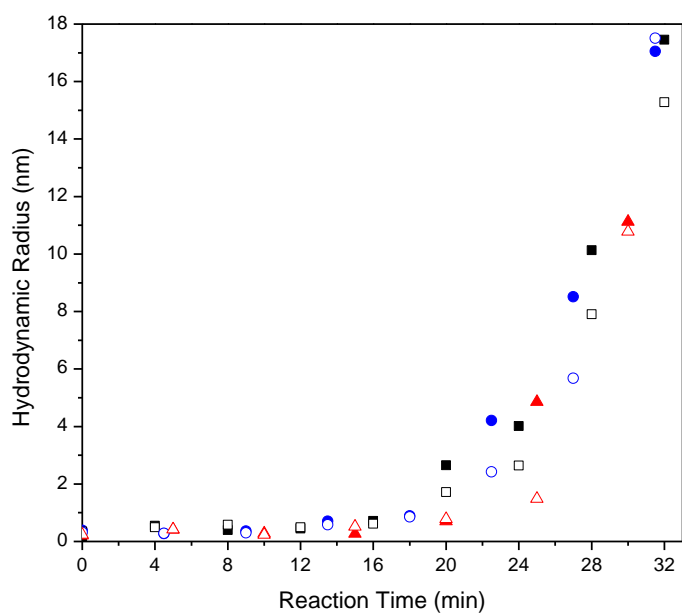
Figure 56: DLS hydrodynamic radii comparison between calcium carbonate (closed symbols) and barium carbonate (open symbols) at R/C ratios of 100 (■), 200 (●) and (▲) 400.

This suggests that the cluster growth is virtually independent of the R/C ratio or metal carbonate used, as for the Group I metal carbonates; however, the dependence of the maximum observable cluster size on R/C does not follow the same overall trend established by the Group I metal carbonates. In this case, both R/C 100 and 200 samples show a very similar maximum. In contrast to the Group I metal carbonates, however, the R/C 400 samples show a smaller maximum size than the lower R/C values. As the turbidity develops at a constant time after placing the samples in the oven (around 34 min), the final measurement point from which an accurate hydrodynamic radius can be determined varies in the amount of time between the analysis and turbidity developing. As R/C increases this gap widens, and it is, therefore, entirely possible that all clusters have the same size at the onset of turbidity. It should be noted, as discussed in Section 5.5, that intervals were kept constant at 10% of the total gel time, and this factor could be addressed in Future Work. As the actual changes in cluster size are unknown after turbidity has developed, it is possible that clusters may continue to grow, with the R/C 400 sample exhibiting larger cluster sizes. It is also possible that networking and aggregation occur, as before, but this is obscured by the turbidity in the samples.

It should also be noted that in the case of both the R/C 100 and 200 samples, the hydrodynamic radii observed with the Group II catalysts are significantly larger than the lithium, sodium, potassium grouping or even caesium carbonate. For the R/C

400 samples, this difference is substantially reduced for lithium, sodium and potassium, while hydrodynamic radii observed for caesium carbonate far exceeds the Group II catalysts. However, as previously stated, due to the development of turbidity these sizes for the Group II catalysts are unlikely to reflect the maximum cluster size achieved during the gelation process.

As the cluster sizes also overlap for the Group II gels, it is once more possible to examine the scattered light intensities for information on the number concentration of clusters present at each R/C. Figure 57 displays this data.
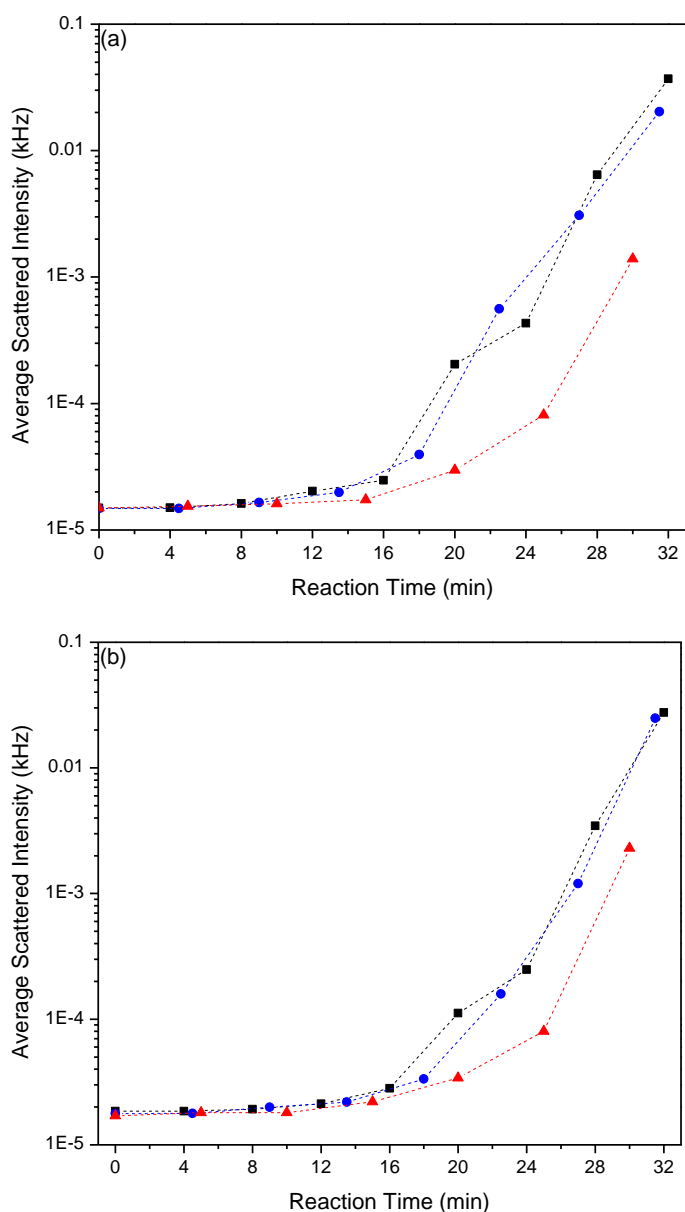
Figure 57: Average DLS scattered intensities for both (a) calcium carbonate and (b) barium carbonate gel series at R/C ratios of 100 (■), 200 (●) and 400 (▲).

It can be seen that for both of the Group II metal carbonates, R/C ratios of 100 and 200 result in very similar intensity values, with R/C 400 samples exhibiting a lower intensity at any given time. Coupled with the information on overlapping cluster growth profiles, this suggests that the R/C 100 and 200 samples produce a very similar number concentration of clusters. On the other hand, R/C 400 gives a lower intensity for the same cluster size, implying that a lower cluster number concentration is present; congruent with the results observed for the Group I metal carbonates.

6.3 Xerogel Characterisation

Surface area and porosity measurements were performed on each of the dried gels, as was the case for the Group I samples. The nitrogen adsorption/desorption isotherms obtained in each case are shown in Figure 58, once more grouped by catalyst.
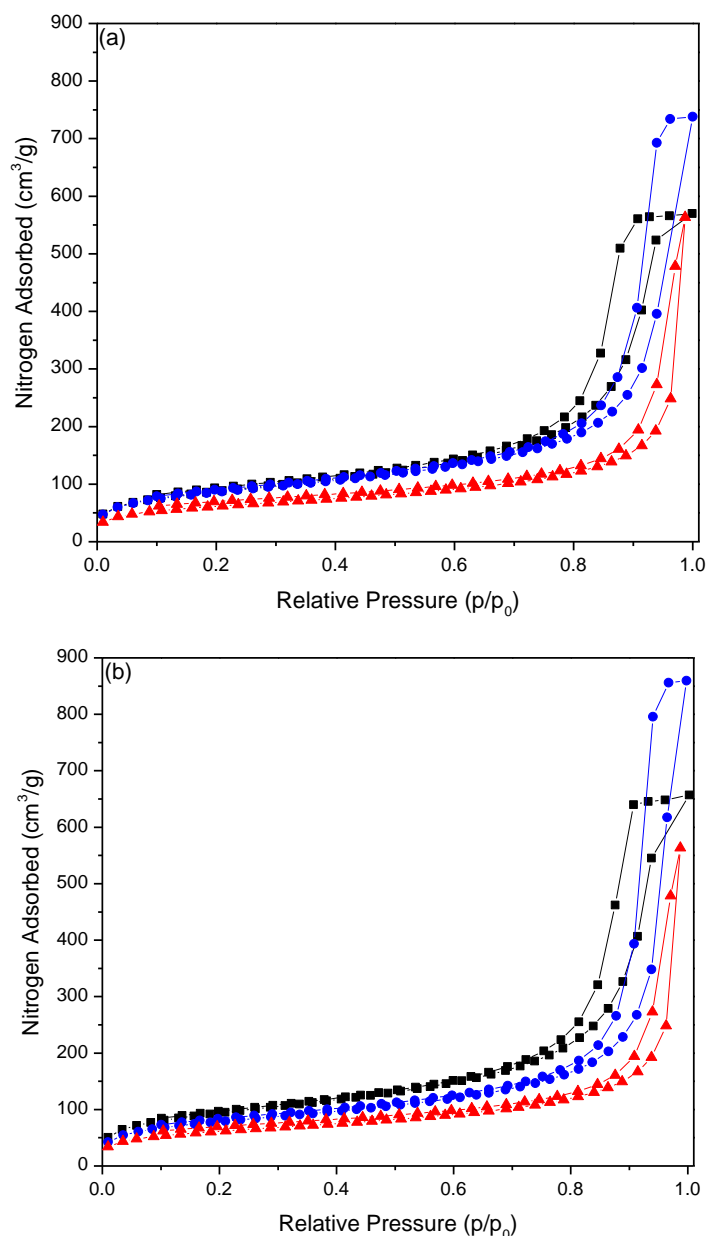
Figure 58: Nitrogen adsorption/desorption isotherms for (a) calcium carbonate and (b) barium carbonate at R/C ratios of 100 (■), 200 (●) and 400 (▲).

It is immediately apparent that, for a given R/C, the nitrogen adsorption isotherms for both catalysts are very similar. It is also evident that for R/C 100 and 200, the nitrogen uptakes have increased significantly, and hysteresis has shifted to higher relative pressures than the corresponding Group I metal carbonate samples, implying larger pores and pore volumes.

The R/C 400 gels show a reduction in uptake compared to the lower R/C gels, similar to the behaviour exhibited for caesium carbonate gels. However, these gels were not soft and weak before solvent exchange, and shrinkage during drying was

113

not significant. This, therefore, suggests that the much lower cluster number concentration has resulted in a substantial decrease in the number of pores in the final structure. Figure 59 gives the pore size distributions of the Group II metal carbonate catalyst gel series.
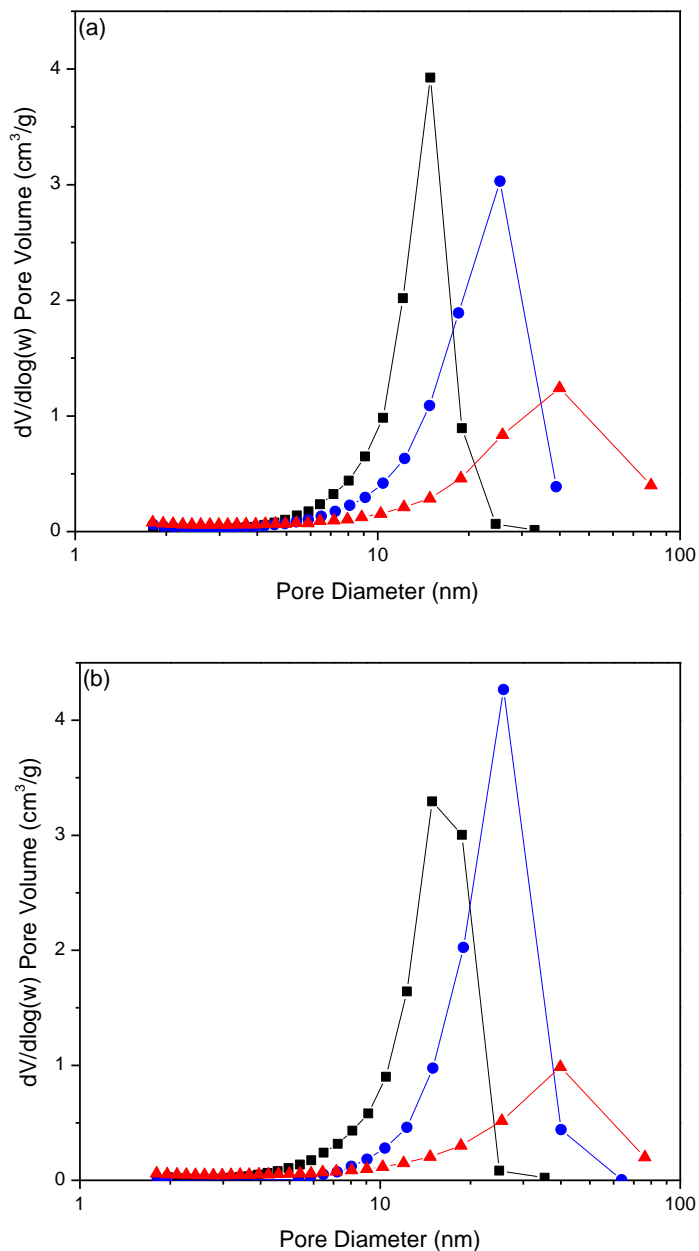
Figure 59: Pore size distributions for (a) calcium carbonate and (b) barium carbonate at R/C ratios of 100 (■), 200 (●) and 400 (▲).

These pore size distributions clearly show how the pore sizes obtained for Group II gels vastly dwarf those of any of the Group I metal carbonates. However, they are

consistent, in that increasing R/C leads to increasing pore diameter. The expected decrease in pore volume for R/C 400 gels is also confirmed.

These results are in line with the Group II catalysts developing larger cluster sizes than the analogous Group I samples, and, in turn, larger intercluster voids. R/C 200 samples for both calcium and barium carbonate show larger pores than the corresponding R/C 100 gels, suggesting that the final cluster size is larger for the R/C 200 gels. In addition, the very large pore sizes exhibited by the R/C 400 gels further supports the assumption that the clusters continue to grow significantly after turbidity has developed.

The differences in pore size observed for the R/C 100 and 200 samples, despite the very similar cluster sizes, may be the result of the solubility of the catalysts. In both cases, substantial amounts of the solid catalyst remain undissolved after the 30 min stirring period during sol preparation. Before DLS analysis was performed, the samples were filtered to remove solid particulates that would otherwise interfere with the measurements. Consequently, any undissolved catalyst would be removed, giving an approximately equal dissolved catalyst concentration for a given metal carbonate, based on its solubility. Dried xerogels were not filtered during production; therefore, the undissolved catalyst was still present and able to influence the gelation process. Table 18 gives the measured textural properties of each xerogel sample.

Table 18: Textural properties of all dried xerogel samples prepared in this study.

R/C	S_{BET} (m^2/g)	V_{Tot} (cm^3/g)	V_μ (cm^3/g)	d_p avg (nm)
$CaCO_3$				
100	307 ± 3	0.88	0.02	12.4
200	301 ± 3	1.14	0.02	17.6
400	213 ± 2	0.87	0.02	21.5
$BaCO_3$				
100	331 ± 3	1.11	0.01	13.3
200	275 ± 3	1.33	0.02	21.8
400	159 ± 2	0.73	0.01	23.2

As also seen for the Group I samples, several observable trends exist that agree with established results. Pore sizes increase with increasing R/C, which is mirrored

in the pore volume results, bar those of the R/C 400 gels previously discussed. This corresponds to a decrease in BET surface area.

6.4 Further Interpretation of the Results

As the hydrodynamic radii data obtained from the DLS results do not seem to show any correlation to the measured average pore diameter, it is not possible to add this information to the Master Curve generated from the corresponding results for the Group I metal carbonates (Figure 38). However, the range of pore diameters accessible using the Group II catalysts (Table 18) indicate that, while the pore diameters are comparable with those attainable through the use of caesium carbonate and high R/C values of lithium, sodium and potassium carbonate, utilising a Group II metal carbonate results in the same pore diameters with a higher catalyst concentration. This has benefits of a shorter gelation time and comparatively stronger material, due to increased cross-linking, less prone to collapse and shrinkage during drying.

6.4.1 Colloidal Stability During RF Gel Formation

Further examination of the Hofmeister series in Figure 39 indicates that the presence of calcium cations results in unfavourable effects in the stabilisation of colloidal suspensions. The 2^+ charge on the cations lead to an increased charge density. As such the calcium cation should lead to less destabilisation of the oligomer interactions, which subsequently salt out and become large clusters. Unlike the results for the Group I metal carbonates, this is reflected in the results for calcium and barium cations which give large clusters, to an even greater degree than the caesium cation. They can therefore be added to the Hofmeister-like series established in this work, such that:

lithium = sodium = potassium > caesium > calcium = barium

The trend presented here, which shows similar results for lithium, sodium and potassium and a separate grouping of results for calcium and barium, albeit vastly different to the Group I metal carbonates, reflects the observations made by Job *et al.*[67] They saw clear groupings for both Group I and Group II catalysts, with the difference in stabilisation ability explained as the result of cation screening of the electrostatic repulsion between the oligomeric clusters in the system. The screening takes place over the Debye-Hückel length, l, which is related to both the cation concentration and the square of the charge on these cations. For a given R/C, a

Group I metal carbonate, with formula M_2CO_3, will have twice the cation concentration as a Group II metal carbonate, formula MCO_3. However, the increasing cation charge (1+ to 2+) will cause a significant decrease in screening length. In the presence of a Group II metal carbonate, the oligomers can approach more closely, resulting in earlier phase separation and consequently larger clusters and pore sizes.

It must also be considered that the presence of the various cations may be influencing the compactness of the clusters. At a given R/C, the amount of carbonate present is the same in all cases, leading to an approximately equal initial number of growing species. However, the sizes of these clusters vary significantly. In the case of sodium, clusters are small. The RF oligomeric chains that make up the clusters are presumably packed tightly together. However, for calcium, where the clusters are much larger, there is potential chain aggregation through the interaction of hydrophobic sites on the RF chains. As a result, the clusters would be less compact and, therefore, larger in size.

6.4.2   RF Sol-Gel Transition

DLS results show freely diffusing clusters in the initial stages of gelation, with cluster size independent of the R/C and metal carbonate used, at a given time. This suggests that, despite the vast differences in cluster size and textural properties, cluster growth in the presence of a Group II metal carbonate remains a thermodynamically controlled process involving a nanoscale phase transition, such as mesostructured liquid phase formation. It also suggests that the model, detailed in Section 5.4 and depicted in Figure 40, holds for these examples. R/C dictates the number concentration of clusters present, and the size to which they will grow before reaching a critical cluster volume fraction. In turn, this dictates the size of intercluster voids which constitute the pores within the network, resulting in larger clusters and greater pore sizes as R/C is increased.

6.5   Thermal Influence on the Growth of Clusters

As the calcium carbonate gels exhibit a delay of around 15 min before the onset of cluster growth, as also observed for the Group I gels, it was again decided to investigate the influence of preheating the initial sol.

6.5.1   Determination of the Temperature Profile

The temperature profile for a calcium carbonate gel synthesised with an R/C of 100 is shown in Figure 60. This was measured in an identical manner as for the sodium

carbonate gels, by recording the temperature of the samples at the same intervals used for DLS (Section 5.5.1).
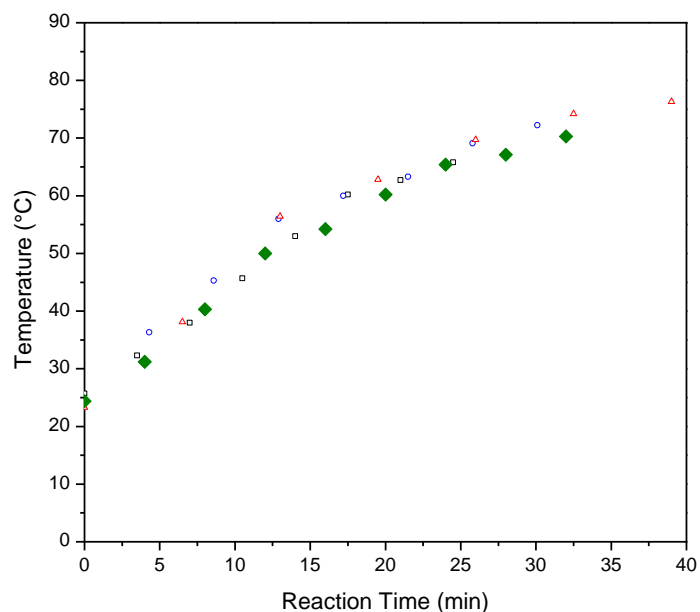
Figure 60: Temperature profile for a CaCO$_3$ gel with R/C of 100 (◆). The results for Na$_2$CO$_3$ [R/C 100 (□), 200 (○) and 400 (△)] as shown in Figure 38 are included for comparison.

As can be seen from the temperature profile for the calcium carbonate R/C 100 sample, it overlaps with those for the sodium carbonate gels previously studied. This is to be expected as the same oven was used for all experiments. These temperatures can then be compared with the cluster growth profile to determine the temperature to which the sol should be preheated. This comparison is shown in Figure 61.
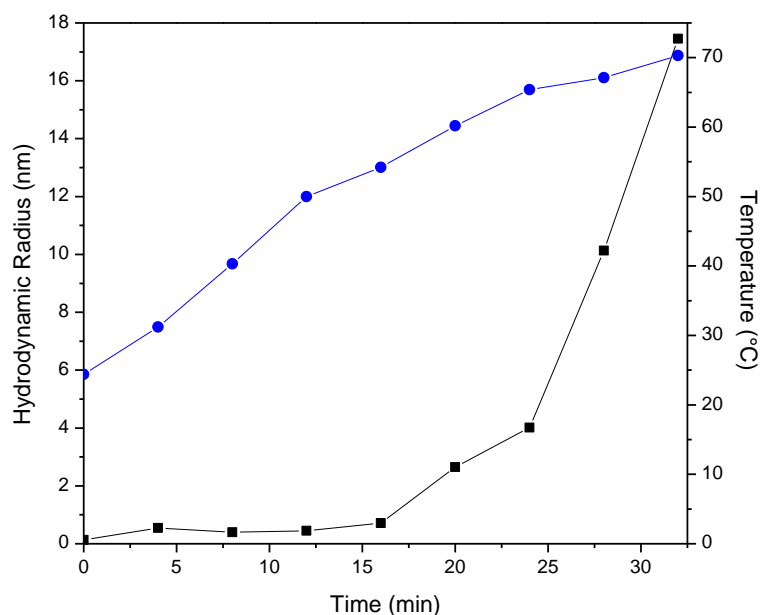
Figure 61: Comparison between DLS hydrodynamic radii (■) and temperature (●) for CaCO₃_100, showing cluster growth begins at 55 °C.

Comparative analysis shows that cluster growth increases rapidly once the sample reaches 55 °C, identical to the sodium carbonate gels. The same conditions could therefore be used to remake the calcium carbonate gel.

6.5.2 Dynamic Light Scattering Studies

DLS experiments were repeated using a gel preheated to 55 °C, as for the sodium carbonate gels. Preheating once more resulted in a reduction in gel time and corresponding DLS interval. The new values are shown in Table 19.

Table 19: Total gelation and DLS interval times for CaCO₃_100 preheated to 55 °C.

Sample	Gelation Time (min)	Interval Time (min)
CaCO3_100	35	3.5

The newly acquired DLS hydrodynamic radii are compared with the room temperature sol results, obtained previously, in Figure 62.
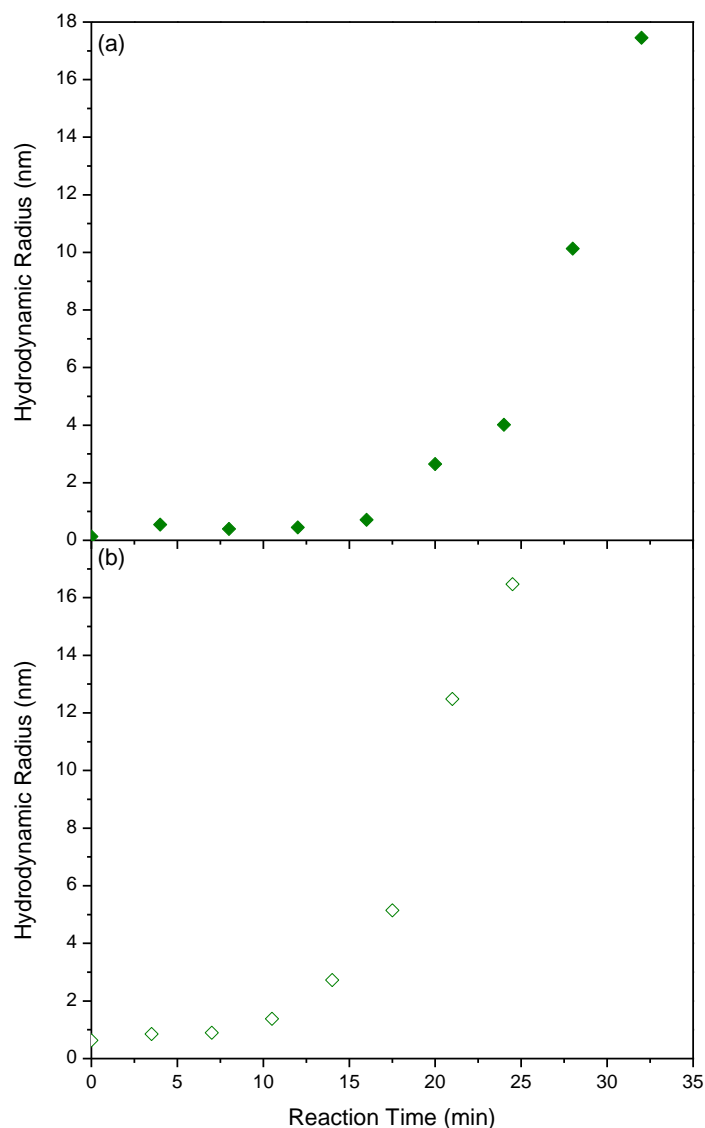
Figure 62: DLS hydrodynamic radii comparison for CaCO$_3$ samples with R/C 100 placed in the oven (a) at room temperature and (b) preheated to 55 °C before placing in the oven.

Once more, it can be seen, from the data in Figure 62, that preheating the sample reduces the delay time before the onset of cluster growth, albeit without eliminating the delay entirely. This is in spite of the temperature profile suggesting that, as for the sodium carbonate gels, cluster growth began in earnest when the temperature reached 55 °C. However, as the growth profiles for Group I and Group II metal carbonates are so different, this is not unexpected.

The maximum observed hydrodynamic radius is also very similar between the room temperature and preheated samples, with this case showing a very slight decrease when preheating. Again, this suggests that the increased starting temperature has little effect on the final cluster size in the gel.

6.5.3 Characterisation of the Preheated Xerogels

In contrast to the sodium carbonate results, the comparative isotherms for the calcium carbonate R/C 100 gels depicted in Figure 63 show a vast difference.
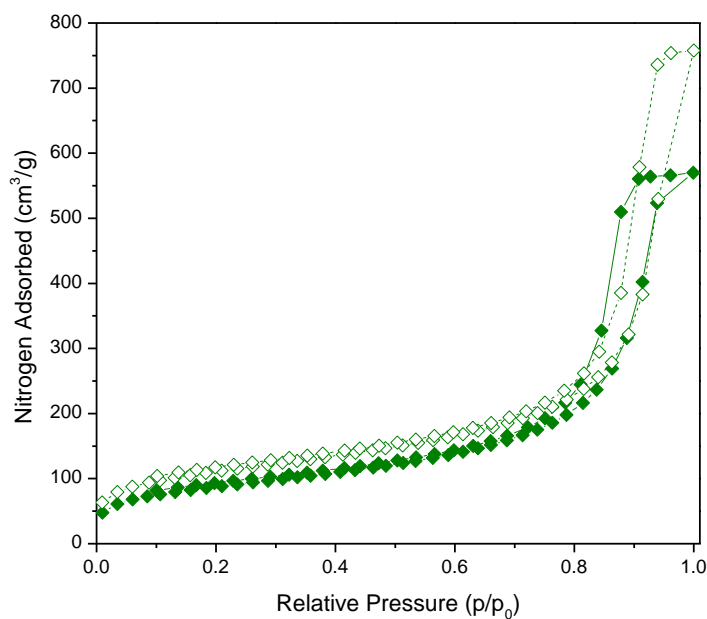
Figure 63: Nitrogen adsorption/desorption isotherm comparisons for CaCO3_100 prepared at room temperature (◆) and 55 °C (◇).

Nitrogen uptake is higher at all relative pressure measurement points, with a significant increase of 35 % in the total uptake figure. This shows that, despite the similar cluster sizes, the gels prepared at room temperature and 55 °C do not share similar properties.

The increased nitrogen uptake implies an increase in the pore volume of the preheated gel. This is reflected in the pore size distribution plot in Figure 64, which shows a widening of the distribution and a shift to larger pore diameters.
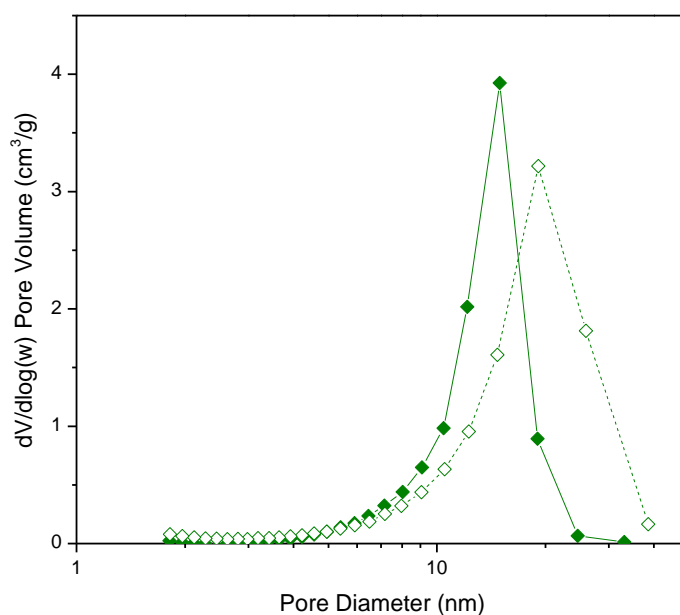
Figure 64: Pore size distribution comparison for CaCO3_100 prepared at room temperature (◆) and 55 °C (◇).

Preheating the gel clearly has an impact on the porous properties of the dried gel. In fact, the isotherm and pore size distribution look closer to those of a calcium carbonate gel with R/C 200. Further properties of the dried xerogel are shown in Table 20.

Table 20: Properties of a $CaCO_3$_100 gel preheated to 55 °C.

Sample	S_{BET} (m^2/g)	V_{Tot} (cm^3/g)	V_μ (cm^3/g)	d_p avg. (nm)
$CaCO_3$_100 @ 55 °C	384 ± 4	1.17	0.03	15.1

The increase in average pore size and total pore volume for the preheated calcium carbonate R/C 100 gel is further confirmed by Table 20. Despite this, the 55 °C sample shows a 25% increase in BET surface area, counter to what is expected from the larger pores and increased volume. However, the sample does show a doubling of the micropore (< 2 nm) volume, which does explain the increase in surface area.

The total pore volume of the preheated calcium carbonate R/C 100 gel is again comparable with that of the standard room temperature R/C 200 sample. Although the average pore size is smaller than expected for the R/C 200 gel, the increased contribution from the micropores within the system decreases this average size.

122

Discounting this additional contribution, the average mesopore size may well, therefore, be comparable with the R/C 200 gel.

6.6 Solubility of Calcium Carbonate

As noted in Chapter 4, calcium carbonate is only sparingly soluble in water. This solubility is highly dependent on temperature, pressure and pH, due to the amount of dissolved carbon dioxide in the water, and is dictated by a series of equilibria.[152] Dissolution of carbon dioxide (or any other gas) in water is a two-step process.[153] First, a pocket, or cavity, must open within the solvent in order to accommodate the gas molecule. Second, the gas molecule enters this pocket to become dissolved.

The formation of pockets within the solvent is an endothermic process, requiring the input of energy. Meanwhile, the filling of a pocket by a gas molecule is exothermic and energy is released. In most organic solvents, the formation of pockets requires more energy than is produced by filling them with gas molecules, resulting in the overall process being endothermic. Increasing the temperature of the system, therefore, encourages the dissolution of more of the gas in question. However, due to the hydrogen bonding present in water, the pockets are already partially formed meaning less energy is required to create them. The energy released by filling the pockets therefore dominates the process and there is a net release of energy during the dissolution. As the temperature increases, the dissolution equilibrium will shift in favour of less pocket filling (to lower the exothermic contribution) and, therefore, the amount of carbon dioxide dissolved will decrease.[153] Figure 65 shows the solubility of carbon dioxide in water over the temperature range of 0 – 60 °C.
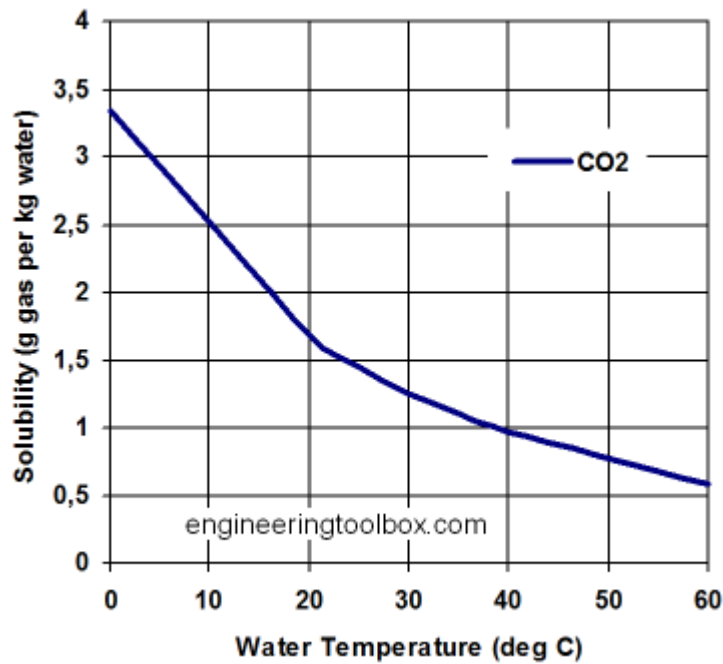
Figure 65: Solubility of carbon dioxide in water with temperature.[154]

As can be seen from the plot, the solubility of carbon dioxide approximately halves for a thermal increase from room temperature to 55 °C.

Carbon dioxide and calcium carbonate dissolve according to the equilibria:

$$CO_2 + H_2O \rightleftharpoons HCO_3^- + H^+$$

$$CaCO_3 \rightleftharpoons Ca^{2+} + CO_3^{2-}$$

$$H^+ + CO_3^{2-} \rightleftharpoons HCO_3^-$$
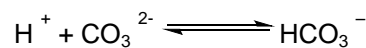
These can then be combined to give:

$$CaCO_3 + CO_2 + H_2O \rightleftharpoons Ca^{2+} + 2.HCO_3^-$$
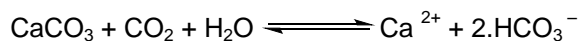
Reaction 3: Calcium carbonate dissolution equilibrium.

As the temperature increases, the level of dissolved carbon dioxide decreases. Following Le Chatelier's principle, this process shifts the equilibrium to the left hand side, forming more calcium carbonate. Therefore, as the temperature rises, the solubility of calcium carbonate will correspondingly decrease. This solubility trend is shown in Figure 66.

124
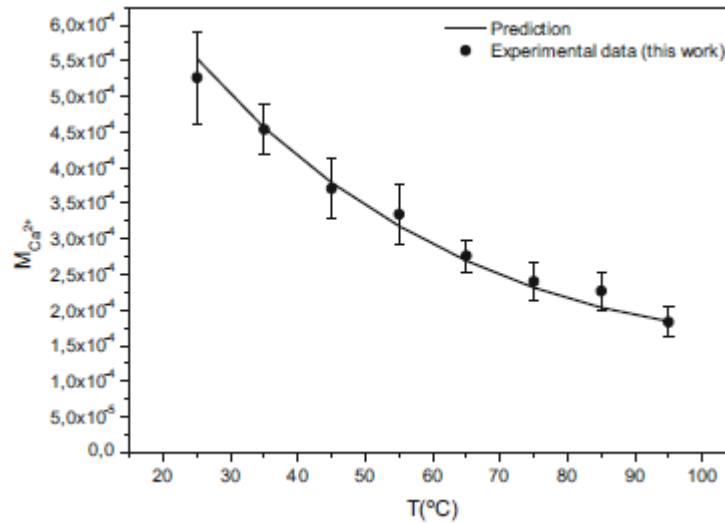
Figure 66: Solubility of CaCO₃ with temperature as calculated experimentally by Coto et al.[152]

As such, with less calcium carbonate able to dissolve, raising the temperature effectively increases the R/C ratio of the initial solution. This is congruent with the increases in pore volume and average pore size witnessed being closer to an R/C 200 gel when compared with the R/C 100 calcium carbonate gels prepared at room temperature and 55 °C, respectively.

The similarity in growth profile and maximum observable hydrodynamic radii between R/C 100 and 200 for calcium carbonate gels means there is little difference when comparing to the preheated sample. It is, therefore, not possible to distinguish between these gels by simply looking at hydrodynamic radii values above.

6.7 Summary of Findings

Gels catalysed with calcium and barium carbonate, with R/C ratios of 100, 200 and 400, were analysed in detail using DLS, in conjunction with surface area and porosity measurements.

Similar to the investigation using sodium carbonate, the influence of heating conditions on the porous properties of the gel were investigated through the preheating of a sample catalysed using calcium carbonate at an R/C of 100. The temperature of preheating was again 55 °C, corresponding to the rapid onset of cluster growth in a sample prepared at room temperature.

It was found that:

- For typical xerogel formation:
  - Average pore size increases with increasing R/C, with a corresponding decrease in surface area, for both catalysts.
  - Pore sizes are considerably larger than the corresponding Group I metal carbonate gels.
  - Pore volume unexpectedly decreases at R/C 400; however, pores are very large, suggesting larger clusters which are fewer in number, with a resulting decrease in the number of pores.
  - In all cases, primary cluster growth is independent of R/C and metal carbonate chosen, suggesting thermodynamic control.
  - Primary cluster sizes are much larger than the corresponding Group I metal carbonate gels.
  - Cluster number concentration is dependent on R/C suggesting kinetic control.
  - Group II metal cations have very high charge densities which disrupt the hydration layer surrounding RF oligomers, resulting in salting out and larger clusters.
  - Larger clusters have correspondingly larger intercluster voids, and larger pore sizes, than the Group I carbonates for an equivalent R/C.
- On preheating to 55 °C:
  - Preheating does not fully eliminate the delay in cluster growth for calcium carbonate gels, as was the case for sodium carbonate.
  - Maximum observable hydrodynamic radius is slightly smaller when preheating a calcium carbonate gel.
  - Properties of the preheated calcium carbonate R/C 100 gel more closely resemble those of an R/C 200 gel than the equivalent R/C 100 gel prepared at room temperature, as the increased temperature decreases the solubility of calcium carbonate and effectively increases the initial R/C of the gel.
  - Resultant clusters are therefore of similar size to those of the R/C 200 gel, with similar pore sizes and textural properties.

Using calcium and barium carbonate, it is possible to produce stable gels with a high catalyst concentration that have very similar porous structure to those only obtainable using low concentrations of lithium, sodium or potassium carbonate.

7 Results Part 3 - Gels Synthesised with Ammonium Carbonate as Catalyst

In order to further distinguish between the roles played by the carbonate anion and metal cation in the formation of RF gel porosity, a series of gels were synthesised using ammonium carbonate as an alternative, non-metallic carbonate source. This allowed direct comparison between gels of an equal carbonate concentration, while no metal cation was present in one case. Subsequently, a further series of gels were produced in which both a metal carbonate and ammonium carbonate were simultaneously used in equal quantities.

7.1 Ammonium Carbonate Gels

As was the case for the carbonate free sample prepared in Section 5.6, to ensure that the comparison between the ammonium carbonate gels and the various metal carbonate gels was valid, all synthesis parameters were kept constant, as for the standard gels, i.e. R/F = 0.5, solids content = 20% w/v and total gel volume = 60 ml, when using ammonium carbonate. Only the R/C ratio was once more altered, whilst still being kept within the previously used range of 100 – 600. As such, values of 100, 200 and 400 were chosen. All stages of the xerogel synthesis were performed in an identical manner to those of the analogous metal carbonate samples.

A simple visual comparison of the products was once more the first observation made. Where the metal carbonate gels were monolithic structures ranging in colour from orange to very dark red, almost black, and the carbonate free sample was a bright red-orange powder, the ammonium carbonate product was different again. Whilst following a similar path to that of the carbonate free sample, the reaction produced a dense solid layer at the bottom of the liquid volume, which dried to a powdery product. However, the colour of the ammonium carbonate powder was darker, now a dull red-brown, as seen in Figure 67. Furthermore, there was no visual difference between samples made with different values of R/C, contrary to the observations made with the metal carbonate gels.

Figure 68 and 69 show the nitrogen adsorption isotherms and pore size distributions for the three ammonium carbonate R/C ratios studied, with the results for sodium carbonate R/C 100 shown for comparison.
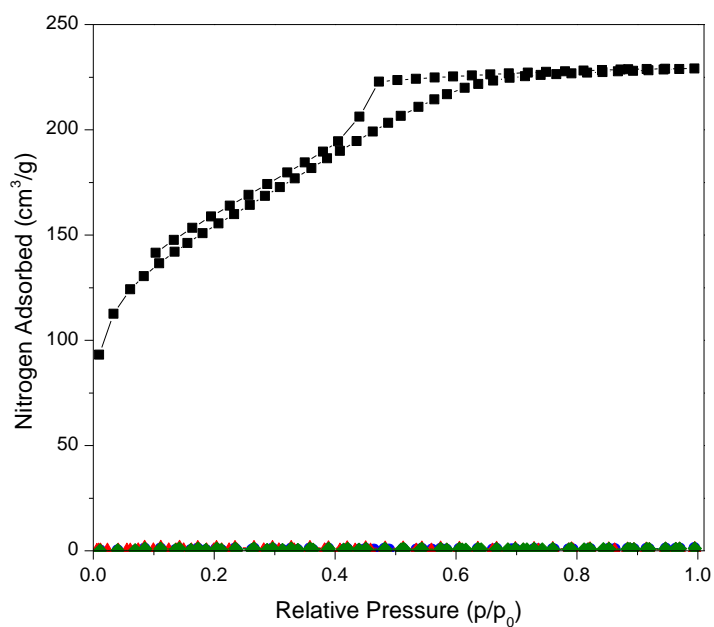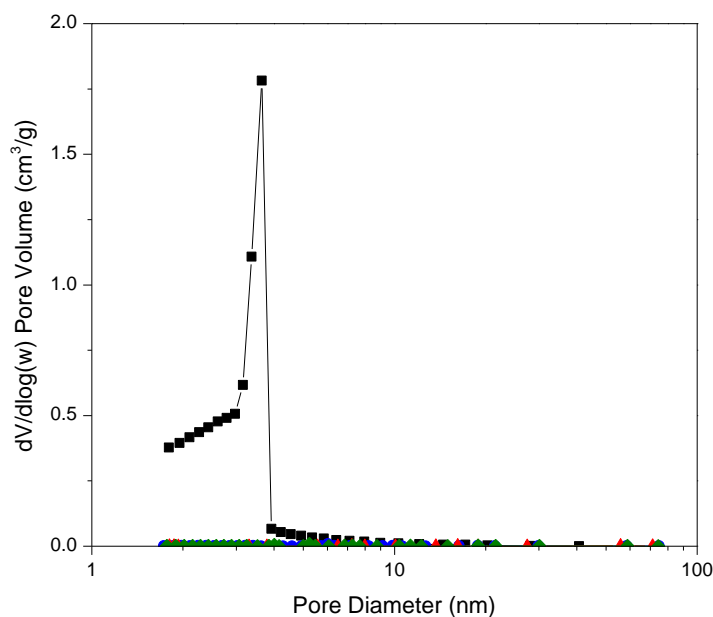
As can be seen, the ammonium carbonate gels have very little nitrogen uptake or discernible porosity when compared to the sodium carbonate gel. These results are reflected in the properties of the products shown in Table 21.

Table 21: Textural properties of $(NH_4)_2CO_3$ and Na_2CO_3 gels.

Sample	S_{BET} (m²/g)	V_{Tot} (cm³/g)	V_μ (cm³/g)	d_p avg. (nm)
$(NH_4)_2CO_3\_100$	2 ± 0	-	-	6.4
$(NH_4)_2CO_3\_200$	1 ± 0	-	-	17.8
$(NH_4)_2CO_3\_400$	1 ± 0	-	-	6.6
$Na_2CO_3\_100$	533 ± 5	0.35	0.05	2.9

It is evident from Table 21 that the ammonium carbonate gels have very low surface areas and negligible pore volumes compared to the sodium carbonate counterpart. However, the values are consistent when compared to the sample prepared with no carbonate present, suggesting that the ammonium carbonate sample is also composed of very large clusters that fail to cross-link into the 3D network.

7.1.1 Dynamic Light Scattering Studies

To further examine the influence of ammonium carbonate, a sample prepared using an R/C ratio of 100 was studied using DLS. This further highlighted the similarities between carbonate free and ammonium carbonate samples, with both samples showing turbidity and visible sedimentation. However, this occurs on vastly different time scales for the two samples. Where the carbonate free sample took 90 minutes to become turbid and 120 minutes to show sedimentation, the ammonium carbonate samples produced turbidity immediately upon being placed in the oven, with visible sedimentation after only 20 minutes. This rapid development of turbidity is shown in Figure 70, where times between samples are 4 minutes.
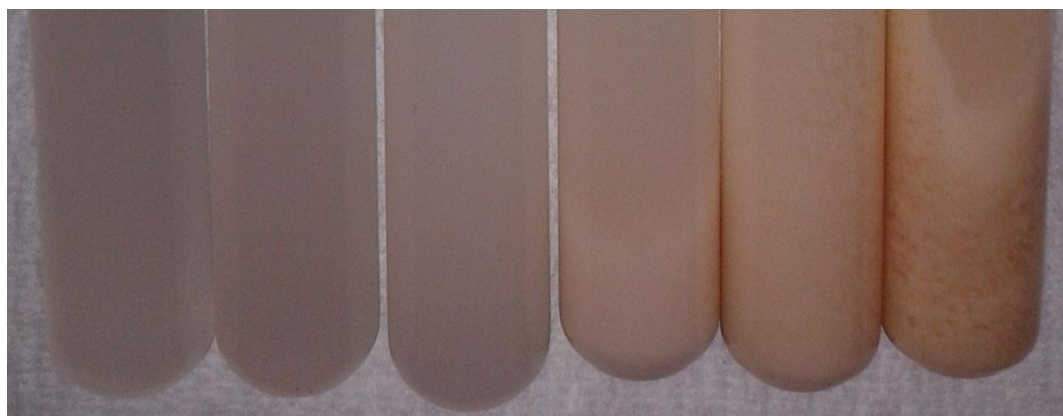
Figure 70: Visible turbidity and sedimentation that occurs during the RF reaction, when in the presence of $(NH_4)_2CO_3$. From left to right, samples are taken at 0, 4, 8, 12, 16 and 20 minutes after placing in the oven respectively.

As the ammonium carbonate sample failed to gel as for a standard sample, 10 % interval times could not be taken at which to run DLS measurements. Intervals of 4 minutes were therefore chosen in order to provide a representative number of measurements within the 20 minutes before sedimentation occurred. Figure 71 shows the autocorrelation functions obtained for these measurement points. As the samples were turbid, it was once more not possible to obtain accurate hydrodynamic radii values; however, the determined values are displayed in Figure 72, to allow comparison between the metal carbonate catalysed and carbonate free systems, as the later also exhibited turbidity and sedimentation.
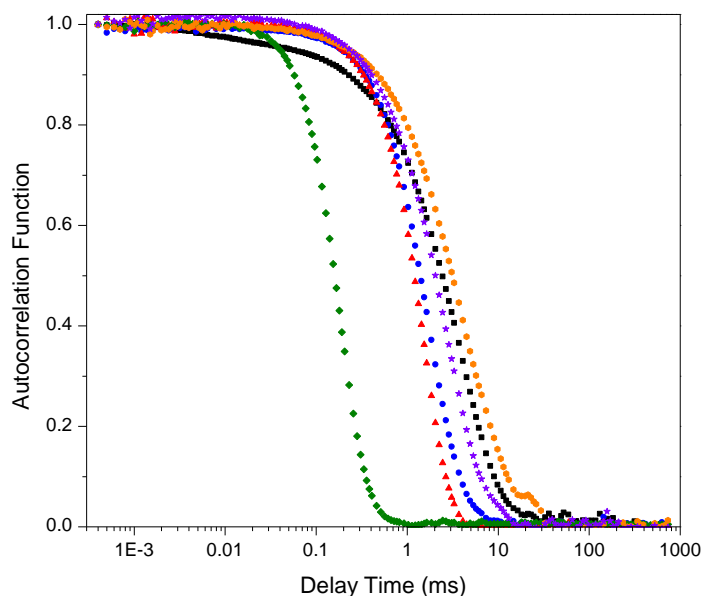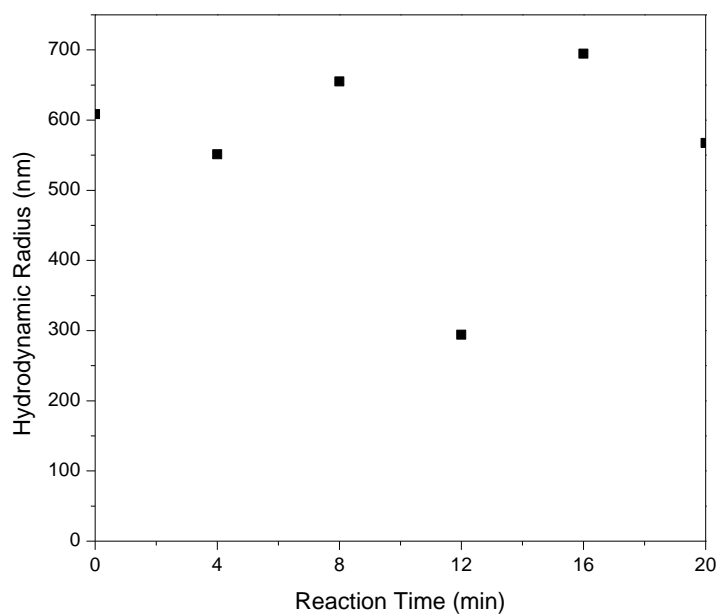
As can be seen, the sizes are considerably larger than those of both the metal carbonate and carbonate free analysis. Nevertheless, the potential inaccuracies in these results prevent definitive conclusions from being drawn.

These results do, however, seem realistic when considering the work of Reuß and Ratke, who synthesised RF gels using ammonium carbonate as a catalyst.[155] They

found the product to be ochre to dark brown in colour, while, more importantly, SEM images of the dried product showed particle sizes on the μm scale. As such, these would correspond to pore sizes well outwith the detectable range of the equipment available, and with severely limited usefulness in regard to the typical uses of RF gels.

7.2   Ammonium Carbonate Decomposition

While it is evident that the addition of ammonium carbonate has increased the rate of reaction between R and F, a stable gel structure has still not been formed. According to the Hofmeister series shown in Figure 39, the ammonium cation should display favourable effects. As a result, oligomers should be destabilised, their solubility increased, and small clusters subsequently formed. However, it has already been shown that the metals used in this study do not follow the typical Hofmeister trend, suggesting that the ammonium cation could have the opposite effect.

It must also be considered that in aqueous solution, and especially upon heating, ammonium carbonate will decompose into ammonia, water and carbon dioxide according to:

$$(NH_4)_2CO_3 \rightarrow NH_4HCO_3 + NH_3$$

$$NH_4HCO_3 \rightarrow NH_3 + H_2O + CO_2$$
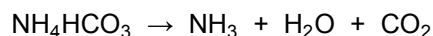
Reaction 4: Two stage decomposition of ammonium carbonate.

This will result in the loss of both NH_4^+ cations, as well as a reduction in the base concentration required to promote the initial addition reaction between R and F. However, some of the liberated ammonia will react with a quantity of F to form hexamethylenetetramine, also known as hexamine (see Figure 73), through a series of intermediates and corresponding condensation reactions.[156]
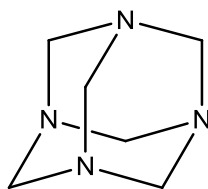
Figure 73: Structure of hexamine.

The hexamine produced may act as a substitute base and therefore continue to promote the addition reaction. It is unlikely that all of the ammonia will react in this way, with some being lost as a gas, meaning that the base concentration is less than that of the initial carbonate, however, it is sufficient to increase the rate of reaction. This is consistent with liquid chromatography observations for the consumption of R, which showed a slower consumption of R for ammonium carbonate when compared with an equivalent R/C of sodium carbonate.[134]

The loss of the NH_4^+ cation prevents any potential interaction between cation and RF oligomers from being realised. Consequently, in the same manner as the carbonate free samples, the small number of growing oligomers will rapidly salt out of solution, resulting in the turbidity and sedimentation observed. The increased rate of the initial reaction, induced by the presence of the base (be it ammonium carbonate before decomposition, or the newly formed hexamine), causes this to happen after much shorter times compared to the carbonate free sample.

7.3   Metal Carbonate/Ammonium Carbonate Gels

In order to expand this investigation into the role of the metal as opposed to the effect of the carbonate on the gel formation process, a series of gels were made using a mixture of metal carbonate and ammonium carbonate with a ratio of 50:50. Comparison could then be made between these gels and those made solely with the corresponding metal carbonate. Evaluation of the gel properties at both equivalent metal cation and equivalent carbonate concentration was then possible. As such, metal carbonate R/C ratios of 100, 200 and 400 were compared with mixed carbonate R/C ratios of 50, 100 and 200 respectively. The compositions and required volumes of these mixed gels are given in Appendices C and D, respectively. This comparison was made for both Group I and Group II metals using sodium, potassium, caesium and calcium carbonate.

7.3.1   Group I Metal Carbonate/Ammonium Carbonate Gels

From Chapter 5, it has been found that for the Group I metal carbonates, lithium, sodium and potassium give very similar results. In turn, these are different to the results of caesium carbonate. It was, therefore, decided to initially investigate both sodium and caesium carbonate when mixed with ammonium carbonate. As a follow up, further investigation using potassium carbonate was performed. This allowed comparison between sodium and potassium to see if the already established similarities held for additional members of the originally observed series.

The first comparison made between gels was a visual inspection. Images of each of the mixed carbonate gels are shown in Figure 74.

Figure 74: Visual comparison of mixed $Na_2CO_3/(NH_4)_2CO_3$ gels with, from left to right, R/C 50, 100 and 200.

It can be seen from these images that the gel products once more take a monolithic form, as opposed to the powder produced when solely using ammonium carbonate. The colour of the bulk material has also returned to the dark red expected of the standard sodium carbonate gels. However, in all cases, there is a powdery orange coating on the surface of the gel. This is most pronounced on the R/C 50 gel, which contains the highest concentration of ammonium carbonate. This trend in the look of the gels was repeated for both the potassium and caesium counterparts.

Figure 75 displays the comparative nitrogen adsorption isotherms between the pure sodium carbonate gels and the mixed sodium carbonate/ammonium carbonate gels. Isotherms of the same colour correspond to gels with an equivalent metal concentration, e.g. $Na_2CO_3\_100$ and $Na_2CO_3/(NH_4)_2CO_3\_50$.
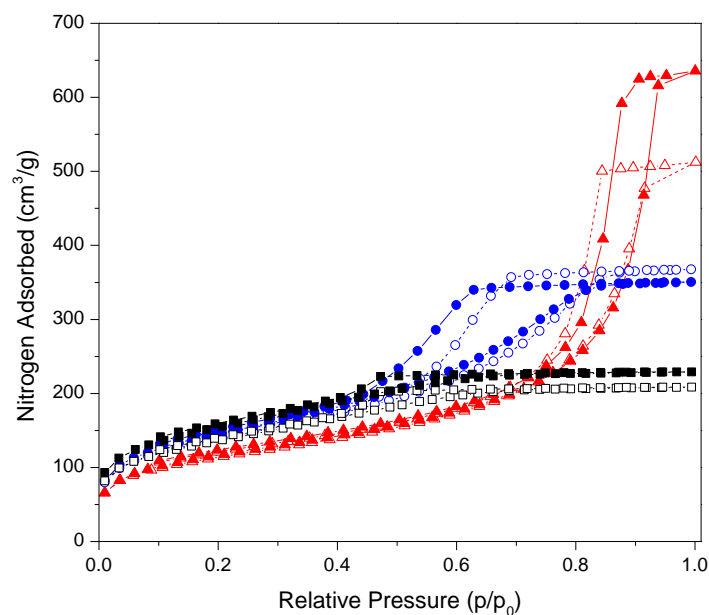
The isotherms show that, in general, gels prepared with an equivalent metal concentration result in similar adsorption/desorption isotherms, as opposed to the concentration of carbonate. This is mirrored in the pore size distributions given in Figure 76.
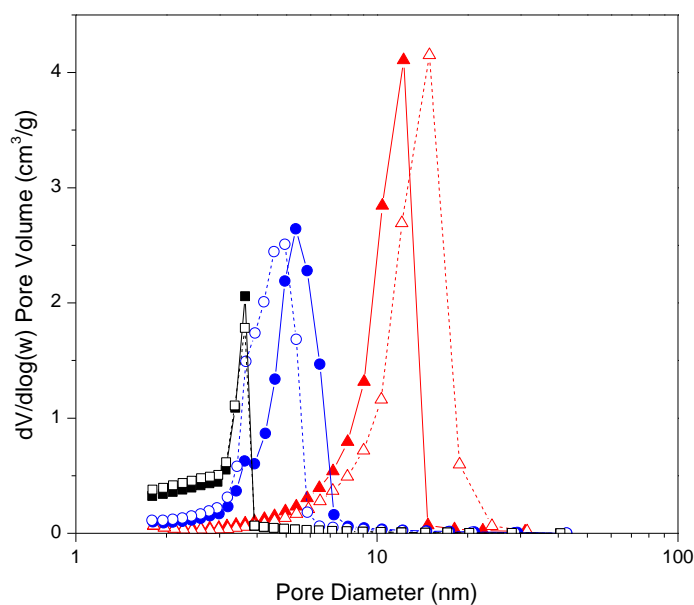
There is significant similarity between the distributions for gels with an equivalent metal concentration. Table 22 provides further textural properties for each of the dried gels. Data from Table 11 is replicated here for ease of comparison.

Table 22: Comparison of gel textural properties for pure Na_2CO_3 gels and mixed $Na_2CO_3/(NH_4)_2CO_3$ gels.

Sample	S_{BET} (m^2/g)	V_{Tot} (cm^3/g)	V_μ (cm^3/g)	d_p avg. (nm)
$Na_2CO_3/$ $(NH_4)_2CO_3\_50$	472 ± 4	0.32	0.04	2.9
$Na_2CO_3/$ $(NH_4)_2CO_3\_100$	483 ± 4	0.57	0.03	4.8
$Na_2CO_3/$ $(NH_4)_2CO_3\_200$	394 ± 4	0.79	0.03	9.3
$Na_2CO_3\_100$	533 ± 5	0.35	0.05	2.9
$Na_2CO_3\_200$	508 ± 4	0.54	0.03	4.2
$Na_2CO_3\_400$	403 ± 4	0.98	0.04	11.5

The properties of the gels follow the trends already established, matching closely for gels of equivalent metal cation concentrations. Only the R/C 400 sample shows a slight variation, with a wider pore size distribution giving rise to an increased average pore size and pore volume.

7.3.1.2 $K_2CO_3/(NH_4)_2CO_3$ Gels

A similar comparison was made between pure potassium carbonate gels, and those made with a mixture of potassium and ammonium carbonate. The results for these gels, given in Appendix K, show very similar trends to those exhibited by the equivalent sodium gels, with the ratio of the metal carbonate dictating the textural properties of the gel.

It can also be seen that the similarities between sodium and potassium gels still exist when made in conjunction with ammonium carbonate. For a given R/C, the mixed carbonate gels have very similar pore sizes and pore volumes, when comparing between sodium and potassium.

7.3.1.3 $Cs_2CO_3/(NH_4)_2CO_3$ Gels

As caesium carbonate gels exhibit markedly different properties to the rest of the Group I metals, it would be expected that these differences would transfer to the mixed carbonate gels.

Indeed, it can be seen from the nitrogen adsorption isotherms and pore size distributions shown in Figure 77 and 78 that the uptakes have increased, hysteresis has shifted to higher relative pressures and pore size distributions have shifted to larger mean sizes for each of the respective R/C values when comparing to the corresponding sodium and potassium gels.
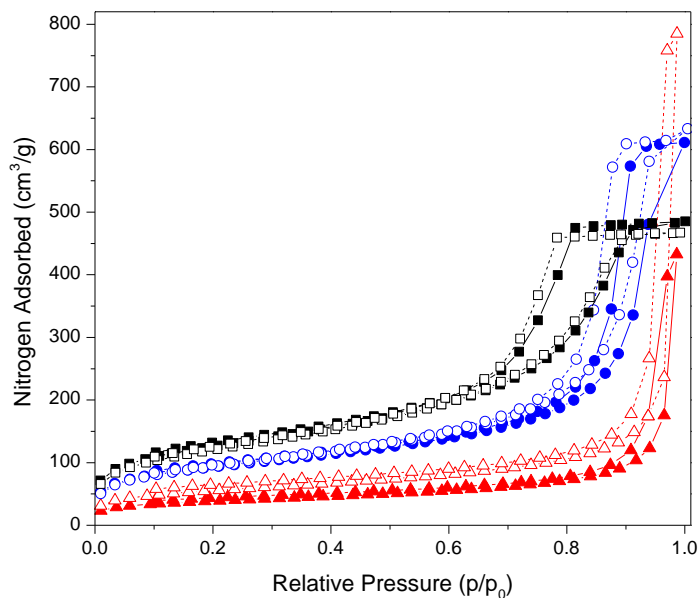
Figure 77: Comparative nitrogen adsorption/desorption isotherms between mixed Cs$_2$CO$_3$/(NH$_4$)$_2$CO$_3$ at R/C 50 (■), 100 (●) and 200 (▲), and pure Cs$_2$CO$_3$ gels at R/C 100 (□), 200 (○), and 400 (△).
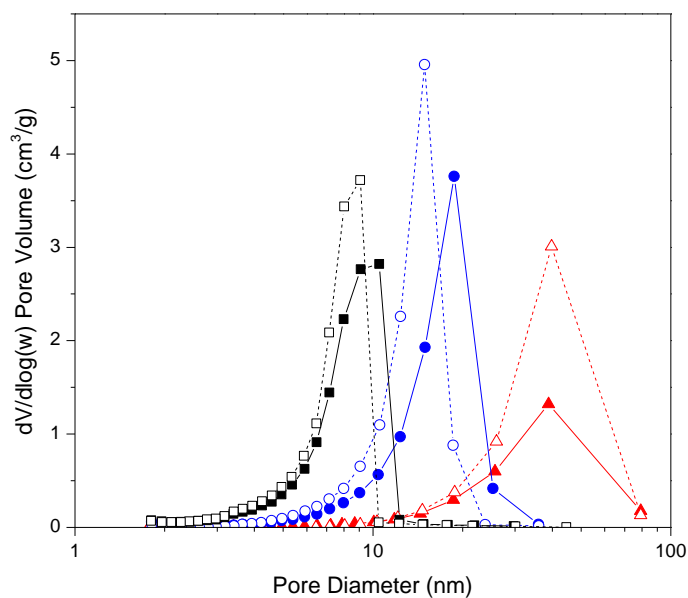
Figure 78: Comparative pore size distributions between mixed Cs$_2$CO$_3$/(NH$_4$)$_2$CO$_3$ gels at R/C 50 (■), 100 (●) and 200 (▲), and pure Cs$_2$CO$_3$ gels at R/C 100 (□), 200 (○), and 400 (△).

However, it is also evident from examination of this data, that the caesium gels follow the same trends as the sodium and potassium gels. For each metal concentration, the isotherms and pore size are very similar in terms of positioning and shape.

The properties displayed in Table 23, reinforce these findings, with almost identical figures for metal concentrations of R/C 100 and 200, respectively. Only the metal concentration of R/C 400 shows a significant reduction in the pore volume, and a corresponding decrease in the surface area.

Table 23: Comparison of gel textural properties for pure Cs_2CO_3 gels and mixed $Cs_2CO_3/(NH_4)_2CO_3$ gels.

Sample	S_{BET} (m^2/g)	V_{Tot} (cm^3/g)	V_μ (cm^3/g)	d_p avg. (nm)
$Cs_2CO_3/$ $(NH_4)_2CO_3\_50$	439 ± 4	0.75	0.03	7.5
$Cs_2CO_3/$ $(NH_4)_2CO_3\_100$	322 ± 3	0.95	0.03	14.3
$Cs_2CO_3/$ $(NH_4)_2CO_3\_200$	133 ± 2	0.67	0.02	28.1
$Cs_2CO_3\_100$	425 ± 3	0.72	0.02	6.9
$Cs_2CO_3\_200$	329 ± 3	0.98	0.02	12.6
$Cs_2CO_3\_400$	206 ± 2	1.15	0.02	28.0

7.3.1.4   Colloidal Stability

With the decomposition of ammonium carbonate, as explained above, the results obtained are not unexpected. As ammonium carbonate decomposes, it will leave the metal carbonate as the only catalyst present, with its corresponding R/C ratio. In all cases, this results in gels which are very similar to their pure metal counterparts. Primary clusters will grow, as before, reaching larger sizes for lower carbonate concentrations. Unfortunately, the mixed carbonate gels became turbid immediately upon placement in the oven, presumably due to the decomposition of the ammonium carbonate, preventing the use of DLS in monitoring cluster growth.

The ability of the sodium and potassium cations to interact with oligomeric RF chains means that at all concentrations they are able to maintain the hydration layer, resulting in gels similar to the pure metal counterparts. The coalescence induced by

the caesium is evidenced by the larger cluster sizes seen. From the Hofmeister series given in Figure 39, it is seen that the tetramethylammonium cation (Me_4N^+) should display favourable effects, that is increase the hydration layer and result in small clusters. However, it may be that it displays a similar effect to caesium, inducing coalescence into larger than expected clusters. Protonation of the hexamine would result in a similar amine based cation, and at the concentration imparted by an overall R/C of 200, may work in conjunction with the caesium cation to produce such large clusters that the observable porosity has been severely reduced.

7.3.2 Group II Metal Carbonate/Ammonium Carbonate Gels

As the gels produced using Group II metal carbonates are very alike for a given R/C, it was decided to study calcium carbonate in conjunction with ammonium carbonate as an example.

Visual inspection of the gels gave the first indication of the differences encountered when using a Group II catalyst in conjunction with ammonium carbonate, as opposed to any of the Group I carbonates, as seen in Figure 79.

Figure 79: Visual comparison of mixed $CaCO_3$/$(NH_4)_2CO_3$ gels with, from left to right, R/C 50, 100 and 200.

Whilst appearing monolithic at first glance, on closer inspection the dried samples actually have little mechanical strength and crumble readily. The orange colour is also more akin to that observed for the catalyst free or ammonium carbonate samples, rather than the dark red-brown expected from pure calcium carbonate gels.

As such, when compared to the pure calcium carbonate data, the nitrogen adsorption/desorption isotherms for the mixed systems, seen in Figure 80, show very little correlation between gels of equivalent R/C or equivalent concentration.
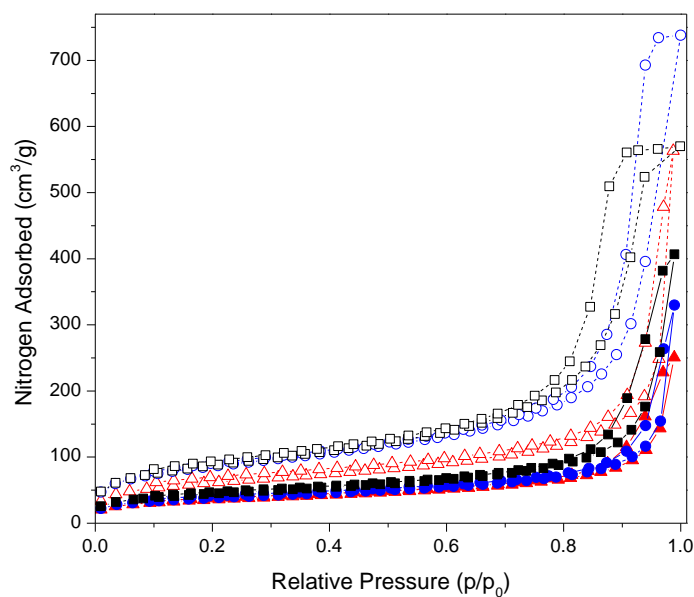
This is reflected in the pore size distributions (Figure 81), which all show a significant change in both pore size and pore volume.
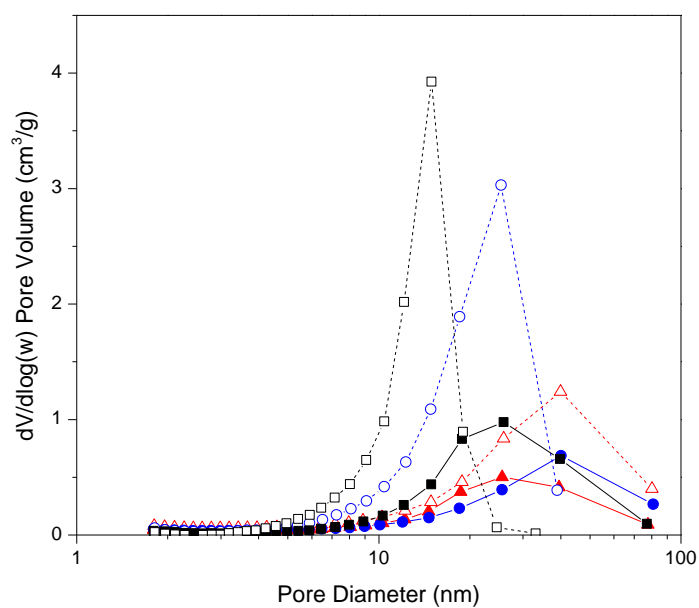
This is confirmed by the textural properties seen in Table 24.

Table 24: Comparison of gel textural properties for pure $CaCO_3$ gels and mixed $CaCO_3/(NH_4)_2CO_3$ gels.

Sample	S_{BET} (m^2/g)	V_{Tot} (cm^3/g)	V_μ (cm^3/g)	d_p avg. (nm)
$CaCO_3/$ $(NH_4)_2CO_3\_50$	154 ± 2	0.63	0.01	20.8
$CaCO_3/$ $(NH_4)_2CO_3\_100$	134 ± 1	0.51	0.01	21.8
$CaCO_3/$ $(NH_4)_2CO_3\_200$	127 ± 1	0.39	0.01	17.2
$CaCO_3\_100$	307 ± 3	0.88	0.02	12.4
$CaCO_3\_200$	301 ± 3	1.14	0.02	17.6
$CaCO_3\_400$	213 ± 2	0.87	0.02	21.5

The textural properties show no similarities between any of the equivalent groupings.

However, as shown in Chapter 6, the Group II metal cations have high charge densities, resulting in disruption of the hydration layer and larger cluster sizes. Under these circumstances, the produced hexamine and calcium cations may have a combined effect on the RF oligomers, which consequently salt out of solution giving very large clusters and an unstable gel network structure. On drying, this leads to reduced detectable porosity, and a very weak product, as evidenced by the lack of mechanical strength in the samples.

7.4 Summary of Findings

Samples catalysed using ammonium carbonate or a mixture of metal carbonate and ammonium carbonate, were synthesised and analysed using DLS and surface area and porosity measurements.

In summary, it was found that:

- With ammonium carbonate as the sole catalyst
    - A sample very similar to that obtained when no catalyst is present, having no porosity detectable with the equipment used, was produced.
    - Ammonium carbonate decomposes, with the ammonia produced reacting with some of the formaldehyde to produce hexamine, a secondary base.

- o The residual presence of a base speeds up the reaction between R and F compared to using no catalyst.
  - o No metal cation to interact with few growing RF oligomers results in clusters salting out and subsequent sedimentation of large particles, hence, samples with very low surface areas and no detectable porosity in the mesopore range.
- When using a mixture of metal carbonate and ammonium carbonate as catalyst
  - o Equal molar ratios of a Group I metal carbonate and ammonium carbonate results in gels with similar properties to gels with the equivalent metal concentration.
  - o Trends observed with the Group I metal carbonates are maintained for the mixed carbonate gels, according to their stabilisation ability.
  - o Sodium and potassium carbonate give very similar gels, which are much different to gels using caesium carbonate.
  - o Equal molar ratios of a Group II metal carbonate and ammonium carbonate results in gels with completely dissimilar properties to gels made with just a Group II metal carbonate.
  - o The Group II metal cation may act in conjunction to give very large clusters, resulting in a gel with only partially detectable porosity.

Due to decomposition, ammonium carbonate cannot be used to differentiate between the roles of the metal cation and carbonate anion in the gelation process. However, its use does reinforce the differences in the interaction process of the various cations used.

8 Results Part 4 - Gels Synthesised with a Secondary Addition of Metal Carbonate Catalyst

In this body of work, different metal carbonate catalysts have been shown to impart different properties into the final gel structure (see Chapters 5 and 6). It was, therefore, decided to investigate whether the use of two metal carbonates in the synthesis of a single sample would have the effect of producing a gel with properties associated with both catalysts. A 50:50 split of the two catalysts was initially chosen, in order to allow for equal contribution, by each catalyst, to the gelation process. The total R/C was kept constant at 100 throughout, giving individual R/C values of 200 for each of the respective carbonates.

As well as simultaneous addition of two carbonates, it was decided to investigate the impact of delaying the addition of a secondary carbonate, and whether this would increase the contribution from a chosen parent carbonate. DLS, and surface area and porosity measurements, were used to study these effects.

8.1 Parent Metal Carbonates and Secondary Metal Carbonates

Previous work in this study has shown that the various metal carbonates can be grouped in terms of the textural properties they impart to a gel. As such, lithium, sodium and potassium form one group, while caesium, calcium and barium can also be grouped, as they produce much larger pores for an equivalent R/C. It was, therefore, decided to use these groupings in the formation of gels containing a secondary metal carbonate.

The group containing caesium, calcium and barium became the parent metal carbonates, added to the sol mixture first. This was primarily due to the limited solubility of the Group II catalysts, and the difficulty that would be encountered in trying to introduce these at a desired concentration at delayed times. The lithium, sodium and potassium grouping, therefore, became the secondary metal carbonates, added to the gelling sol at the appropriate time point. Table 25 shows the various combinations of parent and secondary carbonates used.

Table 25: Combinations used in the study of secondary addition of metal carbonates.

Parent Carbonate	Secondary Carbonate
Caesium	Sodium
Calcium	Sodium
Barium	Sodium
Calcium	Lithium
Calcium	Potassium

8.2 Gelation Time Monitoring

As it was unknown what effect the addition of a secondary metal carbonate would have on the gelation time of the various samples, these times had to be monitored to allow for analysis to be conducted. This was performed for simultaneous addition of each of the carbonate combinations given in Table 26.

Table 26: Gelation times for RF gels catalysed by simultaneous addition of two metal carbonates.

Carbonate Combination	Gelation Time (min)
Caesium/Sodium	35
Calcium/Sodium	40
Barium/Sodium	40
Calcium/Lithium	40
Calcium/Potassium	40

As can be seen from Table 26, the gelation times are equal to those of the parent carbonate systems at R/C 100, as shown in previous chapters. It was therefore possible to use the same DLS intervals as those of the R/C 100 parent systems, corresponding to 10% of the total gelation time, i.e. 3.5 min for caesium carbonate, and 4 min for both calcium and barium carbonate.

In the case of delayed addition of the secondary carbonate, it was decided to use the gelation and interval times determined for the parent carbonate at R/C 200, corresponding to the initial composition of the sol. This meant that analysis of samples prior to addition could be directly compared with the single metal carbonate system. These intervals were maintained after addition of the secondary carbonate; therefore, gelation did not occur at '100%'.

8.3   Dynamic Light Scattering Studies

DLS studies were first performed on each of the simultaneous addition samples. The autocorrelation functions obtained for combinations using sodium carbonate as the secondary catalyst are shown below in Figure 82, 83 and 84. All data pertaining to the combinations of calcium and lithium, and calcium and potassium carbonate are displayed in Appendix L; however, they are also included in the discussion here.
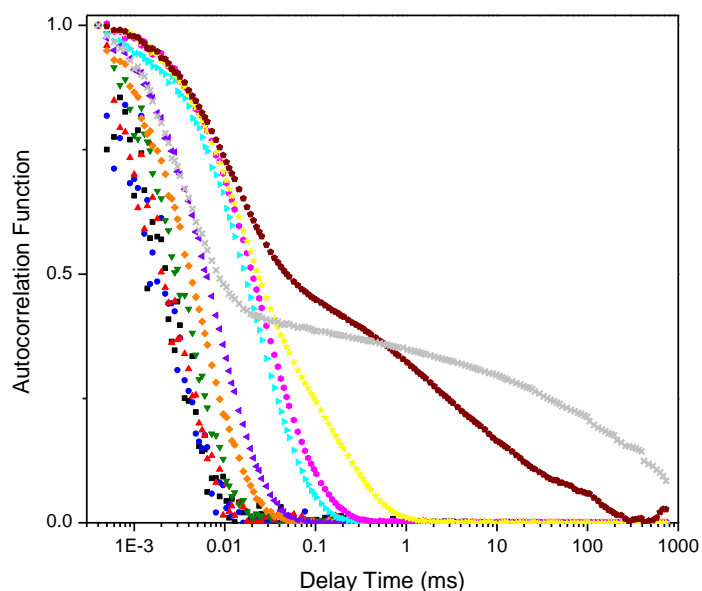
Figure 82: DLS autocorrelation functions obtained for simultaneous addition of caesium and sodium carbonate at 0% (■), 10% (●), 20% (▲), 30% (▼), 40% (◆), 50% (◀), 60% (▶), 70% (●), 80% (★), 90% (⬟) and 100% (✕) of the total gel time.
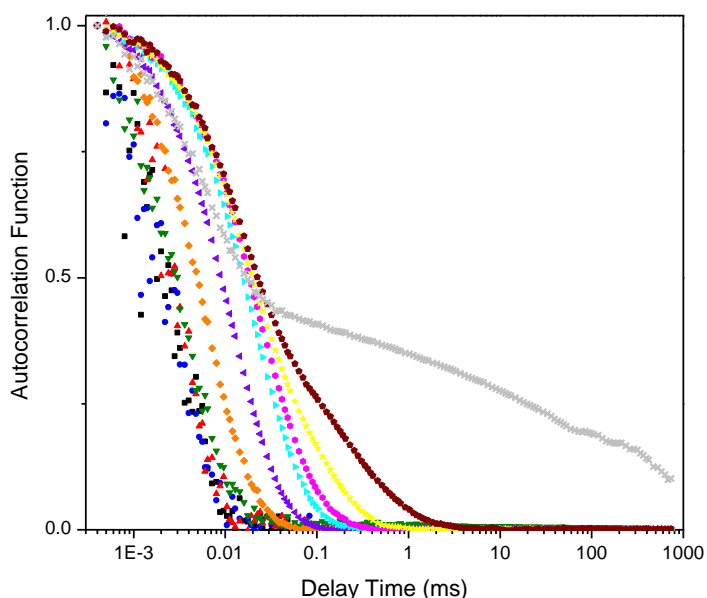
Figure 83: DLS autocorrelation functions obtained for simultaneous addition of calcium and sodium carbonate at 0% (■), 10% (●), 20% (▲), 30% (▼), 40% (◆), 50% (◀), 60% (▶), 70% (●), 80% (★), 90% (⬟) and 100% (✕) of the total gel time.
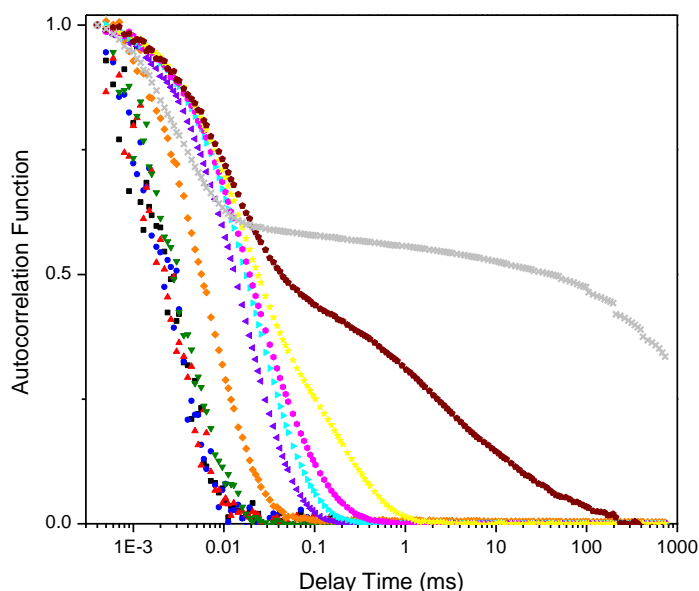
It can be seen that in all cases of simultaneous addition, the profiles of the autocorrelation functions follow the trends established by those of the Group I metal carbonates. At early times, the profiles follow an exponential decay. At later times, near gelation, a secondary decay is introduced, and, at gelation, the profile becomes non-ergodic. The aggregation and networking process is, therefore, indicated by the secondary decay. The delay before the onset of decay is also more consistent with that of the Group I carbonates, suggesting that they influence gel formation.

Delayed addition of the secondary carbonate started at 60% of the gel time of the parent carbonate gel. This was to allow time for the parent carbonate to exert its influence, and ensure that cluster growth had begun. Unfortunately, this limited the number of DLS runs available, due to the formation of the secondary decay in the case of caesium carbonate, and turbidity in the samples prepared with a Group II carbonate. In both cases, this was apparent at 70% of the parent gel time. As an example of this delayed addition, the autocorrelation functions obtained when adding sodium carbonate to calcium carbonate at 60% of the gel time are given in Figure 85. The remaining data sets are given in Appendix L.
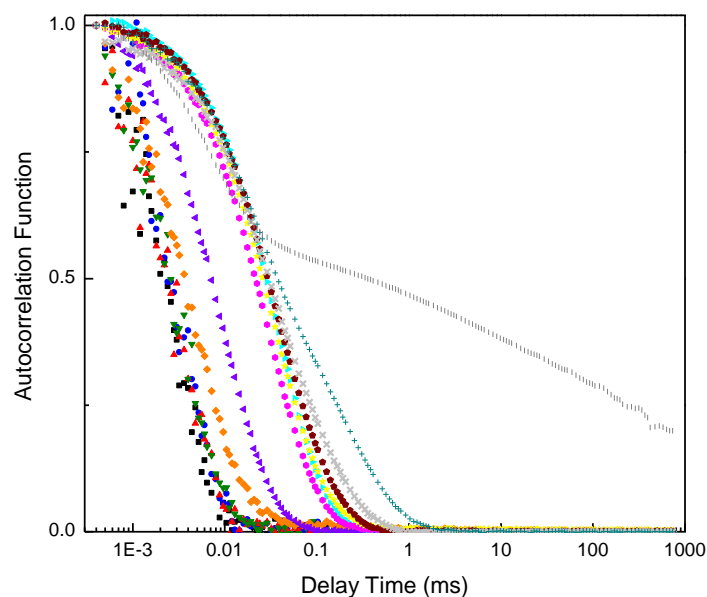
These profiles show that secondary addition at 60% of the parent gel time also results in secondary decay and non-ergodicity. This again suggests that the Group I metal carbonate added strongly influences the gelation process.

Cumulant analysis was performed on each data set that exhibited a purely exponential decay, corresponding to freely diffusing clusters. The results of this analysis, in the form of hydrodynamic radii, are shown below in Figure 86 through 88. Data previously obtained for the corresponding single metal carbonate systems (see Chapters 5 and 6) are included in each plot for reference.
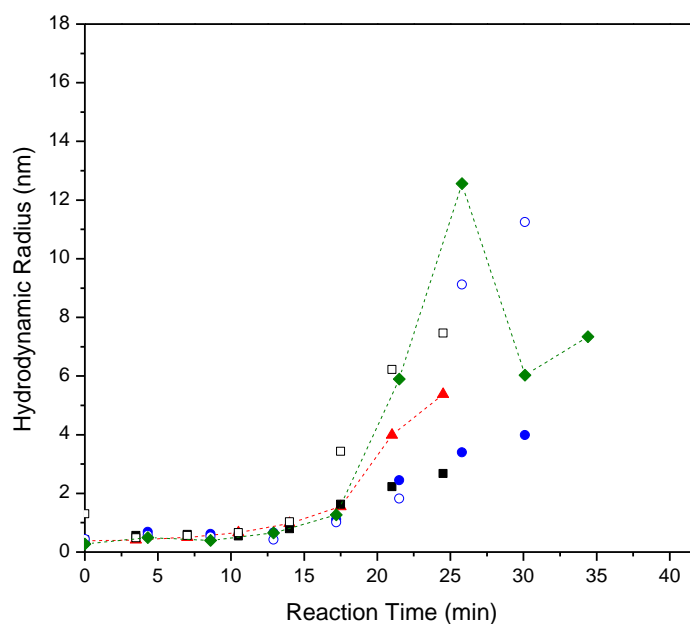
Figure 86: DLS hydrodynamic radii values obtained for sodium carbonate at R/C 100 (■) and 200 (●), caesium carbonate at R/C 100 (□), and 200 (○), simultaneous addition of both carbonates (▲) and 60% delayed addition of sodium carbonate (◆).

Simultaneous addition of caesium and sodium carbonate results in hydrodynamic radii between the data sets of pure caesium carbonate and pure sodium carbonate. It would appear that both metals promote cluster growth, as would be expected from having different cations present, with the resulting average radius lying approximately halfway between those of the individual metal carbonates. This suggests that the presence of the sodium is limiting the coalescence induced by the presence of the caesium.

Addition of sodium carbonate at 60% of the parent gel time results in an apparently significant disruption to the growth profile compared to that of caesium carbonate at R/C 200. Growth is no longer linear with time, as the average size has decreased significantly post addition, when compared to the pure caesium sample. It is, therefore, obvious that the addition of the sodium carbonate has altered the clusters present in some way. It is possible that the secondary cation, known from Chapter 5 to produce smaller clusters, has reversed the coalescence of the clusters, breaking them down into smaller units. It must also be considered that the introduction of further carbonate into the system may initiate the growth of new clusters from any previously unreacted material. The average cluster size increases again after the initial decrease, indicating a further growth of the clusters. As the size increase is not rapid, it is likely controlled by the sodium cation, rather than the coalescence

induced by the caesium cation already present. This increased number of clusters post addition is supported by the final pre-aggregation cluster size, which is much smaller than that observed for the pure caesium carbonate R/C 200 system. If the critical volume fraction is reached at smaller sizes, there must be more clusters present to make up this volume.
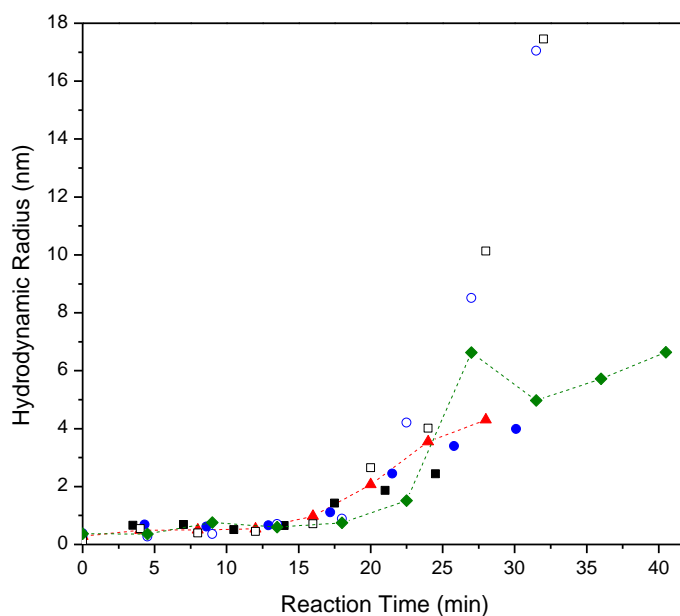
Figure 87: DLS hydrodynamic radii values obtained for sodium carbonate at R/C 100 (■) and 200 (●), calcium carbonate at R/C 100 (□), and 200 (○), simultaneous addition of both carbonates (▲) and 60% delayed addition of sodium carbonate (◆).
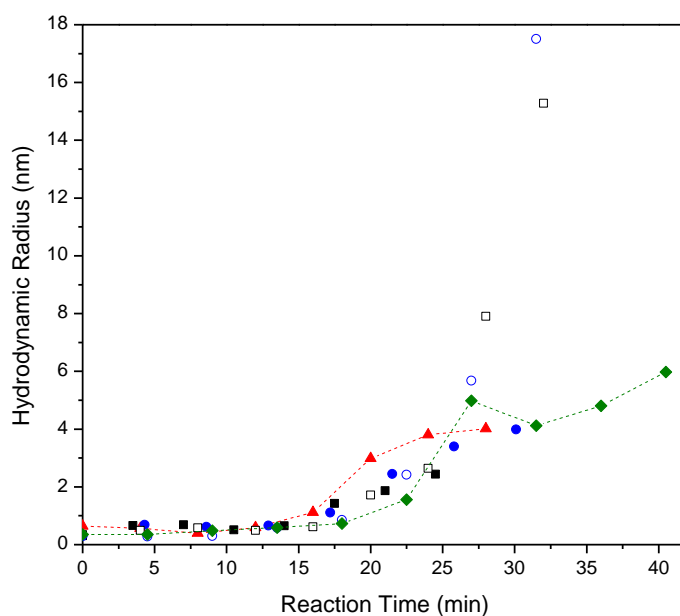
Figure 88: DLS hydrodynamic radii values obtained for sodium carbonate at R/C 100 (■) and 200 (●), barium carbonate at R/C 100 (□), and 200 (○), simultaneous addition of both carbonates (▲) and 60% delayed addition of sodium carbonate (◆).

All combinations of adding a Group I metal carbonate to an established Group II catalysed system (calcium/lithium, calcium/sodium, calcium/potassium and barium/sodium) exhibit very similar results. Simultaneous addition results in cluster sizes that closely follow those exhibited by the secondary carbonate at R/C 200, corresponding to the concentration present in the mixed carbonate gel. This implies that the secondary carbonate, be it lithium, sodium or potassium, is dominant in the gel formation process and the parent Group II carbonate plays little role.

The delayed addition results are very similar to those of the caesium/sodium system, in that the cluster size reduces immediately after addition, followed by a period of growth. However, the reduction in size is not as severe as that experienced by the caesium clusters. The modification of the clusters on addition of a secondary cation would, therefore, appear to be different. Taking the calcium/sodium system as a specific example; from Chapter 6, the high charge density on the calcium cation resulted in potential hydrophobic interactions between RF chains, leaving them loosely packed into clusters. On the other hand, the reduced charge density on the sodium cation gave small, compact clusters. Therefore, on addition of the addition of sodium carbonate to the calcium carbonate system, it would appear that the calcium controlled clusters are shrinking and becoming more compact, as a result of the sodium cations now present. Once more, there is also the possibility of the newly added carbonate initiating further cluster growth. After addition, there is no rapid increase in cluster size. This suggests that after addition, all clusters are growing under the control of the newly added sodium cations.

Examination of the corresponding average scattered light intensities reinforces these theories on the changes induced in the species. The scattered intensities are shown in Figure 89, 90 and 91.
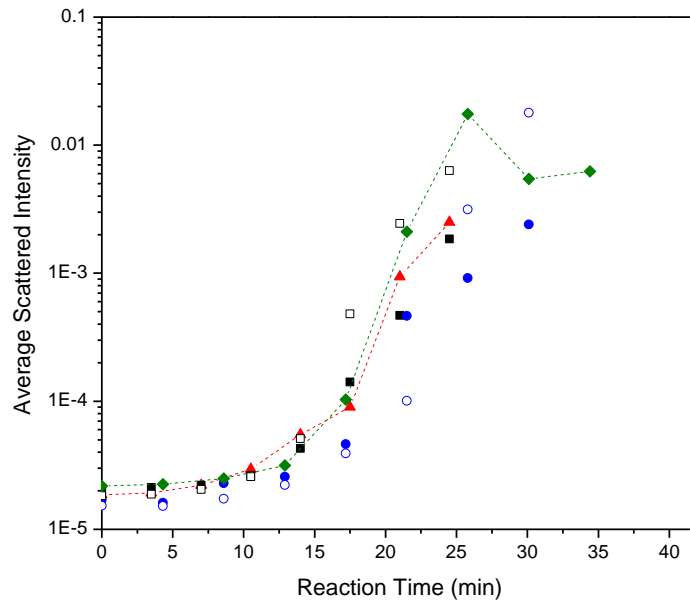
Figure 89: Average DLS scattered intensity for sodium carbonate at R/C 100 (■) and 200 (●), caesium carbonate at R/C 100 (□), and 200 (○), simultaneous addition of both carbonates (▲) and 60% delayed addition of sodium carbonate (◆).

In the case of the caesium and sodium system, the delayed secondary addition sample shows a decrease in the scattered intensity post addition, followed by a slight increase. As the reduction in intensity is not as severe as the reduction in size, this supports the theory that while the cluster size decreases, there is an increase in the number of clusters.
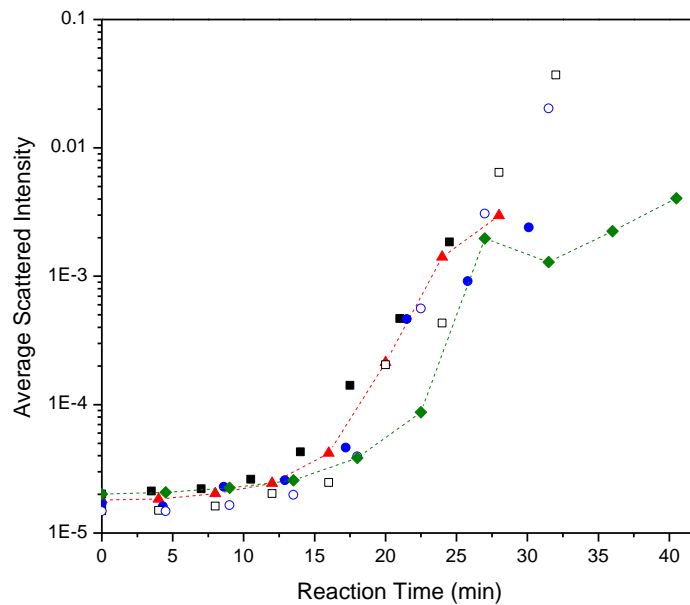
Figure 90: Average DLS scattered intensity for sodium carbonate at R/C 100 (■) and 200 (●), calcium carbonate at R/C 100 (□), and 200 (○), simultaneous addition of both carbonates (▲) and 60% delayed addition of sodium carbonate (◆).

151
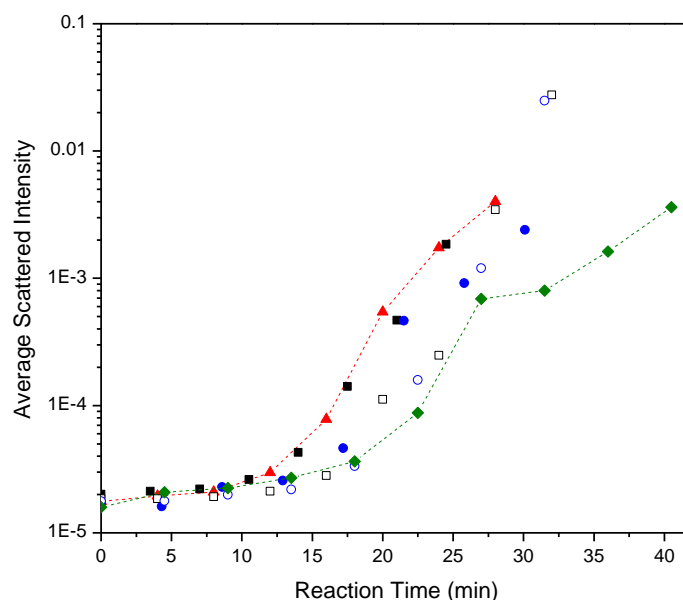
The scattered intensities for all of the Group II/Group I systems are again similar to each other. All show that the intensity again clearly deviates away from that of the pure Group II system, when the secondary carbonate is added. Smaller, more compact species will scatter less, suggesting a decrease in cluster size. The reduction in intensity is again small, potentially as the result of extra clusters being formed. The final scattered intensity exceeds that observed at the time of addition. As the average sizes at addition and the final observable point are very similar, this implies an increase in the number of clusters present.

8.4 Xerogel Characterisation

Each of the xerogels described above underwent surface area and porosity measurements in order to determine their textural properties. Furthermore, delayed addition at 70 and 80% was also performed, and these samples were also analysed. The nitrogen adsorption/desorption isotherms obtained are given in Figure 92, 93 and 94.
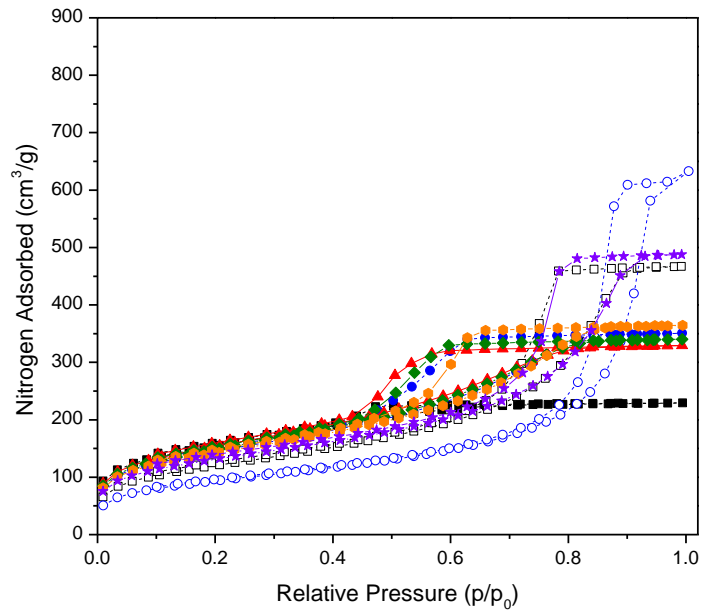
Figure 92: Nitrogen adsorption/desorption isotherms for sodium carbonate at R/C 100 (■) and 200 (●), caesium carbonate at R/C 100 (□) and 200 (○), simultaneous addition of both carbonates (▲) and delayed addition of sodium carbonate at 60% (◆), 70% (●) and 80% (★).
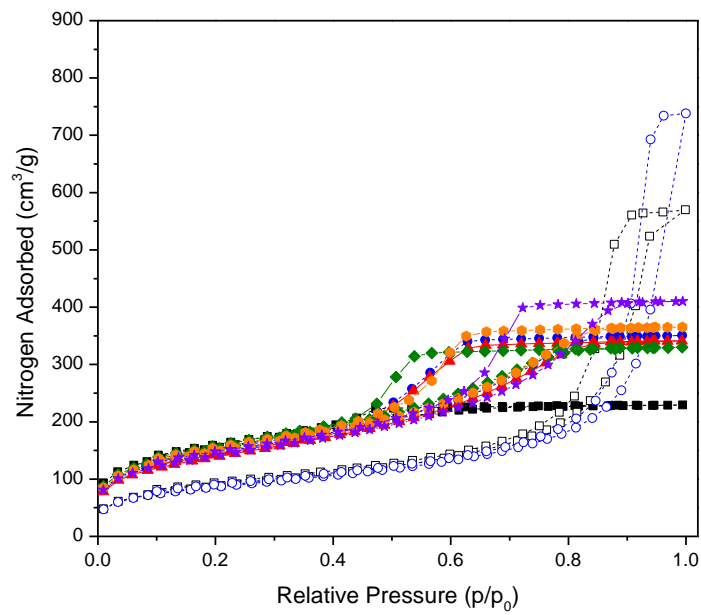
Figure 93: Nitrogen adsorption/desorption isotherms for sodium carbonate at R/C 100 (■) and 200 (●), calcium carbonate at R/C 100 (□) and 200 (○), simultaneous addition of both carbonates (▲) and delayed addition of sodium carbonate at 60% (◆), 70% (●) and 80% (★).
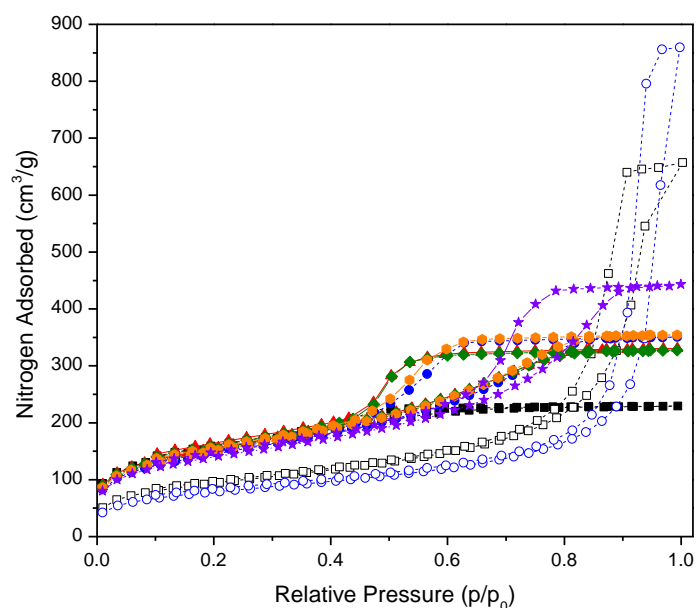
Figure 94: Nitrogen adsorption/desorption isotherms for sodium carbonate at R/C 100 (■) and 200 (●), barium carbonate at R/C 100 (□) and 200 (○), simultaneous addition of both carbonates (▲) and delayed addition of sodium carbonate at 60% (◆), 70% (●) and 80% (★).

All of the gel series show very similar results, with the R/C 200 secondary carbonate gel generally hidden behind those of simultaneous addition and delayed addition at 60 and 70%. Only at 80% is there a difference, showing an increase in uptake and shifting of the hysteresis loop to higher relative pressures. However, even at 80% of the parent gel time, where networking and aggregation are well established, the differences between the nitrogen adsorption/desorption isotherm obtained and those of the parent gel are still significant, indicating that this process can be disrupted. The pore size distributions derived from these nitrogen adsorption isotherms are shown in Figure 95, 96 and 97.
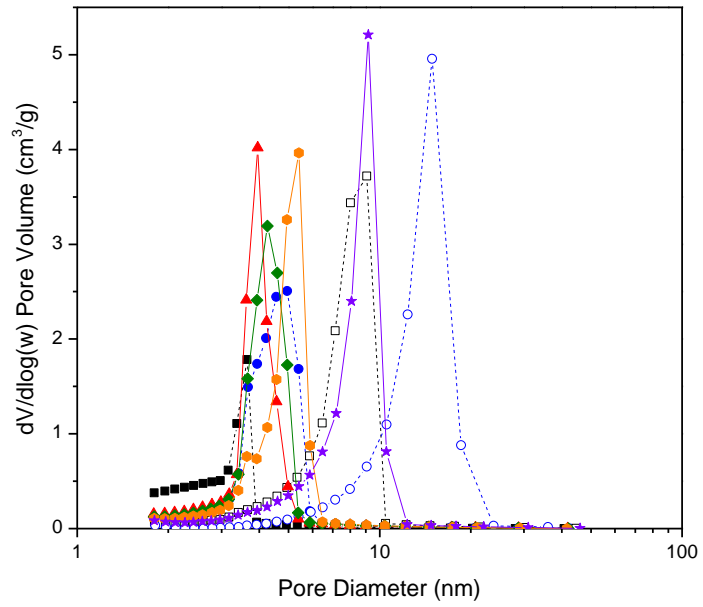
Figure 95: Pore size distributions for sodium carbonate at R/C 100 (■) and 200 (●), caesium carbonate at R/C 100 (□) and 200 (○), simultaneous addition of both carbonates (▲) and delayed addition of sodium carbonate at 60% (◆), 70% (●) and 80% (★).
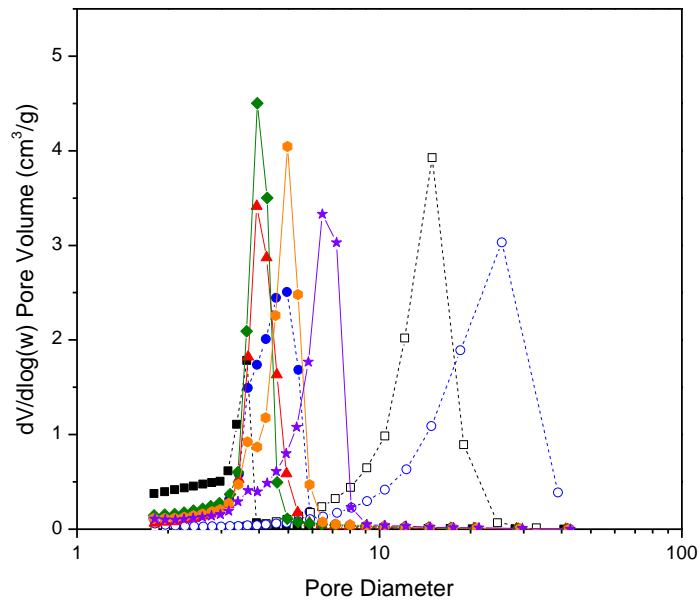
Figure 96: Pore size distributions for sodium carbonate at R/C 100 (■) and 200 (●), calcium carbonate at R/C 100 (□) and 200 (○), simultaneous addition of both carbonates (▲) and delayed addition of sodium carbonate at 60% (◆), 70% (●) and 80% (★).
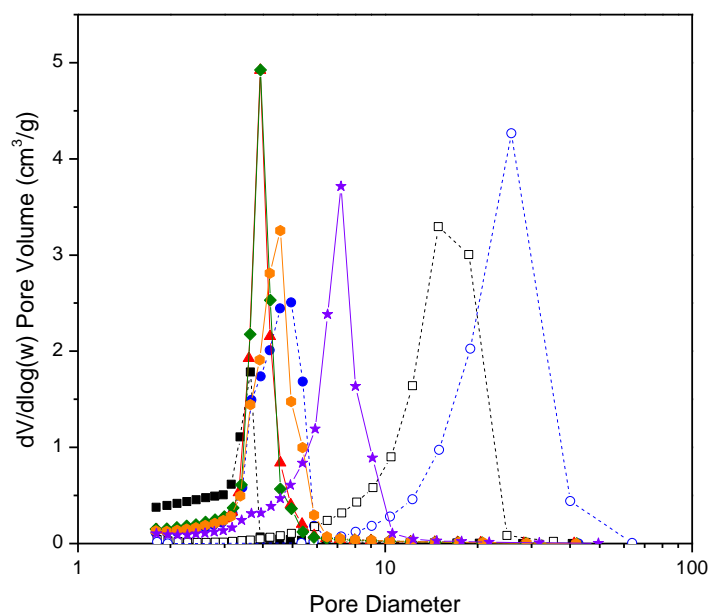
Figure 97: Pore size distributions for sodium carbonate at R/C 100 (■) and 200 (●), barium carbonate at R/C 100 (□) and 200 (○), simultaneous addition of both carbonates (▲) and delayed addition of sodium carbonate at 60% (◆), 70% (●) and 80% (★).

As would be expected from the adsorption isotherms, the majority of samples containing a secondary catalyst have pore sizes grouped around those of the secondary metal carbonate. It is again only addition at 80% of the parent gel time that shows an increase in pore size, although these sizes are still much smaller than those of the single catalyst parent gels, made with caesium, calcium or barium carbonate. It can also be seen that the distributions for the gels containing a secondary catalyst are much narrower than those of the gels synthesised with a single metal carbonate, suggesting a more regular structure and more consistent pores. Additional textural properties of the secondary addition gels are given in Table 27. The comparative data for the single catalyst gels are given in Table 11 for Group I carbonates, and Table 18 for Group II carbonates, respectively.

Addition Time	S_{BET} (m^2/g)	V_{Tot} (cm^3/g)	V_μ (cm^3/g)	d_p avg (nm)
Cs_2CO_3/Na_2CO_3				
Simultaneous	537 ± 4	0.51	0.04	3.8
60%	520 ± 4	0.53	0.03	4.0
70%	498 ± 4	0.56	0.03	4.6
80%	457 ± 4	0.75	0.03	7.3
$CaCO_3/Na_2CO_3$				
Simultaneous	535 ± 4	0.56	0.03	4.2
60%	533 ± 4	0.51	0.03	3.8
70%	526 ± 5	0.63	0.04	5.0
80%	490 ± 4	0.64	0.04	5.5
$BaCO_3/Na_2CO_3$				
Simultaneous	548 ± 5	0.54	0.04	4.0
60%	535 ± 4	0.51	0.04	3.8
70%	528 ± 4	0.55	0.03	4.1
80%	486 ± 4	0.69	0.04	6.1
$CaCO_3/Li_2CO_3$				
Simultaneous	534 ± 4	0.52	0.04	3.9
60%	532 ± 5	0.57	0.04	4.3
70%	540 ± 5	0.57	0.04	4.3
80%	458 ± 4	0.72	0.03	6.8
$CaCO_3/K_2CO_3$				
Simultaneous	385 ± 2	0.45	0.01	4.4
60%	415 ± 2	0.48	0.01	4.3
70%	511 ± 4	0.63	0.03	5.0
80%	457 ± 4	0.68	0.03	6.4

The data in Table 27 shows how the average pore sizes change, with the corresponding changes in surface area. It can also be seen that, despite the narrowing of the distributions, total pore volumes remain consistent with those of the R/C 200 secondary carbonate gels. This again suggests that the porous structure is more regular. It is of interest that while the textural properties of the simultaneous addition gels have textural properties corresponding to those of the secondary carbonate, their gelation times are in line with those of the parent carbonate

systems, as shown in Table 26. It would be expected from these times that the corresponding structure would be similar.

8.5 Further Interpretation of the Results

The previously detailed DLS and textural results for these secondary addition gels have indicated the modified growth of cluster species on addition of the secondary catalyst along with the potential growth of new clusters as a result of additional carbonate being present. This process can again be depicted schematically, as shown in Figure 98, where clusters are once more represented as spherical for clarity.
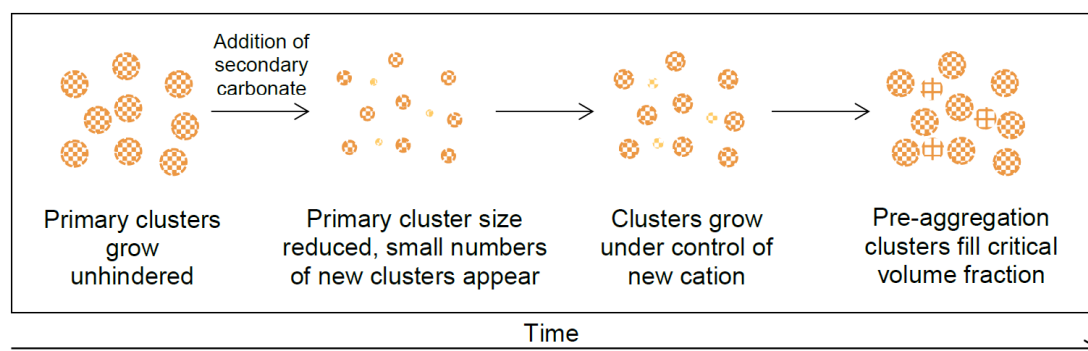
Figure 98: Schematic diagram outlining primary and secondary cluster formation and growth during RF gel synthesis with two different metal carbonates. Clusters are depicted as spheres for clarity.

The modification of the growth of clusters can be thought of in terms of the abilities of the various metal cations to interact with the RF oligomeric chains, and the concentration of catalyst in the system before and after addition of the secondary carbonate.

In the initial stages of the reaction, carbonate will promote the formation of clusters, with the number concentration determined by the R/C, as previously discussed. These clusters will then grow by consuming the unreacted R, F and hydroxymethyl derivatives, with sizes dictated by the influence of the metal cation.

Simultaneous addition of the secondary carbonate will increase the number concentration of clusters, whilst also introducing a competing cation. In the case of caesium and sodium, both cations have a 1^+ charge, but the different cation sizes result in different charge densities. The higher charge density of the sodium cation should lead to larger clusters, but coalescence of the smaller caesium cation leads to much larger sizes. As a result, on addition of both cations their influence is effectively averaged, giving clusters sizes intermediate to the two individual species.

By comparison, the Group II cations have even higher charge densities than the sodium cation, thanks to the 2^+ charge present. When mixed with sodium, this charge density will effectively be diluted resulting in clusters that are much smaller than would be expected from the Group II system.

In contrast, delayed addition of the secondary carbonate will encounter clusters which are already established. The newly added secondary cation, therefore, influences these already grown clusters, rather than dictating their growth from scratch. In the case of already established caesium clusters, the increase in charge density associated with addition of sodium cations appears to disrupt the coalescence process, breaking down the joined clusters into smaller units. Growth then continues without further coalescence as would be expected from a sodium system.

With Group II systems, the clusters produced have hydrophobic interactions, due to the high charge density cations stripping the hydration layer from the RF oligomers. This results in loosely packed clusters of large sizes. On the addition of the secondary sodium cation, the hydration layer is partially restored and the RF chains will pack more tightly, shrinking the size of the clusters. As growth continues, the hydration layer is maintained, and the clusters remain smaller than would be expected from a Group II system.

In both cases, it is also possible that the delayed addition of further carbonate may initiate the growth of a small number of secondary clusters that grow in conjunction with the previously established system. In order to be definitive about this change in the growth of cluster species, it would be necessary to produce further computer modelling of the systems. This would allow for separation of the sizes of the cluster species from the average hydrodynamic radii values produced by the DLS measurements. However, these models are once more outwith the scope of this investigation.

The timing of the delayed addition will dictate the size of the established clusters as well as any unreacted material capable of capable of continuing cluster growth. As time increases, the ability to alter the system will decrease, and more of the established character will be retained, resulting in larger gaps between the clusters and correspondingly larger pores.

The ability to markedly influence the porosity of a gel after 80% of the gelation time has passed is also significant. While it is known, from the non-ergodic decay of the final autocorrelation functions, that there is some residual movement within the gel structure, even at the point of gelation, it was assumed that the clusters making up the structure were partially bound in some way. However, these delayed addition results show that during the aggregation and networking processes, the clusters are not strongly bound, allowing them to be rearranged or disrupted on addition of the secondary carbonate.

Other bodies of work, such as that of Lambert *et al.*[157] and Laskowski *et al.*[158] have studied the effect of secondary addition of catalyst during the gelation period. However, this secondary catalyst was an acid and, therefore, the results are not comparable with those obtained here. Of more interest, for comparison to this set of results, is the study conducted by Feng *et al.* who also investigated a base-base catalysed route to RF gel formation.[159]

The body of work produced by Feng *et al.* showed that on secondary addition of a basic catalyst, the pore size distribution, as calculated by the Dollimore-Heal (DH)[160] method, narrowed. However, the average pore size and peak pore size both increased. As the BJH and DH methods differ only in small details of mathematics, pore sizes should be comparable, in contrast to the work presented here. It also goes against the well-established observations of increased catalyst concentration resulting in smaller pores. No attempt was made by Feng *et al.* to try and explain these observations.

Based on the little procedural data provided by Feng *et al.*, previous work within the research group attempted to recreate the results.[161] However, this work showed once again that the secondary addition of a metal carbonate results in a decrease in the pore size, and properties similar to a scenario where all the catalyst has been added initially.

8.6   Changing the Ratio of Carbonates

All of the above gels were synthesised with an equal concentration of the two metal carbonates used. To take this investigation further, two samples were made with a combination of calcium carbonate and sodium carbonate in the ratio 25:75, while maintaining the overall R/C of 100. The initial gel, therefore, was R/C 400 in terms of calcium carbonate. The samples prepared had simultaneous addition of the two

catalysts, and 70% delayed addition of the sodium carbonate. The nitrogen adsorption/desorption isotherms and the corresponding pore size distributions for these samples are given in Figure 99 and 100. Also included are the pure metal carbonate data for comparison.
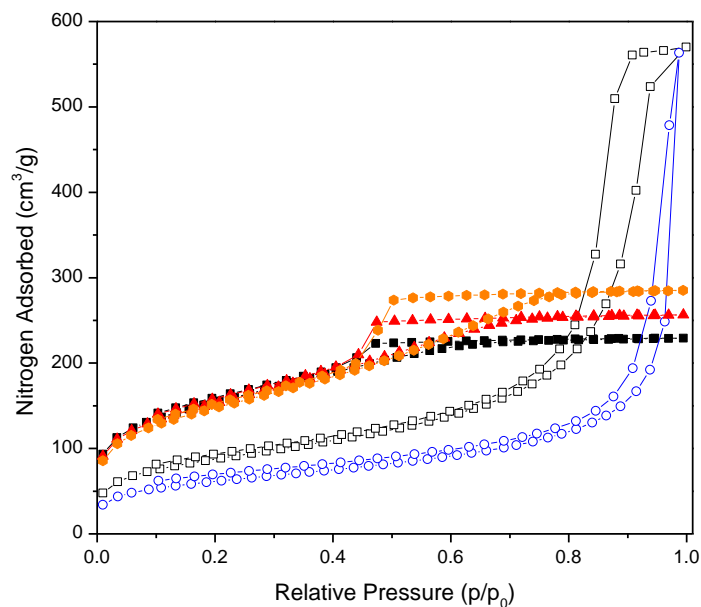
Figure 99: Nitrogen adsorption/desorption isotherms for sodium carbonate at R/C 100 (■), calcium carbonate at R/C 100 (□) and 400 (○), simultaneous addition of both carbonates (▲) and delayed addition of sodium carbonate at 70% (⬢).
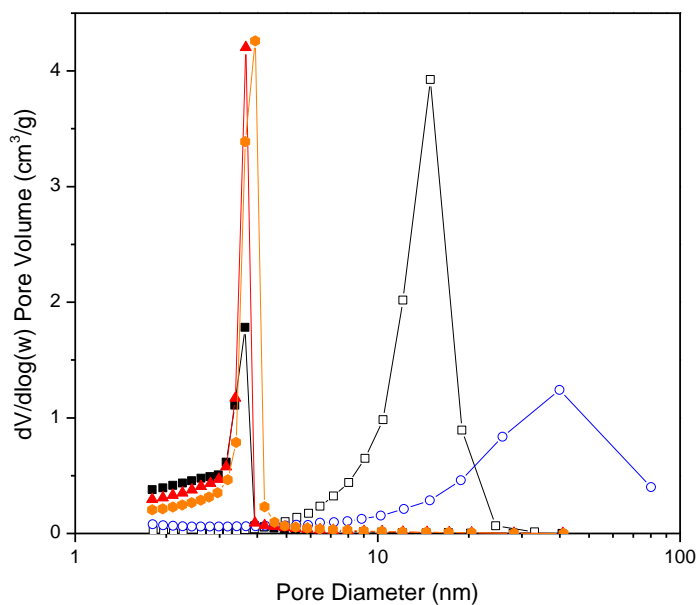
Figure 100: Pore size distributions for sodium carbonate at R/C 100 (■), calcium carbonate at R/C 100 (□) and 400 (○), simultaneous addition of both carbonates (▲) and delayed addition of sodium carbonate at 70% (⬢).

These results show that the new secondary addition gels are both very similar to the sodium carbonate R/C 100 gel, in terms of the isotherm shape, and positioning and width of the pore size distribution. The resultant textural properties of the gels are shown in Table 28.

Table 28: Gel textural properties for samples synthesised with calcium carbonate and sodium carbonate in a ratio of 25:75.

Addition Time	S_{BET} (m^2/g)	V_{Tot} (cm^3/g)	V_μ (cm^3/g)	d_p avg (nm)
Simultaneous	531 ± 5	0.40	0.04	3.1
70%	516 ± 4	0.44	0.03	3.5

When compared with the data on a sodium carbonate gel with R/C 100, it can be seen that the surface area and average pore diameter achieved with simultaneous addition are highly comparable. Of note is the increase in pore volume. The same comparisons can also be made with the 70% delayed addition sample, where only a slight increase in average pore diameter occurs. However, this results in the pore volume increasing further.

In the case of the 25:75 catalyst split, the concentration of calcium has decreased while the concentration of sodium has increased, which has a significant impact on the interaction with RF oligomeric species. With simultaneous addition, the increased sodium concentration further dominates, decreasing the charge density and resulting in a gel almost identical to that of a pure R/C 100 sodium carbonate catalysed gel. With delayed addition at 70% of the parent gel time, the lower initial calcium carbonate concentration leads to the formation of a lower number concentration of large clusters. On addition of the sodium carbonate, these clusters will shrink, and possible break up, as the hydration layer is even further restored than in 50:50 systems. As a result, the post addition clusters, and final pore diameters are very close to the pure sodium gel.

Modifying the ratio of the two catalysts allows for tailoring of the average pore diameter while keeping the ionic strength of the medium constant. It also provides a means of increasing pore volume, while maintaining the small pores associated with high concentrations of the Group I metal carbonates used as secondary catalysts.

8.7 Summary of Findings

Several gels were prepared using a mixture of two catalysts; a parent metal carbonate chosen from caesium, calcium or barium carbonate, and a secondary carbonate chosen from lithium, sodium and potassium carbonate. The time of addition of the secondary catalyst was varied from simultaneously adding with the parent catalyst, to 80% of the gelation time of the parent catalyst sample. These gel samples were analysed using DLS, in conjunction with surface area and porosity measurements to monitor the changes induced by differing catalyst combinations and addition times.

It was found that:

- For equal concentrations of both parent and secondary carbonate, i.e. a 50:50 ratio:
    - A combination of caesium and sodium carbonate gave intermediate cluster sizes with simultaneous addition, and appears to break down the large coalesced caesium clusters into a greater number of smaller clusters on delayed addition
    - All combinations of a Group II carbonate with a Group I carbonate gave cluster sizes congruent with only the Group I carbonate being present with simultaneous addition, and appears to shrink the clusters produced by the Group II system on delayed addition.
    - The clusters continue to grow under the control of the secondary cation.
    - A small number of new clusters may develop on addition of extra carbonate.
    - In almost all cases, the textural properties of the dried gel reflect those of the corresponding Group I carbonate gel prepared with an R/C of 200.
    - Only addition of the secondary carbonate at 80% of the parent gel time results in changing properties, with an increase in pore diameter.
    - At 80%, the established clusters are less able to be disrupted, leading to textural properties closer to the parent system, but still vastly different.
- By decreasing the parent carbonate concentration and increasing the secondary carbonate concentration, i.e. a 25:75 ratio:

- o Textural properties of the gel shifted towards those of the corresponding R/C 100 gel made using pure secondary carbonate.
- o Higher R/C of parent carbonate led to fewer primary clusters, while higher concentration of secondary carbonate led to greater disruption of the established clusters, allowing them to take on more of the characteristics associated with the secondary cation.

Careful choice of the catalyst combination, ratio of catalysts, and addition time can lead to fine tunability of the porous texture of RF xerogels. While maintaining the small average pore sizes associated with high concentrations of lithium, sodium or potassium carbonate, it is possible to narrow the pore size distribution, indicating a more regular structure, whilst also increasing the total pore volume in the system.

9 Results Part 5 – Gels Synthesised with a Secondary Addition of Sol, or Partially Gelled Sol

The results presented in Chapter 8 show the influence of adding a second metal carbonate to a gelling RF sol. To expand on that study, and investigate whether further tuning of the textural properties of gels is possible, additional R and F were added, along with the secondary metal carbonate, at various points in the gelation process. Furthermore, in a separate expansion to the previous work, the secondary sol mixture was allowed to partially gel before adding to the parent sample.

9.1 Gelation Time Monitoring

Throughout this body of work, all gel preparations had a total gel volume of 60 ml, for which the gelation time was correspondingly determined. As the gels in this part of the series were prepared by mixing equal volumes of two separate sols, the volume of each individual sol was, therefore, reduced to 30 ml, in order to maintain the same 60 ml total volume after mixing. As such, a reduction in the gel volume led to a decrease in the gelation time and, as a result, gelation times had to be determined for the new compositions.

The carbonates studied were sodium, caesium, calcium and barium, and, as for the secondary addition of catalyst samples (Chapter 8), these were grouped into several pairings, with caesium, calcium and barium acting as parent carbonates, and sodium as the secondary carbonate. As was also the case for the secondary catalyst addition gels, the final R/C was kept constant at 100, with the corresponding R/C of the half volume sols also being 100 as a result. In the final mixed gel, this corresponded to an R/C of 200 for each respective catalyst. The gelation times for the four half volume samples are displayed in Table 29.

Table 29: Gelation times for R/C 100 samples with total volume of 30 ml.

Carbonate	Gelation Time (min)
Sodium	30
Caesium	30
Calcium	32
Barium	30

It is of note that all of the gel times are approximately equal in this case. For total gel volumes of 60 ml, it was found that, at R/C 100, the Group I carbonates gave a gel time around five minutes shorter than the Group II carbonates.

9.2   Secondary Addition of RF Sol

From secondary addition of carbonate (Chapter 8), it was found that results were very similar when addition occurred up to 70% of the gelation time of the parent gel. Only at 80% was a marked difference in properties observed. It was, therefore, decided to investigate secondary sol addition on either side of this property change, i.e. at 70 and 80% of the parent gel time, as determined in Section 9.1.

Figure 101, 102 and 103 show the nitrogen adsorption/desorption isotherms obtained for each of the carbonate pairings, where, in each case, the delayed sol contains sodium carbonate as the catalyst. The corresponding adsorption isotherms for each of the individual catalysts at R/C ratios of 100 and 200 are included for comparison.
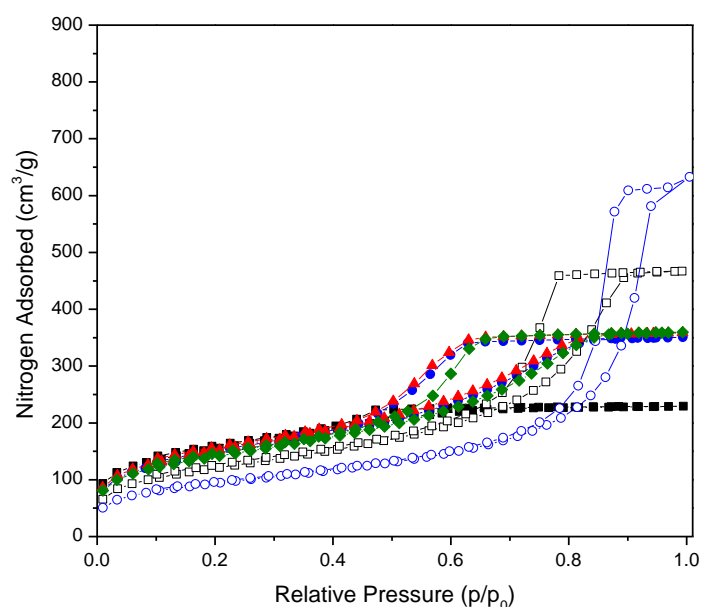
Figure 101: Nitrogen adsorption/desorption isotherms for sodium carbonate at R/C 100 (■) and 200 (●), caesium carbonate at R/C 100 (□) and 200 (○), and delayed addition of sodium carbonate sol at 70% (▲) and 80% (◆) of the parent gel time.
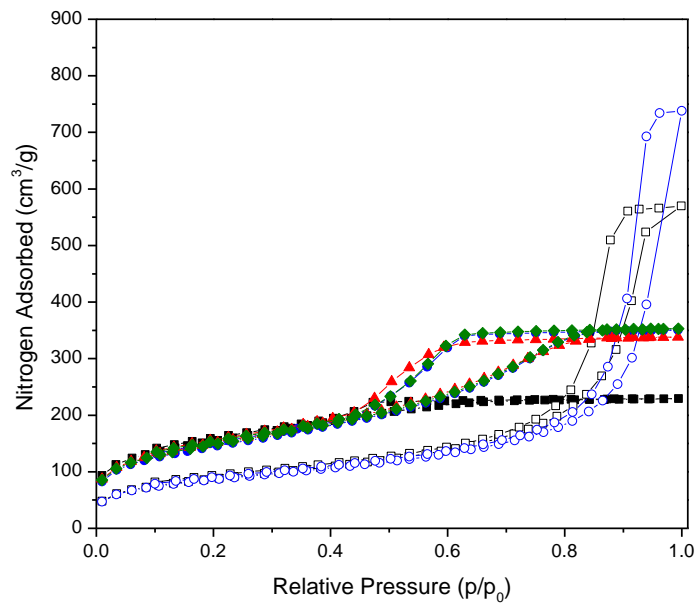
Figure 102: Nitrogen adsorption/desorption isotherms for sodium carbonate at R/C 100 (■) and 200 (●), calcium carbonate at R/C 100 (□) and 200 (○), and delayed addition of sodium carbonate sol at 70% (▲) and 80% (◆) of the parent gel time.
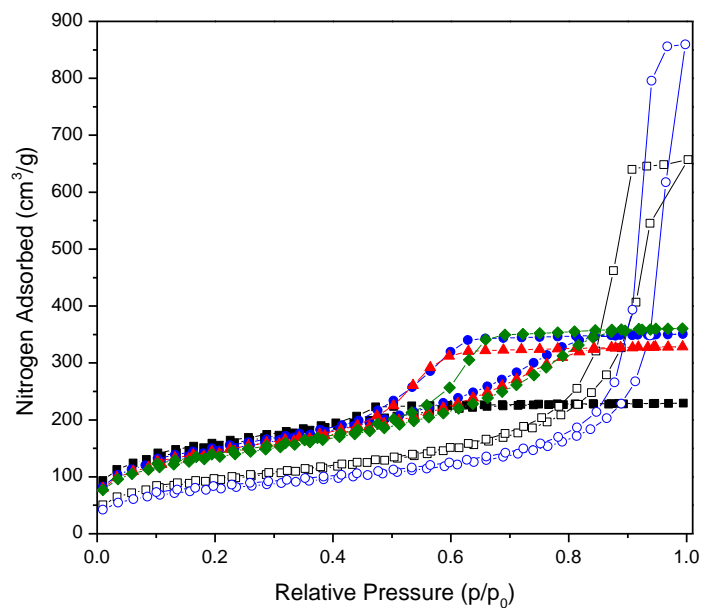
Figure 103: Nitrogen adsorption/desorption isotherms for sodium carbonate at R/C 100 (■) and 200 (●), barium carbonate at R/C 100 (□) and 200 (○), and delayed addition of sodium carbonate sol at 70% (▲) and 80% (◆) of the parent gel time.

It can be seen that, in all cases, the expected difference in properties between additions at 70 and 80%, respectively, does not occur. Instead, at both addition times, the nitrogen adsorption isotherms overlap those of pure sodium carbonate at R/C 200, with very similar nitrogen uptakes for all samples. Any differences are very slight, and concern the width of the hysteresis loop, suggesting slight variations in the pore sizes of the gels. The resulting pore size distributions for each of the

samples are given in Figure 104, 105 and 106. The pure metal carbonate pore size distributions are again included for comparison.
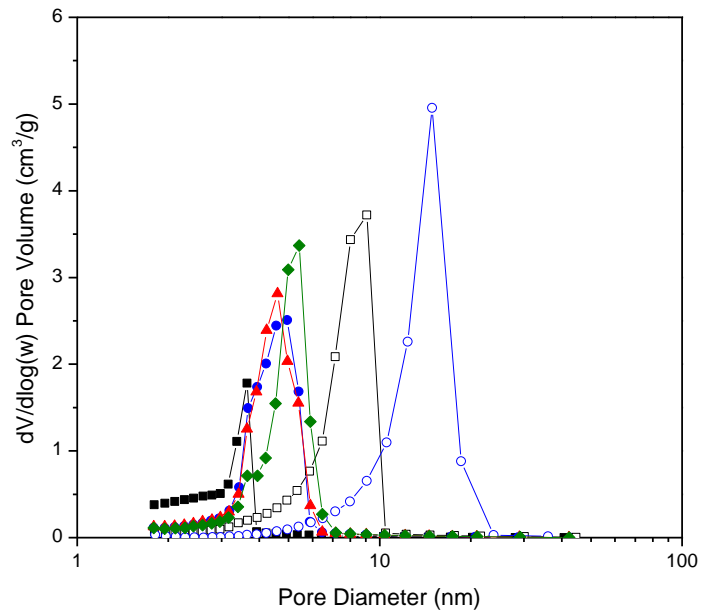
Figure 104: Pore size distributions for sodium carbonate at R/C 100 (■) and 200 (●), caesium carbonate at R/C 100 (□) and 200 (○), and delayed addition of sodium carbonate sol at 70% (▲) and 80% (◆) of the parent gel time.
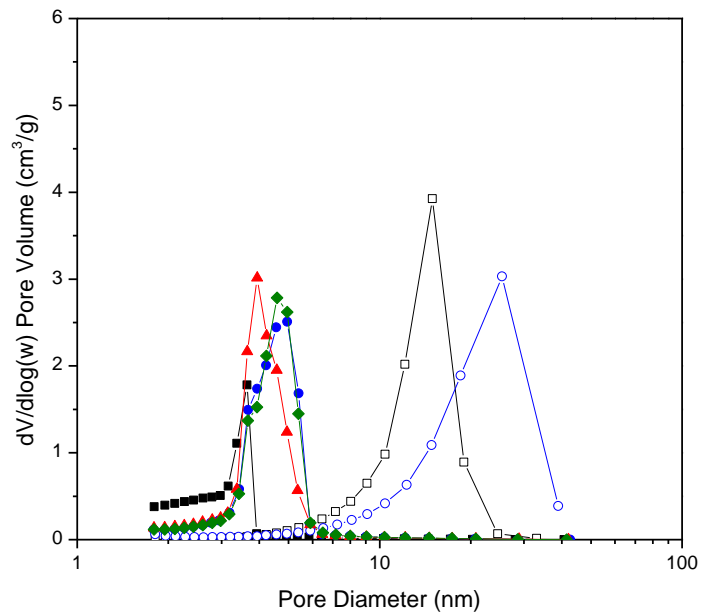
Figure 105: Pore size distributions for sodium carbonate at R/C 100 (■) and 200 (●), calcium carbonate at R/C 100 (□) and 200 (○), and delayed addition of sodium carbonate sol at 70% (▲) and 80% (◆) of the parent gel time.
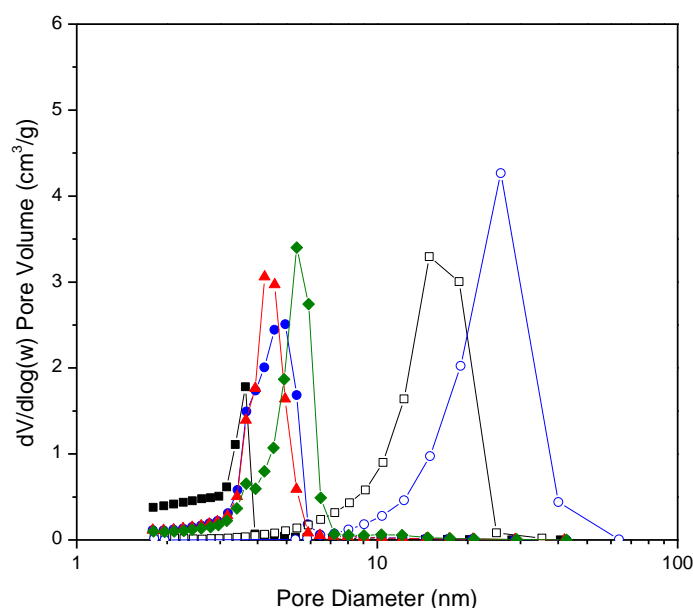
From the pore size distributions it can again be seen that all of the gels are very similar to the sodium carbonate R/C 200 sample, with only slight variations in the positioning and width of the distributions. To confirm these variations, further textural properties of the gels are shown in Table 30.

Table 30: Gel textural properties for all samples prepared with secondary addition of sodium carbonate sol.

Addition Time	S_{BET} (m^2/g)	V_{Tot} (cm^3/g)	V_μ (cm^3/g)	d_p avg (nm)
Cs_2CO_3/Na_2CO_3				
70%	527 ± 4	0.55	0.03	4.2
80%	491 ± 4	0.56	0.03	4.6
$CaCO_3/Na_2CO_3$				
70%	527 ± 4	0.52	0.03	3.9
80%	518 ± 4	0.55	0.03	4.2
$BaCO_3/Na_2CO_3$				
70%	488 ± 4	0.51	0.03	4.1
80%	470 ± 4	0.56	0.03	4.8

Comparison with the data on the pure metal carbonate systems in Table 11, Chapter 5 (sodium and caesium carbonate) and Table 18, Chapter 6 (calcium and

barium carbonate) prove how similar to the secondary carbonate at R/C 200 the mixed gels are, and how different they are to their respective parent carbonate gel.

For 70% addition of the sol, the gels are very similar to those obtained by simply adding the metal carbonate by itself, and appear to follow a similar formation process. Before addition of the secondary sol, cluster growth proceeds as it would for the pure caesium, calcium or barium systems, depending on the carbonate chosen. On addition of the secondary sol, which, having been mixed but not heated should exhibit no cluster growth, the newly added sodium cation again modifies the existing clusters, as was the case in Chapter 8. The additional R and F that is also added allows the clusters to grow further under the influence of the sodium cation, taking on more of the character of a typical sodium gel. It is also possible that a greater number of new clusters may form, as there will be more material available to react in the presence of the newly added carbonate.

This additional R and F also explain the differences, compared to the addition of just carbonate, seen here when adding the secondary sol at 80% of the gel time. On adding just the metal carbonate, very little material remained that had not been consumed by the forming gel network, and the existing clusters were well established in a partially aggregated system. As a result, the system could not be disrupted to such a great level, resulting in large intercluster voids and larger pore sizes. With secondary sol addition, a large quantity of R and F has been additionally provided to the reacting system. Following the limited cluster modification, this material must be incorporated into the network, partially filling the intercluster voids and leading to reduced pore sizes.

In both cases, the modified system is controlled by the secondary catalyst, i.e. sodium carbonate. After mixing with the parent gel, the sodium carbonate is present at R/C 200, and the resultant clusters will have similar size to those of the pure sodium carbonate systems. The clusters will, therefore, pack in a similar manner, resulting in comparable textural properties observed.

9.3 Secondary Addition of Partially Gelled RF Sol

Secondary addition of a metal carbonate, or sol, results in the modification of cluster species after addition. It was, therefore, decided to investigate the impact of adding already established and growing clusters to a parent gel sample. To remain consistent with experiments already performed, this addition was, once more,

carried out at 70 and 80% of the parent gel time. However, the secondary system was also allowed to reach the same point in its own gelation process, such that both samples were at 70%, or both samples were at 80% of their total gelation times. The nitrogen adsorption/desorption isotherms when mixing caesium carbonate and sodium carbonate partial gels are shown in Figure 107.
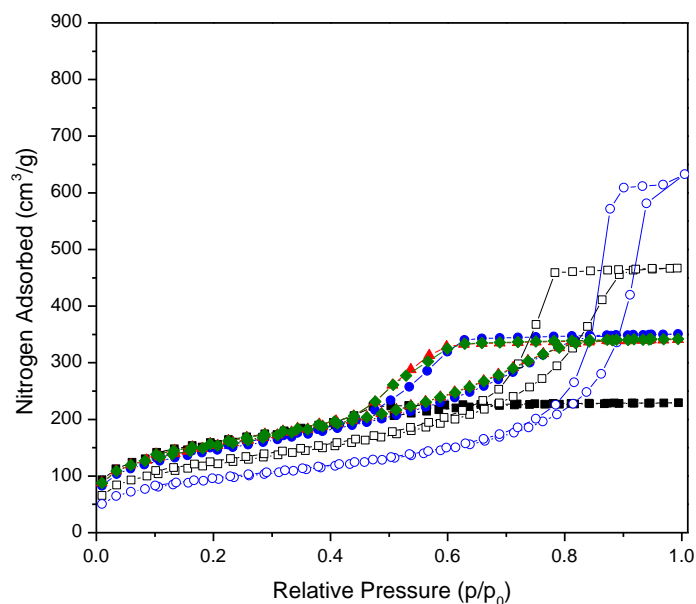
Figure 107: Nitrogen adsorption/desorption isotherms for sodium carbonate at R/C 100 (■) and 200 (●), caesium carbonate at R/C 100 (□) and 200 (O), and delayed addition of partially gelled sodium carbonate sol at 70% (▲) and 80% (◆) of the parent gel time.

It is once again noticeable how similar the two mixed systems are to that of the pure R/C 200 sodium carbonate sample, with almost complete overlap of the nitrogen adsorption isotherms for each system. In contrast, the results obtained for the calcium/sodium systems, and barium/sodium systems differ from the R/C 200 sodium carbonate sample greatly, as can be seen in Figure 108 and 109.
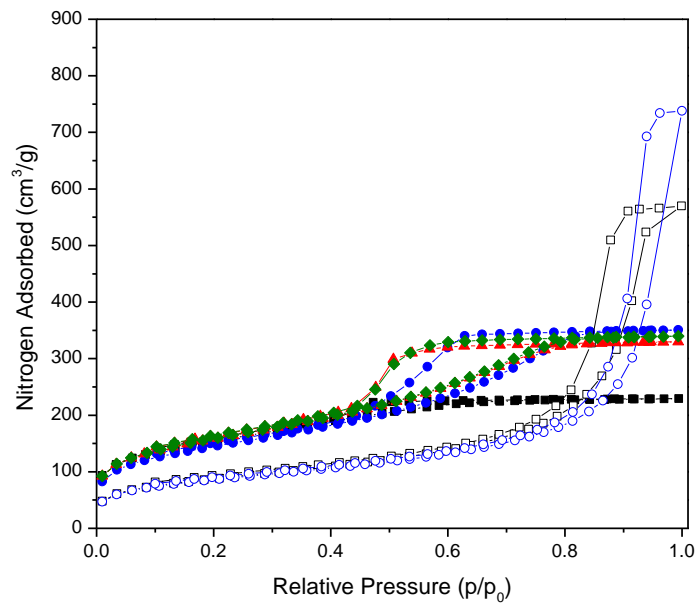
Figure 108: Nitrogen adsorption/desorption isotherms for sodium carbonate at R/C 100 (■) and 200 (●), calcium carbonate at R/C 100 (□) and 200 (○), and delayed addition of partially gelled sodium carbonate sol at 70% (▲) and 80% (◆) of the parent gel time.
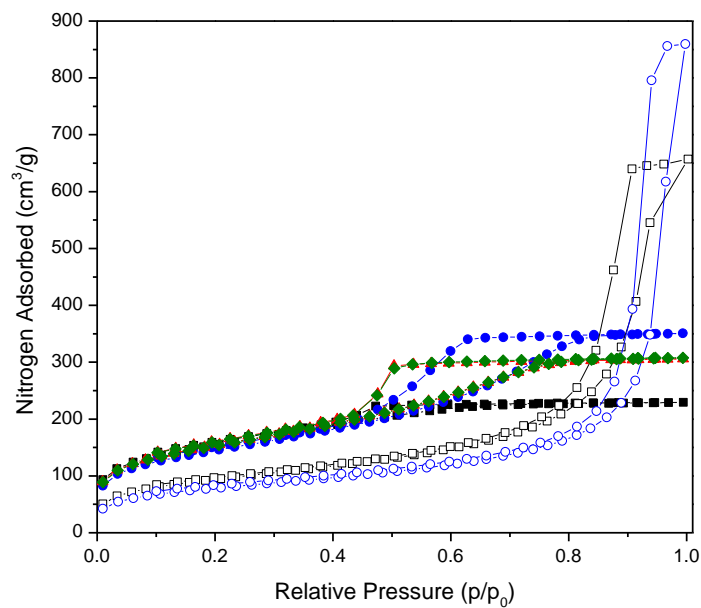
Figure 109: Nitrogen adsorption/desorption isotherms for sodium carbonate at R/C 100 (■) and 200 (●), barium carbonate at R/C 100 (□) and 200 (○), and delayed addition of partially gelled sodium carbonate sol at 70% (▲) and 80% (◆) of the parent gel time.

The calcium/sodium system shows a widening of the hysteresis loop, suggesting a shift to smaller pore sizes, while the nitrogen uptake remains consistent with the pure sodium sample. However, the barium/sodium system shows both a widening of the hysteresis loop and a decrease in the nitrogen uptake, implying that, as well as a decrease in pore size, the total pore volume has also decreased. Examination of the

172

corresponding pore size distributions (Figure 110, 111 and 112) supports these theories.
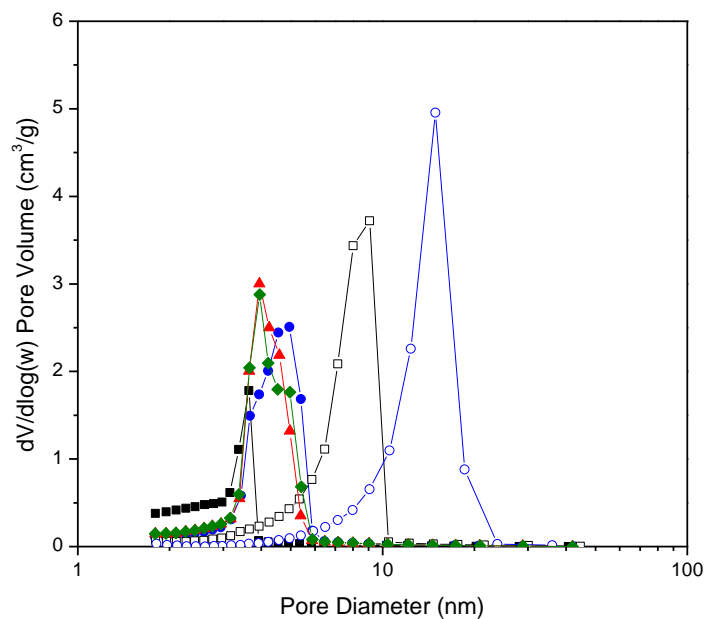
Figure 110: Pore size distributions for sodium carbonate at R/C 100 (■) and 200 (●), caesium carbonate at R/C 100 (□) and 200 (○), and delayed addition of partially gelled sodium carbonate sol at 70% (▲) and 80% (◆) of the parent gel time.
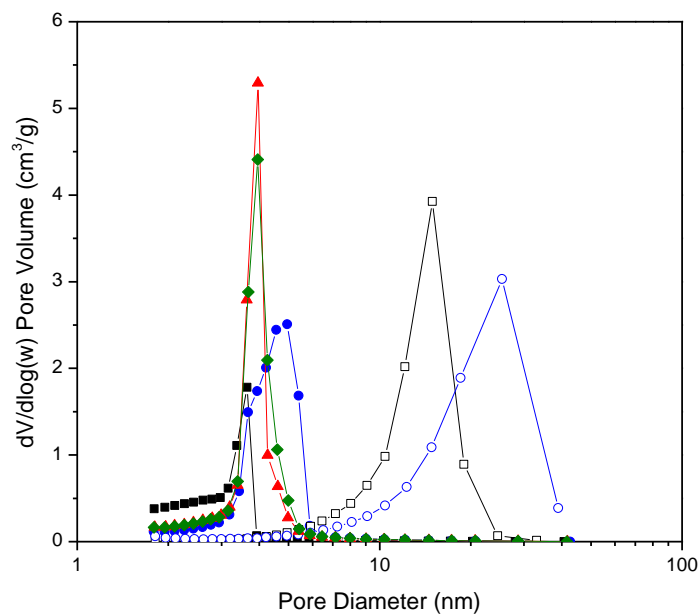
Figure 111: Pore size distributions for sodium carbonate at R/C 100 (■) and 200 (●), calcium carbonate at R/C 100 (□) and 200 (○), and delayed addition of partially gelled sodium carbonate sol at 70% (▲) and 80% (◆) of the parent gel time.
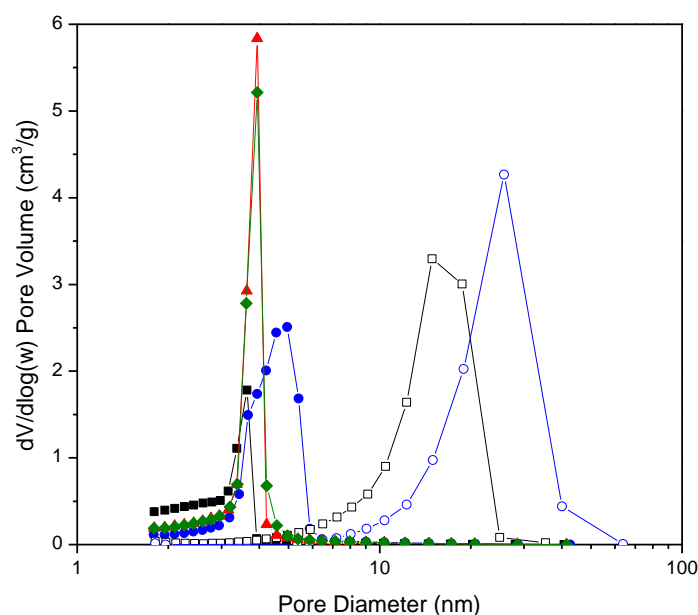
Figure 112: Pore size distributions for sodium carbonate at R/C 100 (■) and 200 (●), barium carbonate at R/C 100 (□) and 200 (○), and delayed addition of partially gelled sodium carbonate sol at 70% (▲) and 80% (◆) of the parent gel time.

The caesium/sodium systems show a great deal of overlap with the R/C 200 sodium carbonate sample, as would be expected. However, the differences in the calcium/sodium and barium/sodium samples are clear to see. Both systems produce a distinct narrowing of the pore size distribution, with the expected shift towards smaller pore sizes. The narrowing is particularly severe for the barium/sodium system, explaining the apparent reduction in pore volume. Textural properties of these gels are given in Table 31.

Table 31: Gel textural properties for all samples prepared through mixing of two partially gelled samples.

Addition Time	S_{BET} (m^2/g)	V_{Tot} (cm^3/g)	V_μ (cm^3/g)	d_p avg (nm)
Cs_2CO_3/Na_2CO_3				
70%	534 ± 4	0.53	0.04	3.9
80%	532 ± 4	0.53	0.03	3.9
$CaCO_3/Na_2CO_3$				
70%	552 ± 4	0.51	0.04	3.7
80%	554 ± 5	0.53	0.04	3.8
$BaCO_3/Na_2CO_3$				
70%	537 ± 4	0.47	0.04	3.5
80%	534 ± 4	0.48	0.04	3.6

Table 31 shows the decreases in pore size exhibited by each of the gel samples. Also confirmed is the decrease in total pore volume for the barium/sodium systems. It is also of note that the calcium/sodium systems display a significant increase in surface area over the sodium carbonate R/C 200 sample.

By again considering the cluster growth processes involved, it is possible to explain these results. As the isolated samples are heated, clusters will develop and grow in both systems, with size and number density congruent with the R/C 100 catalyst concentration present. As a result, the cluster number density post-addition should be much greater in this case, as opposed to the secondary addition of just metal carbonate or sol.

In the case of caesium/sodium, the difference in cluster size between the two individual systems at a given R/C is not as great as the difference between calcium or barium and sodium. On mixing, the sodium still appears to be able to disrupt any coalescence imparted by the caesium cations. Nevertheless, the two sets of clusters will intermingle on mixing; resulting in pore sizes bigger than a sodium carbonate R/C 100 gel, but smaller than the caesium carbonate R/C 100 gel.

For the calcium/sodium and barium/sodium systems, the pore sizes are much closer to those of a sodium carbonate R/C 100 gel. This suggests that the clusters have similar sizes to those of the sodium carbonate gel. On mixing, the calcium/barium controlled clusters would be expected to shrink as previously described. To give the observed pore size, it would suggest that the clusters are either shrinking to around the same size as those from the sodium system, or, they remain larger and the newly added sodium clusters pack between them, resulting in smaller pore sizes seen.

9.4   Summary of Findings

A series of gels were prepared with a secondary addition of either a sodium carbonate containing sol, or partially gelled sol, to a parent gel sample containing caesium, calcium or barium carbonate, at 70 or 80% of the parent gel time. These new gels were analysed using surface area and porosity measurements.

It was found that:

- On addition of a sol to the parent gel sample:
  - All combinations produced a gel with very similar textural properties.

- The properties of these new gels were comparable with those of a sodium carbonate gel at R/C 200, equivalent to the sodium carbonate concentration in the mixed gel.
  - In contrast to the secondary addition of just a metal carbonate, addition at both 70 and 80% of the parent gel time produced a very similar gel.
  - This was as a result of the additionally added R and F allowing for sustained new cluster growth at both addition times.
- On addition of a partially gelled sol to the parent gel sample:
  - Large number concentrations of secondary clusters were formed, due to the higher secondary catalyst concentration present in the initial stages of their growth (R/C 100).
  - The combination of caesium and sodium again produced gels similar to sodium carbonate at R/C 200, with slightly smaller pore size.
  - The clusters produced by each of the individual systems are not too dissimilar in size, especially when considering breakdown of coalescence.
  - Intermingling of clusters during packing into the gel network results in a broader pore size distribution.
  - The combinations of calcium and sodium, and barium and sodium, produce gels with a much narrower pore size distribution than the caesium/sodium system.
  - The two sets of clusters, produced by calcium/barium and sodium, have greatly different sizes before mixing, with sodium producing small clusters, and calcium/barium producing large clusters.
  - Group II clusters expected to shrink, with small sodium clusters packing tightly to fill the gaps between the clusters, resulting in a narrower distribution of small pores.

This route of RF gel synthesis provides further options for the tailoring of their textural properties. As has been shown in this chapter, gels produced from identical sol compositions can have widely different final properties, depending on the route chosen.

10 Conclusions

In order to study the gelation mechanism of the RF sol-gel transition, with a view to being able to tailor the final textural properties of the resulting RF xerogels, several samples of varying composition were synthesised. During gelation, the various systems were analysed using dynamic light scattering, in order to monitor changes in the size of the clusters that compose the 3D RF network structure. The RF xerogel properties were then characterised using low temperature nitrogen adsorption measurements, allowing the resulting textural properties determined to be linked to the formation mechanism of the gel structure.

10.1 Group I Metal Carbonate Catalysed Gels

The first set of gels to be studied were those catalysed using the Group I carbonates of lithium, sodium, potassium and caesium, at R/C ratios between 100 and 600, resulting in detailed analysis of 24 different gel compositions. These analyses allowed for the development of a model describing the growth of clusters during RF gel formation. It was found that cluster growth was a thermodynamically controlled process, independent of catalyst concentration, such that for all R/C ratios, clusters are of the same size at a given time. Kinetic control from the R/C ratio arises because the R/C determines the number concentration of clusters initially formed. Higher R/C ratios, corresponding to lower catalyst concentrations, result in the initial formation of fewer clusters than higher catalyst concentrations. As fewer clusters must grow to larger sizes to fill space and form the gel, this lead to larger intercluster voids in the final structure.

These findings can be directly linked to the results obtained through nitrogen adsorption analysis, where high catalyst concentrations resulted in small pores and low catalyst concentrations led to large pores. From this correlation, a Master Curve can be drawn, showing the range of pore sizes available for RF xerogels, and the corresponding final cluster size required to achieve them. By studying this curve, the synthesis conditions needed for a particular cluster size can be predicted.

The Master Curve demonstrated how, for a given R/C, lithium, sodium and potassium carbonate all gave very similar properties and cluster sizes, falling into an overlapping band. However, for an equivalent R/C, caesium carbonate gave much larger cluster sizes and, therefore, larger pore sizes. The metals could subsequently be arranged into a Hofmeister-like series, with regards to their ability to interact with the growing oligomeric RF chains involved in the sol-gel transition. The charge

density on lithium, sodium and potassium cations retain the hydration layer on the chains, salting in the clusters and resulting in small cluster sizes. On the other hand, caesium appears to lead to salting out of the clusters and consequently larger clusters. However, the lower charge density on the caesium cation should, in theory, result in smaller clusters than those associated with lithium, sodium and potassium. The rapid increase in cluster size observed with caesium may, therefore, be down to coalescence of these very small clusters into much larger units.

In all DLS analyses, it was found that there was a delay before cluster growth was initiated. By studying the temperature development during gelation, it was discovered that cluster growth began when the temperature reached approximately 55 °C. However, preheating the components to 55 °C during sol preparation had no effect on the properties of the final gel.

By further considering the stabilising ability of the metal cation, a series of gels were made in which the addition of the metal carbonate to a reacting solution of R and F was delayed. This showed that even after 105 min, at which time the gelling solution had become turbid, introduction of the stabilising cation would result in a gel with comparable properties to that of the standard gel. Only when addition was delayed so long that sedimentation of clusters was visible, after 120 min, did the final gel lose significant porosity.

10.2 Group II Metal Carbonate Catalysed Gels

The same DLS and nitrogen adsorption analyses were performed on gels catalysed by Group II carbonates: calcium and barium. As for the Group I carbonates, it was found that cluster growth was thermodynamically controlled, independent of R/C, while the number concentration of clusters was kinetically controlled and was dependent on R/C. The Group II gels could, therefore, also be fitted to the cluster growth model proposed for the Group I gels.

The Group II gels were found to have significantly larger cluster sizes at low R/C ratios, when compared to the Group I gels. Calcium and barium could, therefore, be added to the Hofmeister-like series, having even higher charge densities than the Group I cations. This high charge density led to disruption of the hydration layer around the RF chains, resulting in the salting out of larger clusters. Correspondingly, the Group II metal carbonates produced gels with larger pore sizes than the Group I gels, for all R/C ratios studied.

It was also found, as for the Group I gels, that there was a delay before the onset of cluster growth, with 55 °C again being the temperature at which this process began. However, unlike the Group I gels, preheating a Group II gel resulted in an increase in pore size. This was due to the fact that the increased temperature decreases the solubility of the catalyst, causing an increase in the effective initial R/C ratio of the system.

10.3 Ammonium Carbonate Catalysed Gels

To further probe the role of the metal cation in the gelation process, ammonium carbonate was used as an alternative, non-metallic basic catalyst in the synthesis of RF gels. However, it was found that using ammonium carbonate produced a product very similar to that obtained when no carbonate was used, albeit with the product forming over much shorter timescales.

Ammonium carbonate is known to decompose in hot water, resulting in the loss of both the carbonate required to initiate the addition reaction between R and F, and the ammonium cation to interact with the oligomeric chains. As a result, the few clusters that form grow to large sizes and sediment out. Some of the ammonia produced during the decomposition of the ammonium carbonate will react with a quantity of the F in the system producing hexamine. This may act as a substitute base, explaining the reduction in time for product formation.

By combining ammonium carbonate with a metal carbonate, in equal molar ratios, as the catalyst in the gel formation, the influence of ammonium carbonate was further investigated. The results showed that when using a Group I carbonate, the resulting gels had textural properties very similar to those of a gel made with just the Group I carbonate, when an equivalent metal concentration had been used. The Group I cation was able to interact with the RF oligomers, resulting in a very similar gel.

In contrast, when using a Group II carbonate in conjunction with ammonium carbonate, it was found that the resulting textural properties had no correlation to a pure Group II catalysed gel, at any R/C. The Group II metal cation was known to give larger cluster sizes, with an apparent further interaction with the decomposing ammonium carbonate resulting in different cluster sizes and completely dissimilar properties.

10.4 Secondary Metal Carbonate Addition Catalysed Gels

With the various metal cations imparting different properties to the RF gels, it was investigated whether using equal R/C ratios of two cations in the same system would produce gels with mixed sets of properties. For these gels, caesium, calcium and barium carbonate were designated as parent carbonates, with lithium, sodium and potassium as secondary carbonates. The addition time was also varied from simultaneous, during sol preparation, to high percentages of the parent gel time, up to and including 80%.

The simultaneous combination of caesium and sodium carbonate produced clusters with sizes intermediate to those of the individual systems, while delayed addition significantly reduced the size of the clusters before another short period of slight growth occurred. This was thought to be as a result of the newly introduced sodium cation reversing the coalescence in the system, and controlling the subsequent growth. In contrast, the combinations of Group II and Group I catalysts produced clusters of size that was consistent with those of solely the secondary carbonate being present when the carbonates were added simultaneously. Delayed addition again reduced the size of the clusters, which in this case was attributed to the shrinking of clusters, making them more compact. Subsequent growth was again controlled by the newly added Group I cation.

As a result, the pore sizes observed were consistent with those of the secondary catalyst, with concentration equivalent to that in the mixed carbonate gel, albeit with slightly narrower distributions, at addition times up to 70% of the parent gel time. Only at 80% of the parent gel time did these properties change, with an increase in pore size as a result of the more established and partially aggregated clusters being less susceptible to disruption by the new cation.

By decreasing the parent carbonate concentration, and increasing the concentration of the secondary carbonate, the gel properties could be further changed. As would be expected, the average pore diameters moved to smaller sizes, with an accompanying narrowing of the distribution. The increased secondary catalyst concentration further modified the primary clusters, imparting more of the character of the secondary catalyst into the final gel.

10.5 Secondary Sol/Partially Gelled Sol Addition

Addition of a secondary sol to a gelling parent sample provided the system with additional R and F, as well as a secondary metal carbonate. As for the addition of just the secondary carbonate, this resulted in the modification of the cluster species, with their subsequent growth controlled by the secondary carbonate. This resulted in gels with very similar properties to a gel produced using solely the secondary carbonate as catalyst, at the equivalent R/C. In contrast to the secondary carbonate addition, the supplementary R and F added meant that addition at both 70 and 80% of the parent gel time produced gels with very similar properties, because approximately the same amount of material was available for the continued growth of clusters.

On the other hand, the properties of the gels produced by mixing two partially gelled sols depended on the combination of metal carbonates used. In all cases, both partially gelled sols individually contained established clusters when they were mixed, with size dependent on the metal carbonate used. In the combination of caesium and sodium, the two sets of clusters differ in size to a small degree. Combined with a slight disruption to the coalesced clusters, this resulted in a broad pore size distribution, which was interpreted as the clusters intermingling on mixing. However, when combining calcium or barium with sodium, the two sets of clusters have considerably different sizes. As a result, it was after some cluster shrinkage, the smaller sodium clusters pack together in the gaps between the much larger Group II clusters, resulting in a narrower distribution with size congruent to that of the sodium gel added.

10.6 Tailoring of RF Xerogels

By carefully choosing the synthesis conditions and route, it is possible to tune the textural properties of an RF gel as desired. By using a single metal carbonate, from either Group I or Group II, pore sizes can be increased by decreasing the catalyst concentration, with the different catalysts providing different ranges over which the size can change. Increasing the pore size has the corresponding effects of increasing pore volume and decreasing surface area.

Alternatively, control of these same textural properties can be achieved by modifying the synthesis route to include the addition of a secondary metal carbonate, sol, or partially gelled sol to a parent gelling sample. By altering the ratio of the two carbonates, or the time of secondary addition, the textural properties can be

controlled further. For example, pore size can be altered while keeping the overall R/C constant, or the pore volume can be controlled while keeping the pore size constant.

This new found knowledge on the growth of clusters has allowed increased insight into the gelation process, providing further clarity on how the gel formation process influences the final textural properties of RF xerogels.

11 Future Work

Based on the results obtained in this body of work, it would be desirable to further investigate the gelation of RF samples. The proposed future work would take the form of:

- Decreased analysis intervals for DLS studies, allowing:
    - Increased number of data points for each sample.
    - More accurate detection of maximum observable hydrodynamic radii.
    - Direct comparison with past and present work within the research group using UV-Vis-NIR spectroscopy to study the gelation of RF gels, with possible trends between cluster size and absorption at certain wavelengths.
- ^{1}H NMR studies to determine the chemical composition of growing clusters:
    - Techniques available to suppress the water peak, allowing for analysis of aqueous systems.
- Mass spectrometry to look at grown RF chains:
    - Determination of relationship between chain length and cluster size.
- Computer simulations of the cluster growth process, providing:
    - Accurate prediction of the cluster sizes obtained for a given set of synthesis conditions.
    - Further insight into cluster growth after secondary carbonate addition.
- Increased R/C ratios (> 600) for single catalyst systems, to further increase cluster size.
- Mercury porosimetry to determine pore volumes of high R/C systems.
- Investigate consumption of R for various systems for insight into compactness of clusters.
- Further investigation of the relationship between catalyst concentration and the cluster number concentration:
    - Implications for the nucleation mechanism of the growing RF oligomers.
- Expansion of the 'Master Curve' (Figure 38) to determine if truly S-shaped, and the implications for gel formation.
- Investigate the activation energy (physical barrier) for the initial nucleation of RF oligomer growth and tie back to the temperature of 55 °C.

- Investigate further preheating, to 85 °C, to determine whether growth kinetics are linear or exponential.
- Conduct SEM imaging of gels synthesised with delayed addition of catalyst and using two catalysts.
- Use a neutral salt, eg. sodium chloride, as the secondary catalyst, to eliminate pH modification on secondary addition but maintain cation concentration.
- Investigate cluster growth in more dilute systems, i.e. lower the total solids content.

Appendix A – Standard Hydrogel Reaction Compositions

This Appendix details the masses of resorcinol, formaldehyde and, where applicable, metal carbonate required for each of the standard hydrogels studied.

The total mass of solids is fixed at 12 g in each case.

A1   Lithium Carbonate – Li_2CO_3

Table 32: Li_2CO_3_100 composition.

R/C 100	Equivalent Moles	Equivalent Mass (g)	Percentage Mass (%)	Required Mass (g)
Resorcinol	1.0000	110.1100	64.4290	7.7315
Formaldehyde	2.0000	60.0524	35.1386	4.2166
Carbonate	0.0100	0.7389	0.4324	0.05188
Total		170.9013	100.0000	12.0000

Table 33: Li2CO3_200 composition.

R/C 200	Equivalent Moles	Equivalent Mass (g)	Percentage Mass (%)	Required Mass (g)
Resorcinol	1.0000	110.1100	64.5686	7.7482
Formaldehyde	2.0000	60.0524	35.2148	4.2258
Carbonate	0.0050	0.3695	0.2166	0.02600
Total		170.5319	100.0000	12.0000

Table 34: Li_2CO_3_300 composition.

R/C 300	Equivalent Moles	Equivalent Mass (g)	Percentage Mass (%)	Required Mass (g)
Resorcinol	1.0000	110.1100	64.6152	7.7538
Formaldehyde	2.0000	60.0524	35.2402	4.2288
Carbonate	0.0033	0.2463	0.1445	0.01734
Total		170.4087	100.0000	12.0000

Table 35: Li_2CO_3_400 composition.

R/C 400	Equivalent Moles	Equivalent Mass (g)	Percentage Mass (%)	Required Mass (g)
Resorcinol	1.0000	110.1100	64.6386	7.7566
Formaldehyde	2.0000	60.0524	35.2530	4.2304
Carbonate	0.0025	0.1847	0.1084	0.01301
Total		170.3471	100.0000	12.0000

R/C 500	Equivalent Moles	Equivalent Mass (g)	Percentage Mass (%)	Required Mass (g)
Resorcinol	1.0000	110.1100	64.6526	7.7583
Formaldehyde	2.0000	60.0524	35.2606	4.2313
Carbonate	0.0020	0.1478	0.0868	0.01041
Total		170.3102	100.0000	12.0000

Table 37: Li$_2$CO$_3$_600 composition.

R/C 600	Equivalent Moles	Equivalent Mass (g)	Percentage Mass (%)	Required Mass (g)
Resorcinol	1.0000	110.1100	64.6620	7.7594
Formaldehyde	2.0000	60.0524	35.2657	4.2319
Carbonate	0.0017	0.1232	0.0723	0.00868
Total		170.2856	100.0000	12.0000

A2 Sodium Carbonate – Na$_2$CO$_3$

Table 38: Na$_2$CO$_3$_100 composition.

R/C 100	Equivalent Moles	Equivalent Mass (g)	Percentage Mass (%)	Required Mass (g)
Resorcinol	1.0000	110.1100	64.3082	7.7170
Formaldehyde	2.0000	60.0524	35.0728	4.2087
Carbonate	0.0100	1.0599	0.6190	0.07428
Total		171.2223	100.0000	12.0000

Table 39: Na$_2$CO$_3$_200 composition.

R/C 200	Equivalent Moles	Equivalent Mass (g)	Percentage Mass (%)	Required Mass (g)
Resorcinol	1.0000	110.1100	64.5079	7.7409
Formaldehyde	2.0000	60.0524	35.1817	4.2218
Carbonate	0.0050	0.5299	0.3105	0.03726
Total		170.6923	100.0000	12.0000

Table 40: Na$_2$CO$_3$_300 composition.

R/C 300	Equivalent Moles	Equivalent Mass (g)	Percentage Mass (%)	Required Mass (g)
Resorcinol	1.0000	110.1100	64.5747	7.7490
Formaldehyde	2.0000	60.0524	35.2181	4.2262
Carbonate	0.0033	0.3533	0.2072	0.02486
Total		170.5157	100.0000	12.0000

Table 41: Na$_2$CO$_3$_400 composition.

R/C 400	Equivalent Moles	Equivalent Mass (g)	Percentage Mass (%)	Required Mass (g)
Resorcinol	1.0000	110.1100	64.6082	7.7530
Formaldehyde	2.0000	60.0524	35.2364	4.2284
Carbonate	0.0025	0.2650	0.1555	0.01866
Total		170.4274	100.0000	12.0000

Table 42: Na$_2$CO$_3$_500 composition.

R/C 500	Equivalent Moles	Equivalent Mass (g)	Percentage Mass (%)	Required Mass (g)
Resorcinol	1.0000	110.1100	64.6283	7.7554
Formaldehyde	2.0000	60.0524	35.2473	4.2297
Carbonate	0.0020	0.2120	0.1244	0.01493
Total		170.3744	100.0000	12.0000

Table 43: Na$_2$CO$_3$_600 composition.

R/C 600	Equivalent Moles	Equivalent Mass (g)	Percentage Mass (%)	Required Mass (g)
Resorcinol	1.0000	110.1100	64.6417	7.7570
Formaldehyde	2.0000	60.0524	35.2546	4.2306
Carbonate	0.0017	0.1766	0.1037	0.01244
Total		170.3391	100.0000	12.0000

A3 Potassium Carbonate – K$_2$CO$_3$

Table 44: K$_2$CO$_3$_100 composition.

R/C 100	Equivalent Moles	Equivalent Mass (g)	Percentage Mass (%)	Required Mass (g)
Resorcinol	1.0000	110.1100	64.1874	7.7025
Formaldehyde	2.0000	60.0524	35.0069	4.2008
Carbonate	0.0100	1.3821	0.8057	0.09668
Total		171.5445	100.0000	12.0000

Table 45: K$_2$CO$_3$_200 composition.

R/C 200	Equivalent Moles	Equivalent Mass (g)	Percentage Mass (%)	Required Mass (g)
Resorcinol	1.0000	110.1100	64.4471	7.7336
Formaldehyde	2.0000	60.0524	35.1485	4.2178
Carbonate	0.0050	0.6910	0.4045	0.04853
Total		170.8534	100.0000	12.0000

Table 46: K$_2$CO$_3$_300 composition.

R/C 300	Equivalent Moles	Equivalent Mass (g)	Percentage Mass (%)	Required Mass (g)
Resorcinol	1.0000	110.1100	64.5341	7.7441
Formaldehyde	2.0000	60.0524	35.1959	4.2235
Carbonate	0.0033	0.4607	0.2700	0.03240
Total		170.6231	100.0000	12.0000

Table 47: K$_2$CO$_3$_400 composition.

R/C 400	Equivalent Moles	Equivalent Mass (g)	Percentage Mass (%)	Required Mass (g)
Resorcinol	1.0000	110.1100	64.5776	7.7493
Formaldehyde	2.0000	60.0524	35.2197	4.2264
Carbonate	0.0025	0.3455	0.2026	0.02432
Total		170.5079	100.0000	12.0000

Table 48: K$_2$CO$_3$_500 composition.

R/C 500	Equivalent Moles	Equivalent Mass (g)	Percentage Mass (%)	Required Mass (g)
Resorcinol	1.0000	110.1100	64.6038	7.7525
Formaldehyde	2.0000	60.0524	35.2340	4.2281
Carbonate	0.0020	0.2764	0.1622	0.01946
Total		170.4388	100.0000	12.0000

Table 49: K$_2$CO$_3$_600 composition.

R/C 600	Equivalent Moles	Equivalent Mass (g)	Percentage Mass (%)	Required Mass (g)
Resorcinol	1.0000	110.1100	64.6213	7.7546
Formaldehyde	2.0000	60.0524	35.2435	4.2292
Carbonate	0.0017	0.2303	0.1352	0.01622
Total		170.3927	100.0000	12.0000

A4 Caesium Carbonate – Cs$_2$CO$_3$

Table 50: Cs$_2$CO$_3$_100 composition.

R/C 100	Equivalent Moles	Equivalent Mass (g)	Percentage Mass (%)	Required Mass (g)
Resorcinol	1.0000	110.1100	63.4930	7.6192
Formaldehyde	2.0000	60.0524	34.6282	4.1554
Carbonate	0.0100	3.2582	1.8788	0.22545
Total		173.4206	100.0000	12.0000

Table 51: Cs$_2$CO$_3$_200 composition.

R/C 200	Equivalent Moles	Equivalent Mass (g)	Percentage Mass (%)	Required Mass (g)
Resorcinol	1.0000	110.1100	64.0951	7.6914
Formaldehyde	2.0000	60.0524	34.9566	4.1948
Carbonate	0.0050	1.6291	0.9483	0.11380
Total		171.7915	100.0000	12.0000

Table 52: Cs$_2$CO$_3$_300 composition.

R/C 300	Equivalent Moles	Equivalent Mass (g)	Percentage Mass (%)	Required Mass (g)
Resorcinol	1.0000	110.1100	64.2984	7.7158
Formaldehyde	2.0000	60.0524	35.0674	4.2081
Carbonate	0.0033	1.0861	0.6342	0.07610
Total		171.2485	100.0000	12.0000

Table 53: Cs$_2$CO$_3$_400 composition.

R/C 400	Equivalent Moles	Equivalent Mass (g)	Percentage Mass (%)	Required Mass (g)
Resorcinol	1.0000	110.1100	64.4005	7.7281
Formaldehyde	2.0000	60.0524	35.1231	4.2148
Carbonate	0.0025	0.8146	0.4764	0.05717
Total		170.9770	100.0000	12.0000

Table 54: Cs$_2$CO$_3$_500 composition.

R/C 500	Equivalent Moles	Equivalent Mass (g)	Percentage Mass (%)	Required Mass (g)
Resorcinol	1.0000	110.1100	64.4619	7.7354
Formaldehyde	2.0000	60.0524	35.1566	4.2188
Carbonate	0.0020	0.6516	0.3815	0.04578
Total		170.8140	100.0000	12.0000

Table 55: Cs$_2$CO$_3$_600 composition.

R/C 600	Equivalent Moles	Equivalent Mass (g)	Percentage Mass (%)	Required Mass (g)
Resorcinol	1.0000	110.1100	64.5029	7.7404
Formaldehyde	2.0000	60.0524	35.1790	4.2215
Carbonate	0.0017	0.5430	0.3181	0.03817
Total		170.7054	100.0000	12.0000

A5   Calcium Carbonate – CaCO₃

Table 56: CaCO₃_100 composition.

R/C 100	Equivalent Moles	Equivalent Mass (g)	Percentage Mass (%)	Required Mass (g)
Resorcinol	1.0000	110.1100	64.3304	7.7196
Formaldehyde	2.0000	60.0524	35.0849	4.2102
Carbonate	0.0100	1.001	0.5848	0.07017
Total		171.1633	100.0000	12.0000

Table 57: CaCO₃_200 composition.

R/C 200	Equivalent Moles	Equivalent Mass (g)	Percentage Mass (%)	Required Mass (g)
Resorcinol	1.0000	110.1100	64.5190	7.7423
Formaldehyde	2.0000	60.0524	35.1877	4.2225
Carbonate	0.0050	0.5005	0.2932	0.03519
Total		170.6629	100.0000	12.0000

Table 58: CaCO₃_400 composition.

R/C 400	Equivalent Moles	Equivalent Mass (g)	Percentage Mass (%)	Required Mass (g)
Resorcinol	1.0000	110.1100	64.6138	7.7537
Formaldehyde	2.0000	60.0524	35.2394	4.2287
Carbonate	0.0025	0.2502	0.1468	0.01762
Total		170.4126	100.0000	12.0000

A6   Barium Carbonate – BaCO₃

Table 59: BaCO₃_100 composition.

R/C 100	Equivalent Moles	Equivalent Mass (g)	Percentage Mass (%)	Required Mass (g)
Resorcinol	1.0000	110.1100	63.9669	7.6760
Formaldehyde	2.0000	60.0524	34.8866	4.1864
Carbonate	0.0100	1.9734	1.1464	0.13757
Total		172.1358	100.0000	12.0000

Table 60: BaCO₃_200 composition.

R/C 200	Equivalent Moles	Equivalent Mass (g)	Percentage Mass (%)	Required Mass (g)
Resorcinol	1.0000	110.1100	64.3357	7.7203
Formaldehyde	2.0000	60.0524	35.0878	4.2105
Carbonate	0.0050	0.9867	0.5765	0.06918
Total		171.1491	100.0000	12.0000

R/C 400	Equivalent Moles	Equivalent Mass (g)	Percentage Mass (%)	Required Mass (g)
Resorcinol	1.0000	110.1100	64.5217	7.7426
Formaldehyde	2.0000	60.0524	35.1892	4.2227
Carbonate	0.0025	0.4934	0.2891	0.03469
Total		170.6558	100.0000	12.0000

A7 Ammonium Carbonate – (NH$_4$)$_2$CO$_3$

Table 62: (NH$_4$)$_2$CO$_3$_100 composition.

R/C 100	Equivalent Moles	Equivalent Mass (g)	Percentage Mass (%)	Required Mass (g)
Resorcinol	1.0000	110.1100	64.3454	7.7214
Formaldehyde	2.0000	60.0524	35.0931	4.2112
Carbonate	0.0100	0.9609	0.5615	0.06738
Total		171.1233	100.0000	12.0000

Table 63: (NH$_4$)$_2$CO$_3$_200 composition.

R/C 200	Equivalent Moles	Equivalent Mass (g)	Percentage Mass (%)	Required Mass (g)
Resorcinol	1.0000	110.1100	64.5266	7.7432
Formaldehyde	2.0000	60.0524	35.1919	4.2230
Carbonate	0.0050	0.4805	0.2816	0.03379
Total		170.6429	100.0000	12.0000

Table 64: (NH$_4$)$_2$CO$_3$_400 composition.

R/C 400	Equivalent Moles	Equivalent Mass (g)	Percentage Mass (%)	Required Mass (g)
Resorcinol	1.0000	110.1100	64.6175	7.7541
Formaldehyde	2.0000	60.0524	35.2415	4.2290
Carbonate	0.0025	0.2402	0.1410	0.01692
Total		171.4026	100.0000	12.0000

A8 No Carbonate

Table 65: No carbonate composition.

	Equivalent Moles	Equivalent Mass (g)	Percentage Mass (%)	Required Mass (g)
Resorcinol	1.0000	110.1100	64.7088	7.7651
Formaldehyde	2.0000	60.0524	35.2912	4.2349
Total			100.0000	12.0000

Appendix B – Standard Hydrogel Calculated Reaction Volumes

This Appendix details the volumes of both formalin and additional deionised water required for each of the standard hydrogel compositions detailed in Appendix A.

B1   Lithium Carbonate – Li_2CO_3

Table 66: Li_2CO_3 volumes required.

R/C	100	200	300	400	500	600
Volume of Formalin (ml)	10.46	10.48	10.49	10.49	10.49	10.49
Volume due to F (ml)	5.17	5.19	5.19	5.19	5.19	5.19
Volume due to H_2O/MeOH (ml)	5.29	5.29	5.30	5.30	5.30	5.30
Volume of H_2O	4.71	4.71	4.70	4.70	4.70	4.70

B2   Sodium Carbonate – Na_2CO_3

Table 67: Na_2CO_3 volumes required.

R/C	100	200	300	400	500	600
Volume of Formalin (ml)	10.44	10.47	10.48	10.48	10.49	10.49
Volume due to F (ml)	5.16	5.18	5.19	5.19	5.19	5.19
Volume due to H_2O/MeOH (ml)	5.28	5.29	5.29	5.29	5.30	5.30
Volume of H_2O	4.72	4.71	4.71	4.71	4.70	4.70

B3   Potassium Carbonate – K_2CO_3

Table 68: K_2CO_3 volumes required.

R/C	100	200	300	400	500	600
Volume of Formalin (ml)	10.42	10.46	10.47	10.48	10.48	10.49
Volume due to F (ml)	5.15	5.18	5.18	5.19	5.19	5.19
Volume due to H_2O/MeOH (ml)	5.27	5.28	5.29	5.29	5.29	5.30
Volume of H_2O	4.73	4.72	4.71	4.71	4.71	4.70

B4   Caesium Carbonate – Cs_2CO_3

Table 69: Cs_2CO_3 volumes required.

R/C	100	200	300	400	500	600
Volume of Formalin (ml)	10.30	10.40	10.43	10.45	10.46	10.47
Volume due to F (ml)	5.10	5.15	5.16	5.17	5.18	5.18
Volume due to H_2O/MeOH (ml)	5.20	5.25	5.27	5.28	5.28	5.29
Volume of H_2O	4.80	4.75	4.73	4.72	4.72	4.71

B5   Calcium Carbonate – CaCO$_3$

Table 70: CaCO$_3$ volumes required.

R/C	100	200	400
Volume of Formalin (ml)	10.44	10.47	10.49
Volume due to F (ml)	5.17	5.18	5.19
Volume due to H$_2$O/MeOH (ml)	5.27	5.29	5.30
Volume of H$_2$O	4.73	4.71	4.70

B6   Barium Carbonate – BaCO$_3$

Table 71: BaCO$_3$ volumes required.

R/C	100	200	400
Volume of Formalin (ml)	10.38	10.44	10.47
Volume due to F (ml)	5.14	5.17	5.18
Volume due to H$_2$O/MeOH (ml)	5.24	5.27	5.29
Volume of H$_2$O	4.76	4.73	4.71

B7   Ammonium Carbonate – (NH$_4$)$_2$CO$_3$

Table 72: (NH$_4$)$_2$CO$_3$ volumes required.

R/C	100	200	400
Volume of Formalin (ml)	10.44	10.47	10.49
Volume due to F (ml)	5.17	5.18	5.19
Volume due to H$_2$O/MeOH (ml)	5.27	5.29	5.30
Volume of H$_2$O	4.73	4.71	4.70

B8   No Carbonate

Table 73: No carbonate volumes required.

R/C	-
Volume of Formalin (ml)	10.50
Volume due to F (ml)	5.20
Volume due to H$_2$O/MeOH (ml)	5.30
Volume of H$_2$O	4.70

Appendix C – Metal Carbonate/Ammonium Carbonate (50:50) Hydrogel Reaction Compositions

This Appendix details the masses of resorcinol, formaldehyde, metal carbonate and ammonium carbonate required for each combination studied. Total mass is again fixed at 12 g.

C1   Sodium Carbonate/Ammonium Carbonate

Table 74: $Na_2CO_3/(NH_4)_2CO_3\_50$ composition.

R/C 50	Equivalent Moles	Equivalent Mass (g)	Percentage Mass (%)	Required Mass (g)
Resorcinol	1.0000	110.1100	63.9493	7.6739
Formaldehyde	2.0000	60.0524	34.8770	4.1852
Na_2CO_3	0.0100	1.0599	0.6156	0.07387
$(NH_4)_2CO_3$	0.0100	0.9609	0.5581	0.06697
Total		172.1832	100.0000	12.0000

Table 75: $Na_2CO_3/(NH_4)_2CO_3\_100$ composition.

R/C 100	Equivalent Moles	Equivalent Mass (g)	Percentage Mass (%)	Required Mass (g)
Resorcinol	1.0000	110.1100	64.3268	7.7192
Formaldehyde	2.0000	60.0524	35.0829	4.2099
Na_2CO_3	0.0050	0.5299	0.3096	0.03715
$(NH_4)_2CO_3$	0.0050	0.4805	0.2807	0.03368
Total		171.1728	100.0000	12.0000

Table 76: $Na_2CO_3/(NH_4)_2CO_3\_200$ composition.

R/C 200	Equivalent Moles	Equivalent Mass (g)	Percentage Mass (%)	Required Mass (g)
Resorcinol	1.0000	110.1100	64.5172	7.7421
Formaldehyde	2.0000	60.0524	35.1868	4.2224
Na_2CO_3	0.0025	0.2650	0.1553	0.01863
$(NH_4)_2CO_3$	0.0025	0.2402	0.1408	0.01689
Total		170.6676	100.0000	12.0000

C2 Potassium Carbonate/Ammonium Carbonate

Table 77: K_2CO_3/$(NH_4)_2CO_3$_50 composition.

R/C 50	Equivalent Moles	Equivalent Mass (g)	Percentage Mass (%)	Required Mass (g)
Resorcinol	1.0000	110.1100	63.8299	7.6596
Formaldehyde	2.0000	60.0524	34.8119	4.1774
K_2CO_3	0.0100	1.3821	0.8012	0.09614
$(NH_4)_2CO_3$	0.0100	0.9609	0.5570	0.06684
Total		172.5054	100.0000	12.0000

Table 78: K_2CO_3/$(NH_4)_2CO_3$_100 composition.

R/C 100	Equivalent Moles	Equivalent Mass (g)	Percentage Mass (%)	Required Mass (g)
Resorcinol	1.0000	110.1100	64.2663	7.7120
Formaldehyde	2.0000	60.0524	35.0499	4.2060
K_2CO_3	0.0050	0.6910	0.4033	0.04840
$(NH_4)_2CO_3$	0.0050	0.4805	0.2804	0.03365
Total		171.3339	100.0000	12.0000

Table 79: K_2CO_3/$(NH_4)_2CO_3$_200 composition.

R/C 200	Equivalent Moles	Equivalent Mass (g)	Percentage Mass (%)	Required Mass (g)
Resorcinol	1.0000	110.1100	64.4868	7.7384
Formaldehyde	2.0000	60.0524	35.1702	4.2204
K_2CO_3	0.0025	0.3455	0.2024	0.02428
$(NH_4)_2CO_3$	0.0025	0.2402	0.1407	0.01688
Total		170.7481	100.0000	12.0000

C3 Caesium Carbonate/Ammonium Carbonate

Table 80: Cs_2CO_3/$(NH_4)_2CO_3$_50 composition.

R/C 50	Equivalent Moles	Equivalent Mass (g)	Percentage Mass (%)	Required Mass (g)
Resorcinol	1.0000	110.1100	63.1432	7.5772
Formaldehyde	2.0000	60.0524	34.4374	4.1325
Cs_2CO_3	0.0100	3.2582	1.8684	0.22421
$(NH_4)_2CO_3$	0.0100	0.9609	0.5510	0.06612
Total		174.3815	100.0000	12.0000

R/C 100	Equivalent Moles	Equivalent Mass (g)	Percentage Mass (%)	Required Mass (g)
Resorcinol	1.0000	110.1100	63.9164	7.6700
Formaldehyde	2.0000	60.0524	34.8591	4.1831
Cs$_2$CO$_3$	0.0050	1.6291	0.9457	0.11348
(NH$_4$)$_2$CO$_3$	0.0050	0.4805	0.2789	0.03347
Total		172.2720	100.0000	12.0000

Table 82: Cs$_2$CO$_3$/(NH$_4$)$_2$CO$_3$_200 composition.

R/C 200	Equivalent Moles	Equivalent Mass (g)	Percentage Mass (%)	Required Mass (g)
Resorcinol	1.0000	110.1100	64.3101	7.7172
Formaldehyde	2.0000	60.0524	35.0738	4.2089
Cs$_2$CO$_3$	0.0025	0.8146	0.4757	0.05709
(NH$_4$)$_2$CO$_3$	0.0025	0.2402	0.1403	0.01684
Total		171.2172	100.0000	12.0000

C4   Calcium Carbonate/Ammonium Carbonate

Table 83: CaCO$_3$/(NH$_4$)$_2$CO$_3$_50 composition.

R/C 50	Equivalent Moles	Equivalent Mass (g)	Percentage Mass (%)	Required Mass (g)
Resorcinol	1.0000	110.1100	63.9712	7.6765
Formaldehyde	2.0000	60.0524	34.8890	4.1867
CaCO$_3$	0.0100	1.001	0.5815	0.06978
(NH$_4$)$_2$CO$_3$	0.0100	0.9609	0.5583	0.06699
Total		172.1242	100.0000	12.0000

Table 84: CaCO$_3$/(NH$_4$)$_2$CO$_3$_100 composition.

R/C 100	Equivalent Moles	Equivalent Mass (g)	Percentage Mass (%)	Required Mass (g)
Resorcinol	1.0000	110.1100	64.3379	7.7205
Formaldehyde	2.0000	60.0524	35.0890	4.2107
CaCO$_3$	0.0050	0.5005	0.2924	0.03509
(NH$_4$)$_2$CO$_3$	0.0050	0.4805	0.2807	0.03369
Total		171.1433	100.0000	12.0000

R/C 200	Equivalent Moles	Equivalent Mass (g)	Percentage Mass (%)	Required Mass (g)
Resorcinol	1.0000	110.1100	64.5228	7.7427
Formaldehyde	2.0000	60.0524	35.1898	4.2228
CaCO$_3$	0.0025	0.2502	0.1466	0.0176
(NH$_4$)$_2$CO$_3$	0.0025	0.2402	0.1408	0.0169
Total		170.6529	100.0000	12.0000

Appendix D – Metal Carbonate/Ammonium Carbonate Hydrogel Calculated Reaction Volumes

This Appendix details the volumes of both formalin and additional deionised water required for each of the hydrogel compositions detailed in Appendix C.

D1   Sodium Carbonate/Ammonium Carbonate

Table 86: $Na_2CO_3/(NH_4)_2CO_3$ volumes required.

R/C	50	100	200
Volume of Formalin (ml)	10.37	10.44	10.47
Volume due to F (ml)	5.14	5.17	5.18
Volume due to H_2O/MeOH (ml)	5.23	5.27	5.29
Volume of H_2O	4.77	4.73	4.71

D2   Potassium Carbonate/Ammonium Carbonate

Table 87: $K_2CO_3/(NH_4)_2CO_3$ volumes required.

R/C	50	100	200
Volume of Formalin (ml)	10.36	10.43	10.46
Volume due to F (ml)	5.13	5.16	5.18
Volume due to H_2O/MeOH (ml)	5.23	5.27	5.28
Volume of H_2O	4.77	4.73	4.72

D3   Caesium Carbonate/Ammonium Carbonate

Table 88: $Cs_2CO_3/(NH_4)_2CO_3$ volumes required.

R/C	50	100	200
Volume of Formalin (ml)	10.25	10.37	10.44
Volume due to F (ml)	5.07	5.13	5.16
Volume due to H_2O/MeOH (ml)	5.18	5.24	5.28
Volume of H_2O	4.82	4.76	4.72

D4   Calcium Carbonate/Ammonium Carbonate

Table 89: $CaCO_3/(NH_4)_2CO_3$ volumes required.

R/C	50	100	200
Volume of Formalin (ml)	10.38	10.44	10.47
Volume due to F (ml)	5.14	5.17	5.18
Volume due to H_2O/MeOH (ml)	5.24	5.27	5.29
Volume of H_2O	4.76	4.73	4.71

Appendix E – Secondary Metal Carbonate Addition Hydrogel Reaction Compositions

This Appendix details the masses of resorcinol, formaldehyde and metal carbonate required for each secondary addition of carbonate hydrogel. The total mass of solids is maintained at 12 g. Metal carbonates are added in a ratio of 50:50, with a total R/C of 100.

E1   Caesium Carbonate Parent

Table 90: $Cs_2CO_3/Na_2CO_3\_100$ 50:50 composition.

Na_2CO_3	Equivalent Moles	Equivalent Mass (g)	Percentage Mass (%)	Required Mass (g)
Resorcinol	1.0000	110.1100	63.8980	7.6678
Formaldehyde	2.0000	60.0524	34.8491	4.1819
Cs_2CO_3	0.0050	1.6291	0.9454	0.11345
Na_2CO_3	0.0050	0.5299	0.3075	0.03690
Total		172.3214	100.0000	12.0000

E2   Calcium Carbonate Parent

Table 91: $CaCO_3/Li_2CO_3\_100$ 50:50 composition.

Li_2CO_3	Equivalent Moles	Equivalent Mass (g)	Percentage Mass (%)	Required Mass (g)
Resorcinol	1.0000	110.1100	64.3797	7.7256
Formaldehyde	2.0000	60.0524	35.1117	4.2134
$CaCO_3$	0.0050	0.5005	0.2926	0.03511
Li_2CO_3	0.0050	0.3695	0.2160	0.02592
Total		171.0323	100.0000	12.0000

Table 92: $CaCO_3/Na_2CO_3\_100$ 50:50 composition.

Na_2CO_3	Equivalent Moles	Equivalent Mass (g)	Percentage Mass (%)	Required Mass (g)
Resorcinol	1.0000	110.1100	64.3193	7.7183
Formaldehyde	2.0000	60.0524	35.0788	4.2095
$CaCO_3$	0.0050	0.5005	0.2923	0.03508
Na_2CO_3	0.0050	0.5299	0.3096	0.03715
Total		171.1928	100.0000	12.0000

Table 93: CaCO$_3$/K$_2$CO$_3$_100 50:50 composition.

K$_2$CO$_3$	Equivalent Moles	Equivalent Mass (g)	Percentage Mass (%)	Required Mass (g)
Resorcinol	1.0000	110.1100	64.2588	7.7111
Formaldehyde	2.0000	60.0524	35.0458	4.2055
CaCO$_3$	0.0050	0.5005	0.2921	0.03505
K$_2$CO$_3$	0.0050	0.6910	0.4033	0.04839
Total		171.3539	100.0000	12.0000

E3 Barium Carbonate Parent

Table 94: BaCO$_3$/Na$_2$CO$_3$_100 50:50 composition.

Na$_2$CO$_3$	Equivalent Moles	Equivalent Mass (g)	Percentage Mass (%)	Required Mass (g)
Resorcinol	1.0000	110.1100	64.1371	7.6965
Formaldehyde	2.0000	60.0524	34.9795	4.1975
BaCO$_3$	0.0050	0.9867	0.5747	0.06897
Na$_2$CO$_3$	0.0050	0.5299	0.3087	0.03704
Total		171.6790	100.0000	12.0000

E4 Alternative Catalyst Ratio

The alternative catalyst ratio of 25:75 was also used. Total solids remained at 12 g and the total R/C kept at 100.

Table 95: CaCO$_3$/Na$_2$CO$_3$_100 25:75 composition.

Na$_2$CO$_3$	Equivalent Moles	Equivalent Mass (g)	Percentage Mass (%)	Required Mass (g)
Resorcinol	1.0000	110.1100	64.3138	7.7177
Formaldehyde	2.0000	60.0524	35.0758	4.2091
CaCO$_3$	0.0025	0.2502	0.1462	0.01754
Na$_2$CO$_3$	0.0075	0.7949	0.4643	0.05572
Total		171.2075	100.0000	12.0000

Appendix F – Secondary Metal Carbonate Addition Calculated Reaction Volumes

This Appendix details the volumes of both formalin and additional deionised water required for each of the hydrogel compositions detailed in Appendix E.

F1   Caesium Carbonate Parent

Table 96: Caesium carbonate parent volumes required, 50:50 ratio.

Secondary Carbonate	Na
Volume of Formalin (ml)	10.37
Volume due to F (ml)	5.13
Volume due to H_2O/MeOH (ml)	5.24
Volume of H_2O	4.76

F2   Calcium Carbonate Parent

Table 97: Calcium carbonate parent volumes required, 50:50 ratio.

Secondary Carbonate	Li	Na	K
Volume of Formalin (ml)	10.45	10.44	10.43
Volume due to F (ml)	5.17	5.17	5.16
Volume due to H_2O/MeOH (ml)	5.28	5.27	5.27
Volume of H_2O	4.72	4.73	4.73

F3   Barium Carbonate Parent

Table 98: Barium carbonate parent volumes required, 50:50 ratio.

Secondary Carbonate	Na
Volume of Formalin (ml)	10.41
Volume due to F (ml)	5.15
Volume due to H_2O/MeOH (ml)	5.26
Volume of H_2O	4.74

F4   Calcium Carbonate Parent Alternative Ratio

Table 99: Calcium carbonate parent volumes required, 25:75 ratio.

Secondary Carbonate	Na
Volume of Formalin (ml)	10.44
Volume due to F (ml)	5.16
Volume due to H_2O/MeOH (ml)	5.28
Volume of H_2O	4.72

Appendix G – Half Volume Hydrogel Reaction Compositions

This Appendix details the masses of resorcinol, formaldehyde and metal carbonate required for each of the hydrogels studied which had their total volume reduced to 30 ml.

The total mass of solids is fixed at 6 g in each case.

G1   Sodium Carbonate – Na$_2$CO$_3$

Table 100: Na$_2$CO$_3$_100 composition.

R/C 100	Equivalent Moles	Equivalent Mass (g)	Percentage Mass (%)	Required Mass (g)
Resorcinol	1.0000	110.1100	64.3082	3.8585
Formaldehyde	2.0000	60.0524	35.0728	2.1044
Carbonate	0.0100	1.0599	0.6190	0.03714
Total		171.2223	100.0000	6.0000

G2   Caesium Carbonate – Cs$_2$CO$_3$

Table 101: Cs$_2$CO$_3$_100 composition.

R/C 100	Equivalent Moles	Equivalent Mass (g)	Percentage Mass (%)	Required Mass (g)
Resorcinol	1.0000	110.1100	64.3304	3.8598
Formaldehyde	2.0000	60.0524	35.0849	2.1051
Carbonate	0.0100	1.001	0.5848	0.03509
Total		171.1633	100.0000	6.0000

G3   Calcium Carbonate – CaCO$_3$

Table 102: CaCO$_3$_100 composition.

R/C 100	Equivalent Moles	Equivalent Mass (g)	Percentage Mass (%)	Required Mass (g)
Resorcinol	1.0000	110.1100	64.3304	3.8598
Formaldehyde	2.0000	60.0524	35.0849	2.1051
Carbonate	0.0100	1.001	0.5848	0.03509
Total		171.1633	100.0000	6.0000

G4   Barium Carbonate – BaCO$_3$

Table 103: BaCO$_3$_100 composition.

R/C 100	Equivalent Moles	Equivalent Mass (g)	Percentage Mass (%)	Required Mass (g)
Resorcinol	1.0000	110.1100	63.9669	3.8380
Formaldehyde	2.0000	60.0524	34.8866	2.0932
Carbonate	0.0100	1.9734	1.1464	0.06879
Total		172.1358	100.0000	6.0000

Appendix H – Half Volume Hydrogel Calculated Reaction Volumes

This Appendix details the volumes of both formalin and additional deionised water required for each of the half volume hydrogel compositions detailed in Appendix I.

Table 104: R/C 100 volumes required.

Carbonate	Na	Cs	Ca	Ba
Volume of Formalin (ml)	5.22	5.15	5.22	5.24
Volume due to F (ml)	2.58	2.55	2.58	2.59
Volume due to H_2O/MeOH (ml)	2.64	2.60	2.64	2.65
Volume of H_2O	2.36	2.40	2.36	2.35

Appendix I – Additional Results Related to Gels Synthesised with Group I Metal Carbonate Catalysts.

This Appendix displays the results cited in Chapter 5, but not included in the main text.

It contains additional DLS autocorrelation functions, average DLS scattered light intensities, nitrogen adsorption/desorption isotherms and pore size distributions.
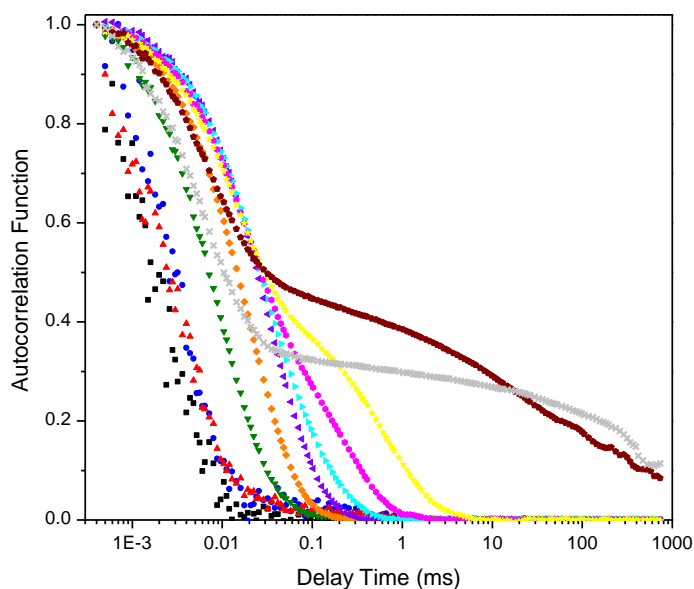
Figure 113: DLS autocorrelation functions for a sodium carbonate gel with R/C 400 at 0% (■), 10% (●), 20% (▲), 30% (▼), 40% (◆), 50% (◀), 60% (▶), 70% (●), 80% (★), 90% (⬟) and 100% (✕) of the total gel time.
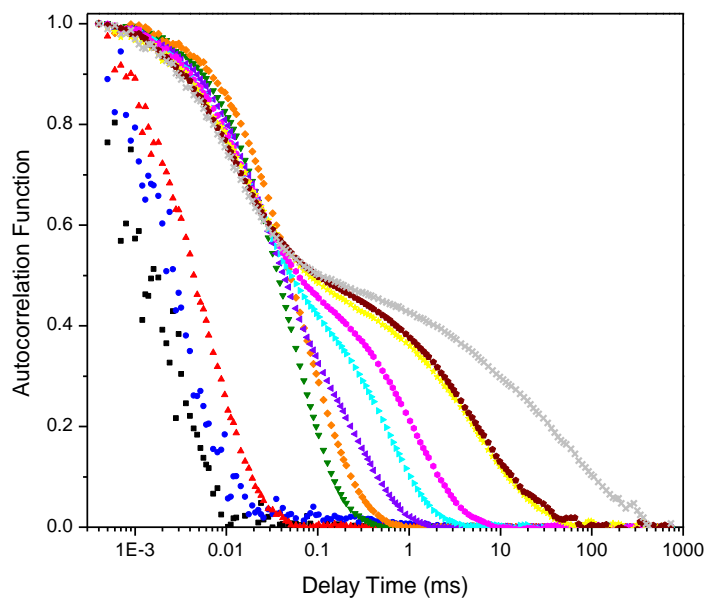
Figure 114: DLS autocorrelation functions for a sodium carbonate with R/C 600 at 0% (■), 10% (●), 20% (▲), 30% (▼), 40% (◆), 50% (◀), 60% (▶), 70% (⬢), 80% (★), 90% (⬢) and 100% (✕) of the total gel time.
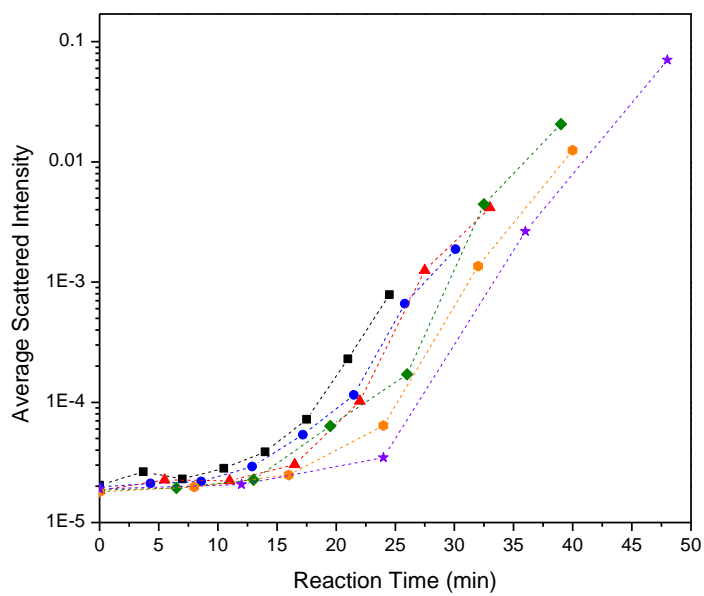
Figure 115: Average DLS scattered intensities for the lithium carbonate gels series at R/C ratios of 100 (■), 200 (●), 300 (▲), 400 (◆), 500 (●) and 600 (★).
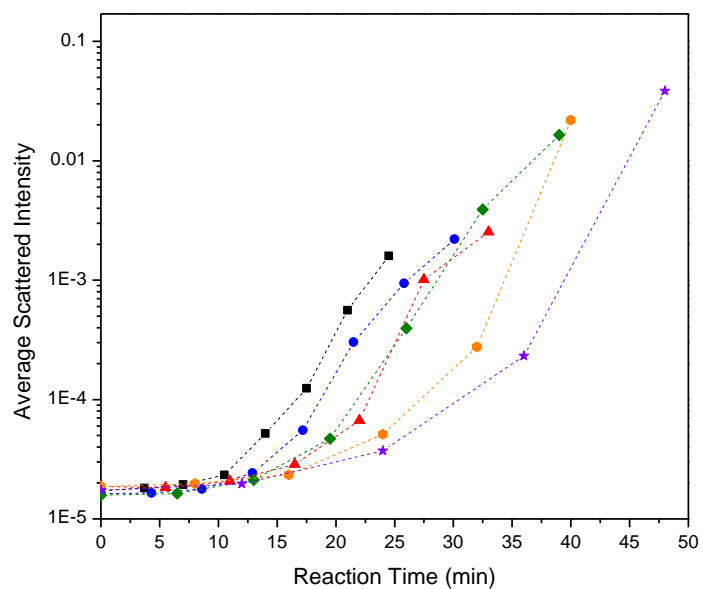
Figure 116: Average DLS scattered intensities for the potassium carbonate gels series at R/C ratios of 100 (■), 200 (●), 300 (▲), 400 (◆), 500 (●) and 600 (★).
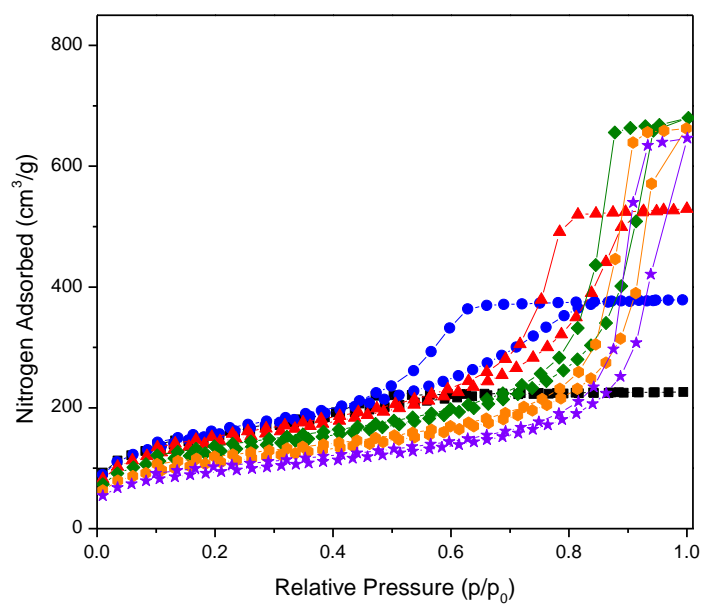
Figure 117: Nitrogen adsorption/desorption isotherms for lithium carbonate gels, at R/C ratios of 100 (■), 200 (●), 300 (▲), 400 (◆), 500 (●) and 600 (★).
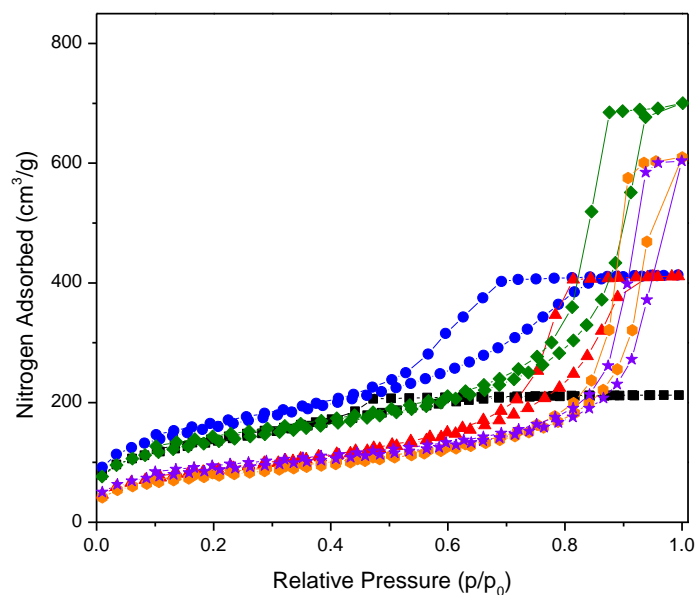
Figure 118: Nitrogen adsorption/desorption isotherms for potassium carbonate gels, at R/C ratios of 100 (■), 200 (●), 300 (▲), 400 (◆), 500 (●) and 600 (★).
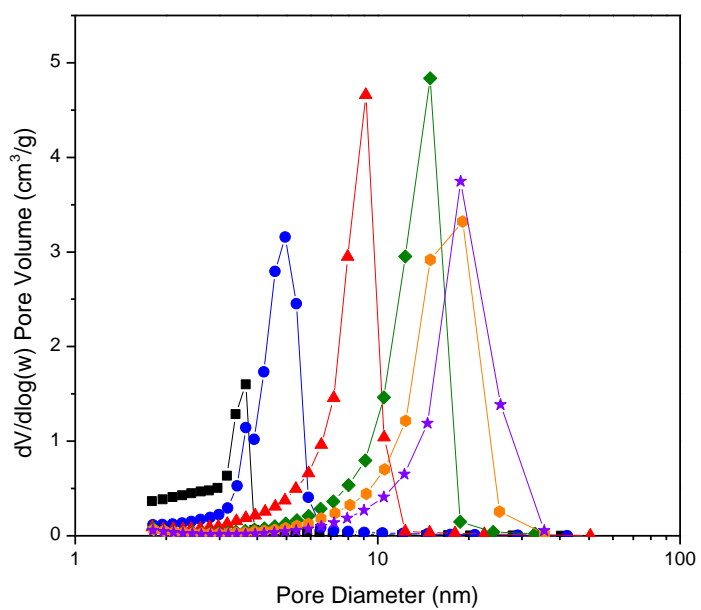
Figure 119: Pore size distributions for lithium carbonate gels, at R/C ratios of 100 (■), 200 (●), 300 (▲), 400 (◆), 500 (●) and 600 (★).
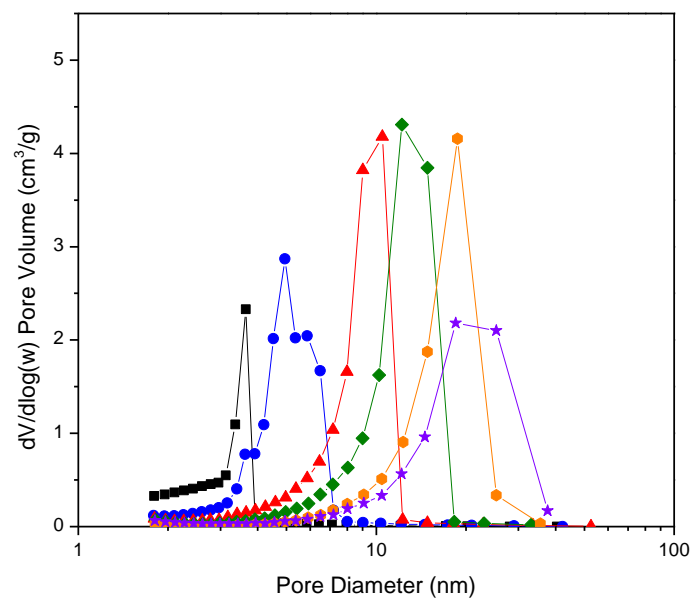
Figure 120: Pore size distributions for potassium carbonate gels, at R/C ratios of 100 (■), 200 (●), 300 (▲), 400 (◆), 500 (⬡) and 600 (★).

This Appendix details the results cited in Chapter 6, but not included in the main text.

It contains additional DLS autocorrelation functions.
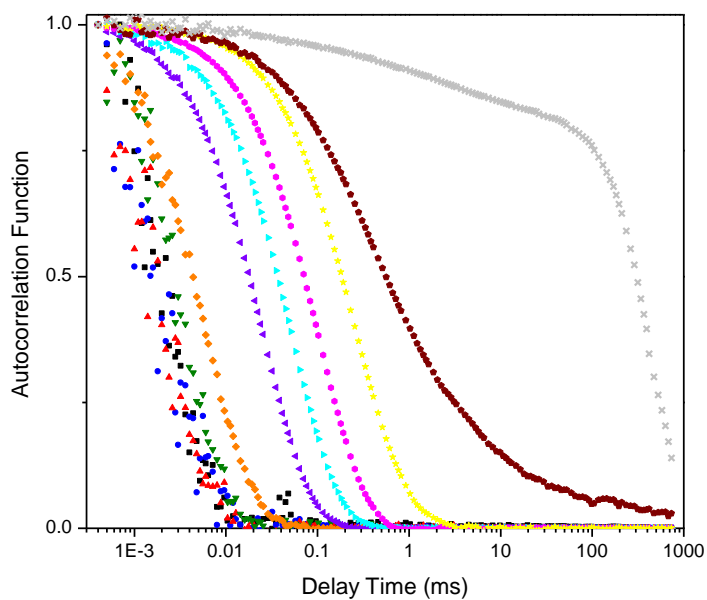
Figure 121: DLS autocorrelation functions obtained for a calcium carbonate gel with R/C 200 at 0% (■), 10% (●), 20% (▲), 30% (▼), 40% (◆), 50% (◀), 60% (▶), 70% (●), 80% (★), 90% (⬠) and 100% (✕) of the total gel time.
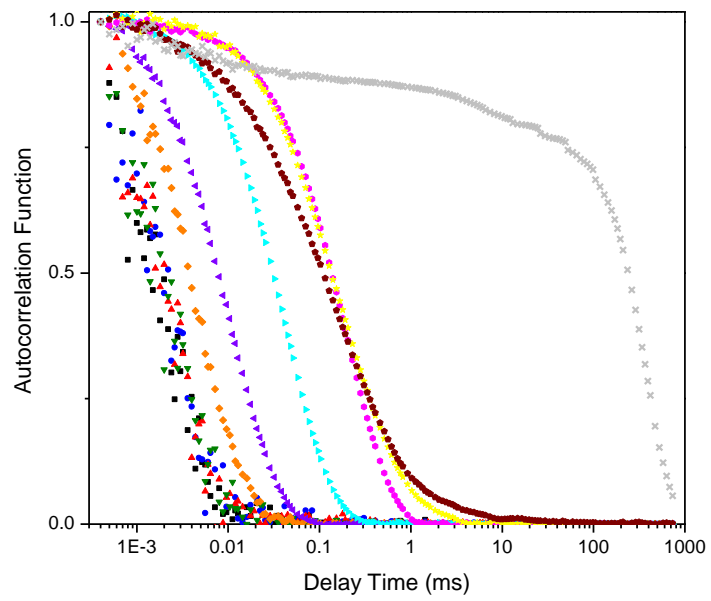
Figure 122: DLS autocorrelation functions obtained for a calcium carbonate gel with R/C 400 at 0% (■), 10% (●), 20% (▲), 30% (▼), 40% (◆), 50% (◀), 60% (▶), 70% (⬣), 80% (★), 90% (⬟) and 100% (✕) of the total gel time.

Appendix K – Additional Results Related to Gels Synthesised with Ammonium Carbonate as a Catalyst

This Appendix displays the results cited in Chapter 7, but not included in the main text.

It contains additional nitrogen adsorption/desorption isotherms, pore size distributions and textural properties.
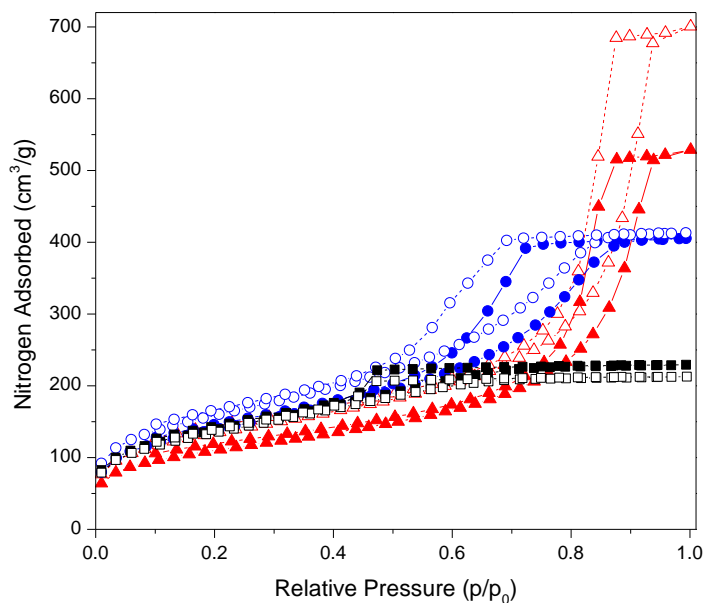
Figure 123: Comparative nitrogen adsorption/desorption isotherms between mixed K_2CO_3/$(NH_4)_2CO_3$ gels at R/C 50 (■), 100 (●) and 200 (▲), and pure K_2CO_3 gels at R/C 100 (□), 200 (○), and 400 (△).
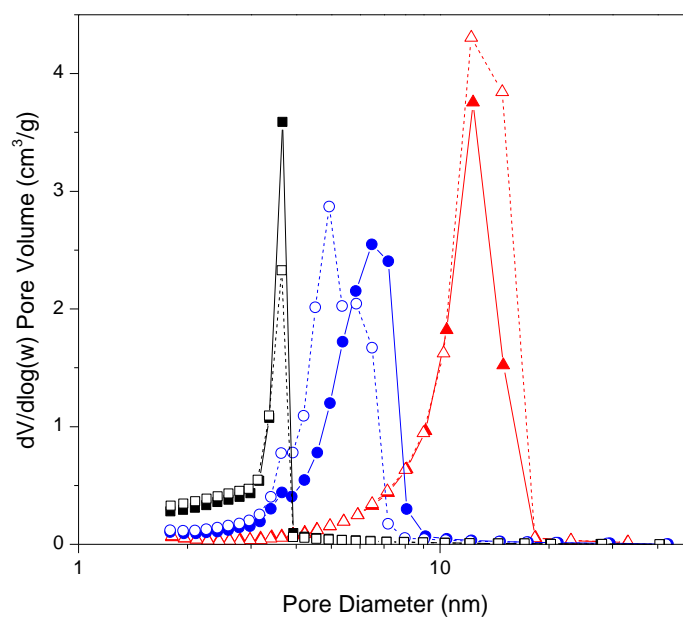
Figure 124: Comparative pore size distributions between mixed $K_2CO_3/(NH_4)_2CO_3$ gels at R/C 50 (■), 100 (●) and 200 (▲), and pure K_2CO_3 gels at R/C 100 (□), 200 (○), and 400 (△).

Table 105: Comparison of gel textural properties for pure K_2CO_3 gels and mixed $K_2CO_3/(NH_4)_2CO_3$ gels.

Sample	S_{BET} (m^2/g)	V_{Tot} (cm^3/g)	V_μ (cm^3/g)	d_p avg. (nm)
$K_2CO_3/$ $(NH_4)_2CO_3\_50$	481 ± 4	0.35	0.04	3.1
$K_2CO_3/$ $(NH_4)_2CO_3\_100$	484 ± 4	0.63	0.03	5.4
$K_2CO_3/$ $(NH_4)_2CO_3\_200$	381 ± 4	0.82	0.03	10.1
$K_2CO_3\_100$	472 ± 4	0.33	0.03	3.0
$K_2CO_3\_200$	554 ± 5	0.64	0.04	4.7
$K_2CO_3\_400$	465 ± 5	1.08	0.04	10.9

Appendix L – Additional Results Related to Gels Synthesised with Secondary Addition of Metal Carbonate

This Appendix displays the results cited in Chapter 8, but not included in the main text.

It contains additional DLS autocorrelation functions, average DLS scattered light intensities, nitrogen adsorption/desorption isotherms and pore size distributions.
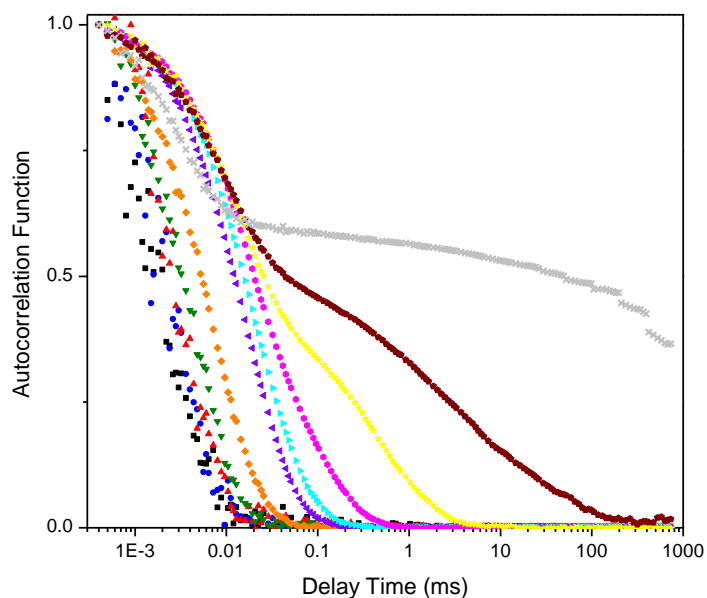
Figure 125: DLS autocorrelation functions obtained for simultaneous addition of calcium and lithium carbonate at 0% (■), 10% (●), 20% (▲), 30% (▼), 40% (◆), 50% (◀), 60% (▶), 70% (⬤), 80% (★), 90% (⬠) and 100% (✕) of the total gel time.
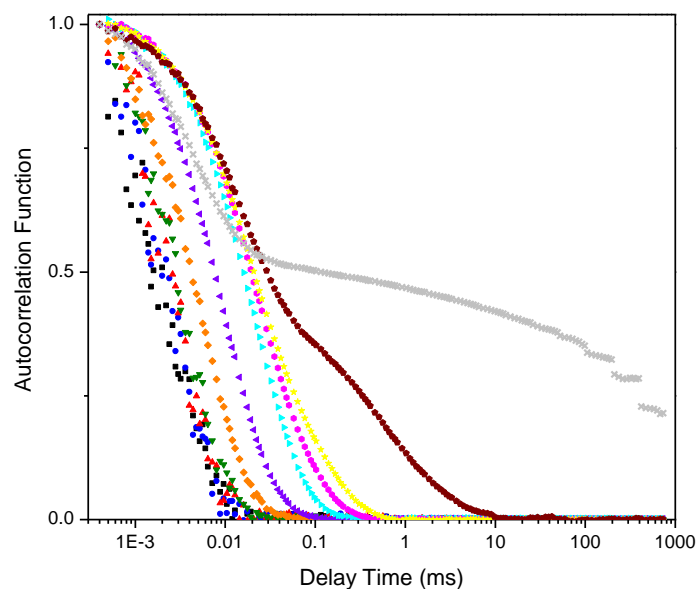
Figure 126: DLS autocorrelation functions obtained for simultaneous addition of calcium and potassium carbonate at 0% (■), 10% (●), 20% (▲), 30% (▼), 40% (◆), 50% (◀), 60% (▶), 70% (●), 80% (★), 90% (⬟) and 100% (✕) of the total gel time.
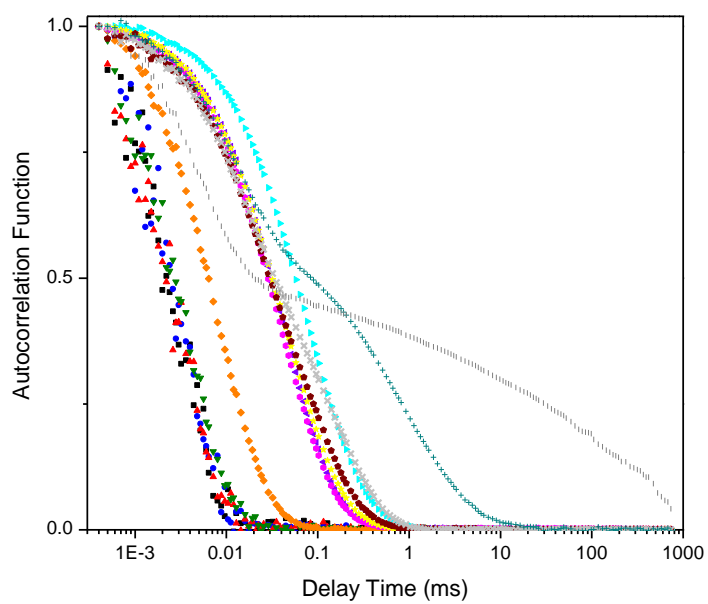
Figure 127: DLS autocorrelation functions obtained for 60% addition of sodium carbonate to caesium carbonate at 0% (■), 10% (●), 20% (▲), 30% (▼), 40% (◆), 50% (◀), 60% (▶), 70% (●), 80% (★), 90% (⬟), 100% (✕), 110% (+) and 120% (I) of the parent total gel time.
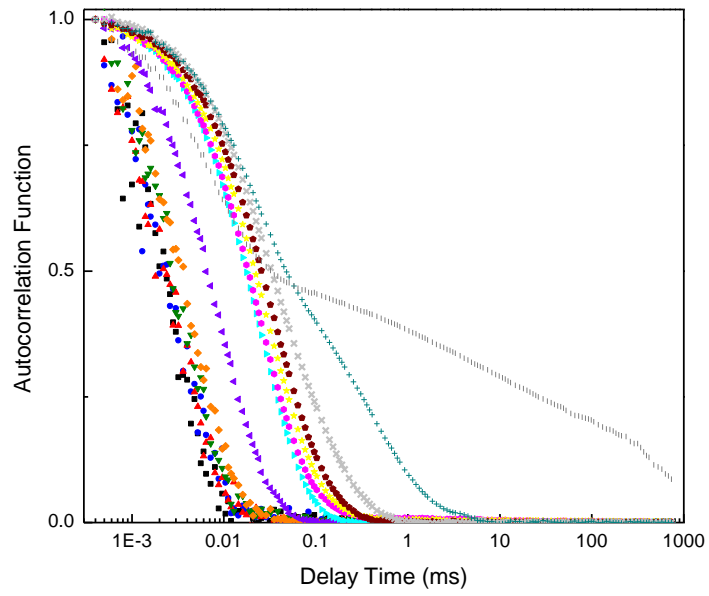
Figure 128: DLS autocorrelation functions obtained for 60% addition of sodium carbonate to barium carbonate at 0% (■), 10% (●), 20% (▲), 30% (▼), 40% (◆), 50% (◀), 60% (▶), 70% (●), 80% (★), 90% (⬟), 100% (✕), 110% (✛) and 120% (Ɩ) of the parent total gel time.
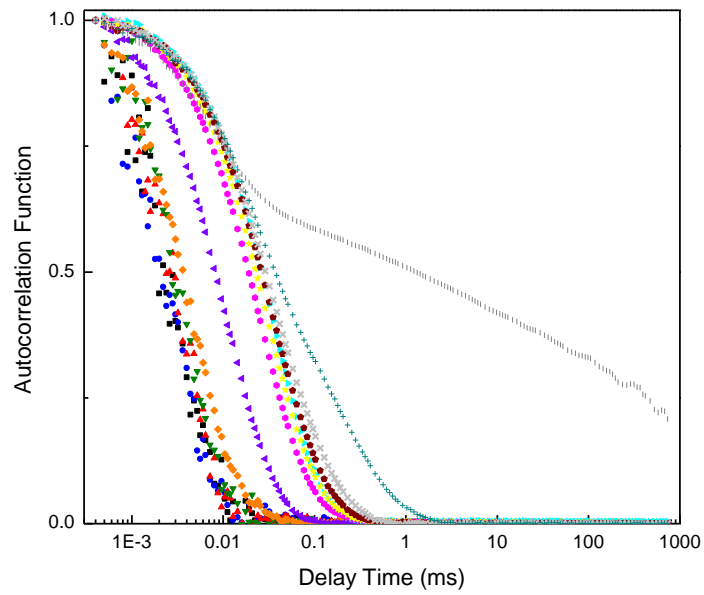
Figure 129: DLS autocorrelation functions obtained for 60% addition of lithium carbonate to calcium carbonate at 0% (■), 10% (●), 20% (▲), 30% (▼), 40% (◆), 50% (◀), 60% (▶), 70% (●), 80% (★), 90% (⬟), 100% (✕), 110% (✛) and 120% (Ɩ) of the parent total gel time.

216
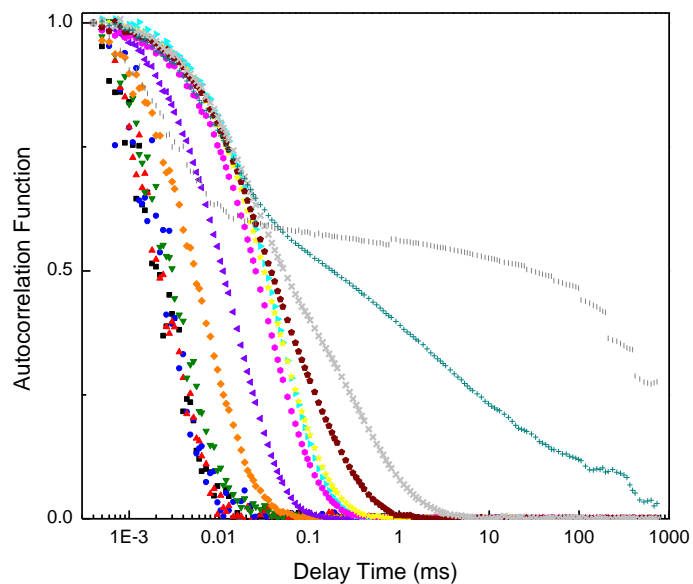
Figure 130: DLS autocorrelation functions obtained for 60% addition of potassium carbonate to calcium carbonate at 0% (■), 10% (●), 20% (▲), 30% (▼), 40% (◆), 50% (◀), 60% (▶), 70% (●), 80% (★), 90% (⬟), 100% (✕), 110% (✛) and 120% (Ɩ) of the parent total gel time.
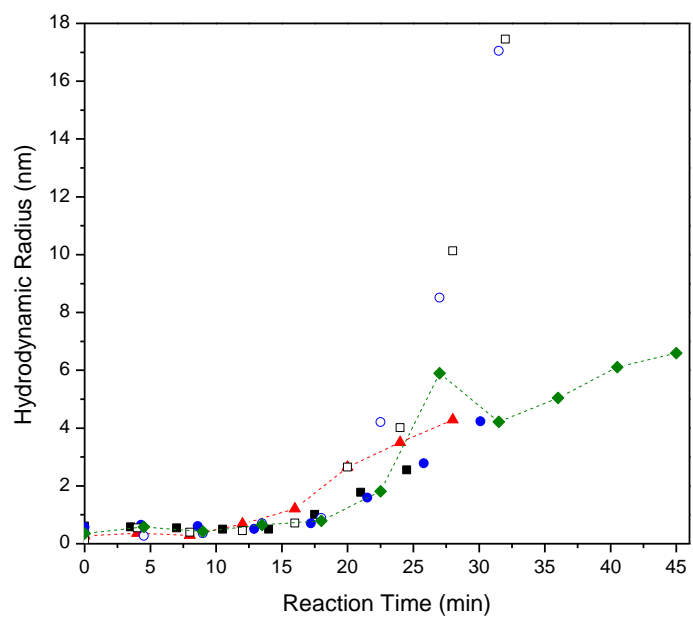
Figure 131: DLS hydrodynamic radii values obtained for lithium carbonate at R/C 100 (■) and 200 (●), calcium carbonate at R/C 100 (□), and 200 (○), simultaneous addition of both carbonates (▲) and 60% delayed addition of lithium carbonate (◆).
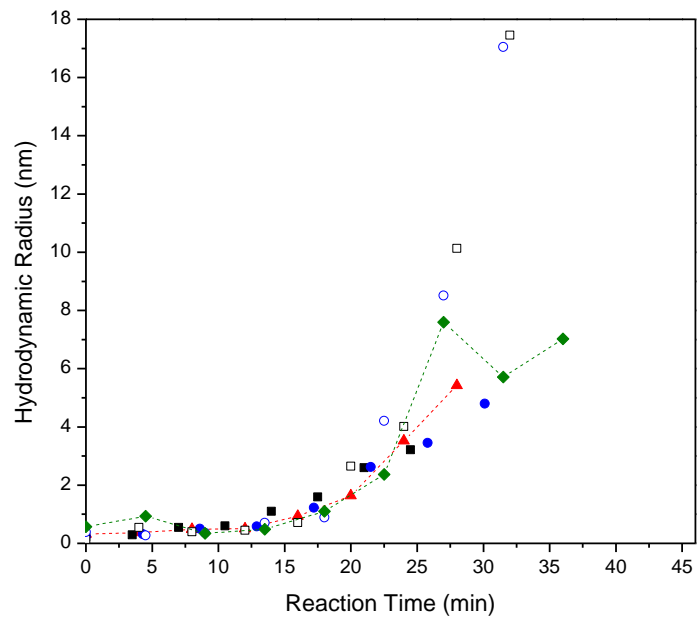
Figure 132: DLS hydrodynamic radii values obtained for potassium carbonate at R/C 100 (■) and 200 (●), calcium carbonate at R/C 100 (□), and 200 (○), simultaneous addition of both carbonates (▲) and 60% delayed addition of potassium carbonate (◆).
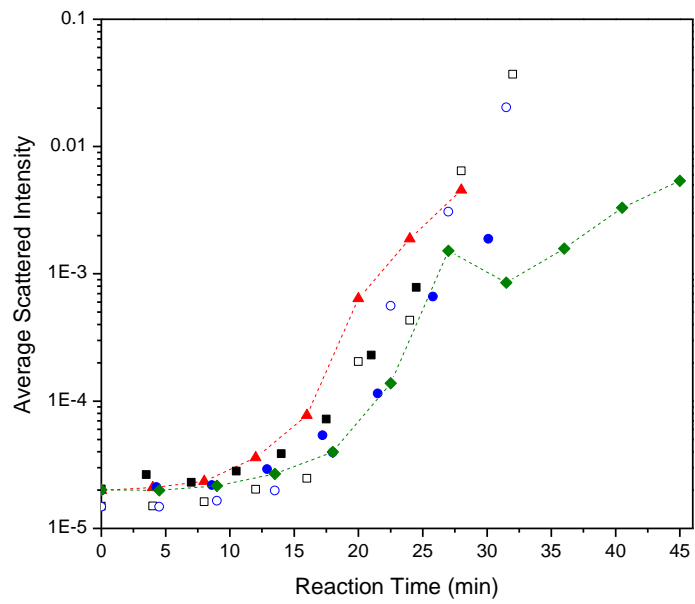
Figure 133: Average DLS scattered intensity for lithium carbonate at R/C 100 (■) and 200 (●), calcium carbonate at R/C 100 (□), and 200 (○), simultaneous addition of both carbonates (▲) and 60% delayed addition of lithium carbonate (◆).
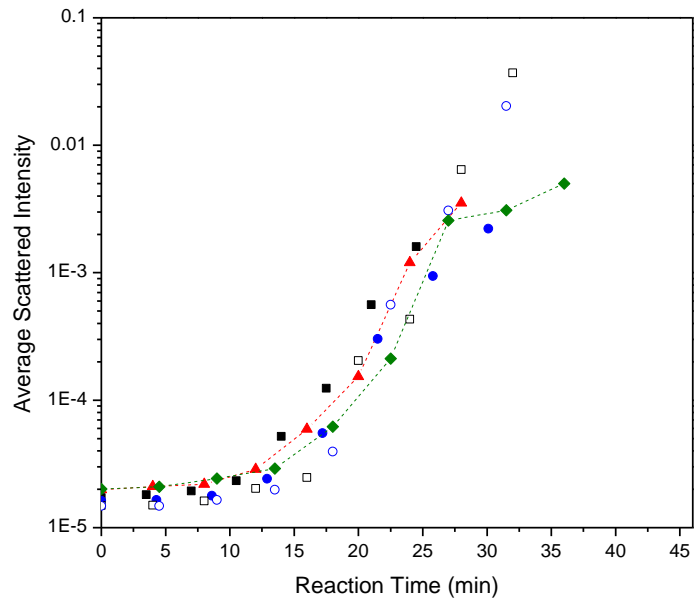
Figure 134: Average DLS scattered intensity for potassium carbonate at R/C 100 (■) and 200 (●), calcium carbonate at R/C 100 (□), and 200 (○), simultaneous addition of both carbonates (▲) and 60% delayed addition of potassium carbonate (◆).
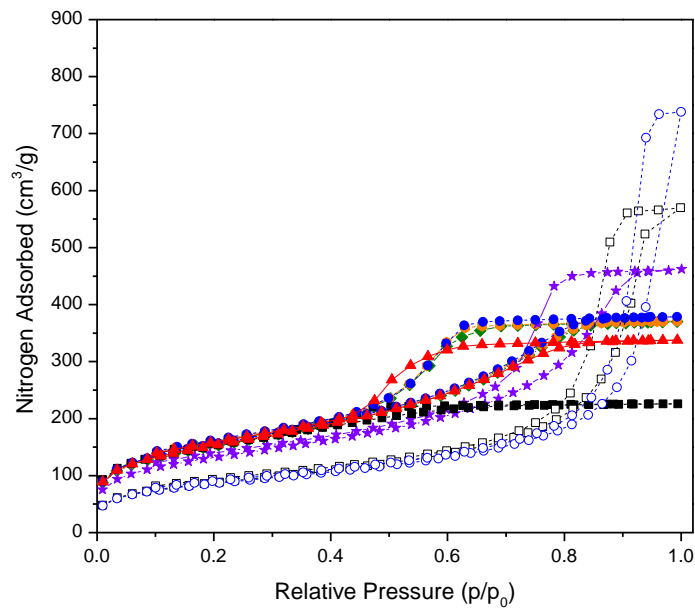
Figure 135: Nitrogen adsorption/desorption isotherms for lithium carbonate at R/C 100 (■) and 200 (●), calcium carbonate at R/C 100 (□) and 200 (○), simultaneous addition of both carbonates (▲) and delayed addition of lithium carbonate at 60% (◆), 70% (●) and 80% (★).
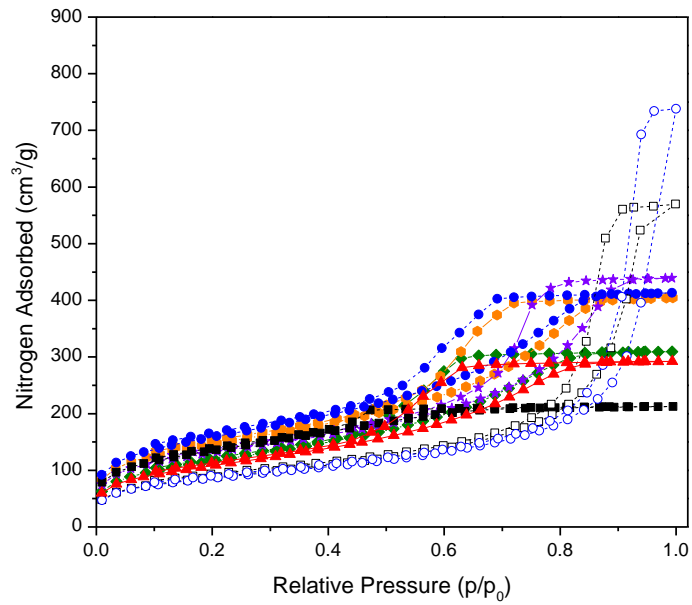
Figure 136: Nitrogen adsorption/desorption isotherms for potassium carbonate at R/C 100 (■) and 200 (●), calcium carbonate at R/C 100 (□) and 200 (○), simultaneous addition of both carbonates (▲) and delayed addition of potassium carbonate at 60% (◆), 70% (●) and 80% (★).
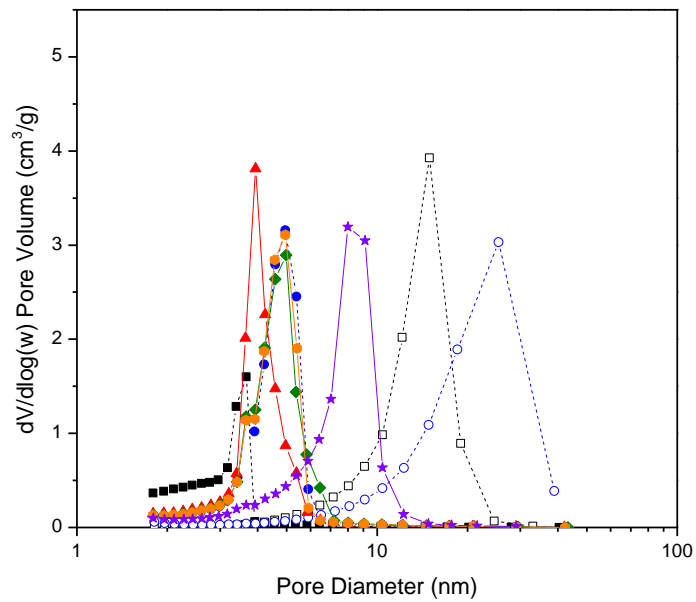
Figure 137: Pore size distributions for lithium carbonate at R/C 100 (■) and 200 (●), calcium carbonate at R/C 100 (□) and 200 (○), simultaneous addition of both carbonates (▲) and delayed addition of lithium carbonate at 60% (◆), 70% (●) and 80% (★).
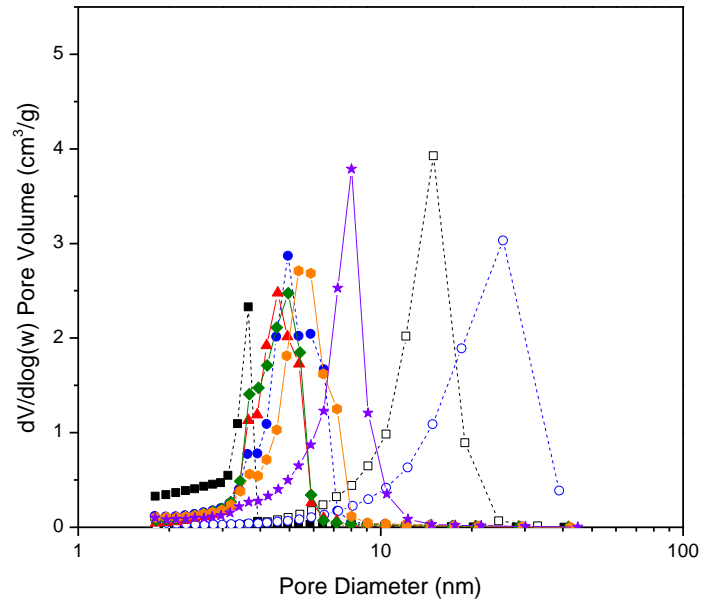
Figure 138: Pore size distributions for potassium carbonate at R/C 100 (■) and 200 (●), calcium carbonate at R/C 100 (□) and 200 (○), simultaneous addition of both carbonates (▲) and delayed addition of potassium carbonate at 60% (◆), 70% (●) and 80% (★).

References

1.   S. S. Kistler, *The Journal of Physical Chemistry*, 1931, **36**, 52-64.
2.   T. Graham, *Journal of the Chemical Society*, 1864, **17**, 318-327.
3.   G. A. Nicolaon and S. J. Teichner, U.S. patent # 3,672,833.
4.   J. L. Gurav, I.-K. Jung, H.-H. Park, E. S. Kang and D. Y. Nadargi, *Journal of Nanomaterials*, 2010, **2010**, 11.
5.   M. Schmidt and F. Schwertfeger, *Journal of Non-Crystalline Solids*, 1998, **225**, 364-368.
6.   J. P. Farinha, Superinsulating Aerogels Arriving on the Construction Market, http://www.ordemengenheiros.pt/fotos/dossier_artigo/josepaulofarinha_aerogel_2014_oeng_137821396053207596d950c.pdf.
7.   NASA, Preventing heat escape through insulation called "aerogel", http://mars.jpl.nasa.gov/mer/mission/sc_rover_temp_aerogel.html, Accessed 10th October, 2014.
8.   Aerogel Image Gallery, http://www.aerogel.org/?p=891&px=%2FFrom+the+Web%2Fcrayonsonaerogel.jpg, Accessed 10th October, 2014.
9.   NASA, Spacecraft Photos - Dust Collector with Aerogel, http://stardust.jpl.nasa.gov/photo/spacecraft.html, Accessed 10th October, 2014.
10.   L. W. Hrubesh, *Journal of Non-Crystalline Solids*, 1998, **225**, 335-342.
11.   J. F. Poco, J. H. Satcher Jr and L. W. Hrubesh, *Journal of Non-Crystalline Solids*, 2001, **285**, 57-63.
12.   G. Zu, J. Shen, X. Wei, X. Ni, Z. Zhang, J. Wang and G. Liu, *Journal of Non-Crystalline Solids*, 2011, **357**, 2903-2906.
13.   V. Štengl, S. Bakardjieva, J. Šubrt and L. Szatmary, *Microporous and Mesoporous Materials*, 2006, **91**, 1-6.
14.   Y. Shimoyama, Y. Ogata, R. Ishibashi and Y. Iwai, *Chemical Engineering Research and Design*, 2010, **88**, 1427-1431.
15.   J. Aguado-Serrano and M. L. Rojas-Cervantes, *Microporous and Mesoporous Materials*, 2006, **88**, 205-213.
16.   T. Skapin, *Journal of Non-Crystalline Solids*, 2001, **285**, 128-134.
17.   H. Rotter, M. V. Landau, M. Carrera, D. Goldfarb and M. Herskowitz, *Applied Catalysis B: Environmental*, 2004, **47**, 111-126.
18.   J. Mrowiec-Białoń, L. Pająk, A. B. Jarzębski, A. I. Lachowski and J. J. Malinowski, *Journal of Non-Crystalline Solids*, 1998, **225**, 115-119.
19.   Z. G. Wu, Y. X. Zhao, L. P. Xu and D. S. Liu, *Journal of Non-Crystalline Solids*, 2003, **330**, 274-277.
20.   D. J. Suh, T.-J. Park, W.-I. Kim and I.-K. Hong, *Journal of Power Sources*, 2003, **117**, 1-6.
21.   A. E. Gash, T. M. Tillotson, J. H. Satcher Jr, L. W. Hrubesh and R. L. Simpson, *Journal of Non-Crystalline Solids*, 2001, **285**, 22-28.
22.   Metal Oxide Aerogels, http://www.aerogel.org/?p=44, Accessed 18th September, 2014.
23.   J. L. Mohanan and S. L. Brock, *Journal of Non-Crystalline Solids*, 2004, **350**, 1-8.
24.   K. K. Kalebaila, D. G. Georgiev and S. L. Brock, *Journal of Non-Crystalline Solids*, 2006, **352**, 232-240.
25.   T. M. Tillotson, W. E. Sunderland, I. M. Thomas and L. W. Hrubesh, *Journal of Sol-Gel Science and Technology*, 1994, **1**, 241-249.
26.   U. Klett and J. Fricke, *Journal of Non-Crystalline Solids*, 1998, **225**, 188-191.

27. P. Fabrizioli, T. Burgi, M. Burgener, S. van Doorslaer and A. Baiker, *Journal of Materials Chemistry*, 2002, **12**, 619-630.
28. B. J. Clapsaddle, D. W. Sprehn, A. E. Gash, J. H. Satcher Jr and R. L. Simpson, *Journal of Non-Crystalline Solids*, 2004, **350**, 173-181.
29. T. M. Tillotson, A. E. Gash, R. L. Simpson, L. W. Hrubesh, J. H. Satcher Jr and J. F. Poco, *Journal of Non-Crystalline Solids*, 2001, **285**, 338-345.
30. B. J. Clapsaddle, L. Zhao, A. E. Gash, J. H. Satcher, K. J. Shea, M. L. Pantoya and R. L. Simpson, *MRS Online Proceedings Library*, 2003, **800**, null-null.
31. R. W. Pekala, *J. Mater. Sci.*, 1989, **24**, 3221-3227.
32. R. W. Pekala and F. M. Kong, *Journal de Physique*, 1989, **50**, 33.
33. P. H. Tewari, A. J. Hunt and K. D. Lofftus, in *Aerogels*, ed. J. Fricke, Springer Berlin Heidelberg, 1986, pp. 31-37.
34. R. B. Durairaj, *Resorcinol: Chemistry, Technology and Applications*, Springer, Verlag Berlin Heidelberg, 2005.
35. D. Wu, R. Fu, Z. Sun and Z. Yu, *Journal of Non-Crystalline Solids*, 2005, **351**, 915-921.
36. C. Scherdel and G. Reichenauer, *Microporous and Mesoporous Materials*, 2009, **126**, 133-142.
37. L. M. Hair, R. W. Pekala, R. E. Stone, C. Chen and S. R. Buckley, *Journal of Vacuum Science & Technology A*, 1988, **6**, 2559-2563.
38. H.-J. Kim, J.-H. Kim, W.-I. Kim and D. Suh, *Korean Journal of Chemical Engineering*, 2005, **22**, 740-744.
39. W. Li and S. Guo, *Carbon*, 2000, **38**, 1520-1523.
40. W.-C. Li, A.-H. Lu and S.-C. Guo, *Carbon*, 2001, **39**, 1989-1994.
41. W. Li, G. Reichenauer and J. Fricke, *Carbon*, 2002, **40**, 2955-2959.
42. W.-C. Li, A.-H. Lu and S.-C. Guo, *Journal of Colloid and Interface Science*, 2002, **254**, 153-157.
43. H. Y. Tian, C. E. Buckley, M. Paskevicius and S. B. Wang, *The Journal of Supercritical Fluids*, 2011, **55**, 1115-1117.
44. H. Y. Tian, C. E. Buckley, M. Paskevicius and D. A. Sheppard, *International Journal of Hydrogen Energy*, 2011, **36**, 671-679.
45. D. Wu, R. Fu, S. Zhang, M. S. Dresselhaus and G. Dresselhaus, *Journal of Non-Crystalline Solids*, 2004, **336**, 26-31.
46. G. C. Ruben and R. W. Pekala, *Journal of Non-Crystalline Solids*, 1995, **186**, 219-231.
47. M. H. Nguyen and L. H. Dao, *Journal of Non-Crystalline Solids*, 1998, **225**, 51-57.
48. H. F. Gorgulho, F. Gonçalves, M. F. R. Pereira and J. L. Figueiredo, *Carbon*, 2009, **47**, 2032-2039.
49. R. P. Rocha, J. Restivo, J. P. S. Sousa, J. J. M. Órfão, M. F. R. Pereira and J. L. Figueiredo, *Catalysis Today*.
50. S. Mulik, C. Sotiriou-Leventis and N. Leventis, *Chemistry of Materials*, 2007, **19**, 6138-6144.
51. S. A. Al-Muhtaseb and J. A. Ritter, *J. Adv. Mater.*, 2003, **15**, 101-114.
52. A. M. El Khatat and S. A. Al-Muhtaseb, *Adv. Mater.*, 2011, **23**, 2887-2903.
53. Aerogel Image Gallery, http://www.aerogel.org/?p=891&px=%2FAerogels+of+Different+Compositions%2Flif eofacarbonaerogelwithlabels-aerogeldotorg.jpg, Accessed 3rd November, 2011.
54. Sol-Gel Transition, http://soft-matter.seas.harvard.edu/index.php/Sol-Gel_Transition, Accessed 8th June, 2012.

55. C. J. Brinker and G. W. Scherer, *Sol-Gel Science: The Physics and Chemistry of Sol-Gel Processing*, Academic Press Inc., San Diego, 1990.
56. R. W. Jones, *Fundamental Principles of Sol-Gel Technology*, The Institute of Metals, London, 1989.
57. C. J. Gommes and A. P. Roberts, *Physical Review E*, 2008, **77**, 041409.
58. T. Yamamoto, T. Yoshida, T. Suzuki, S. R. Mukai and H. Tamon, *Journal of Colloid and Interface Science*, 2002, **245**, 391-396.
59. C. I. Merzbacher, S. R. Meier, J. R. Pierce and M. L. Korwin, *Journal of Non-Crystalline Solids*, 2001, **285**, 210-215.
60. D. W. Schaefer, R. Pekala and G. Beaucage, *Journal of Non-Crystalline Solids*, 1995, **186**, 159-167.
61. R. W. Pekala and D. W. Schaefer, *Macromolecules*, 1993, **26**, 5487-5493.
62. A. S. Aroca, M. M. Pradas and J. L. Gómez Ribelles, *Colloid and Polymer Science*, 2007, **285**, 753-760.
63. I. Najeh, N. Ben Mansour, M. Mbarki, A. Houas, J. P. Nogier and L. El Mir, *Solid State Sciences*, 2009, **11**, 1747-1751.
64. S. J. Kim, S. W. Hwang and S. H. Hyun, *Journal of Materials Science*, 2005, **40**, 725-731.
65. Electrical Conductivity of the elements, http://periodictable.com/Properties/A/ElectricalConductivity.an.html#Carbon.Electrica lConductivity.note, Accessed 24th October, 2014.
66. R. Petričević, M. Glora and J. Fricke, *Carbon*, 2001, **39**, 857-867.
67. N. Job, C. J. Gommes, R. Pirard and J.-P. Pirard, *Journal of Non-Crystalline Solids*, 2008, **354**, 4698-4701.
68. D. Fairén-Jiménez, F. Carrasco-Marín and C. Moreno-Castilla, *Carbon*, 2006, **44**, 2301-2307.
69. T. Horikawa, J. i. Hayashi and K. Muroyama, *Carbon*, 2004, **42**, 1625-1633.
70. R. Brandt, R. Petricevic, H. Pröbstle and J. Fricke, *Journal of Porous Materials*, 2003, **10**, 171-178.
71. R. Brandt and J. Fricke, *Journal of Non-Crystalline Solids*, 2004, **350**, 131-135.
72. N. Job, R. Pirard, J. Marien and J.-P. Pirard, *Carbon*, 2004, **42**, 619-628.
73. C. Lin and J. A. Ritter, *Carbon*, 1997, **35**, 1271-1278.
74. N. Job, F. Panariello, J. Marien, M. Crine, J.-P. Pirard and A. Léonard, *Journal of Non-Crystalline Solids*, 2006, **352**, 24-34.
75. V. Bock, A. Emmerling and J. Fricke, *Journal of Non-Crystalline Solids*, 1998, **225**, 69-73.
76. H. Tamon, H. Ishizaka, M. Mikami and M. Okazaki, *Carbon*, 1997, **35**, 791-796.
77. O. Barbieri, F. Ehrburger-Dolle, T. P. Rieker, G. M. Pajonk, N. Pinto and A. Venkateswara Rao, *Journal of Non-Crystalline Solids*, 2001, **285**, 109-115.
78. S. Berthon, O. Barbieri, F. Ehrburger-Dolle, E. Geissler, P. Achard, F. Bley, A.-M. Hecht, F. Livet, G. M. Pajonk, N. Pinto, A. Rigacci and C. Rochas, *Journal of Non-Crystalline Solids*, 2001, **285**, 154-161.
79. H. Tamon and H. Ishizaka, *Journal of Colloid and Interface Science*, 2000, **223**, 305-307.
80. K. Z. Gaca and J. Sefcik, *Journal of Colloid and Interface Science*, 2013, **406**, 51-59.
81. F. Despetis, K. Barral, L. Kocon and J. Phalippou, *Journal of Sol-Gel Science and Technology*, 2000, **19**, 829-831.
82. C. Liang, G. Sha and S. Guo, *Journal of Non-Crystalline Solids*, 2000, **271**, 167-170.
83. U. Fischer, R. Saliger, V. Bock, R. Petricevic and J. Fricke, *Journal of Porous Materials*, 1997, **4**, 281-285.

84.   N. Job, A. Théry, R. Pirard, J. Marien, L. Kocon, J.-N. Rouzaud, F. Béguin and J.-P. Pirard, *Carbon*, 2005, **43**, 2481-2494.
85.   T. Yamamoto, T. Nishimura, T. Suzuki and H. Tamon, *Journal of Non-Crystalline Solids*, 2001, **288**, 46-55.
86.   O. Czakkel, K. Marthi, E. Geissler and K. László, *Microporous and Mesoporous Materials*, 2005, **86**, 124-133.
87.   N. Tonanon, Y. Wareenin, A. Siyasukh, W. Tanthapanichakoon, H. Nishihara, S. R. Mukai and H. Tamon, *Journal of Non-Crystalline Solids*, 2006, **352**, 5683-5686.
88.   L. Zubizarreta, A. Arenillas, A. Domínguez, J. A. Menéndez and J. J. Pis, *Journal of Non-Crystalline Solids*, 2008, **354**, 817-825.
89.   L. Zubizarreta, A. Arenillas, J. A. Menéndez, J. J. Pis, J. P. Pirard and N. Job, *Journal of Non-Crystalline Solids*, 2008, **354**, 4024-4026.
90.   C. Moreno-Castilla and F. J. Maldonado-Hódar, *Carbon*, 2005, **43**, 455-465.
91.   E. G. Rodrigues, M. F. R. Pereira and J. J. M. Órfão, *Applied Catalysis B: Environmental*, 2012, **115–116**, 1-6.
92.   N. Job, B. Heinrichs, F. Ferauche, F. Noville, J. Marien and J.-P. Pirard, *Catalysis Today*, 2005, **102–103**, 234-241.
93.   H. Sun, H. Tian, Y. Hardjono, C. E. Buckley and S. Wang, *Catalysis Today*, 2012, **186**, 63-68.
94.   N. Job, R. Pirard, J. Marien and J.-P. Pirard, *Carbon*, 2004, **42**, 3217-3227.
95.   W. Kiciński and J. Lasota, *Journal of Materials Science & Technology*, 2012, **28**, 294-302.
96.   P. V. Samant, J. B. Fernandes, C. M. Rangel and J. L. Figueiredo, *Catalysis Today*, 2005, **102–103**, 173-176.
97.   B. F. Machado, H. T. Gomes, P. Serp, P. Kalck, J. L. Figueiredo and J. L. Faria, *Catalysis Today*, 2010, **149**, 358-364.
98.   N. Job, S. Lambert, M. Chatenet, C. J. Gommes, F. Maillard, S. Berthon-Fabry, J. R. Regalbuto and J.-P. Pirard, *Catalysis Today*, 2010, **150**, 119-127.
99.   N. Job, J. Marie, S. Lambert, S. Berthon-Fabry and P. Achard, *Energy Conversion and Management*, 2008, **49**, 2461-2470.
100.   C. Arbizzani, S. Beninati, E. Manferrari, F. Soavi and M. Mastragostino, *Journal of Power Sources*, 2007, **172**, 578-586.
101.   H. Jin, H. Zhang, Y. Ma, T. Xu, H. Zhong and M. Wang, *Journal of Power Sources*, 2010, **195**, 6323-6328.
102.   R. W. Pekala, J. C. Farmer, C. T. Alviso, T. D. Tran, S. T. Mayer, J. M. Miller and B. Dunn, *Journal of Non-Crystalline Solids*, 1998, **225**, 74-80.
103.   J. Fricke and T. Tillotson, *Thin Solid Films*, 1997, **297**, 212-223.
104.   M. Dirjish, Ultracapacitors Branch Out Into Wider Markets, http://electronicdesign.com/energy/ultracapacitors-branch-out-wider-markets, Accessed 9th October, 2014.
105.   B. S. Girgis, I. Y. El-Sherif, A. A. Attia and N. A. Fathy, *Journal of Non-Crystalline Solids*, 2012, **358**, 741-747.
106.   M. Sánchez-Polo, J. Rivera-Utrilla, E. Salhi and U. von Gunten, *Journal of Colloid and Interface Science*, 2006, **300**, 437-441.
107.   S. Porada, L. Weinstein, R. Dash, A. van der Wal, M. Bryjak, Y. Gogotsi and P. M. Biesheuvel, *ACS Applied Materials & Interfaces*, 2012, **4**, 1194-1199.
108.   L. Zubizarreta, J. A. Menéndez, N. Job, J. P. Marco-Lozar, J. P. Pirard, J. J. Pis, A. Linares-Solano, D. Cazorla-Amorós and A. Arenillas, *Carbon*, 2010, **48**, 2722-2733.
109.   K. Y. Kang, B. I. Lee and J. S. Lee, *Carbon*, 2009, **47**, 1171-1180.

110. A. Shukla, S. Karmakar and R. B. Biniwale, *International Journal of Hydrogen Energy*, 2012, **37**, 3719-3726.
111. D. Sebastián, C. Alegre, L. Calvillo, M. Pérez, R. Moliner and M. J. Lázaro, *International Journal of Hydrogen Energy*, 2014, **39**, 4109-4115.
112. T. Yamamoto, A. Endo, T. Ohmori and M. Nakaiwa, *Carbon*, 2004, **42**, 1671-1676.
113. V. M. Magueijo, L. G. Anderson, A. J. Fletcher and S. J. Shilton, *Chemical Engineering Science*, 2013, **92**, 13-20.
114. J. Rouquerol, D. Avnir, C. W. Fiarbridge, D. H. Everett, J. H. Haynes, N. Pernicone, J. D. F. Ramsay, K. S. W. Sing and K. K. Unger, *Pure and Applied Chemistry*, 1994, **66**, 1739-1758.
115. K. S. W. Sing, D. H. Everett, R. A. W. Haul, L. Moscou, R. A. Pierotti, J. Rouquerol and T. Siemieniewska, *Pure and Applied Chemistry*, 1985, **57**, 603-619.
116. MicromeriticsInstrumentCorporation, Gas Adsorption Theory, http://www.micromeritics.com/repository/files/gas_adsorption_theory_poster.pdf.
117. G. V. Burgess, D. H. Everett and S. Nuttall, *Pure and Applied Chemistry*, 1989, **61**, 1845-1852.
118. I. Langmuir, *Journal of the American Chemical Society*, 1916, **38**, 2221-2295.
119. S. Brunauer, P. H. Emmett and E. Teller, *Journal of the American Chemical Society*, 1938, **60**, 309-319.
120. E. P. Barrett, L. G. Joyner and P. P. Halenda, *Journal of the American Chemical Society*, 1951, **73**, 373-380.
121. W. Thomson, *Philosophical Magazine Series 4*, 1871, **42**, 448-452.
122. MicromeriticsInstrumentCorporation, *Micromeritics ASAP 2420 Operators Manual*.
123. G. Halsey, *The Journal of Chemical Physics*, 1948, **16**, 931-937.
124. I. Siminiceanu, I. Lazau, Z. Ecsedi, L. Lupa and C. Burciag, *Chem. Bull. "POLITEHNICA" Univ. (Timisoara)*, 2008, **53**, 38-44.
125. B. C. Lippens and J. H. de Boer, *Journal of Catalysis*, 1965, **4**, 319-323.
126. J. H. de Boer, B. C. Lippens, B. G. Linsen, J. C. P. Broekhoff, A. van den Heuvel and T. J. Osinga, *Journal of Colloid and Interface Science*, 1966, **21**, 405-414.
127. G. Jura and W. D. Harkins, *Journal of the American Chemical Society*, 1944, **66**, 1356-1362.
128. MalvernInstruments, Dynamic Light Scattering: An Introduction in 30 Minutes, http://www.malvern.com/en/support/resource-center/technical-notes/TN101104DynamicLightScatteringIntroduction.aspx.
129. R. Finsy, *Advances in Colloid and Interface Science*, 1994, **52**, 79-143.
130. A. R. Barron and S. Ozden, Physical Methods in Chemistry and Nano Science, http://cnx.org/contents/ba27839d-5042-4a40-afcf-c0e6e39fb454@20.15:24/Physical_Methods_in_Chemistry_.
131. P. N. Pusey, *Neutrons, X-rays and Light: Scattering Methods Applied to Soft Condensed Matter*, Elsevier, North Holland, 2002.
132. G. G. Stokes, *Cambridge Philos. Trans.*, 1851, **9**, 8-106.
133. A. Einstein, *Ann. der Physik*, 1905, **17**, 549-560.
134. L. Anderson, in *Chemical and Process Engineering*, University of Strathclyde, Glasgow, 2014.
135. HannaInstruments, Benchtop pH Meters, http://www.hannainst.com/Usa/prods2.cfm?id=040002&ProdCode=pH%2020, Accessed 19th June, 2014.
136. MicromeriticsInstrumentCorporation, Micromeritics ASAP 2420 Overview, http://www.micromeritics.com/product-showcase/ASAP-2420.aspx, Accessed 19th June, 2014.

137. MicromeriticsInstrumentCorporation, Micromeritics ASAP 2420, http://www.micromeritics.com/Quote/RequestQuote.aspx?instrumentId=2418, Accessed 19th June, 2014.

138. ALV, ALV/CGS-3 Compact Goniometer System, http://www.alvgmbh.de/Products/goniometers/ALV_CGS3/alv_cgs3.html, Accessed 19th June, 2014.

139. N. Job, F. Panariello, M. Crine, J.-P. Pirard and A. Léonard, *Colloids and Surfaces A: Physicochemical and Engineering Aspects*, 2007, **293**, 224-228.

140. S. Morales-Torres, F. J. Maldonado-Hodar, A. F. Perez-Cadenas and F. Carrasco-Marin, *Physical Chemistry Chemical Physics*, 2010, **12**, 10365-10372.

141. P. Sandkühler, M. Lattuada, H. Wu, J. Sefcik and M. Morbidelli, *Advances in Colloid and Interface Science*, 2005, **113**, 65-83.

142. J.-P. Hsu and B.-T. Liu, *Journal of Colloid and Interface Science*, 1998, **198**, 186-189.

143. F. Hofmeister, *Arch. Exp. Pathol. Pharmakol.*, 1888, **24**, 247-260.

144. D. K. Eggers, Hofmeister Series, http://www.chemistry.sjsu.edu/deggers/Hofmeister.htm, Accessed 20th October, 2014.

145. I. Persson, *Pure Appl. Chem.*, 2010, **82**, 1901-1917.

146. A. Jawor-Baczynska, B. D. Moore, H. S. Lee, A. V. McCormick and J. Sefcik, *Faraday Discussions*, 2013, **167**, 425-440.

147. P. Sandkühler, J. Sefcik and M. Morbidelli, *Langmuir*, 2005, **21**, 2062-2077.

148. W. C. K. Poon and M. D. Haw, *Advances in Colloid and Interface Science*, 1997, **73**, 71-126.

149. R. Fartaria, N. Javid, R. A. Pethrick, J. J. Liggat, J. Sefcik and M. B. Sweatman, *Soft Matter*, 2011, **7**, 9157-9166.

150. N. Javid, K. Vogtt, S. Roy, A. R. Hirst, A. Hoell, I. W. Hamley, R. V. Ulijn and J. Sefcik, *The Journal of Physical Chemistry Letters*, 2011, **2**, 1395-1399.

151. C. Scherdel, T. Scherb and G. Reichenauer, *Carbon*, 2009, **47**, 2244-2252.

152. B. Coto, C. Martos, J. L. Peña, R. Rodríguez and G. Pastor, *Fluid Phase Equilibria*, 2012, **324**, 1-7.

153. D. D. Eley, *Transactions of the Faraday Society*, 1939, **35**, 1281-1293.

154. EngineeringToolbox, Solubility of Gases in Water, http://www.engineeringtoolbox.com/gases-solubility-water-d_1148.html, Accessed 29th September, 2014.

155. M. Reuß and L. Ratke, *Journal of Sol-Gel Science and Technology*, 2010, **53**, 85-92.

156. H. H. Richmond, G. S. Myers and G. F. Wright, *Journal of the American Chemical Society*, 1948, **70**, 3659-3664.

157. S. M. Lambert, G. E. Overturf, G. Wilemski, S. A. Letts, D. Schroen-Carey and R. C. Cook, *Journal of Applied Polymer Science*, 1997, **65**, 2111-2122.

158. J. Laskowski, B. Milow and L. Ratke, *Microporous and Mesoporous Materials*, 2014, **197**, 308-315.

159. Y. N. Feng, L. Miao, M. Tanemura, S. Tanemura and K. Suzuki, *Materials Science and Engineering: B*, 2008, **148**, 273-276.

160. D. Dollimore and G. R. Heal, *Journal of Applied Chemistry*, 1964, **14**, 109-114.

161. E. McCall, in *Pure and Applied Chemistry*, University of Strathclyde, Glasgow, 2012.

Langmuir

Gelation Mechanism of Resorcinol-Formaldehyde Gels Investigated by Dynamic Light Scattering

Stewart J. Taylor, Mark D. Haw, Jan Sefcik, and Ashleigh J. Fletcher*

Department of Chemical and Process Engineering, University of Strathclyde, Glasgow G1 1XJ, United Kingdom

S *Supporting Information*

ABSTRACT: Xerogels and porous materials for specific applications such as catalyst supports, CO_2 capture, pollutant adsorption, and selective membrane design require fine control of pore structure, which in turn requires improved understanding of the chemistry and physics of growth, aggregation, and gelation processes governing nanostructure formation in these materials. We used time-resolved dynamic light scattering to study the formation of resorcinol-formaldehyde gels through a sol−gel process in the presence of Group I metal carbonates. We showed that an underlying nanoscale phase transition (independent of carbonate concentration or metal type) controls the size of primary clusters during the preaggregation phase; while the amount of carbonate determines the number concentration of clusters and, hence, the size to which clusters grow before filling space to form the gel. This novel physical insight, based on a close relationship between cluster size at the onset of gelation and average pore size in the final xerogel results in a well-defined master curve, directly linking final gel properties to process conditions, facilitating the rational design of porous gels with properties specifically tuned for particular applications. Interestingly, although results for lithium, sodium, and potassium carbonate fall on the same master curve, cesium carbonate gels have significantly larger average pore size and cluster size at gelation, providing an extended range of tunable pore size for further adsorption applications.
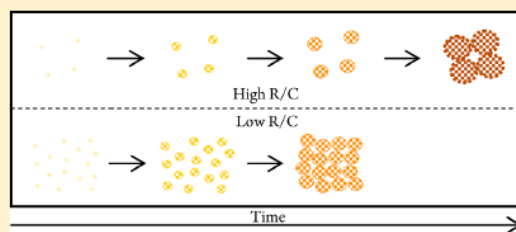
■ INTRODUCTION

Applications such as catalyst supports,[1] carbon capture,[2] hydrogen storage,[3] soil remediation,[4] water purification,[5] fuel cell,[6] and electrochemical processes,[7] and the design of selective membranes[8] all require fine control of the properties of porous materials, in particular pore sizes, size distributions, and connectivity. Such materials are often made using sol−gel processes, where chemical and physical interactions in solution lead to nucleation, growth and aggregation of clusters and eventual formation of porous solid gels when clusters contact each other to fill space. Our understanding of such aggregation and gelation processes, especially when both chemical reactions, such as polymerization, and physical effects, such as nanoscale phase separation, are occurring simultaneously, on competing time scales and length scales, remains limited. Hence, design and manufacture of bespoke gel materials for specific applications, with pore sizes and other properties easily determined through control of process conditions, is a challenge. In this paper, we provide a novel physical insight into the relationship between size and number of primary clusters and final gel properties for one class of porous materials, resorcinol-formaldehyde (RF) gels. This improved understanding of the chemical and physical processes leading to gel formation facilitates the rational design of porous gels with properties specifically tuned for particular applications.

RF gels were first prepared by Pekala in 1989.[9] They were formed through the polycondensation reaction of resorcinol and formaldehyde, in the presence of a base, as part of a sol−gel process. The dried gels had properties of low density, large surface area and high pore volume, as well as becoming electrically conductive, through pyrolysis which has seen them become potential materials for many of the applications stated above. The proposed reaction mechanism for RF polymerization occurs in two stages (as outlined in Scheme 1). Resorcinol and formaldehyde react to form substituted resorcinol, or the hydroxymethyl derivative, with mono-, di-, and trisubstituted resorcinol being produced. This is followed by polycondensation of these intermediates to form growing oligomers, which subsequently make up the clusters that compose the gel structure. The reaction is commonly carried out in the presence of a base, typically sodium carbonate; however, alternative cations such as lithium and potassium[10,11] have been used, as well as hydroxide[10] and hydrogen carbonate[12] anions. It has been shown that resorcinol and formaldehyde will react slowly by themselves, but the resulting product is an apparently nonporous powder.[13] Similarly, in the presence of ammonium carbonate (a nonmetallic base), a comparable nonporous product is formed.[13] Ammonium carbonate will decompose in the system producing ammonia, which will subsequently react with F. However, as the

Scheme 1. Two-Step Polymerization Process through the Addition Reaction of Resorcinol and Formaldehyde, Followed by the Subsequent Polycondensation of the Hydroxymethyl Derivative[a]
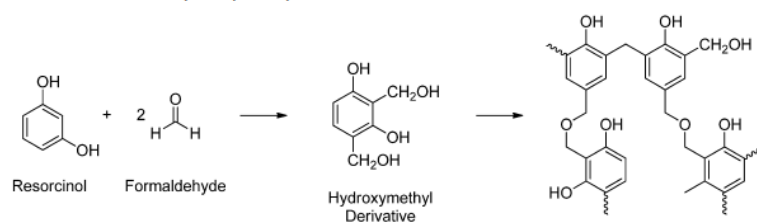
[a]The initial reaction is shown with representative stoichiometry of 1:2, producing the disubstituted hydroxymethyl. Mono- and trisubstituted hydroxymethyl derivatives will also form but these are omitted for clarity.

ammonium carbonate is added in such small quantities, less than 1% of the available F should react in this way and have little impact on the gel formation. This suggests that although the base is important, the metal also plays a role in the gelation process, determining the final porous characteristics of the materials.

Since the discovery of RF gels,[9] it has become common within the literature to refer to the added base as a catalyst.[14,15] This is primarily due to its role in speeding up the formation of the final gel product. However, the metal carbonate appears to decompose during the gel formation reaction and is, therefore, not recoverable at the end of the process. In addition, the complicated role the metal plays in the formation of the gel structure makes it more than just a catalyst. Hence, the added base will be referred to as simply carbonate (C) from here on in.

During the years since they were first synthesized, much work has been carried out on RF gels.[14,15] As previously noted, the metal counterion of the carbonate plays an important role in determining the porous properties of the dried gels. However, there are several other variables in the sol−gel reaction that can be altered in order to change the porous nature of the resulting gels. Some of these variables include total solids content (also referred to as the resorcinol to water ratio R/W in g/mL), resorcinol to formaldehyde molar ratio (R/F), resorcinol to carbonate molar ratio (R/C), and initial solution pH. In this regard, R/C and pH are closely related in RF gel synthesis.

Lin and Ritter[16] tried to decouple the relationship between R/C and pH, by fixing the R/C at 50, while altering the pH through the addition of nitric acid. However, the acid added will react with the carbonate present, reducing the concentration of acid or base available to participate in the sol−gel process.

There have been many findings indicating that initial pH is vitally important to the final properties of the gel.[14,15] Much work has shown that gel synthesis in the presence of a base will typically only give a viable gel structure within the limited pH range of 5.5−7.5.[15,17] More basic pH values give a nonporous structure,[16] while pH values less than 5.5 give a very long gelation time.[18] However, further lowering of the pH to within the range of approximately 1−4, through the addition of an acid instead of a base, will once more promote viable gel formation and reduce gelation times.[18,19] A pH of less than 0.8 will cause precipitation of the reactants.[15]

These useable ranges can be attributed to the requirements of the two stages in the polymerization process. The initial addition reaction can be favored by basic conditions, to abstract a proton from R, or by acidic conditions, wherein F is protonated, both of which promote the reaction between R and F. Consequently, when the pH is out with the stated ranges, the addition reaction is slowed and the gel time will increase.[18] The subsequent condensation reaction is also favored by acidic conditions. If the initial pH is too basic, there will be a lack of condensation reactions and the resulting gel structure will be very weak. This will result in the total collapse of the porous structure during drying, leading to a nonporous product.[16] The initial system pH can also have a secondary impact on the growth of polymer chains. High pH values resulting from low R/C values will lead to highly branched polymer chains. Conversely, low pH values as a result of high R/C ratios will produce less-branched polymer chains.[17]

Altering the solids content, i.e., total resorcinol, formaldehyde, and carbonate, can have a substantial impact on the properties of the dried gel.[14] The effective dilution of the reactant solution, by decreasing the solids content, gives rise to larger gaps between the growing clusters. This leads to an increase in the pore size and a corresponding decrease in surface area.[11] Tamon et al.[20] reported that with high solids content, the porosity of the gel was monodisperse, i.e., all pores were of a similar size. Conversely, low solids content produced polydisperse porosity with multiple pore sizes observed.

From the first synthesis of RF gels, resorcinol and formaldehyde have most commonly been combined in the stoichiometric proportion of 1:2, giving an R/F ratio of 0.5.[9] Increasing the formaldehyde concentration present, to give a 1:3 ratio, leads to the observation of much larger final clusters.[21]

Dynamic light scattering (DLS) has previously been used to study the formation of RF gels. However, these studies have been limited, in that they focus on only the most commonly used base, sodium carbonate. Yamamoto et al.[22] observed that for a given resorcinol to water ratio, the growth of primary clusters was highly dependent on the carbonate concentration in the initial RF solution. They showed that as resorcinol: carbonate molar ratio (R/C) increased; the growth rate slowed such that, at a given time, high R/Cs gave a smaller cluster size than low R/C values. Conversely, Gaca and Sefcik[23] argued that in the early gelation stages, primary cluster size changed minimally as the carbonate concentration was altered. Instead, the process was thermodynamically driven and primary cluster growth rates were essentially independent of R/C values.

The aim of this work was to study the influence of four Group I metal carbonates, at various R/C ratios, on the RF sol−gel process and the subsequent properties of the dried gels. This was achieved through the use of DLS to monitor primary

229

cluster growth in the initial stages of the gelation process, followed by characterization through low temperature nitrogen adsorption/desorption measurements of the final xerogels, allowing direct comparison between gel formation and the resulting sample textural properties.

■ EXPERIMENTAL SECTION

Materials and Synthesis. The composition of the RF solution was determined using the molar ratios of resorcinol to carbonate (R/C) and resorcinol to formaldehyde (R/F). The total solids content of the gel, i.e., resorcinol, formaldehyde, and carbonate, was kept constant at 20% weight by volume. A gel volume of 60 mL was used in each case; corresponding to a solid mass of 12 g. R/C was varied between 100 and 600 for each of the carbonates used, whereas R/F was fixed at 0.5.

Resorcinol (ReagentPlus, 99%), aqueous formaldehyde solution (37 wt % formaldehyde, stabilized with 10−15% methanol), lithium carbonate (purum, ≥99%), sodium carbonate (anhydrous, ≥99.5%), potassium carbonate (anhydrous powder, 99.99%) and cesium carbonate (ReagentPlus, 99%) were all used as purchased from SigmaAldrich.

For a chosen carbonate and R/C ratio, the required resorcinol was weighed out and placed in a sealable 500 mL jar with 50 mL of deionized water (produced in house as required using a Millipore Elix 5 system), and magnetically stirred until completely dissolved. The carbonate was weighed out and added to the resorcinol solution with continued stirring, again until completely dissolved. The required volume of formaldehyde solution and additional deionized water, to give the total volume of 60 mL, was added to the jar, which was sealed and allowed to stir uninterrupted for 30 min. At the end of this stirring period, the initial pH of the solution was recorded (Hanna pH 20 meter, fitted with an HI-1110B pH electrode) and the sealed jars placed in an oven preheated to 85 ± 5 °C until gelation occurred. Gelation times were monitored for each of the metal carbonates used at all of the chosen R/C ratios. Gelation was determined by periodically tilting the jars to a 45° angle until no flow was observed. To allow for curing of the newly formed gel, we left the samples at 85 ± 5 °C for 3 days.

Water entrained within the cured gel network was removed through solvent exchange, by shaking the cured gel in 180 mL of acetone (ACS reagent, ≥99.5%, Sigma-Aldrich) for 3 days at room temperature. This step reduced shrinkage of the structure during drying, especially for high R/C gels. Subsequently, the gels were dried under vacuum at 85 °C for 2 days to produce the final xerogel product.

Xerogel Characterization. Surface area and porosity measurements were performed on a Micromeritics ASAP 2420, using nitrogen adsorption/desorption measurements. Approximately 0.5 g of the dried gel was accurately weighed into a sample tube, which was attached to a degas port of the equipment. After securing a heating mantle around the tube, the sample was evacuated by attached vacuum pump first to 5 mmHg, then to 10 μmHg, while being heated to 50 °C. After being held at these conditions for 30 min, the temperature was ramped to 110 °C and this temperature maintained for 120 min. On completion of the degas cycle, the sample and tube were reweighed to determine the mass lost. An analysis port was prepared and analysis performed at −196 °C, maintained by liquid nitrogen, and consisting of 40 point adsorption and 30 point desorption cycles.

Brunauer−Emmett−Teller (BET) theory[24] was applied to the adsorption branch of the acquired nitrogen uptake isotherm, resulting in a linear plot between the relative pressures (p/p_0) of 0.05 and 0.3. This allowed calculation of the BET surface area (S_{BET}) for each of the gel samples. Similarly, the Barrett-Joyner-Halenda (BJH) method[25] was applied to the desorption branch of the isotherm. This generated a pore size distribution for the gel samples and allowed calculation of the average pore size.

Dynamic Light Scattering. DLS experiments were carried out on an ALV/CGS-3 compact goniometer system in conjunction with an ALV/LSE-5004 multiple tau digital correlator. The laser used had wavelength, λ, 632.8 nm, with a scattering angle, θ, of 90°. After

measuring the solution pH, portions of the solution were passed through a 0.2 μm pore size syringe filter (Whatman Puradisc) into 11 borosilicate glass cells with 10 mm diameter and height of 75 mm (Fisher Scientific). All 11 cells were then sealed with a cap, and 10 were transferred to an oven set to 85 ± 5 °C, whereas the 11th cell was taken for immediate analysis and designated $t = 0$. Making use of the predetermined gel times, further cells were removed from the oven at intervals of 10% of these times, upon which they were rapidly quenched to room temperature and analyzed.

For each experimental time point, the digital correlator generated an autocorrelation function of the scattered light intensity. When the autocorrelation function decay followed an exponential time dependence, indicative of free Brownian motion of the species present, the cumulant method[26] was applied in order to estimate the initial decay rate, Γ (s^{-1}). Subsequently, the mean diffusion coefficient, D, was calculated

$$\Gamma = Dq^2$$

where q is the scattering vector magnitude

$$q = \frac{4\pi}{\lambda}\sin\frac{\theta}{2}$$

From this, the Stokes−Einstein equation[27,28] can be used to calculate the mean hydrodynamic radius, R_H

$$R_H = \frac{k_b T}{6\pi\mu D}$$

where k_B is the Boltzmann constant, T is absolute temperature, and μ is the dynamic viscosity. For all calculations, μ was assumed to be that of pure water at the experimental temperature.

■ RESULTS AND DISCUSSION

Gelation times as determined in this work are 35 min for R/C 100, 43 min for R/C 200, 55 min for R/C 300, 65 min for R/C 400, 80 min for R/C 500, and 120 min for R/C 600. It was found that for an equivalent R/C the gelation time for each of the carbonates was identical, while it is clear that increasing R/C leads to increased gelation times. This contrasts with Morales-Torres et al. who found that for a fixed R/C of 300, and thermal regime of 1 day at room temperature followed by heating to 50 °C, the gel time increased over the Group I metal series, with lithium giving the shortest time and cesium the longest.[29] However, our results agree with those of Job et al. who also found that gel time increased with increasing R/C.[30]

It should be noted that the sample synthesized using cesium carbonate with R/C 600 failed to gel within a time frame experimentally viable for DLS to be conducted.

For the gel times obtained, intervals of 10% of the total gel time were chosen with which to run DLS measurements, as opposed to a fixed time interval. This allowed for direct comparison between all of the gel compositions at an equivalent point in the gelation process.

Upon analysis of the gelling samples, the experimental equipment provided two sets of raw data for each measurement time point, both of which provide valuable information on the gelation process. The first of these data sets were autocorrelation functions for each sample, whereas the second contained the corresponding scattered light intensities.

Figure 1 shows the normalized autocorrelation functions obtained over the entire gelation period for both sodium and cesium carbonate, with a fixed R/C of 100 in both cases (see the Supporting Information for the corresponding lithium and potassium data, as well as those for sodium carbonate at both R/C 400 and 600).
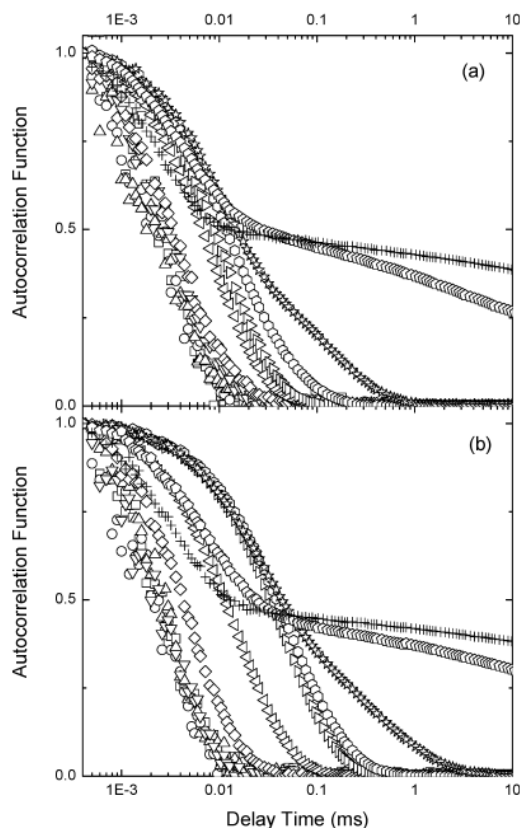
230

Figure 1. Autocorrelation functions for (a) sodium carbonate and (b) cesium carbonate at R/C 100. Measurements are taken every 10% of the total gel time such that (□) 0%, (○) 10%, (△) 20%, (▽) 30%, (◇) 40%, (left-facing triangle) 50%, (right-facing triangle) 60%, (○) 70%, (☆) 80%, (○) 90%, and (+) 100%.

Initially, the decay of the autocorrelation function demonstrates a strictly exponential dependence on time. This corresponds to free Brownian motion of monodisperse cluster population and suggests that, while the primary clusters are growing, they are moving without obstruction, or intercluster interaction. As the experimental time increases (for example, $t =$ 80%, i.e., 28 min for R/C 100), the shape of the autocorrelation function changes, moving away from a purely exponential decay and introducing a small secondary decay. This implies that further species with slower dynamics are now present, suggesting that aggregation or networking of primary clusters has begun and their movement is beginning to become hindered. To clearly discriminate between aggregation and networking of the clusters, more detailed models of cluster populations evolving over time and fitted to the measured autocorrelation functions would be required.[31]

At times very close to, and at, the total gel time, the autocorrelation function fails to decay completely, becoming nonergodic. This feature is indicative of a gel structure. The small initial decay that remains suggests that some degree of motion is still possible and the gel has not become completely rigid. Indeed, Job et al. found that between 24 and 48 h of aging

the gel was required to give a stable pore texture.[18] It is possible that these residual movements are caused by polymeric branches that have still to connect completely with the formed clusters, resulting in additional decay contributions to the autocorrelation functions. However, these contributions are likely to be slower than those of the corresponding diffusivity of primary clusters.[31] Figure 2 illustrates each of these profile
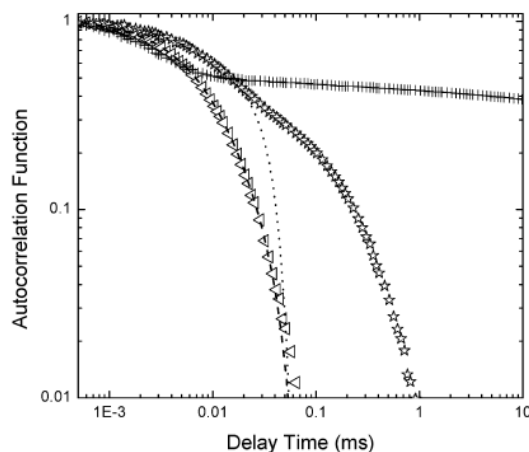
Figure 2. Autocorrelation functions for sodium carbonate R/C 100 at (left-facing triangle) 50%, (☆) 80%, and (+) 100%, illustrating the changing decay profile shape. Dashed lines represent the theoretical exponential decay of a monodisperse cluster population with hydrodynamic radius determined from the initial decay rate.

types on a log−log scale, showing how, earlier in the gelation process, the profile follows the exponential decay. At later times, it clearly deviates away from that of a purely exponential profile.

As stated above, the hydrodynamic radius of the growing clusters can be determined by the cumulant method. This analysis was limited to only those autocorrelation functions showing purely exponential decay, where the clusters are moving freely. As the clusters start aggregating or networking near gelation, their movement is no longer free and the exponential decay is lost. The combination of these factors means that the true hydrodynamic radius of clusters can no longer be determined using the cumulant method.

Figure 3 shows the hydrodynamic radii determined from the initial decay of the autocorrelation function for each carbonate at all R/C ratios. It can be seen that, in all cases, there is a period of time wherein the hydrodynamic radii are less than 1 nm and do not grow. This size compares with the 0.4 nm hydrodynamic radius for a hydrated resorcinol molecule,[23] suggesting that only hydroxymethyl derivatives are present at this time.

This delay in growth is the consequence of the time taken for samples to heat up after being placed in the oven. After measurement of the temperature of each individual sample on removal from the oven and before quenching, during experimental runs using sodium carbonate at R/C ratio of 100, it was found that growth began when the samples reached approximately 55 °C. As such, preheating of the initial solution to 55 °C eliminates this delay (see the Supporting Information, Figure SI3 and SI4).
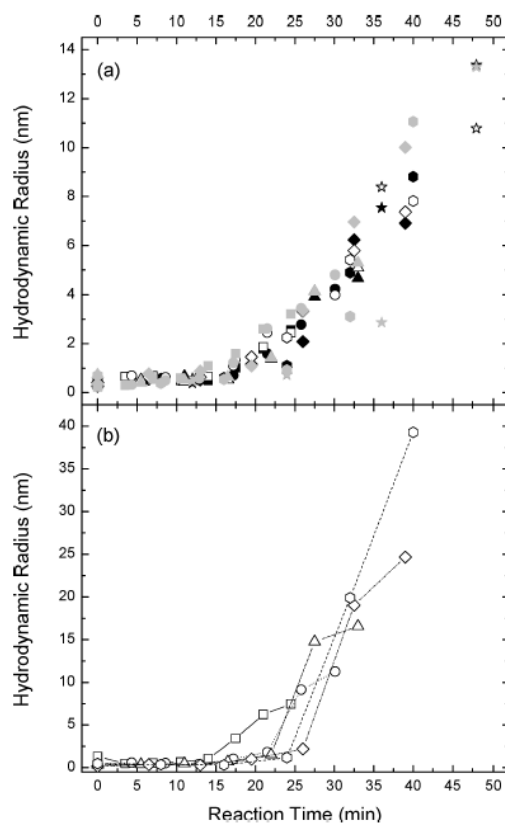
Figure 3. Hydrodynamic radii as determined from autocorrelation functions for (a) lithium carbonate (black symbols), sodium carbonate (open symbols), and potassium carbonate (gray symbols) and (b) cesium carbonate, at (□) 100, (○) 200, (△) 300, (◇) 400, (◯) 500, and (☆) 600.

When comparing the growth of clusters produced when using lithium, sodium and potassium carbonate (Figure 3a), it can be seen that the hydrodynamic radii fall into an overlapping narrow band. This indicates that the growth of the clusters is virtually independent of the R/C ratio or metal carbonate used. The maximum pregelation hydrodynamic radius does, however, show a dependence on R/C, with the maximum hydrodynamic radius increasing as R/C ratio increases. This trend is shown in Figure 4.

In contrast, the cluster growth in the presence of cesium carbonate is much different to the corresponding lithium, sodium, and potassium carbonate systems (Figure 3b). The growth is no longer consistent across the R/C spectrum, with low R/C ratio clusters growing faster than those with higher R/C. Despite identical thermal conditions, the time delay before the onset of growth also varies significantly, with longer times for the higher R/C systems, ranging from less than 15 min for R/C 100, to more than 25 min for R/C 500. It should also be noted that for a given R/C ratio, the maximum calculated pregelation hydrodynamic radius is much larger for cesium carbonate systems when compared with the lithium, sodium and potassium carbonate counterparts, as seen in Figure 4.
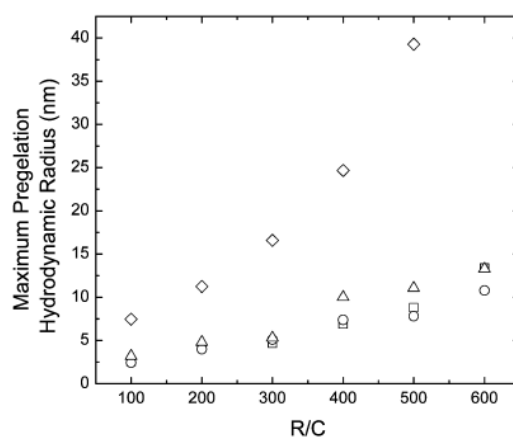
Figure 4. Maximum pregelation hydrodynamic radius as determined for each R/C used for (□) Li_2CO_3, (○) Na_2CO_3, (△) K_2CO_3, and (◇) Cs_2CO_3.

The time dependent scattered light intensities are shown in Figure 5 (see the Supporting Information for the corresponding
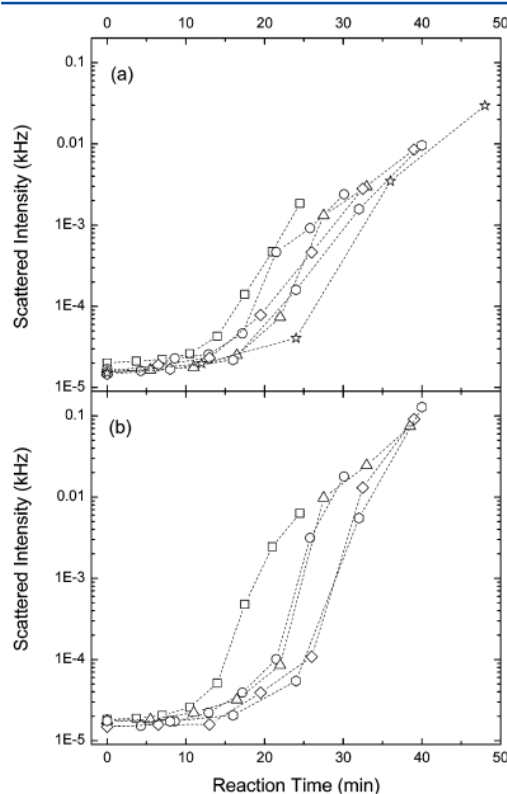
Figure 5. Scattered light intensities for (a) sodium carbonate and (b) cesium carbonate at R/C ratios of (□) 100, (○) 200, (△) 300, (◇) 400, (◯) 500, and (☆) 600.
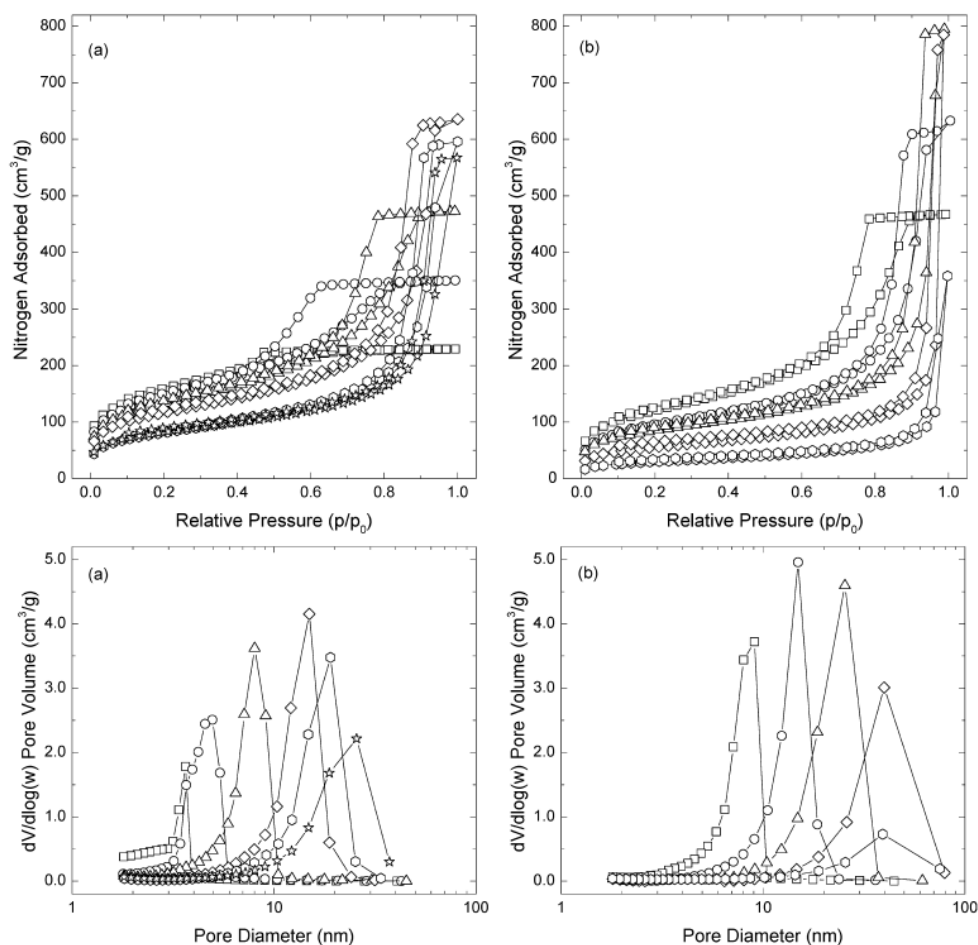
Figure 6. Adsorption/desorption isotherms (top) and pore size distributions (bottom) for (a) sodium carbonate and (b) cesium carbonate at R/C ratios of (□) 100, (○) 200, (△) 300, (◇) 400, (⬠) 500, and (☆) 600.

lithium and potassium carbonate results). Examination of this data provides further information on the cluster growth process. In the case of lithium, sodium, and potassium, the results are once more very similar. In general, for a given time the scattered light intensity decreases with increasing R/C. As hydrodynamic radius measurements indicate that, at any given time, cluster size is very similar for all R/C values; this decrease in scattered intensity implies a decrease in the number concentration of scatterers, i.e. clusters. An increase in R/C ratio therefore leads to a decrease in the number concentration of clusters at a given time. A sample made with an R/C of 100 generates many more clusters than an R/C 600 sample, yet they grow at the same rate.

The scattered light intensities recorded for gels made with cesium carbonate follow the same general trend as the other metals, with increasing R/C resulting in decreasing intensity at a given time. However, changes in the scattered intensity at a given time for the different R/C ratios are due to not only changes in the cluster number concentration but also in cluster size. While still being monodisperse, the hydrodynamic radii of

the clusters in these cesium carbonate gels, are dependent on R/C ratio at a given time. As a result, it was not possible to decouple the relationship between cluster size and their number concentration in cesium carbonate systems.

Surface area and porosity measurements were carried out on each of the dried gels. Example subsets of the adsorption/desorption isotherms and pore size distributions obtained are shown in Figure 6 (see the Supporting Information for results for lithium and potassium carbonate gels).

Consistent with observations from hydrodynamic radii obtained by DLS, it can be seen that in the case of both isotherms and pore size distributions, the results for lithium, sodium and potassium are very similar, whereas those for cesium differ greatly. However, there are discernible trends that apply to all four of the cations studied. As shown by the isotherm data, for each carbonate, increasing the R/C ratio leads to a general increase in the amount of nitrogen adsorbed. This is accompanied by a shifting of the hysteresis loop to higher relative pressures. These observations are indicative of an increase in both pore diameter and total pore volume, as

233

supported by the pore size distributions. At a given R/C, the equivalent cesium gels show a greater nitrogen uptake than the other carbonates. This is mirrored in the greatly increased pore size. The results obtained for cesium carbonate at R/C 500 do not follow the trends established by the other cesium gels; the nitrogen uptake is much lower than expected, as is the pore volume. At high R/C values, the presolvent exchanged, cured cesium gels are much softer than those of the other carbonates used. This leads to greater shrinkage during the drying phase, causing a reduction in pore volume. In conjunction with the R/C 600 cesium sample failing to gel, this suggests that the upper R/C limit to produce feasible cesium gels has been reached.

Further details on the properties of each gel are given in Table 1. The initial solution pH, as measured at the end of the

Table 1. BET Surface Area (S_{BET}), BJH Average Pore Size (d_p avg.), Total Pore Volume (V_{Tot}), and Initial pH for Each Dried Gel Sample

R/C	S_{BET} (m²/g)[a]	d_p avg. (nm)	V_{Tot} (cm³/g)	pH
		Li₂CO₃		
100	527 ± 5	2.9	0.35	7.31
200	542 ± 4	4.4	0.59	7.07
300	498 ± 5	7.3	0.82	6.91
400	438 ± 5	11.4	1.05	6.85
500	376 ± 4	13.7	1.03	6.74
600	320 ± 4	16.0	1.00	6.65
		Na₂CO₃		
100	533 ± 5	2.9	0.35	7.39
200	508 ± 4	4.2	0.54	7.09
300	461 ± 4	6.7	0.73	6.91
400	403 ± 4	11.5	0.98	6.84
500	284 ± 2	14.3	0.92	6.77
600	282 ± 4	16.5	0.88	6.66
		K₂CO₃		
100	472 ± 4	3.0	0.33	7.36
200	554 ± 5	4.7	0.64	7.07
300	476 ± 5	7.9	0.85	6.92
400	465 ± 5	10.9	1.08	6.84
500	272 ± 2	15.2	0.94	6.75
600	299 ± 3	16.4	0.93	6.66
		Cs₂CO₃		
100	425 ± 3	6.9	0.72	7.37
200	329 ± 3	12.6	0.98	7.09
300	293 ± 3	20.3	1.23	6.92
400	206 ± 2	28.0	1.15	6.85
500	103 ± 1	27.5	0.55	6.74

[a]All BET surface areas had a corresponding positive C value.

30 min stirring period, is included for reference. For each carbonate there are several trends that agree with the literature described above. As expected, initial pH decreases with increasing R/C and is consistent between the four cations, with a given R/C resulting in approximately the same pH. Average pore sizes increase with increasing R/C, agreeing with the visual analysis of the adsorption/desorption isotherms. The values for lithium, sodium, and potassium compare well, with a large increase for the corresponding cesium gels. Once more, this agrees with examination of the pore size distributions. This increase in pore size gives an associated decrease in the BET surface area.

By combining the data on the maximum pregelation hydrodynamic radii of clusters and the average pore size of

the gels it can be seen that there is a clear correlation between these two values, where all data for lithium, sodium, and potassium fall on a single master curve. Figure 7 shows this
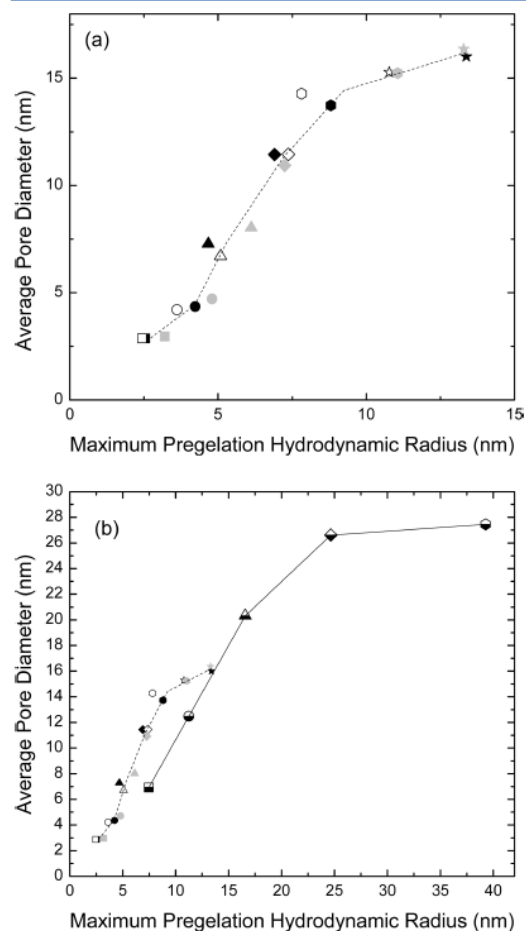
Figure 7. Master curve showing average pore diameter vs maximum hydrodynamic radii for (a) lithium carbonate (black symbols), sodium carbonate (open symbols) and potassium carbonate (gray symbols)- and (b) cesium carbonate (half-filled symbols) at R/C ratios of (□) 100, (○) 200, (△) 300, (◇) 400, (⬠) 500, and (☆) 600. Data from (a) are overlaid with reduced symbol size to allow for direct scale comparison in (b).

master curve, and the range of values of pore size accessible in these systems. As expected from analysis of the above results, the cesium gels do not conform to the master curve exhibited by the other Group I metal carbonates used. However, the data follows the same trend, with the cesium carbonate results following a similar dependence between the average pore size and maximum pregelation size of clusters. In Figure 7b, we can see that these xerogels can provide a wide range of average pore sizes, which can be systematically tailored for the number of potential applications as required.

It is likely that this correlation will hold with regard to average pore diameter vs final particle size of the dried gel.

234

High R/C – lower cluster number concentration, longer gelation time and larger pore size.

Low R/C – higher cluster number concentration, shorter gelation time and smaller pore size.
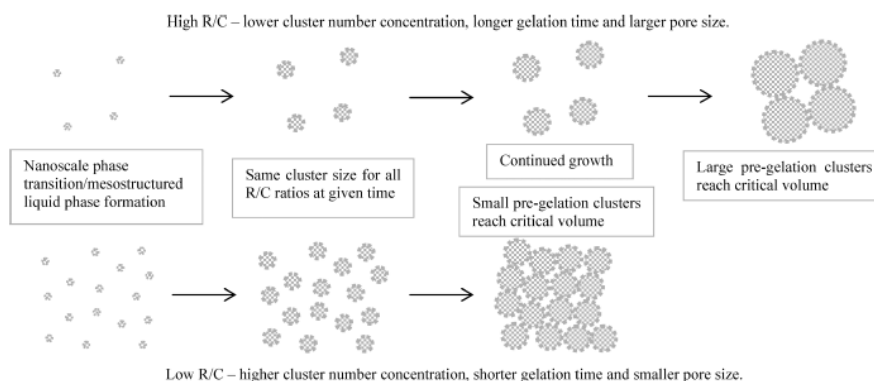
Figure 8. Schematic diagram outlining the cluster formation and growth process in resorcinol-formaldehyde gel synthesis. Clusters are depicted as spheres with sizes corresponding to hydrodynamic radii determined by DLS for clarity.

However, electron microscopy imaging has not been performed at this time, preventing a definitive conclusion about dry gel particle size from being drawn.

The ordering of the metals in this work, where lithium = sodium = potassium < cesium with regard to cluster size produced appears to follow a Hofmeister like series, all be it in reverse order. Hofmeister found that lithium > sodium > potassium at salting out egg protein from solution, by stabilizing the protein molecules and making them less soluble.[32] Our observations appear to show that lithium, sodium and potassium have approximately equal ability to stabilize the RF colloidal suspension by destabilizing the oligomers and increasing their solubility, resulting in small clusters. On the other hand, the larger, more hydrated cesium cation[33] appears to be less able to stabilize the colloidal suspension, making the oligomers less soluble and leading to larger clusters.

Previous literature on the formation of RF gels has been mainly focused on the microphase separation mechanism.[10,34,35] As resorcinol becomes substituted and the subsequent condensation polymerization proceeds, a complex mixture of water, alcohol, salt, and organic oligomers is formed. As the oligomer length increases, the miscibility of the chain with water decreases, leading to demixing of the components into two microphases.

However, the classical microphase separation scenario results in two interpenetrating microphases, which is inconsistent with DLS observations of freely diffusing primary clusters. Therefore, another kind of nanoscale phase transition needs to be considered, such as mesostructured liquid phase formation, where a single liquid phase consists of the bulk solution containing localized liquid-like regions of the organic species.[23,36]

The DLS results obtained here appear to support this theory. In the case of lithium, sodium and potassium, the primary cluster size growth in the initial pregelation stages is independent of the metal cation and R/C ratio used. This implies the formation of similar oligomeric species in all cases, which form monodisperse clusters of the observed hydrodynamic radius, surrounded by the bulk solution containing water/resorcinol/formaldehyde. This process is depicted schematically in Figure 8. The schematic depicts primary clusters as spherical for clarity, as the exact shape and internal structure of the clusters is not yet known. Primary clusters can

contain variously branched oligomers which are likely to be physically aggregated while also undergoing further polymerization. We do not believe that clusters are individual polymeric species, because their size has been previously found to be independent of R and F concentration at a given carbonate concentration, and therefore appears to be controlled thermodynamically rather than by kinetics of the polymerization process.[23]

In reality, these primary clusters can have any arbitrary shape (be it irregular and/or fractal). However, they do have a well-defined hydrodynamic radius, as demonstrated here, and corresponding occupied volume.[37] These clusters are then subject to further physical aggregation which leads to formation of a 3D network and in turn gelation, as the total volume occupied by clusters reaches a critical value. Formation of the physically aggregated 3D network may be accompanied and/or followed by chemical bonding due to underlying polymerization processes.

The lower number concentration of clusters associated with higher R/C ratios implies that clusters will have to grow larger before they reach this critical occupied volume. Conversely, the large number concentration of clusters produced at low R/C ratios will reach this occupied volume at much smaller sizes. As all clusters grow at the same rate, the larger the clusters have to grow before reaching this volume will result in an increasing gelation time as observed.

Although it is theoretically possible for differently branched polymers to have the same hydrodynamic radius, for this to happen here, primary cluster size would need to be controlled by polymerization kinetics. However, this is not the case here, as this work shows that the size of primary clusters appears to be thermodynamically controlled. Therefore, it is likely that primary clusters are formed by nanoscale phase transition involving RF oligomers which are physically aggregated. As such, formation of 3D networks in various molecular and colloidal systems has been demonstrated to be the result of physical aggregation of primary particles or clusters.[38−40]

The gel formation mechanism proposed here differs from the model proposed by Yamamoto et al.[22,41] in several key aspects. Their model proposed that both size and growth rate of clusters were driven by chemical reaction kinetics, being highly dependent on the R/C used. The higher the carbonate concentration used, the greater the apparent cluster growth rate became. However, in their work, nonexponential

235

autocorrelation functions were analyzed to determine the apparent cluster sizes under conditions that were likely to be in the regime of aggregation and networking, where cluster mobility is severely hindered and, therefore, cluster sizes cannot be reliably determined. In contrast, we propose that primary cluster size is determined by nanoscale phase transition and is, therefore, as previously stated thermodynamically controlled, rather than determined by reaction kinetics. However, the number concentration of primary clusters is kinetically controlled through reaction kinetics, where higher carbonate concentrations results in faster production of the substituted resorcinol and resulting oligomers, leading to a larger number of primary clusters.

The results presented here are inconsistent with the mechanism first proposed by Pekala and Kong,[42] that of the "autocatalytic growth" mechanism. Through this mechanism, Pekala and Kong intimated that with increasing carbonate concentration came an increasing number of more reactive substituted resorcinol molecules and, therefore, a greater number of the initial bridged dimer condensation products. The quadruple functionality on these dimer species increased the probability that they would react further to produce larger oligomers. The greater number of dimers produced by the higher carbonate concentration therefore led to a faster reaction rate, with lower carbonate concentration leading to a correspondingly slower reaction. The results obtained in this work suggest that this is not the case, with cluster growth proceeding at the same rate, independent of the carbonate concentration.

CONCLUSIONS

From the results obtained through DLS, it was found that lithium, sodium, and potassium exhibited very similar trends in size and growth kinetics of primary clusters. The cluster growth kinetics were found to be very similar for all samples studied, independent of the metal carbonate and R/C used. This suggests that clusters have the same mean size at a given time until the sample nears the gelation time, indicative of a thermodynamically controlled process of primary cluster formation. The R/C ratio determines the number concentration of these clusters present, with an increase in the quantity of clusters as R/C decreases. A greater number concentration of clusters results in the clusters reaching a critical occupied volume more quickly, which, in turn, leads to smaller final pregelation cluster sizes and shorter gelation times. This is consistent with the pore sizes observed, with smaller diameters corresponding to lower R/C values.

These results lend weight to a mechanism consisting of a nanoscale phase transition, such as mesostructured liquid phase formation. With mesostructured liquid phase formation, the growing oligomers reach their miscibility limit and the solution undergoes a phase transformation, resulting in the formation of primary clusters dispersed in the bulk aqueous solution. This phase transition is dependent on the size of the oligomers produced by the condensation reaction, and so occurs once a certain temperature and/or composition threshold is reached, irrespective of R/C.

This reinforces the point that the metal cation species plays an important role in the gel formation process. However, the high degree of similarity in the results of lithium, sodium and potassium, coupled with the vastly different results for cesium means the understanding of this role is still not complete. Cesium carbonate shows different behavior, where pregelation

cluster sizes are significantly larger than those of the other metals studied at equivalent R/C ratios. This leads to greatly increased pore sizes. The metal cations appear to follow a Hofmeister like series, with the smaller, less hydrated lithium, sodium, and potassium cations giving smaller clusters than the larger, more hydrated cesium cation.

However, the insight developed here means that the average pore sizes of the resulting xerogels can be precisely tailored, allowing for the development of numerous applications for these materials. Use of cesium carbonate gives access to a region of properties which are unobtainable using lithium, sodium or potassium carbonate. Although the pore sizes obtained for these three metals are ideal for gas phase applications, the larger pores of cesium gels fall into the range required for aqueous phase processes. This means that the number and scope of potential applications for these materials is significantly expanded.

ASSOCIATED CONTENT

Ⓢ Supporting Information

Autocorrelation functions for lithium and potassium carbonate at R/C 100, autocorrelation functions for sodium carbonate at R/C 400 and 600, temperature profile for sodium carbonate at R/C 100, hydrodynamic radii for sodium carbonate when preheated to 55 °C, scattered light intensities for lithium and potassium carbonate, adsorption/desorption isotherms for lithium and potassium carbonate, pore size distributions for lithium and potassium carbonate (PDF). This material is available free of charge via the Internet at http://pubs.acs.org.

AUTHOR INFORMATION

Corresponding Author
*E-mail: ashleigh.fletcher@strath.ac.uk.

Notes
The authors declare no competing financial interest.

ACKNOWLEDGMENTS

ABBREVIATIONS

R, resorcinol; F, formaldehyde; C, metal carbonate; R/C, resorcinol to carbonate molar ratio; R/F, resorcinol to formaldehyde molar ratio; DLS, dynamic light scattering; BET, Brunauer−Emmett−Teller; BJH, Barrett−Joyner−Halenda

REFERENCES

(1) Rodrigues, E. G.; Pereira, M. F. R.; Orfao, J. J. M. Glycerol oxidation with gold supported on carbon xerogels: Tuning selectivities by varying mesopore sizes. *Appl. Catal., B* **2012**, *115-116*, 1−6.

(2) Luo, C.; Zheng, Y.; Zheng, C.; Yin, J.; Qin, C.; Feng, B. Manufacture of calcium-based sorbents for high temperature cyclic CO_2 capture via sol-gel process. *Int. J. Greenhouse Gas Control* **2013**, *12*, 193−199.

(3) Zubizarreta, L.; Menéndez, J. A; Job, N.; Marco-Lozar, J. P.; Pirard, J. P.; Pis, J. J.; Linares-Solano, A.; Cazorla-Amorós, D.; Arenillas, A. Ni-doped carbon xerogels for H_2 storage. *Carbon* **2010**, *48*, 2722−2733.

(4) Tang, J.; Zhu, W.; Kookana, R.; Katayama, A. Characteristics of biochar and its application in remediation of contaminated soil. *J. Biosci. Bioeng.* **2013**, *116*, 653−659.

(5) Porada, S.; Weinstein, L.; Dash, R.; van der Wal, A.; Bryjak, M.; Gogotsi, Y.; Biesheuvel, P. M. Water desalination using capacitive deionization with microporous carbon electrodes. *ACS Appl. Mater. Interfaces* **2012**, *4*, 1194−1199.

(6) Jin, H.; Zhang, H.; Ma, Y.; Xu, T.; Zhong, H.; Wang, M. Stable support based on highly graphitic carbon xerogel for proton exchange membrane fuel cells. *J. Power Sources* **2010**, *195*, 6323−6328.

(7) Pekala, R. W.; Farmer, J. C.; Alviso, C. T.; Tran, T. D.; Mayer, S. T.; Miller, J. M.; Dunn, B. Carbon electrodes for electrochemical applications. *J. Non-Cryst. Solids* **1998**, *225*, 74−80.

(8) Magueijo, V. M.; Anderson, L. G.; Fletcher, A. J.; Shilton, S. J. Polysulfone mixed matrix gas separation hollow fibre membranes filled with polymer and carbon xerogels. *Chem. Eng. Sci.* **2013**, *92*, 13−20.

(9) Pekala, R. W. Organic aerogels from the polycondensation of resorcinol with formaldehyde. *J. Mater. Sci.* **1989**, *24*, 3221−3227.

(10) Job, N.; Gommes, C. J.; Pirard, R.; Pirard, J.-P. Effect of the counter-ion of the basification agent on the pore texture of organic and carbon xerogels. *J. Non-Cryst. Solids* **2008**, *354*, 4698−4701.

(11) Fairén-Jiménez, D.; Carrasco-Marín, F.; Moreno-Castilla, C. Porosity and surface area of monolithic carbon aerogels prepared using alkaline carbonates and organic acids as polymerization catalysts. *Carbon* **2006**, *44*, 2301−2307.

(12) Horikawa, T.; Hayashi, J.; Muroyama, K. Controllability of pore characteristics of resorcinol-formaldehyde carbon aerogel. *Carbon* **2004**, *42*, 1625−1633.

(13) Anderson, L. The Effect of the Catalyst on the Formation of RF Xerogels. Ph.D. Thesis, University of Strathclyde, Glasgow, 2014.

(14) Al-Muhtaseb, S. A.; Ritter, J. A. Preparation and properties of resorcinol-formaldehyde organic and carbon gels. *Adv. Mater.* **2003**, *15*, 101−114.

(15) El Khatat, A. M.; Al-Muhtaseb, S. A. Advances in tailoring resorcinol-formaldehyde organic and carbon gels. *Adv. Mater.* **2011**, *23*, 2887−2903.

(16) Lin, C.; Ritter, J. A. Effect of synthesis pH on the structure of carbon xerogels. *Carbon* **1997**, *35*, 1271−1278.

(17) Job, N.; Pirard, R.; Marien, J.; Pirard, J.-P. Porous carbon xerogels with texture tailored by pH control during sol−gel process. *Carbon* **2004**, *42*, 619−628.

(18) Job, N.; Panariello, F.; Marien, J.; Crine, M.; Pirard, J.-P.; Léonard, A. Synthesis optimization of organic xerogels produced from convective air-drying of resorcinol−formaldehyde gels. *J. Non-Cryst. Solids* **2006**, *352*, 24−34.

(19) Mulik, S.; Sotiriou-Leventis, C.; Leventis, N. Time-Efficient Acid-Catalyzed Synthesis of Resorcinol−Formaldehyde Aerogels. *Chem. Mater.* **2007**, *19*, 6138−6144.

(20) Tamon, H.; Ishizaka, H.; Mikami, M.; Okazaki, M. Porous structure of organic and carbon aerogels synthesized by sol-gel polycondensation of resorcinol with formaldehyde. *Carbon* **1997**, *35*, 791−796.

(21) Petričević, R.; Glora, M.; Fricke, J. Planar fibre reinforced carbon aerogels for application in PEM fuel cells. *Carbon* **2001**, *39*, 857−867.

(22) Yamamoto, T.; Yoshida, T.; Suzuki, T.; Mukai, S. R.; Tamon, H. Dynamic and static light scattering study on the sol-gel transition of resorcinol-formaldehyde aqueous solution. *J. Colloid Interface Sci.* **2002**, *245*, 391−396.

(23) Gaca, K. Z.; Sefcik, J. Mechanisms and kinetics of nanostructure evolution during early stages of resorcinol-formaldehyde polymerization. *J. Colloid Interface Sci.* **2013**, *406*, 51−59.

(24) Brunauer, S.; Emmett, P. H.; Teller, E. Adsorption of gases in multimolecular layers. *J. Am. Chem. Soc.* **1938**, *60*, 309−319.

(25) Barrett, E. P.; Joyner, L. G.; Halenda, P. P. The determination of pore volume and area distributions in porous substances. I. computations from nitrogen isotherms. *J. Am. Chem. Soc.* **1951**, *73*, 373−380.

(26) Finsy, R. Particle sizing by quasi-elastic light scattering. *Adv. Colloid Interface Sci.* **1994**, *52*, 79−143.

(27) Einstein, A. On the movement of small particles suspended in stationary liquids required by the molecular theory of heat. *Ann. Phys.* **1905**, *17*, 549−560.

(28) Stokes, G. G. On the effects of the internal friction of fluids on the motion of pendulums. *Cambridge Philos. Trans.* **1851**, *9*, 8−106.

(29) Morales-Torres, S.; Maldonado-Hodar, F. J.; Perez-Cadenas, A. F.; Carrasco-Marin, F. Textural and mechanical characteristics of carbon aerogels synthesized by the polymerization of resorcinol-formaldehyde using alkali carbonates as basification agents. *Phys. Chem. Chem. Phys.* **2010**, *12*, 10365−10372.

(30) Job, N.; Panariello, F.; Crine, M; Pirard, J.-P.; Léonard, A. Rheological determination of the sol−gel transition during the aqueous synthesis of resorcinol-formaldehyde resins. *Colloids Surf., A* **2007**, *293*, 224−228.

(31) Sandkühler, P.; Lattuada, M.; Wu, H.; Sefcik, J.; Morbidelli, M. Further insights into the universality of colloidal aggregation. *Adv. Colloid Interface Sci.* **2005**, *113*, 65−83.

(32) Hofmeister, F. About the science of the effect of salts. *Arch. Exp. Pathol. Pharmakol.* **1888**, *24*, 247−260.

(33) Persson, I. Hydrated metal ions in aqueous solution: How regular are their structures? *Pure Appl. Chem.* **2010**, *82*, 1901−1917.

(34) Pekala, R. W.; Schaefer, D. W. Structure of organic aerogels. 1. Morphology and scaling. *Macromolecules* **1993**, *26*, 5487−5493.

(35) Schaefer, D. W.; Pekala, R.; Beaucage, G. Origin of porosity in resorcinol-formaldehyde aerogels. *J. Non-Cryst. Solids* **1995**, *186*, 159−167.

(36) Jawor-Baczynska, A.; Moore, B. D.; Lee, H. S.; McCormick, A. V.; Sefcik, J. Population and size distribution of solute-rich mesospecies within mesostructured aqueous amino acid solutions. *Faraday Discuss.* **2013**, *167*, 425−440.

(37) Sandkühler, P.; Sefcik, J.; Morbidelli, M. Scaling of the Kinetics of Slow Aggregation and Gel Formation for a Fluorinated Polymer Colloid. *Langmuir* **2005**, *21*, 2062−2077.

(38) Poon, W. C. K.; Haw, M. D. Mesoscopic structure formation in colloidal aggregation and gelation. *Adv. Colloid Interfac.* **1997**, *73*, 71−126.

(39) Fartaria, R.; Javid, N.; Pethrick, R. A.; Liggat, J. J.; Sefcik, J.; Sweatman, M. B. Structure of laponite-styrene precursor dispersions for production of advanced polymer-clay nanocomposites. *Soft Matter* **2011**, *7*, 9157−9166.

(40) Javid, N.; Vogtt, K.; Roy, S.; Hirst, A. R.; Hoell, A.; Hamley, I. W.; Ulijn, R. V.; Sefcik, J. Supramolecular Structures of Enzyme Clusters. *J. Phys. Chem. Lett.* **2011**, *2*, 1395−1399.

(41) Yamamoto, T.; Nishimura, T.; Suzuki, T.; Tamon, H. Control of mesoporosity by sol-gel polycondensation and freeze drying. *J. Non-Cryst. Solids* **2001**, *288*, 46−55.

(42) Pekala, R. W.; Kong, F. M. A synthetic route to organic aerogels — mechanism, structure, and properties. *J. Phys.* **1989**, *50*, 33−40.

237

In Draft Form

A further two manuscripts, containing results from this body of work, are currently in incomplete draft form.

Effects of secondary metal carbonate addition on the porous character of resorcinol-formaldehyde xerogels.

Stewart J. Taylor, Mark D. Haw, Jan Sefcik and Ashleigh J. Fletcher*

Department of Chemical and Process Engineering, University of Strathclyde, Glasgow, G1 1XJ

ABSTRACT:

Introduction

Pekala published the first work on resorcinol-formaldehyde gels in 1989. The sol-gel polycondensation of resorcinol and formaldehyde, in the presence of sodium carbonate acting as a base, produced a solid 3D network with water entrained within the porous system. After exchanging the water for acetone and following drying with supercritical carbon dioxide, the resulting dried gel hade very low density, large surface area and high pore volume. Subsequent pyrolysis in an inert atmosphere rendered the material electrically conductive.

The proposed mechanism of the sol-gel reaction involved two main stages. In the first stage, the base promotes the reaction between resorcinol and formaldehyde to produce mono-, di-, and tri-substituted resorcinol known as the hydroxymethyl derivative. These intermediates then undergo acid promoted polycondensation into growing oligomers, which form clusters that though cross-linking make up the gel structure. The sol-gel process is highly flexible, allowing a number of process variables to be changed. These include the molar ratio of resorcinol to formaldehyde, the total solids content, or dilution, and the type of catalyst.

The reaction is typically carried out in the presence of basic sodium carbonate. However, alternative bases such as lithium and potassium carbonate or sodium hydroxide will also work equally well. It is also possible to promote the reaction between resorcinol and formaldehyde through the use of mineral acids such as nitric acid, or organic acids such as acetic acid.

As such, it has been widely recognized that the initial pH during the sol-gel process plays an important role in the gel formation, and therefore the range of initial pH values with which a viable gel can be made is limited. When using a base, this range is between 5.5 – 7.5, while for the acid promoted system this drops to between 1 and 4. If the pH is too high initially, the acid promoted polymerization will be inhibited and the resulting product is non-porous. Between the two ranges, the addition reaction between resorcinol and formaldehyde is not promoted, resulting in unrealistically long gelation times. Finally, too acidic a pH will cause precipitation of the reactants.

Control of the initial pH is therefore vital in the formation of RF gels. This control is commonly achieved by altering the amount of catalyst present, in turn modifying the H^+/OH^- ratio. The

catalyst added is typically expressed as a molar ration of resorcinol to catalyst (R/C). The lower the R/C value, the greater the concentration of catalyst present. Changing the R/C therefore changes the porous properties of the dry gel. For sodium carbonate, R/C values typically fall within the range of 50 – 3000. Increasing the R/C leads to an increasing of the cluster size, resulting in an increased pore size and corresponding decrease in surface area. This has been found to be due to controlling the number of clusters present. Increasing the R/C leads to a lower number concentration of clusters, which can subsequently grow larger in the available space.

Both Barral and Laskowski et al. investigated resorcinol-formaldehyde gel formation through the use of a double catalyzed synthesis route. In both cases, after initially catalyzing the reaction with a base, an acid was added, causing a significant decrease in the gelation time. The double catalyzed route played to the requirements of the two steps in the gel formation process. The base promoted the initial reaction between resorcinol and formaldehyde, while the acid promoted the polymerization and cross-linking steps. Both studies found that the resulting double catalyzed gels featured very broad pore size distributions, stretching from around 10 nm to 100 nm.

Feng et al. took this process even further, investigating both a base-acid route and a base-base route, with a comparison to a standard base catalyzed gel. In agreement with the work of Barral and Laskowski et al., the addition of an acid produced a broadening of the pore size distribution. Interestingly, the addition of a base also produced a broadening of the distribution, whilst also shifting to a larger average pore size.

Dynamic light scattering is a commonly used technique in the sizing of particle in suspension in a liquid medium. It has subsequently been used to study the formation RF gels. In agreement with Gaca et al., the authors found that cluster growth was thermodynamically driven, being independent of the catalyst concentration for lithium, sodium and potassium carbonate. As previously stated, the catalyst concentration determined the number density of clusters. High R/C values produced a lower number of clusters, which could grow to larger sizes before reaching critical volume.

The aim of this work was to study the effect of various Group I metal carbonates when added to a differing Group I or Group II metal carbonate catalyzed gel system at various times throughout the gelation process. This was accomplished by monitoring the growth of RF clusters within the system using DLS, coupled with the use of low temperature nitrogen adsorption/desorption measurements. This subsequent analysis of the dried xerogels provided information on the textural properties of the samples prepared.

Experimental

Materials and Synthesis

RF solution compositions were determined by fixing R/F at 0.5, the total gel volume at 60 mL and the solids content at 20 % weight by volume, resulting in a solids mass of 12 g. As the R/C and chosen metal carbonate changed, the individual masses of R, F and C were adjusted accordingly to maintain a total mass of 12 g.

When using a single Group II metal carbonate, R/C values of 100 and 200 were chosen. When two metal carbonates were used, these were combined in a ratio of 50:50 with a total R/C of 100. This corresponded to an individual R/C of 200 for each of the metal carbonates.

Resorcinol (ReagentPlus, 99 %), aqueous formaldehyde solution (37 wt. % formaldehyde, stabilised with 10-15 % methanol), lithium carbonate (purum, ≥99 %), sodium carbonate (anhydrous, ≥99.5 %), potassium carbonate (anhydrous powder, 99.99 %), caesium carbonate (ReagentPlus, 99 %), calcium carbonate (≥99 %) and barium carbonate (ACS reagent ≥99 %) were all used as purchased from SigmaAldrich.

For samples containing a single carbonate, and simultaneous addition of two carbonates, the required mass of resorcinol was completely dissolved in 50 mL of deionised water (Millipore Elix 5) in a 500 mL sealable jar under magnetic stirring. The appropriate mass of carbonate(s) was then added to this solution with continued stirring until dissolved. As both calcium and barium carbonate have such low solubilities in water, complete dissolution was not possible, even with the small quantities used. The solution was therefore left to stir for 5 minutes before proceeding. Subsequently, the required volume of formaldehyde solution and additional deionised water were added to the jar to give a total volume of 60 mL. The jar was then sealed and allowed to stir continuously for 30 minutes. After measuring the initial solution pH (Hanna pH 20 meter fitted with an HI-1110B pH probe), the sealed jars were transferred to a preheated oven set to 85 ± 5 °C until gelation occurred. Gelation times were monitored by periodically tilting the jars to an angle of 45° until no flow was observed. The gels were then left to cure in the oven, with the temperature maintained at 85 ± 5 °C.

Secondary addition of metal carbonate required a slight change to the synthesis procedure. The resorcinol and parent carbonate were dissolved in only 40 mL of deionised water, while the remaining 10 mL was used to dissolve the secondary metal carbonate in a second, smaller vial. Formaldehyde and additional water were added as before and the RF solution stirred for 30 minutes. With the pH recorded, the sample was placed in the 85 ± 5 °C oven along with the secondary carbonate solution. At a predetermined point during the gelation process, both containers were removed from the oven and the secondary carbonate solution added to the main RF jar. The mixture was stirred for 30 seconds to ensure thorough mixing, before being returned to the oven to complete the gelation and curing step.

After curing for 3 days, the gels were removed from the oven. The aqueous pore liquid was exchanged for acetone by shaking the sample in 180 mL of acetone (ACS reagent, ≥99.5%, SigmaAldrich) for a further 3 days at room temperature. The sample was finally dried under vacuum for 2 days at 85 °C to produce the xerogel product.

Xerogel Characterisation

Each of the dried xerogels underwent nitrogen adsorption/desorption measurements on a Micromeritics ASAP 2420 in order to determine surface areas and porosities. Approximately 0.5 g of the dried xerogel was first degased under vacuum at 110 °C for 2 hours in order to remove any residual solvent or other contaminants from the material surface. Analysis was then performed at -196 °C, maintained through the use of liquid nitrogen, and consisted of a 40 point adsorption and 30 point desorption cycle.

The resulting nitrogen uptake isotherms were subsequently analysed to provide data on the materials properties. Brunauer-Emmett-Teller (BET) theory was applied to the adsorption branch, giving a linear plot between the relative pressures (p/p_0) of 0.05 and 0.3, while allowing for the calculation of the BET surface area (S_{BET}). Meanwhile, pore size distributions were generated using the Barrett-Joyner-Halenda (BJH) method, applied to the desorption branch of the isotherms, and allowed for the calculation of average pore sizes.

Dynamic Light Scattering

All DLS measurements were performed on an ALV/CGS-3 compact goniometer and ALV/LSE-5004 multiple tau digital correlator. Measurements were taking at a scattering angle, θ, of 90° while the laser had a wavelength, λ, of 632.8 nm.

Samples prepared in the presence of either a single metal carbonate or simultaneous addition of two metal carbonates were analysed in the same manner. After measuring the initial pH of the RF solution, 11 equal portions were passed through a 0.2 μm pore size PTFE syringe filter (Whatman Puradisc) into separate borosilicate glass cells, 10 mm in diameter and 75 mm in height (Fisher Scientific). Each cell was sealed with a cap, and 10 were placed in an oven at 85 ± 5 °C. The remaining cell, designated t = 0, was taken for immediate analysis. Subsequent cells were removed from the oven after the appropriate time intervals, upon which they were rapidly quenched to room temperature and analysed.

Secondary addition of carbonate samples once again required a slight modification of the analysis procedure. Before the secondary addition, the parent carbonate solution was analysed as previously described. Post addition, small volumes of the newly mixed solution were transferred into further glass cells and returned to the oven, before being removed, quenched and analysed as before at the appropriate time intervals.

The digital correlator generated an autocorrelation of the scattered light intensity for each experimental point. The cumulant method was applied to each these autocorrelation functions in order to estimate the initial decay rate, Γ (s^{-1}). From this value, the mean diffusion coefficient, D, was calculated

$$\Gamma = Dq^2$$

where q is the scattering vector magnitude

$$q = \frac{4\pi n_0}{\lambda} sin\frac{\theta}{2}$$

From this, the Stokes-Einstein equation can be used to calculate the mean hydrodynamic radius, R_H

$$R_H = \frac{k_b T}{6\pi\mu D}$$

where k_B is the Boltzmann constant, T is absolute temperature and μ is the dynamic viscosity. For all calculations, μ was assumed to be that of pure water at the experimental temperature.

Results and Discussion

Gelation times in this work were determined for all gels synthesized with both a single metal carbonate, and those with simultaneous addition of 2 metal carbonates. These results were then combined and compared with the previously obtained gelation times for gels made with Group I metal carbonates.[Paper1] As for the Group I metal carbonates, it was found that for an equivalent R/C, both calcium carbonate and barium carbonate had the same gelation time; this being 40 minutes for R/C 100 and 45 minutes for R/C 200. Furthermore, it was found that combining cesium carbonate and sodium carbonate, both Group I, gave a gelation time

of 35 minutes – identical to that of the individual metals. When combining a Group II and Group I metal carbonates, it was found that no matter the combination used, the gelation was constant at 40 minutes.

These gelation times were then used to determine the interval times used for DLS measurements. Instead of using a fixed time interval, DLS measurements were run at every 10 % of the gelation time. This choice therefore allowed for direct comparison between samples at an equivalent point in the gelation process.

Figure 1 shows the normalized autocorrelation functions generated by the digital correlator over the entire gelation period for calcium carbonate at an R/C of 100. As can be seen, all but the final decay profile follows an exponential dependence on time. This is indicative of free Brownian motion within the sample. The final profile exhibits nonergodicity and implies that the gel structure is predominantly formed, as would be expected at the gelation time. Unlike the autocorrelation functions displayed by the Group I metals, the Group II samples display no secondary decay. These secondary decays implied that at later times in the gelation process, networking and aggregation was occurring. Instead, the clusters appear to be growing unhindered to larger sizes. This is supported by visual inspection of the samples during gelation. Whereas the Group I samples remained translucent throughout the entire gelation, turbidity developed when a Group II metal was used. This turbidity is indicative of larger particle sizes.

Cumulant analysis was applied to all of the autocorrelation functions corresponding to non-turbid samples, in order to determine hydrodynamic radii. Turbidity leads to a high optical contrast, which in turn leads to multiple scattering of the light and prevents accurate radii from being calculated. Figure 2 shows the hydrodynamic radii as determined from the initial decay of these autocorrelation functions.

It can be seen that all 4 of the Group II metal carbonate samples have cluster sizes which fall into a narrow overlapping band, in a similar manner to the results previously obtained for lithium, sodium and potassium carbonate. However, the radii values are much larger than anything witnessed for the Group I metals. It is also noticeable that despite the difference in R/C ratio, the maximum observed hydrodynamic radius is very similar in each case, in contrast to the results for the Group I metals. This supports the theory that rather than aggregating and networking to form the gel network, clusters grow continuously to larger sizes until the gel is formed.

Figure 3 contains both the adsorption/desorption isotherms and pore size distributions for the Group II metal carbonate samples. The isotherms show a considerably greater nitrogen uptake than that observed for lithium, sodium and potassium carbonate at the corresponding R/C ratio. While the uptakes for caesium carbonate are closer to those of the Group II metal carbonates, the increase is still significant. Pore sizes follow a similar trend and are also much larger in the presence of a Group II metal carbonate when compared to the Group I analogues. As the pores within the RF gel network are composed of the gaps between clusters, these larger pores support the theory that clusters grow to much larger sizes, can pack less tightly, and result in larger intercluster voids.

Table 1 outlines all of the metal carbonate combinations studied in this work. Caesium carbonate was chosen as a parent carbonate due to the vast differences between it and the other Group I carbonates. Similarly, sodium carbonate was picked as the initial representative of the Group I species. This provided systems containing both two 1^+ cations and both a 1^+ and a 2^+ cation.

Figure 4 shows the hydrodynamic radii results for each of the three parent cations when mixed with sodium carbonate at the chosen time interval. Unfortunately, due to the development of secondary decays in the case of caesium carbonate, and turbidity in the case of calcium and barium carbonate, only the experimental runs with simultaneous addition and addition at 60 % of the parent gel time provided accurate data on the hydrodynamic radii.

The differences between the systems are clear to see. In the case of simultaneous addition of caesium and sodium carbonate, this results in clusters of sizes which fall directly between those of the pure caesium carbonate and sodium carbonate systems. Secondary addition at 60 % produces a noticeable flattening of the growth profile. As the calculated value of hydrodynamic radius is an average, this flattening suggests that while the already established clusters continue to grow at a reduced rate, the addition of sodium carbonate has created a secondary set of clusters with much smaller size. These grow in unison with the primary clusters until the entire system networks and aggregates into the gel structure.

In contrast, both the calcium carbonate/sodium carbonate and barium carbonate/sodium carbonate systems are much different. In both cases, the simultaneous addition closely follows the growth profile of the pure sodium carbonate system, with radii of the same size as the R/C 200 sample in particular. As the sodium carbonate is present at R/C 200 in the simultaneous addition gel, this suggests that the sodium is dominant in the gel formation process and the calcium or barium plays very little part.

Subsequently, before secondary addition, the growth profiles follow those of the parent carbonate at R/C 200, as would be expected from being the only carbonate species initially present. However, after addition at 60 %, both systems show an immediate dramatic decrease in the observed cluster size. This corresponds to a similar drop in the scattered light intensity (see S. I.). The combination of these factors suggests that on addition of sodium carbonate, a secondary, much smaller species develops. The severity of the decrease in average radius and the limited growth after addition suggests that only these secondary species are growing, filling the gaps between the existing clusters and resulting in the final cluster size being much smaller than that of the pure Group II sample. The Group I metal carbonate is therefore dominant in the process once more.

This pattern is replicated when using the alternative Group I carbonates of lithium and potassium in conjunction with calcium carbonate as the parent species, with all data available in the S.I. These results are to be expected from the similarities previously observed for the three Group I metal carbonates. It should, however, be noted that the number of useable points after addition decreases on going down the group, despite all three systems having virtually identical gel times of approximately 54 minutes. It therefore takes the potassium system longest to aggregate and network. However, in all cases, the hydrodynamic radius at the onset of aggregation and networking is 7 nm.

Further evidence of the dominance of the Group I metal comes in the form of the autocorrelation functions, in particular those of the calcium and barium systems. Where the pure metal systems show no secondary decay as gelation is approached, secondary addition of the Group I metal carbonate at any point reintroduces the secondary decay observed with the pure Group I metal samples. An example set of these autocorrelation functions is given in the S.I.

Figure 5 shows the nitrogen adsorption/desorption isotherms obtained for the three parent cations with secondary addition of sodium carbonate simultaneously and at 60, 70 and 80 %

of the parent gel time. Pure metal data for both halves of the system is once more included for reference. As can be seen from the plot there is a distinct clustering of the isotherms for all of the systems, centering on that of sodium carbonate at R/C 200. Only addition at 80 % causes a significant change in the isotherm, with a greater nitrogen uptake and shifting of the hysteresis loop to higher relative pressures. This change is indicative of an increase in pore size and total pore volume.

Examination of the pore size distributions displayed in Figure 6 reinforces these observations. The distributions for simultaneous, 60 % and 70 % addition are again grouped around those of the sodium carbonate gels. Meanwhile, addition at 80 % gives rise to larger pore sizes. The lack of clearly distinguishable bimodal porosity backs up the assumption that the newly formed secondary clusters fill the gaps between the existing clusters, resulting in a uniform pore size. This process is depicted schematically in Figure 7.

Like for the hydrodynamic radii data, the isotherms and pore size distributions that result from the addition of lithium or potassium carbonate to a calcium carbonate gel once more follow a very similar pattern. This data is again available in the S.I.

Table 2 gives further properties of each of the dried xerogels, these properties being the BET surface area (S_{BET}), the total pore volume (V_{Tot}), the micropore volume ($V_\square$) and the average pore size (d_p avg.). Once more, the pure metal data is included for reference, while the data for adding lithium or potassium carbonate to a calcium carbonate gel is again included in the S.I. The data in the table again shows how the simultaneous, 60 % and 70% addition samples can be grouped in terms of surface area, pore volume and average pore size, with these values being comparable to those of the sodium carbonate gels as opposed to those of their respective parent metal cation. As for the isotherms and pore size distributions, only the samples with addition at 80 % show any meaningful difference in these properties.

By studying all of these results in tandem it can be seen how it is possible to tune the pore size of the xerogels, while keeping the total ionic strength constant. This is opposed to the most common method of inducing this control, wherein the R/C ratio is altered. Furthermore, the gels with average pore size and total pore volume similar to those of the sodium gels have a much narrower distributions. This implies a less disperse porosity, with more pores of the same size and making the material more consistent. This feature is inconsistent with Feng et al., who found that on secondary addition of a base, the pore size distribution as calculated by the Dollimore-Heal method broadened, while the average pore size also increased.

The results also show that, even at times up to 80 % of the initial parent gel time, when structure formation is well underway, it is still possible to manipulate the growth of clusters to a great degree. This suggests that even at this time there is still free resorcinol, formaldehyde, hydroxymethyl derivative and small RF oligomers available to participate in the reaction and form new clusters. This is especially prevalent in the case of caesium carbonate as the parent cation. By 70 % of the gel time, previous work has established that aggregation and networking has begun. The addition of sodium carbonate during this period disrupts the process to a certain degree, forcing a reorganization of the structure before the aggregation can be completed. By 80 % of the gel time, aggregation is well established, making it more difficult to disrupt. This system therefore has properties which are closer to the initial caesium carbonate gel than any of the other combinations studied.

When using calcium or barium carbonate as the parent cation, primary cluster size increases as the gelation process occurs. As such, there is less available material for the secondary

clusters. These clusters therefore cannot fill the gaps in the system as fully at later addition times, resulting in the larger pore sizes observed.

In a previous study, we have proposed a Hofmeister like series relating the metal cations used to their ability to destabilize RF oligomer molecules and in turn keeping them salted in to solution by increasing their solubility; effectively stabilizing the colloidal suspension. Lithium, sodium and potassium were found to have a greater ability than caesium to destabilize the oligomers, resulting in caesium producing larger clusters than the other Group I metals. This work shows that calcium and barium produce larger again clusters, suggesting an even lesser ability to destabilize the oligomer molecules.

These differences in stability can be used to explain the observations made with regards to the sizes of RF clusters. Simultaneous addition of the two chosen carbonates introduces two cations with different destabilization abilities e.g. sodium being very destabilizing and calcium being less destabilizing. The sodium destabilizes the oligomers to the full extent of its ability, resulting in the small clusters observed being consistent in size with those of the pure sodium gel. This overpowers the less destabilizing nature of the calcium cation and prevents it from exerting its influence.

When the secondary addition is delayed, the clusters initially form as per the destabilization ability of the parent cation. On addition of the more destabilizing secondary cation, the remaining unincorporated material forms new, more soluble oligomers, instead of joining the established clusters, resulting in the termination of the growth of these primary clusters and secondary clusters growing in the resulting gaps.

By controlling the destabilization ability of the cations present, it is therefore possible to control the final pore size in dried xerogels. This is possible while maintaining a constant R/C and therefore constant ionic strength.

Conclusions
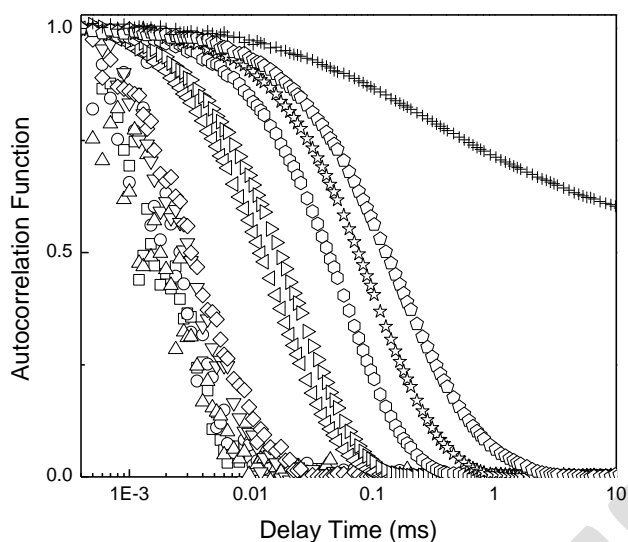
Figure 1. Autocorrelation functions for calcium carbonate at R/C 100. Measurements are taken every 10 % of the total gel time such that (□) 0 %, (○) 10 %, (△) 20 %, (▽) 30 %, (◇) 40 %, (◁) 50 %, (▷) 60 %, (⬡) 70 %, (☆) 80 %, (⬠) 90 % and (+) 100 %.
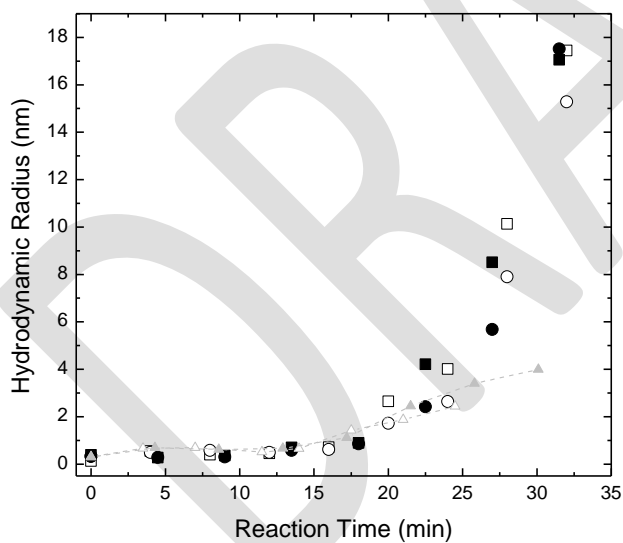
Figure 2. Hydrodynamic radii as determined from autocorrelation functions for calcium carbonate at (□) R/C 100 and (■) R/C 200, and barium carbonate at (○) R/C 100 and (●) R/C 200. Radii for sodium carbonate at (△) R/C 100 and (▲) R/C 200 are included for comparison, with complete data for the Group I metals available in the Supporting Information.[Paper1]
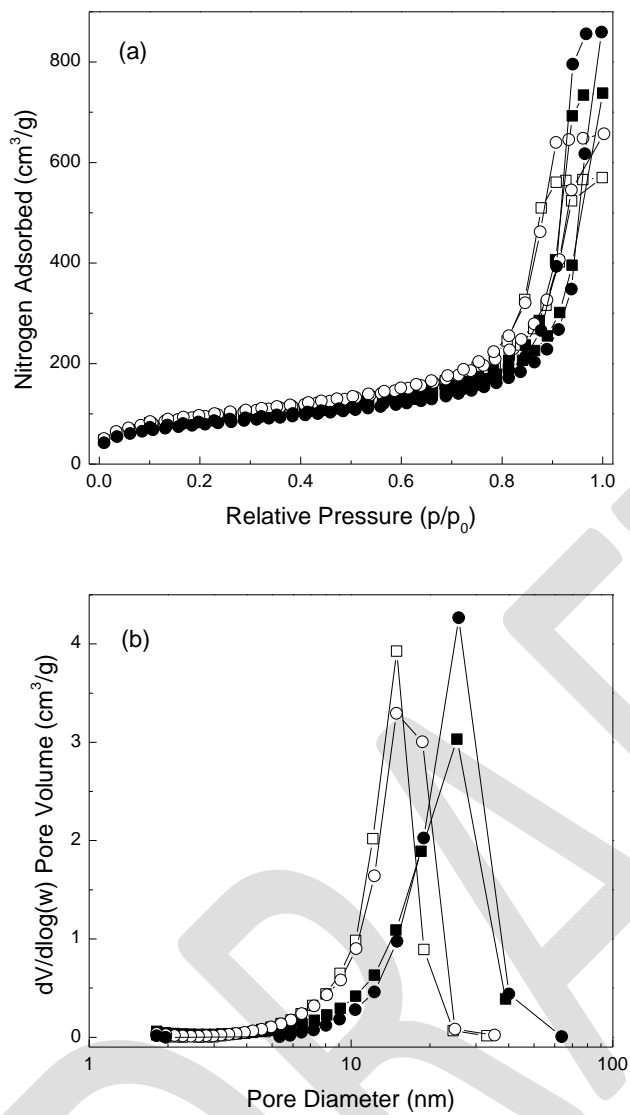
Figure 3. Adsorption/desorption isotherms (a) and pore size distributions (b) for calcium carbonate at (□) R/C 100 and (■) R/C 200 and barium carbonate at (○) R/C 100 and (●) R/C 200.
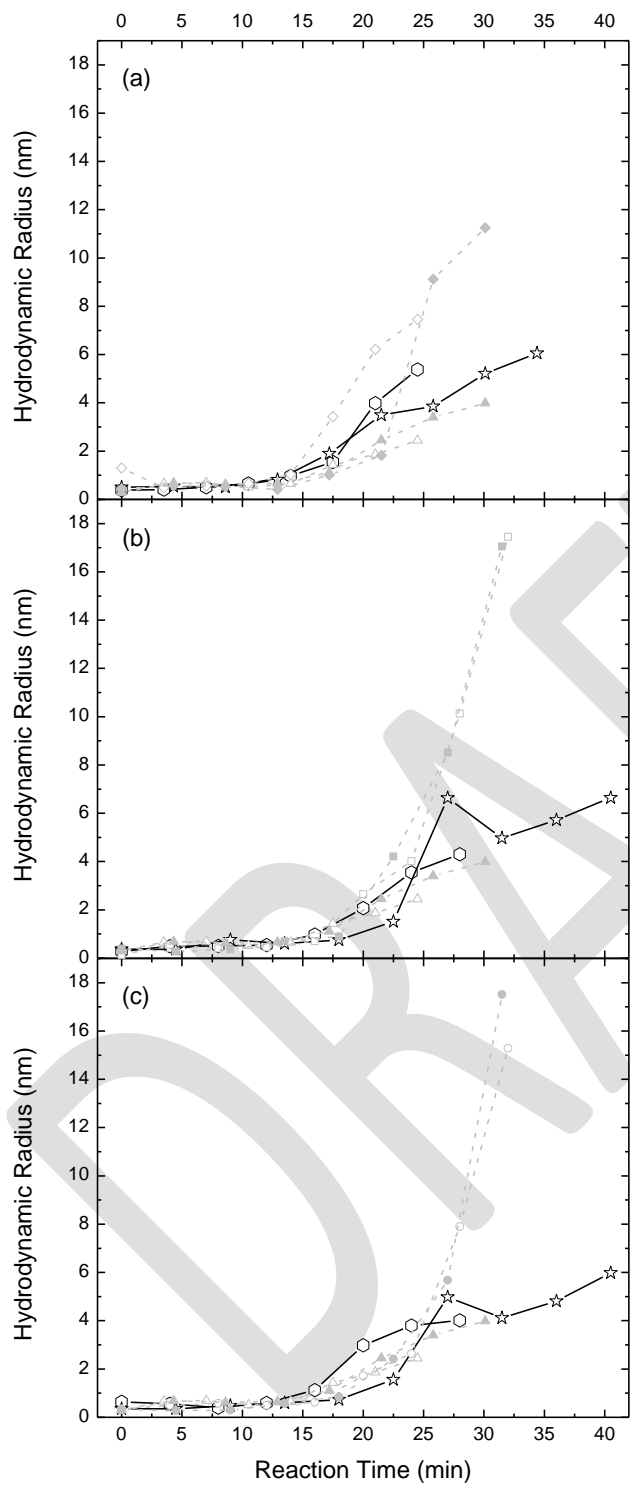
Figure 4. Hydrodynamic radii for (a) caesium carbonate/sodium carbonate, (b) calcium carbonate/sodium carbonate and (c) barium carbonate/sodium carbonate at (○) simultaneous addition and (☆) secondary addition at 60%. Pure metal data for (△) sodium carbonate, (◇) caesium carbonate, (□) calcium carbonate and (○) barium carbonate is also included with open symbols showing R/C 100 and closed symbols showing R/C 200.
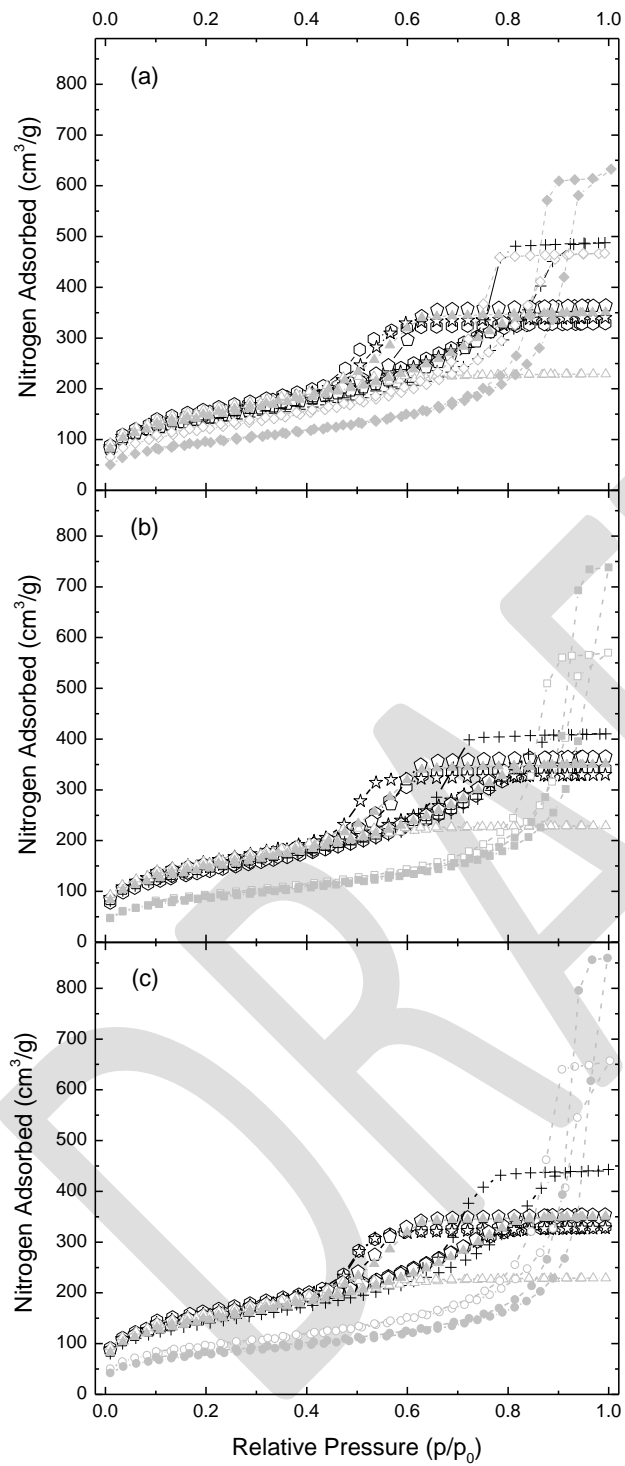
Figure 5. Adsorption/desorption isotherms for (a) caesium carbonate/sodium carbonate, (b) calcium carbonate/sodium carbonate and (c) barium carbonate/sodium carbonate at (○) simultaneous addition, (☆) secondary addition at 60%, (⬠) secondary addition at 70% and (＋) secondary addition at 80%. Pure metal data for (△) sodium carbonate, (◇) caesium carbonate, (□) calcium carbonate and (○) barium carbonate is also included with open symbols for R/C 100 and closed symbols for R/C 200.

249
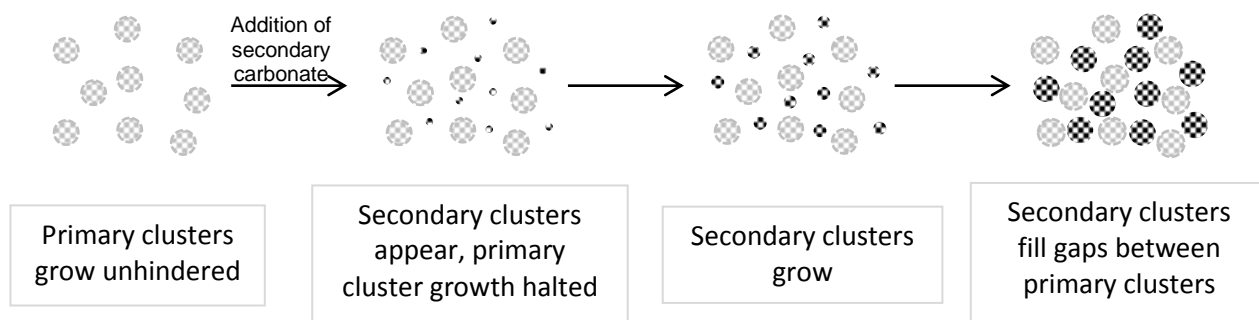
Figure 7. Schematic diagram illustrating the growth of new clusters after addition of the secondary metal carbonate. Clusters are depicted as spheres for clarity.

Table 1. Metal carbonate combinations

Parent Metal Carbonate	Secondary Metal Carbonate
Caesium	Sodium
Calcium	Sodium
Barium	Sodium

Table 2. Gel properties[a]

Sample	S_{BET}	V_{TOT}	V_μ	d_p avg.
Na_2CO_3_100	533 ± 5	0.35	0.05	2.9
Na_2CO_3_200	508 ± 4	0.54	0.03	4.2
Cs_2CO_3_100	425 ± 3	0.72	0.02	6.9
Cs_2CO_3_200	329 ± 3	0.98	0.02	12.6
$CaCO_3$_100	307 ± 3	0.88	0.02	12.4
$CaCO_3$_200	301 ± 3	1.14	0.02	17.6
$BaCO_3$_100	331 ± 3	1.11	0.01	13.3
$BaCO_3$_200	275 ± 3	1.33	0.02	21.8
Cs/Na sim	537 ± 4	0.51	0.04	3.8
Cs/Na 60	520 ± 4	0.53	0.03	4.0
Cs/Na 70	498 ± 4	0.56	0.03	4.6
Cs/Na 80	457 ± 4	0.75	0.03	7.3
Ca/Na sim	535 ± 4	0.56	0.03	4.2
Ca/Na 60	533 ± 4	0.51	0.03	3.8
Ca/Na 70	526 ± 5	0.63	0.04	5.0
Ca/Na 80	490 ± 4	0.64	0.04	5.5
Ba/Na sim	548 ± 5	0.54	0.04	4.0
Ba/Na 60	535 ± 4	0.51	0.04	3.8
Ba/Na 70	528 ± 4	0.55	0.03	4.1
Ba/Na 80	486 ± 4	0.69	0.04	6.1

[a]Data for sodium carbonate and caesium carbonate taken from Paper1

251

Rapid determination of particle sizes of RF sol-gels using UV-Vis spectrometry

Lynsey G. Anderson[a,b], Stewart J. Taylor[a,b], Christopher J. McLean[b], Suresh N. Thennadil[a] and Ashleigh J. Fletcher[a1]

a. Department of Chemical and Process Engineering, University of Strathclyde Glasgow, G1 1XJ
b. WestCHEM, Department of Pure and Applied Chemistry, University of Strathclyde, Glasgow, G1 1XL

Abstract

Existing methods of determining particle size in sol-gels is time-consuming with regards to sample preparation and data interpretation. Here, UV-Vis spectrometry was shown to be a quick analytical tool to determine changes in particle size during the sol-gel transformation of Resorcinol-Formaldehyde (RF) sol-gels. The method requires no sample manipulation and results can be obtained within a few minutes, allowing particle formation for different sol compositions to be rapidly compared. Results presented here demonstrate application of the technique to sol samples prepared with Group I and Group II metal carbonate catalysts, where UV-Vis absorbance at 500, 600 and 750 nm increases linearly with particle size (> 20 nm). These preliminary results suggest that, with the aid of a reference library, UV-Vis spectrometry could be used as an alternative technique, with the potential for in-line integration, for the determination of RF particle sizes, offering quicker and simpler analysis compared to traditional techniques.

Introduction

Since their first synthesis by Pekala *et al.* [1] Resorcinol-Formaldehyde (RF) gels have been widely studied, with significant interest stemming from their highly tuneable porous properties, which can be altered through the variation of synthesis parameters. RF gels with a range of pores, extending from microporous (<2 nm) to macroporous (>50 nm), can be prepared, making them useful for a wide range of potential applications, including electrochemical applications, for example as electrodes in Electrochemical Double Layer Capacitors (EDLCs) [2] and LiO_2 batteries [3]. The ability to prepare different forms of carbon gels with tuneable properties also make them attractive for adsorption and catalysis applications [4].

Pore sizes of RF gels can be manipulated by controlled aggregation of primary particles within the sol [5, 6] and, as described by Pekala *et al.* [1, 7, 8], this is mainly achieved via selection of catalyst concentration or the molar ratio of R to catalyst (R/C). When high catalyst concentrations (i.e. low R/C) are present, many small clusters are initially formed resulting in materials with small particles and pores, whereas low catalyst concentrations (i.e. high R/C) promote preferential growth of polymer clusters, resulting in gels with larger particles and pores. The catalyst is not the only factor affecting particle size of RF gels and many other variables have been shown to have an effect. Lee *et al.* [9] prepared gels using an emulsion technique and demonstrated that particle size could be controlled by altering stirring rate, with increased agitation resulting in smaller RF particles. Similar results were reported by Sharma *et al.* [10] who established that stirring time also influenced particle aggregation, with longer stirring times resulting in larger particles. Solid content, i.e. the percentage of reactants to sol volume, may also be varied, which affects the rate of reaction

---
[1] Corresponding author
ashleigh.fletcher@strath.ac.uk
Tel – 0141 548 2431

and, as a result, can be used to control particle size. High solid content cause the reaction between R and F to occur rapidly, causing a similar effect to that observed for high catalyst concentrations leading to small mass fragments and small pores, the inverse is observed for low solid content [11]. Scherdel *et al.* [12] reported that particles as large as a few micrometres (>1000 nm) could be prepared by using low percentage solids (R+F) and very low catalyst concentrations.

As a number of parameters influence RF particle size, in turn impacting on final porosity of the organic gels, it is of significance that the process of aggregation can be easily monitored. Traditional monitoring methods include Dynamic Light Scattering (DLS), Small Angle X-Ray Scattering (SAXS) and microscopic techniques such as Scanning Electron Microscopy (SEM) or Transmission Electron Microscopy (TEM). DLS is a spectroscopic technique that involves the determination of a time autocorrelation function for scattered light. Interaction of light with the sample is dependent upon the size of suspended particles [13, 14]; consequently interpretation of the autocorrelation function allows average particle sizes to be determined. This technique typically involves minimal sample preparation; however work within this group has shown that sample filtration prior to DLS analysis reduces the noise component, therefore, increasing the sensitivity of the results obtained [15]. Obtaining the auto correlation function for a sample takes only a few minutes, however, subsequent analysis to can be complex and time consuming. SAXS is a similar technique to DLS but involves measurement of X-ray scattering, like DLS, SAXS requires intricate data analysis [16]. Microscopic techniques, SEM and TEM, are typically used for examining the external and internal structure of solid RF gels and are, therefore, not suitable for monitoring particle size growth within solutions [17-19].

As stated above, although DLS and SAXS allow the particle sizes of RF sols to be monitored as the reaction progresses [20-22], the complex data analysis required makes it difficult to compare different sols as they are prepared. Consequently this study investigates the use of UV-Vis spectrometry as a means of rapidly monitoring RF particles, eliminating the need for further sample preparation and complex data manipulation. Various RF sols were prepared with a number of different Group I and Group II metal carbonate catalysts and their UV-Vis absorbance monitored over the range of 200-800 nm, throughout the sol-gel transition. DLS was used to measure changes in RF particle size and the relationship between absorbance and particle size was investigated.

Experimental

RF xerogel preparation

RF xerogels were synthesised by the polycondensation of resorcinol (R) and formaldehyde (F) in aqueous medium, using sodium carbonate (Na_2CO_3), potassium carbonate (K_2CO_3), caesium carbonate (Cs_2CO_3) or calcium carbonate ($CaCO_3$) as catalyst (C). Molar R/C ratios of 200 and 400 were used for all four catalysts. An appropriate amount of R was dissolved in deionised water, the required weight of C was added, before the addition of the corresponding quantity of F, such that R:F ratio was constant at 1:2 with 20% total solids, in a total reaction volume of 60 ml. The sol was stirred at room temperature for 30 min, after this time the sol was placed in an oven at 85 ± 5 °C to allow the gelation and curing processes to proceed.

DLS

Particle growth in the initial stages of the RF reaction was monitored using an ALV/CGS 3 Compact Goniometer System in conjunction with an ALV/LSE 5004 Multiple Tau Digital Correlator. This system used a He:Ne laser at 632.8 nm, and measured the scattered intensity at an angle of 90° to the beam path. After the 30 minute stir the sol was passed through a 0.2 μm PTFE filter (Whatman™ Puradisc™), which removed any undesired particulates. Small sample cells were then filled with equal volumes of the filtered sol. One of the cells was placed directly in the cell holder of the DLS equipment, allowing a measurement at time zero to be obtained. The other cells were placed in an oven at 85 ± 5 °C to begin gelation and were removed sequentially at the required percentage time intervals and quenched to room temperature before the scattered intensity was measured.

The scattered intensities obtained were used to generate autocorrelation functions. In order to obtain diffusion coefficients these functions were fitted with a third order cumulant and the calculated coefficients were substituted into the Stokes Einstein Equation (Equation 1) to give hydrodynamic radii of the particles at each stage of the gelation process:

$$d(H) = \frac{kT}{3\pi\eta D}$$

Equation 1

Where $d(H)$ is the hydrodynamic diameter (m), D is the translational diffusion coefficient (m^2 s^{-1}), k is Boltmann's constant (m^2 kg s^{-2} K^{-1}), T is absolute temperature (K) and η is the viscosity (Pa s).

UV-Vis absorbance measurements

UV-Vis absorbance measurements were performed using a Varian Cary 5000 UV-Vis-NIR spectrometer over a range of 200 nm to 800 nm. Representative parent sols were prepared as outlined in Section 3.1 up to the end of the 30 min stir period, at this point a small sub sample (~ 0.8 ml) was removed, pipetted into a 2mm wide quartz cuvette and the absorbance spectrum measured. This initial sample was classified as $T_{0\%}$. The remaining sol was placed in the oven, upon extraction of sample $T_{0\%}$, allowing thermal equilibration to occur, subsequently, small samples were extracted at sequential time intervals and the absorbance spectra measured. This allowed time resolved spectra to be obtained. Spectra were obtained, for each prepared sol, until the parent gel viscosity was such that samples could not be extracted into the quartz cell, at these stages the sols were close to their gelation points.

Results and discussion

Relationship between absorbance and RF particle size

Figure 1 shows a representative UV-Vis spectrum for an RF sol (R/C 200 for Na_2CO_3 at 9 min, 20% gelation time), clearly illustrating three main absorbance peaks which can be assigned using adsorption bands previously reported in the literature. The peak at approximately 295 nm is ascribed to phenol and aldehyde groups within the forming gel, and the peaks at approximately 220 nm and 340 nm result from conjugated benzene rings [23]. Similar scattering, as a result of conjugation, was demonstrated for the UV-Vis absorbance of fullerene (C_{60}) solutions by Mzerl *et al.* [24] and Kato *et al.* [25].
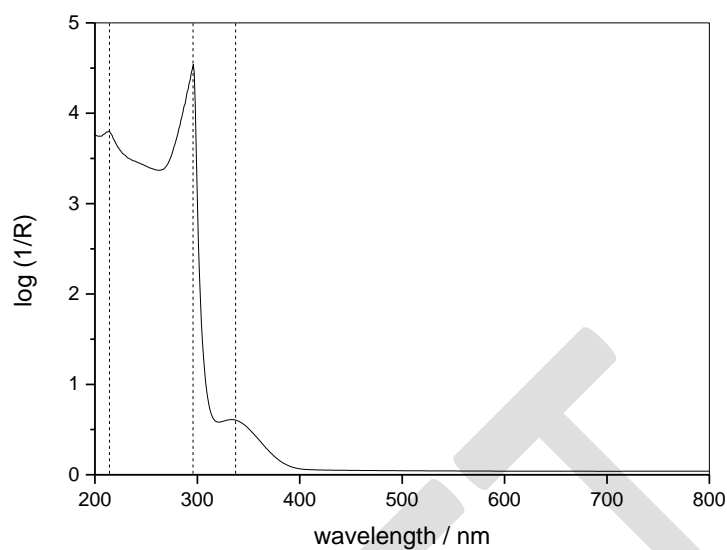
Figure 1: UV-Vis absorbance spectrum (in the range 200-800 nm) taken 9 minutes ($T_{20\%}$) into the reaction for an RF gel synthesized as 1R:2F, 20% solids, 60 ml volume and Na_2CO_3 catalyst at R/C 200.

Time resolved spectra for all RF sols studied are shown in Figure 2, demonstrating that absorbance at 340 nm intensifies with increasing reaction time. Similar to results reported by Kato *et al.* [25], for fullerene solutions, this increased absorbance can be explained by a change in the sol colour (colourless to red) indicative of increasing particle size, growing conjugation [26] and dense packing of RF particles, as the polymerisation reaction proceeds.
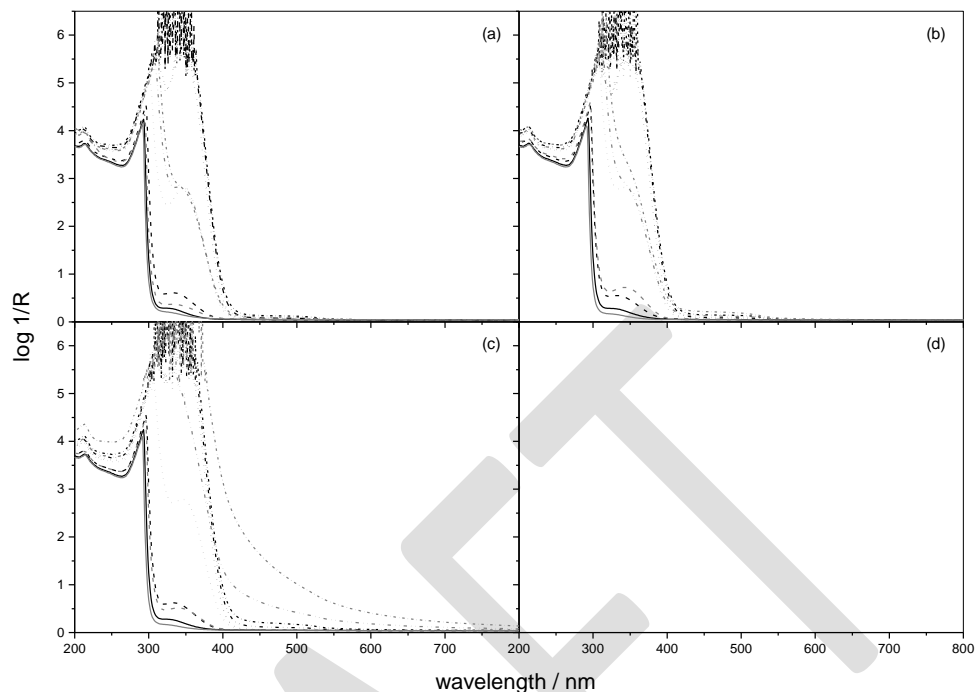
Figure 2: UV-Vis spectra for RF gel synthesized as 1R:2F, 20% solids, 60 ml volume and R/C 200 (black) or R/C 400 (grey) for (a) Na_2CO_3, (b) K_2CO_3, (c) Cs_2CO_3, (d) $CaCO_3$ at percentage time intervals: $T_{0\%}$ (—), $T_{20\%}$ (– –), $T_{40\%}$ (·····), $T_{60\%}$ (-··), and $T_{80\%}$ (----).

For particle sizes in the region of 100 - 250 nm, Kato *et al.* [25] reported an almost linear relationship at an absorbance of 340 nm. To investigate whether a similar relationship existed between RF particle size and absorbance, the DLS particle sizes (Figure 3) obtained at the same percentage time intervals were plotted against the UV-Vis absorbance observed at 340 nm for each corresponding sample. The specific wavelength of 340 nm was chosen as this corresponds to one of the conjugated benzene peak maxima observed in the full range spectra, as shown in **Figure 2**.

256
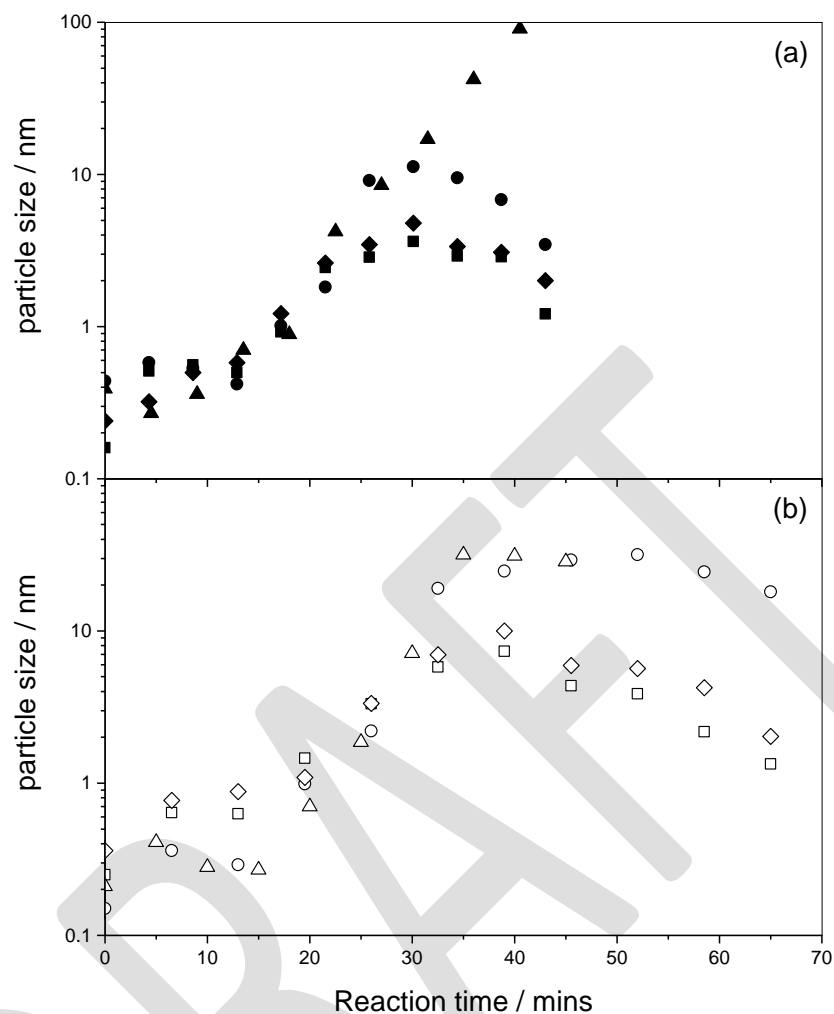
Figure 3: DLS particle size as a function of reaction time for RF gels synthesized as 1R:2F, 20% solids, 60 ml volume and (a) R/C 200 for Na_2CO_3 (■), K_2CO_3 (◆), Cs_2CO_3 (●), $CaCO_3$ (▲) and (b) R/C 400 for Na_2CO_3 (□), K_2CO_3 (◇), Cs_2CO_3 (○) and $CaCO_3$ (△).

In contrast to the previous study on fullerenes [25], Figure 4 shows that no discernible correlation exists between RF particle size and UV-Vis scattering at 340 nm. One explanation for this is that the total external surface area of the RF particles also has an effect on the amount of light absorbed by the sol. This effect was demonstrated by Fu *et al.* [27] who reported that as the particle size of a pigment dispersion decreased, the surface area increased and the absorption increased.
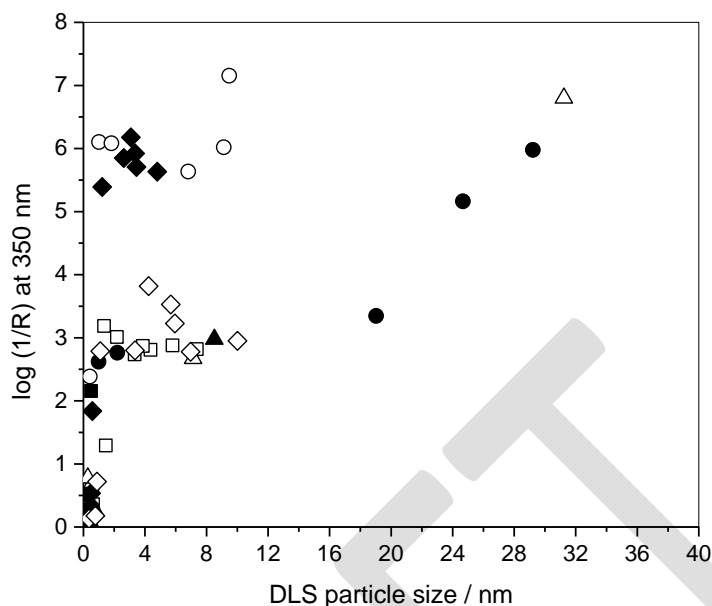
Figure 4: UV-Vis absorbance at 340 nm for RF gels synthesized as 1R:2F, 20% solids, 60 ml total volume and catalyst of: Na_2CO_3 at R/C 200 (■) and R/C 400 (□), K_2CO_3 at R/C 200 (◆) and R/C 400 (◇), Cs_2CO_3 at R/C 200 (○) and R/C 400 (●), and $CaCO_3$ at R/C 200 (▲) and R/C 400 (△).

In order to test this theory, absorbance spectra for Na, K, Cs and Ca catalysed gels were directly compared (Figure 5). The spectra for R/C 200 sols at $T_{20\%}$ indicate that, absorbance at 340 nm is in the order Na > Cs < Ca. This order of absorption is not as expected, as the Cs and Ca sols exhibit favoured particle aggregation and as a result increased colloidal particle size (as demonstrated by Figure 3), however, the smaller Na particles will have a larger surface area, which will scatter incident light in all directions, limiting the amount of light passing through and increasing sample absorbance. However, the spectra for sols prepared with R/C 400 at $T_{60\%}$, display the opposite trend, with Na_2CO_3 displaying lower absorbance than Cs_2CO_3 and $CaCO_3$. This order is as expected, with absorption increasing in the order of increasing particle size. At this lower concentration (i.e. R/C 400) the density of particles is reduced, thus the effect of particle surface area is less significant and UV absorption is based on particle size, with absorbance at $T_{60\%}$ in the order of increasing pore diameter (Na_2CO_3 = 7.37 nm, Cs_2CO_3 = 24.67 nm, $CaCO_3$ = 31.78 nm). From these results it appears that there are two opposing factors contributing to the UV-Vis scattering of RF sols (i.e. decreasing particle size increases surface area, which increases absorbance, but in general absorbance increases with increasing particle size) and as a result the absorbance at approximately 340 nm cannot be used to determine particle size within the sol.
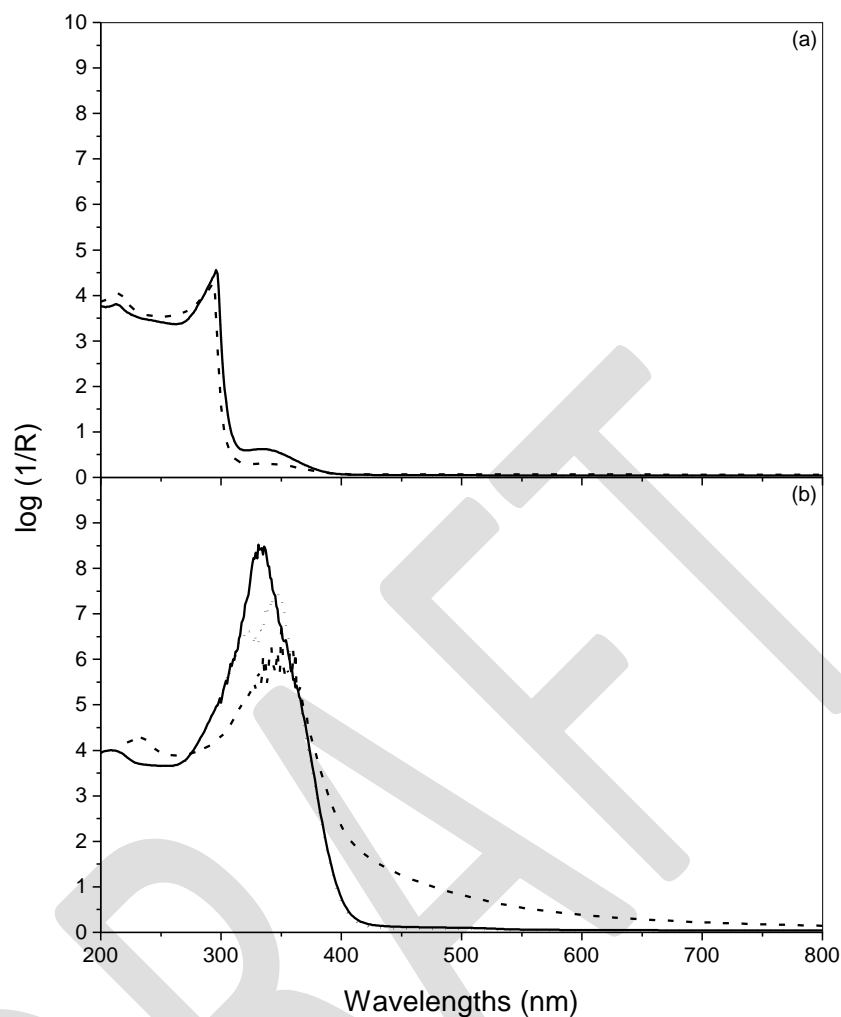
Figure 5: UV-Vis spectra (in the range 200-800 nm) for RF gels synthesized as 1R:2F, 20% solids, 60 ml total volume and catalyst R/C 200 for: Na_2CO_3 (·····), K_2CO_3 (-··-), Cs_2CO_3 (—) and $CaCO_3$ (--) sols at (a) $T_{20\%}$ and (b) $T_{60\%}$.

Goodner [28, 29] demonstrated that change in adsorption in the red region was dependent only on the turbidity of the sample and not on the sample chemistry. Goodner established that samples with the same chemical structure but different turbidities showed varying absorbance at 750 nm, demonstrating a linear relationship between absorbance at 750 nm and sample turbidity. Inspection of RF absorbance spectra (Figure 2) shows that, as reaction proceeds, absorbance in the green to red region (500 to 800 nm) increases. If the first region of decay in DLS is considered (i.e. the initial reaction, where particles grow gradually, before clusters aggregate quickly causing a significant increase in particle size) and the average particle size is plotted against the UV-Vis absorbance (log 1/R), at 500, 600 and 750 nm, it is evident that there is a relationship between particle size and absorbance. Figure 6 (a) to (c) illustrate that there is little change in the absorbance as the particles grow to approximately 20 nm, as the reaction proceeds further, particles grow and aggregate, resulting in a significant increase in turbidity (cloudiness) of the sample and a change in colour from pale

yellow to deep red, at this stage there is a linear relationship between particle size and absorbance at 500, 600 and 750 nm as shown in Figure 6.
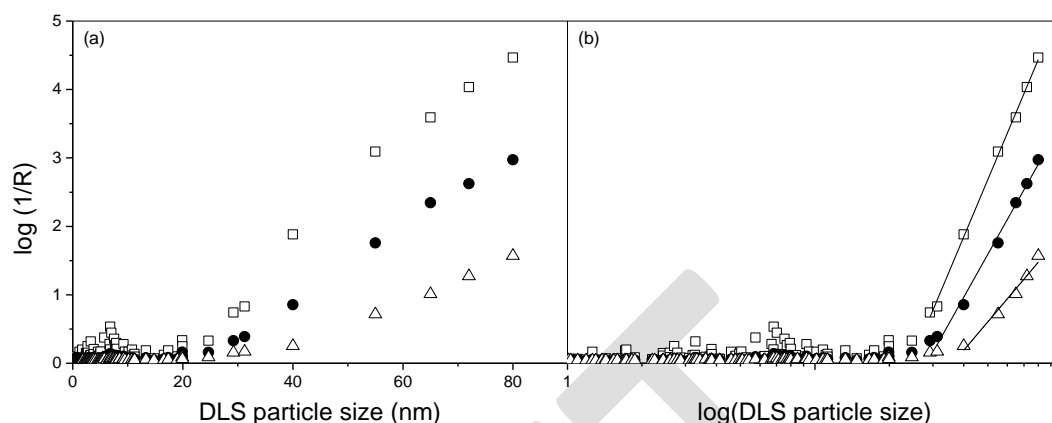
Figure 6: Plot of log (1/R) as (a) a function of DLS particle size and (b) log(DLS particle size) at 500 nm ($\square$), 600 nm ($\bullet$) and 750 nm ($\triangle$) for Na_2CO_3, K_2CO_3, Cs_2CO_3 and $CaCO_3$ at R/C ratios of 100, 200, 300, 400 and 500 (R/C 600 data also included for Group I catalysts).

Conclusion

The method presented in this study demonstrates that UV-Vis spectrometry can be used to monitor particle formation, during the sol-gel transition of RF xerogels. The UV-Vis absorbance measurements can be applied directly to RF sols, requiring no further sample preparation or dilution. Subsequently, as demonstrated by Figure 6, UV-Vis spectrometry can be used as a quick analysis tool to determine whether there are significant changes in particle size during gelation, and could be applied to different RF sol compositions or used to compare varying synthesis processes.

The linear relationships shown for these preliminary results also suggest that, with the collation of a reference library of particle sizes, it may possible to use UV-Vis spectrometry to determine RF particle sizes above 20 nm. This study demonstrates that wavelengths of 500, 600 and 750 nm can be used for particle size determination; however, as displayed in Figure 6, measurements at 500 nm provide absorbance values 2 x and 4 x as high as measurements at 600 and 750 nm respectively. For this reason 500 nm would be optimum wavelength for monitoring RF sol – gel transitions. In comparison to other methods used for particle size determination, i.e. DLS, SAXS and microscopic techniques, this method is simple and rapid allowing sol samples to be analysed straight from the oven and for results to be obtained in a matter of minutes.

References

1. Pekala RW, Kong FM (1989) A synthetic route to organic aerogels - mechanism, structure and properties. Journal De Physique 50 (C4):33-40
2. Pekala RW, Farmer JC, Alviso CT, Tran TD, Mayer ST, Miller JM, Dunn B (1998) Carbon aerogels for electrochemical applications. In: 5th International Symposium on Aerogels, Montpellier, France, Sep 08-10
Apr 1997. pp 74-80
3. Fricke J, Tillotson T (1997) Aerogels: production, characterization, and applications. Thin Solid Films 297:212-223
4. Moreno-Castilla C, Maldonado-Hodar FJ (2005) Carbon aerogels for catalysis applications: An overview. Carbon 43 (3):455-465. doi:10.1016/j.carbon.2004.10.022
5. Schaefer DW, Pekala R, Beaucage G (1995) Origin of porosity in resorcinol-formaldehyde aerogels. Journal of Non-Crystalline Solids 186:159-167
6. Horikawa T, Hayashi J, Muroyama K (2004) Controllability of pore characteristics of resorcinol-formaldehyde carbon aerogel. Carbon 42 (8-9):1625-1633. doi:10.1016/j.carbon.2004.02.016
7. Pekala RW, Kong FM (1988) Resorcinol-formaldehyde aerogels and their carbonized derivatives. National meeting of the American Chemical Society. Dallas, Texas, USA
8. Pekala RW, Schaefer DW (1993) Structure of organic aerogels. 1. morphology and scaling. Macromolecules 26 (20):5487-5493
9. Lee H-J, Song J-H, Kim J-H (1998) Synthesis of resorcinol/formaldhyde gel particles by the sol-gel emulsion gel technique. Materials Letters 37:1998
10. Sharma CS, Kulkarni MM, Sharma A, Madou M (2009) Synthesis of carbon xerogel particles and fractal-like structures. Chem Eng Sci 64 (7):1536-1543. doi:10.1016/j.ces.2008.12.013
11. Bock V, Emmerling A, Fricke J (1998) Influence of monomer and catalyst concentration on RF and carbon aerogel structure. Journal of Non-Crystalline Solids 225:69-73
12. Scherdel C, Scherb T, Reichenauer G (2009) Spherical porous carbon particles derived from suspensions and sediments of resorcinol-formaldehyde particles. Carbon 47 (9):2244-2252. doi:10.1016/j.carbon.2009.04.015
13. Bruce J, Berne J, Pecora R (2000) Dynamic light scattering: with applications to chemistry, biology and physics. Dover Publications, New York
14. Brown W (ed) (1993) Dynamic light scattering: the method and some applications. Clarendon Press, Oxford
15. Taylor S (2012) DLS study of the formation of RF xerogels. The University of Strathclyde, Glasgow
16. Yamamoto T, Mukai SR, Endo A, Nakaiwa M, Tamon H (2003) Interpretation of structure formation during the sol-gel transition of a resorcinol-formaldehyde solution by population balance. Journal of Colloid and Interface Science 264 (2):532-537. doi:10.1016/s0021-9797(03)00481-8
17. Wang JB, Yang XQ, Wu DC, Fu RW, Dresselhaus MS, Dresselhaus G (2008) The porous structures of activated carbon aerogels and their effects on electrochemical performance. Journal of Power Sources 185 (1):589-594. doi:10.1016/j.jpowsour.2008.06.070
18. Sepehri S, Garcia BB, Zhang QF, Cao GZ (2009) Enhanced electrochemical and structural properties of carbon cryogels by surface chemistry alteration with boron and nitrogen. Carbon 47 (6):1436-1443. doi:10.1016/j.carbon.2009.01.034
19. El Mir L, Kraiem S, Bengagi M, Elaloui E, Ouederni A, Alaya S (2007) Synthesis and characterization of electrical conducting nanoporous carbon structures. Physica B-Condensed Matter 395 (1-2):104-110. doi:10.1016/j.physb.2007.02.068
20. Berthon S, Barbieri O, Ehrburger-Dolle F, Geissler E, Achard P, Bley F, Hecht AM, Livet F, Pajonk GM, Pinto N, Rigaci A, Rochas C (2001) DLS and SAXS investigations of organic gels and aerogels. Journal of Non-Crystalline Solids 285 (1-3):154-161. doi:10.1016/s0022-3093(01)00447-1
21. Huber MM, Klein H, Ratke L (2004) DLS-based fractal analysis in early stage gelation. Particle & Particle Systems Characterization 20 (6):379-381. doi:10.1002/ppsc.200300899

22. Yamamoto T, Yoshida T, Suzuki T, Mukai SR, Tamon H (2002) Dynamic and static light scattering study on the sol-gel transition of resorcinol-formaldehyde aqueous solution. Journal of Colloid and Interface Science 245 (2):391-396. doi:10.1006/jcis.2001.8006

23. Laboratory NP (2012) http://www.kayelaby.npl.co.uk/chemistry/3_8/3_8_7.html. Accessed September 2012

24. Mrzel A, Mertelj A, Omerzu A, opic MC, Mihailovic D (1999) Investigation of Encapsulation and Solvatochromism of Fullerenes in Binary Solvent Mixtures. J Phys Chem B (103):11256-11260

25. Kato H, Nakamura A, Takahashi K, Kinugasa S (2009) Size effect on UV-Vis absorption properties of colloidal C60 particles in water. Phys Chem Chem Phys (11):4946–4948

26. Hart H, Craine LE, Hart DJ (eds) (2003) Organic chemistry - a short course. 11 edn. Houghton Mifflin Company, Boston, NY

27. Fu JM, Li Y, Guo JL (1998) Optical behavior of organic pigments in aqueous dispersions and its application. J Colloid Interface Sci 202 (2):450 - 455

28. Goodner KL (2008) www.sensusflavors.com, Turbidity, Tea, And UV-VIS. Sensus Technical Note (SEN-TN-0008). Accessed Sep 2012

29. Goodner KL (2008) www.sensusflavors.com, Estimating Turbidity (NTU) From Absorption Data. Sensus Technical Note (SEN-TN-0010). Accessed Sep 2012